Probing fundamentals of galaxy evolution and cosmology using supernovae

by

Thomas M. Sedgwick

A thesis submitted in partial fulfilment of the requirements of
Liverpool John Moores University
for the degree of
Doctor of Philosophy.
July 2021

Declaration

The work presented in this thesis was carried out at the Astrophysics Research Institute, Liverpool John Moores University. It is the original work of the author in its entirety with the exception of the following items:

Paragraph 4 of Section 1.3.1 was written by the author together will Phil James and has since been re-worked by the author. The code utilised to produce colour IAC STRIPE 82 LEGACY coadded images was written by Lee Kelvin. Equations 3.1 – 3.9 were derived by Ivan Baldry. Figure 1.1 was reproduced from Filippenko (1997) by the author. Figure 1.2 was reproduced from a combination of data from Wheeler & Harkness (1990) and Richardson et al. (2014). Figure 2.18 was reproduced from Jackson et al. (2021) by the author. Figure 3.1 was produced by Ivan Baldry.

While registered as a candidate for the degree of Doctor of Philosophy, for which submission is now made, the author has not been registered as a candidate for any other award. This thesis has not been submitted in whole, or in part, for any other degree.

Thomas M. Sedgwick
Astrophysics Research Institute
Liverpool John Moores University
IC2, Liverpool Science Park
146 Brownlow Hill
Liverpool
L3 5RF
UK

NOVEMBER 2021

Abstract

Supernovae are the explosive and luminous ends of life for a variety of types of star. They exhibit a wide diversity of light-curve shapes and chemical abundances as a function of their type. The physics of supernova explosions is one topic of ongoing research, particularly the mechanisms by which supernovae expel their outer layers and create remnants such as black holes and neutron stars. There is also much to be learnt about the progenitor stars of supernovae, from observing, for instance, the sites of SN explosions in pre-supernova imaging. Such a comparison of progenitor and supernova properties yields a direct picture of the end of the stellar evolutionary process. Supernovae also show fundamentals of nuclear and particle physics acting on human timescales and thus are perfect test-beds for such areas of science. However, what is of most interest in this thesis is the connection between supernovae, galaxy evolution, and our Universe's cosmology. This thesis presents novel techniques using supernovae as probes of galaxy evolution and cosmology. The tight connection between core-collapse supernova rates and star formation rates is firstly exploited to make significant contributions to 2 outstanding problems in the area of galaxy evolution: Core-collapse supernovae are used to probe the sub-structure problem, or the surplus of observed low-mass galaxies relative to the number predicted by simulations invoking a Λ-CDM cosmology, by detecting previously missed low surface brightness galaxies at these supernova positions and by utilising the relationship between the volumetric star formation rate density, specific star formation rate and the galaxy stellar mass function. These supernova rates are then utilised to measure the mean star formation rates of elliptical galaxies. It is currently unknown whether these galaxies are entirely quiescent or are instead maintaining a hard-to-measure low level of star formation at current epochs. Many Λ-CDM simulations predict that the latter is the case, due to the ongoing influence of minor mergers. Finally, the predictable luminosities of Type Ia supernovae are exploited for their use as 'standard candle' distance indicators, allowing definitive tests to be made for the effects of supernova environment on local measurements of the current rate of expansion of our Universe.

Thomas M. Sedgwick November 2021

Contents

List of Figures

List of Tables

Publications

During the course of the preparation of this thesis, the contents of Chapters 2.1 and 3 have been published in refereed journals:

- *The galaxy stellar mass function and low surface brightness galaxies from core-collapse supernovae*
  Sedgwick, T. M., Baldry, I. K., James, P. A., Kelvin, L. S., 2019, MNRAS 484, 5278

- *The galaxy stellar mass function from CCSNe with improved photo-z techniques*
  Sedgwick, T. M., Baldry, I. K., James, P. A., Kelvin, L. S., 2019,
  IAU Symposium 355: The Realm of the Low Surface Brightness Universe
  eds: D. Valls-Gabaud, I. Trujillo & S. Okamoto

- *The effects of peculiar velocities in SN Ia environments on the local H_0 measurement*
  Sedgwick, T. M., Collins, C. A., Baldry, I. K., James, P. A., 2021, MNRAS 500, 3728

- *The origin of low-surface-brightness galaxies in the dwarf regime*
  Jackson, R. A., Martin, G., Kaviraj, S., Ramsøy, M., Devriendt, J. E. G., **Sedgwick, T. M.**, Laigle, C., Choi, H., Beckmann, R. S., Volonteri, M., Dubois, Y., Pichon, C., Yi, S. K., Slyz, A., Kraljic, K., Kimm, T., Peirani, S., Baldry, I., 2021, MNRAS 502, 4262

The contents of Chapter 2.2 have been submitted for publication in a refereed journal:

- *The Star Formation Rates of Elliptical Galaxies from Core-Collapse Supernovae*
  Sedgwick, T. M., Baldry, I. K., James, P. A., Kaviraj, S., Martin, G., 2021, arXiv:2106.13812

Thomas M. Sedgwick November 2021

Acknowledgements

There is no other place to start a list of acknowledgements than with my first supervisor, Ivan Baldry. Ivan, you have been my guidance since 2016. On your first day as my masters supervisor, I remember you asking me whether I'd ever coded in Python before. When I replied 'No', I guess I expected some pointers or references to learn about key functions. Instead your reply was 'Good luck then'. In hindsight, this sentence summarised our relationship perfectly. You have always known when to tell me things, and when I will learn more by trying something out myself.

I would not be half as independent a researcher as I am without your judgement of such situations. Furthermore, your research ideas are the foundation of this work. I aspire to a career that leads me to even a fraction of your expertise.

With that said, it fitting to acknowledge my second supervisor, Phil James. Your lectures were my first exposure to extragalactic astrophysics. You showed me that astronomy is an exciting, ever-developing discipline. Your knowledge of astronomy is encyclopedic. I could say any term in astrophysics and you would provide me with an overview fit for MNRAS, straight off the cuff.

I also thank Chris Collins, for being my unofficial third supervisor. Aside from your unrivalled cosmological expertise, you have always provided humour when it was needed most.

I sincerely thank all members of the ARI that have passed through during my time as a PhD student, for making the atmosphere of the department so professional and inclusive. As I write this, in the second year of lockdown, what I miss most the coffee breaks, pub trips and football games that broke up the day and kept me motivated.

I thank Meghan Hughes as we've worked in parallel for nearly 8 years. You may not know it, but you have always set the bar for me for what it means to be passionate, disciplined and driven. I thank many other amazing friends; including Jon for always being there when a deep conversation was needed; Joaquin for his ability to add drums to any song idea and for being the perfect housemate; Conor for always being on hand

to discuss craft ale, Kingdom Come and whippets; and Mark, for being the closest thing I have to a brother. Other thanks go to lifelong friends Tom Parslow, Emmett Moore, Luca Mangano, Tiziano Tomasello, Serena Restivo, Charlotte Oddo and Craig McDonald.

I thank my parents, Caroline and Michael, and my sister, Ceri, whom I owe everything to. You have always believed in me, and have given me the resilience and support I needed to get through a total of 9 years of Physics & Mathematics, and to face the future without fear. I also thank my grandparents, George, Louise, Hilda and Wilf. It is such a shame that I cannot share my adult life with you, but I feel your support in all that I do.

Finally, I thank Sarah and Ziggy for their unwavering love. You have kept me just the right amount of crazy. I love you both.

The funding for this PhD was provided by an STFC doctoral studentship, jointly supported by the Faculty of Engineering and Technology at LJMU.

This thesis project has made use of data from the following resources:

- The SLOAN DIGITAL SKY SURVEY. Funding for the SDSS-II, SDSS-III and SDSS-IV has been provided by the Alfred P. Sloan Foundation, the National Science Foundation, the U.S. Department of Energy Office of Science, the National Aeronautics and Space Administration, the Japanese Monbukagakusho, the Max Planck Society, the Higher Education Funding Council for England, and the Participating Institutions. SDSS-IV acknowledges support and resources from the Center for High-Performance Computing at the University of Utah. The SDSS web site is www.SDSS.org.

- The TWO MICRON ALL SKY SURVEY, which is a joint project of the University of Massachusetts and the Infrared Processing and Analysis Center at the California Institute of Technology, funded by the National Aeronautics and Space Administration and the National Science Foundation.

- The COSMOSIM database, a service by the Leibniz-Institute for Astrophysics Potsdam (AIP). The MultiDark database was developed in cooperation with the Spanish MultiDark Consolider Project CSD2009-00064. I gratefully acknowledge the Gauss Centre for Supercomputing e.V. (www.gauss-centre.eu) and the Partnership for Advanced Supercomputing in Europe (PRACE, www.prace-ri.eu)

for funding the MultiDark simulation project by providing computing time on the GCS Supercomputer SuperMUC at Leibniz Supercomputing Centre (LRZ, www.lrz.de). The Bolshoi simulations have been performed within the Bolshoi project of the University of California High-Performance AstroComputing Center (UC-HiPACC) and were run at the NASA Ames Research Center.

- The Zooniverse.org platform, development of which is funded by generous support, including a Global Impact Award from Google, and by a grant from the Alfred P. Sloan Foundation. I acknowledge the role of citizen science in the production of GALAXY ZOO data.

- The GALEX-SDSS-WISE LEGACY CATALOG. The construction of GSWLC data was funded through NASA award NNX12AE06G.

All results and plots presented in this thesis were produced by myself using the `Python` language, barring Figure 3.1, which was produced by Ivan Baldry using the `IDL` language.

`Python` packages most notably utilised for this work include `numpy`, `scipy`, `matplotlib`, and `astropy`.

In the midst of winter
I finally learned
That there was in me an invincible summer

- Albert Camus

For George and Louise

Chapter 1

Introduction

1.1 Supernovae: A History

Supernovae (SNe) are the explosive and luminous ends of life for a variety of types of star. These phenomena play a crucial role in the chemical enrichment of our Universe, as it is within these violent events that the vast majority of the heavy elements are produced (e.g. Woosley & Weaver, 1986). As such, it is ancient SNe occurring about our location in the Universe that we have to thank for many of the constituents of the human body (Zoroddu et al., 2019).

Though originating in stars which are one in millions to trillions within their host galaxy, these objects can briefly, over the timescale of weeks to months, rival the luminosity of their host, and in the case of low-mass or dwarf galaxies even outshine them entirely (e.g. Hamuy et al., 1996; Sabatini et al., 2003). This property of SNe means that they have played a crucial role in the development of astronomy since antiquity. The year 185 AD marks the earliest known record of a potential SN event, when Chinese astronomers recorded a 'guest star' in their night sky (Zhao et al., 2006). As this event, like all SN discovered before the late 19th century, was within our own Milky Way, the object would have been visible for many months with the naked eye. One can only imagine the list of omens such an object would have been associated with.

Also recorded by Chinese astronomers in July 1054 was what is now known to be the SN associated with the Crab Nebula (Collins et al., 1999). The central pulsar of this nebula is the core remnant of the SN, and as such, is one of the only objects of its kind with a precise birth-date (Lundgren et al., 1995). Tycho Brahe was the discoverer of another early SN of the last millennium, which he labelled 'Nova Stella' in 1572 (e.g. Krause et al., 2008). This is where the suffix, 'nova' originates. The Prefix, 'super', first

introduced by Baade & Zwicky (1934), distinguishes the phenomena from novae, their far less luminous cousins.

Given recent estimates of the stellar mass and star formation rate (SFR) of the Milky Way (Licquia & Newman, 2015), SNe are expected to occur at an average rate of 2 per century in our galaxy. However, the last known Milky Way SN was recorded by Johannes Kepler in 1604 (Baade, 1943), and so either an event is statistically long overdue, measurements of our galaxy's mass and SFR are significantly miscalculated, or more-recent local SNe have occurred in particularly dust-obscured regions of our galaxy which has prevented their detection (Van Den Bergh & Tammann, 1991).

The advent of astronomical instrumentation led to the first observation of an extra-galactic SN in the late 19th century (De Vaucouleurs & Corwin, 1985). The 1970s saw the introduction of the CCD chip (Boyle & Smith, 1970), the high sensitivity of which, compared to photographic plates, accelerated the number of known SNe. Advances in both instrumentation and computing power allowed for the first robotic SN surveys in the 1990s, leading to the most periodic and unbiased scanning of the sky to date (e.g. Perlmutter et al., 1992).

These milestones, plus the ever-increasing magnitude depth of SN surveys mean that the number of SNe detected each year is ever increasing. As this text is written, in 2021, there are approximately 8×10^4 SNe recorded in the Open Supernova Catalogue (Guillochon et al., 2017), and over 6×10^4 of these have been detected in the last decade. Furthermore, we are at the edge of another acceleration in their detection with the next generation of wide-field SN surveys, such as that which is part of the 10-year Legacy Survey of Space and Time (LSST), conducted by the Vera C. Rubin Observatory, expected to come online in 2022 (Ivezić et al., 2019).

SNe are interesting phenomena to study in their own right: They exhibit a wide variety of light-curve shapes (or luminosity time evolution) and chemical abundances as a function of their type (Botticella et al., 2016). The physics of SN explosions is one topic of ongoing research, particularly the mechanisms by which SNe expel their outer layers and create remnants such as black holes and neutron stars (Umeda & Nomoto, 2003).

SNe show fundamentals of nuclear and particle physics acting on human timescales and thus are perfect test-beds for such areas of physics. There is also much to be learnt about the progenitor stars of SNe from their violent deaths. For instance, the sites of SN explosions can be examined in pre-SN imaging. By relating properties of a now-deceased star such as luminosity, mass, metallicity and environment (including

binarity) to the counterpart properties of the SNe, a direct picture of the end of the stellar evolutionary process is obtained, available for comparison with the predictions of evolutionary models (e.g. Eggenberger et al., 2008; Bersten et al., 2011). The most famous example of a study of pre-SN imaging from a stellar evolution perspective relates to SN1987A (McNaught et al., 1987; Gilmozzi, 1987). More recently, Hubble Space Telescope (HST) imaging has made use of this technique to study several progenitor stars (e.g. Li et al., 2006).

However, what is of most interest in this thesis is the connection between SNe, galaxy evolution, and our Universe's cosmology.

1.2 The Hierarchical Process & the Λ-CDM model

The now widely accepted picture for the evolution of galaxies is a 'bottom-up' hierarchical process in which structure first began to form via small dark matter (DM) density fluctuations in the primordial Universe. As DM collapsed about the locations of overdense peaks, low-mass haloes formed, and the first galaxies subsequently formed from the in-fall of baryonic matter into the potential wells of such haloes, before material cooled to the point that star formation could be triggered (White & Rees, 1978).

Dark matter is the dominant mass constituent of the universe with ~ 5 times the abundance of ordinary baryonic matter (e.g. Bennett et al., 2013), and the evolution of a galaxy's gas structure is thus determined by the evolution of the host DM halo. Haloes in denser environments began to assemble into larger and more massive haloes via gravitational interaction, producing the range of galaxy masses we observe at current epochs (Mo & White, 1996).

This hierarchical process is a key property of the Λ-CDM model, i.e. the parameterisation of the cosmological model which invokes a cosmological constant associated with the Universe's observed accelerating expansion ('Λ' in Einstein's field equations of general relativity; Einstein 1916) and which features DM particles travelling at velocities of a small fraction of the speed of light (the 'Cold' in Cold Dark Matter). This model is widely accepted as the 'standard model' of cosmology due to the fact that it simultaneously reproduces various observed properties of the Universe, one of which is the existence and structure of the cosmic microwave background. Its fluctuation size power spectrum indicates the preferential size of initial density fluctuations in the primordial Universe; a size consistent with Λ-CDM model predictions and a hierarchical formation of structure (Smoot et al., 1992; Bennett et al., 2013; Planck Collaboration et al., 2014).

Invoking instead the differing prescription of Warm Dark Matter (WDM), density fluctuations would be expected to be suppressed below a certain mass as a function of the DM particle mass (Bode et al., 2001), affecting the number of predicted low mass haloes. Forcing WDM models to match low mass halo counts, the slope of the observationally well-constrained Tully-Fisher (Luminosity vs Rotational Velocity) relation (Tully & Fisher, 1977) no longer matches observations (Kang et al., 2013), indicating the role of WDM in early structure formation is, at most, small. Λ-CDM also reproduces the observed large-scale structure, with model results matching the observed complex filaments and cosmic web (Benson, 2010). The predicted relative abundances of elements in the Universe are also found to be consistent with observation, as is the acceleration of the Universe (one mode of calculation of this acceleration is through the study of SNe as discussed in Chapter 3), explained through the invocation of dark energy.

For the numerous successes of Λ-CDM and the hierarchical process, there remain a number of fundamental problems that have yet to be explained through existing methodologies. **In this thesis, the overriding aim is to reach a solution to the following three problems:**

1. **The Sub-Structure Problem:** Is the observed surplus of low-mass / dwarf galaxies, relative to the number predicted by simulations invoking Λ-CDM, genuine ?
2. **The Star Formation Rates of Elliptical Galaxies**: At present epochs, are ellipticals truly quiescent, given that Λ-CDM predicts a low-level of star formation maintained by mergers?
3. **The Hubble Tension:** What is the cause of the persistent discrepancy between local ($z \lesssim 0.1$) estimates of the Hubble Constant (or the current rate of expansion of the Universe) and predictions from sound-horizon physics?

Problems **1** & **2** will be described in detail in Chapter 2 (in Sections 2.1 & 2.2, respectively), as will Problem 3, in Chapter 3. **The novel concept of this thesis is the way in which a solution for each of these problems will be attempted to be found: using SNe as statistical tools.**

1.3 Supernovae Physics and Properties

The most physically motivated mode to split SNe is into the classes of Core-Collapse Supernovae (CCSNe) and Thermonuclear (Type Ia) SN. Sections 1.3.1 and 1.3.2 outline the physical origins of these two SN types, respectively, and discuss the reasons for their applications to problems in galaxy evolution and cosmology within this thesis. Section 1.3.3 then gives a more empirical overview of the range of observational properties of supernovae and how they can be separated into alternative sub-classes according to empirical signatures.

1.3.1 Core-Collapse Supernovae

During the life of a star, the force of gravity is balanced by outward pressures maintained by fusion reactions in the stellar core. During the main-sequence lifetime, hydrogen is fused to form helium, dominantly via the pp-chain process in solar and sub-solar mass systems, which are relatively cool stars, with temperatures between 10-14 MK, and dominantly via the CNO-cycle in more massive, hotter systems, such as those which will end their lives as core-collapse supernovae (Salaris & Cassisi, 2005). The latter is a cyclic fusion chain in which carbon, nitrogen, and oxygen successively react with hydrogen nuclei to form helium along with neutrino, positron and gamma ray bi-products (Borexino Collaboration et al., 2020). In CCSN progenitors, it takes approximately 5-20 Myrs for the hydrogen in their cores to be exhausted in this manner (Bressan et al., 1981).

Next, hydrogen is burnt in a shell surrounding what is now a predominantly helium core, causing an expansion of the star and a consequential cooling of the outer layers. The massive star is now observed on the red supergiant branch. This cooling reduces the pressure in the core, increasing the core temperature and allowing for the fusion of helium. A convective, carbon-burning core is next surrounded by shells of He and H. This process continues for successively heavier elements up to the masses of iron and nickel. For such elements, more energy is required for further fusion reactions than can be generated at the corresponding core temperatures due to their extremely high binding energies (Fewell, 1995).

Once fusion reactions cease, outward pressures can no longer prevent gravitational collapse. The outer layers of the core collapse inwards at up to 70000 km s^{-1} (Fryer & New, 2011). Once a given pressure is reached, it becomes favourable for protons and electrons to merge via inverse beta decay into neutrons and neutrinos. Core-collapse

is eventually halted by neutron degeneracy pressure and strong-force repulsion. In the case of stars with initial masses $\gtrsim$ 40 $M_\odot$, where the intense associated gravity may overcome the gravitational potential energy, all that may be produced is a direct black hole (Heger et al., 2003). Yet for stars with initial masses of $\sim$ 8-40 $M_\odot$, almost instantaneously, the neutrinos produced in the aforementioned decay carry away energy from the core and initiate a supernova explosion via their mass absorption by the outer layers of the star (Hayakawa et al., 2006). The initial spike in luminosity is powered in this manner, but the light curve is dominated and sustained by radioactive heating of the ejecta, mainly through the decay of Ni-56 to Co-56 and Fe-56 which produces gamma-rays (Hillebrandt & Niemeyer, 2000a).

The key property of CCSNe which will be exploited in this thesis is the extremely short lifetimes of their progenitor stars, relative to the timescale of galaxy evolution. The lower mass limit for zero-age main sequence stars that end their lives as CCSNe has been closely constrained by numerous studies, with the review of Smartt (2009) presenting a consensus value of $8 \pm 1\,M_\odot$. The upper-mass limit is much more uncertain, due to the possibility that the highest mass stars may collapse directly to black holes, with no visible explosion. However, it seems likely that stars at least as massive as $30\,M_\odot$ explode as luminous CCSNe; Botticella et al. (2017) adopt an upper mass limit of $40\,M_\odot$. The corresponding range of lifetimes of CCSN progenitors is then something like 6 – 40 Myr, for single star progenitors (see, e.g. Maund, 2017); mass-exchange in high-mass binary stars can extend these lifetimes (e.g. Smith & Tombleson, 2015). Even with this extension, it is clear that on the timescales relevant for studies of galaxy evolution, rates of CCSNe can be taken as direct and virtually instantaneous tracers of the current rate of star formation.

1.3.2 Type Ia Supernovae

Type Ia SNe originate in binary star systems and do not require either star in this system to be of high mass. The traditional picture of their progenitor system sees the accretion of matter onto a carbon-oxygen white dwarf from a companion star, for example, a red giant star (e.g. Nugent et al., 2011). This process continues until the dwarf approaches a critical mass of 1.44 solar masses ($M_\odot$), known as the Chandrasekhar Limit. A competing theory for the origin of the majority of Type Ia SNe is the double-degenerate channel, which instead involves the interaction of two white dwarfs (e.g. Han, 1998).

What is not debated however is that these explosions are powered by a runaway explosion within the core of a white dwarf (e.g. Hillebrandt & Niemeyer, 2000b). The

fact that these objects explode at a critical mass means they produce a notably narrow distribution of luminosities once corrected empirically for light curve shape (Phillips, 1993; Tripp, 1998; Guy et al., 2007; Richardson et al., 2014, see also Figure 1.2). This factor has led to their frequent use as 'Standard Candle' distance indicators, which gives them 2 main applications. Firstly, by measuring the distance to a galaxy via a Type Ia SN residing within it, intrinsic galaxy properties such as stellar mass and physical size can be accurately inferred (e.g. Holwerda et al., 2015). Secondly, and most importantly for this thesis, they can be used as cosmological probes (e.g. Tully et al., 2013; Riess et al., 2016), as is discussed in detail in Chapter 3.

The delay-time distribution of Type Ia Supernovae is the probability of such a supernova type occurring at a given location in the Universe as a function of time since a burst of star formation at that same location. Following this burst, there is an initial period of zero probability of observing an associated Type Ia, corresponding to the time taken for the first white dwarfs to form from this burst. Estimates of this initial period vary from $\sim$ 40 to 100 Myr (Maoz et al., 2012; Heringer et al., 2019). The shape of the delay-time distribution is still an active source of debate, and depends on factors such as the distribution of orbital separations of white dwarfs after a common-envelope phase (in the double-degenerate scenario; Ivanova et al. 2013), and the mass transfer efficiency and binary ratio of stars (in the single-degenerate scenario; Greggio 2005). The broad consensus is that the Type Ia SN probability peaks $\sim$ 1 Gyr following star formation and decays according to a power law with a slope between –1 and –1.5 (Maoz et al., 2012; Heringer et al., 2017, 2019). This means that, unlike core-collapse supernovae, the lifetimes of Type Ia progenitors can rival the timescales of galaxy evolution, and therefore, their frequencies are not directly linked to their environments' recent star formation rates.

1.3.3 Observational Properties of Supernovae

One alternative, more observationally motivated way to subdivide SNe is by the quantity of hydrogen in their early-time spectra: Type I SNe are characterised by a lack of hydrogen in their spectra near peak light, whereas Type II SN spectra instead exhibit hydrogen lines in abundance at similar epochs (e.g. Turatto, 2003). Type Ia SNe also have pronounced Si-II absorption features in their spectra. Type Ib and Ic SN spectra are distinguished by the respective presence or absence of He I lines.

Type II SNe are most commonly divided into 4 sub-classes via a combination of their spectral and light curve properties. Type IIP SNe are the most common Type II variety

(Richardson et al., 2014), which are characterised by a short decline from maximum light followed by a plateau of 2-3 months (Wheeler & Harkness, 1990). It should be noted that any chemical-based SN classifications are based on abundances in the optically thin outermost layers of the supernovae: The Type IIP plateau is thought to be caused by the increase in opacity of the outer layers of the supernova which occurs due to shock heating and ionization of these layers' hydrogen as the supernova wave-front propagates. This high opacity prevents the escape of photons, keeping the luminosity relatively constant. Once the hydrogen in the outer layers has cooled sufficiently for recombination, the opacity is reduced and photons can escape, ending the plateau phase (Doggett & Branch, 1985).

Type IIL SNe show the most rapid linear decline to luminosity of the 4 sub-types as shown in Figure 1.2. Type IIn SNe have a notably slow light curve evolution. Strong Balmer lines dominate the spectra for this subclass, thought to be caused by the interaction of the SN ejecta with a particularly dense circumstellar medium, itself thought to be associated with mass loss from the progenitor star (Filippenko, 1997).

Finally, Type IIb SNe show evidence of hydrogen in spectra taken close to the epoch of maximum light, yet this abundance fades soon after peak light, and is replaced by spectral properties similar to a Type Ib supernova, when a notable abundance of He-I arises. Type IIb SNe could occur if a progenitor star had expelled almost all of its hydrogen envelope. With the expansion of the ejecta, the hydrogen layers would eventually become transparent, revealing a hidden abundance of helium (Utrobin, 1996).

Figure 1.1 highlights some key differences in the spectra of common supernova types. Figure 1.2 shows schematic light curves for several of the aforementioned SN types. It is clear from the similarities in several of these light curves that the combination of spectral and photometric information is often required for the confident classification of SNe (see Chapter 2).

1.4 This Thesis

To summarise the motivations of this chapter, this thesis will attempt to solve 3 key outstanding problems in the topics of galaxy evolution and cosmology using SNe as novel tools. These problems are:

1. **The Sub-Structure Problem**

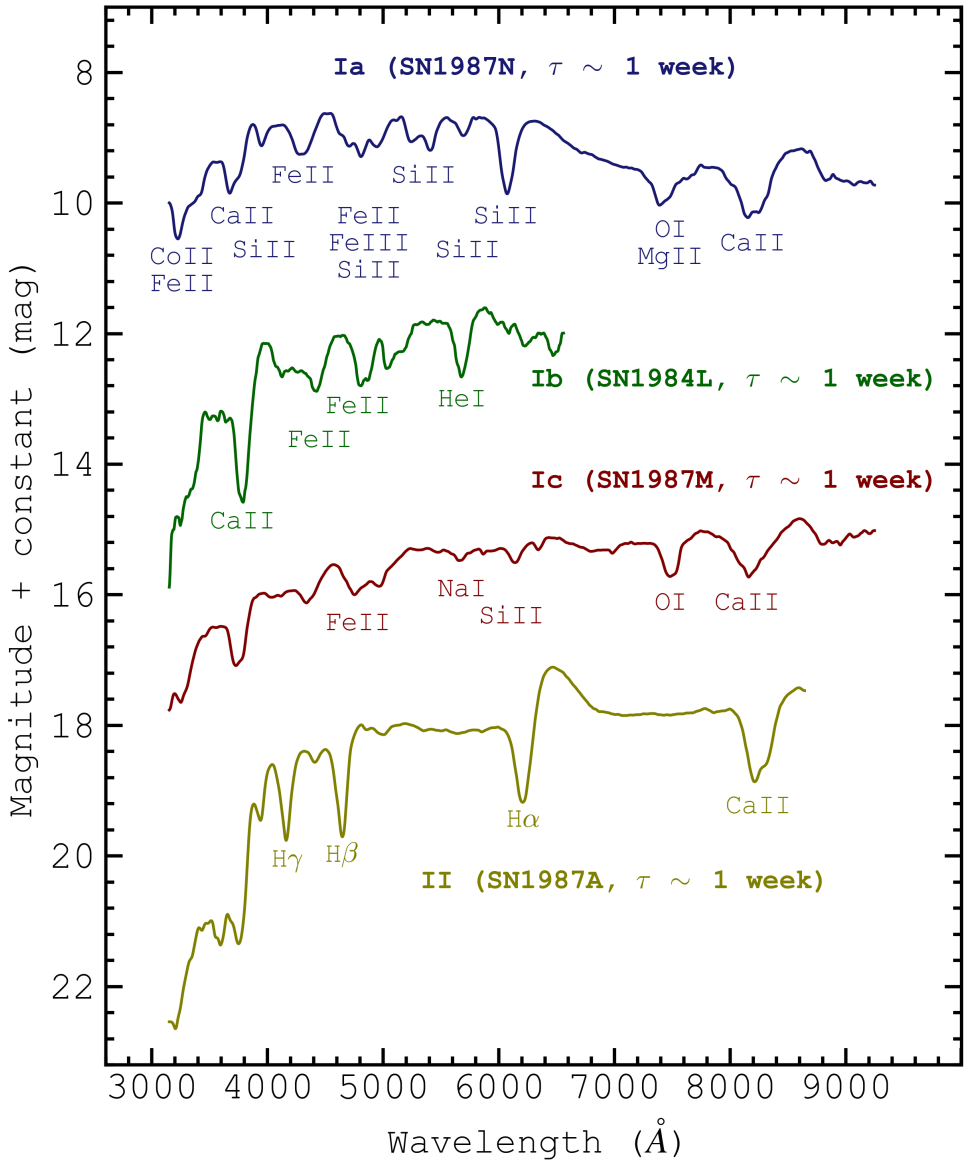

FIGURE 1.1: Example spectra demonstrating the chemical properties of differing SN types as a function of rest-frame wavelength (adapted from Filippenko 1997). Each spectrum shown was measured approximately 1 week after the epoch of maximum light.

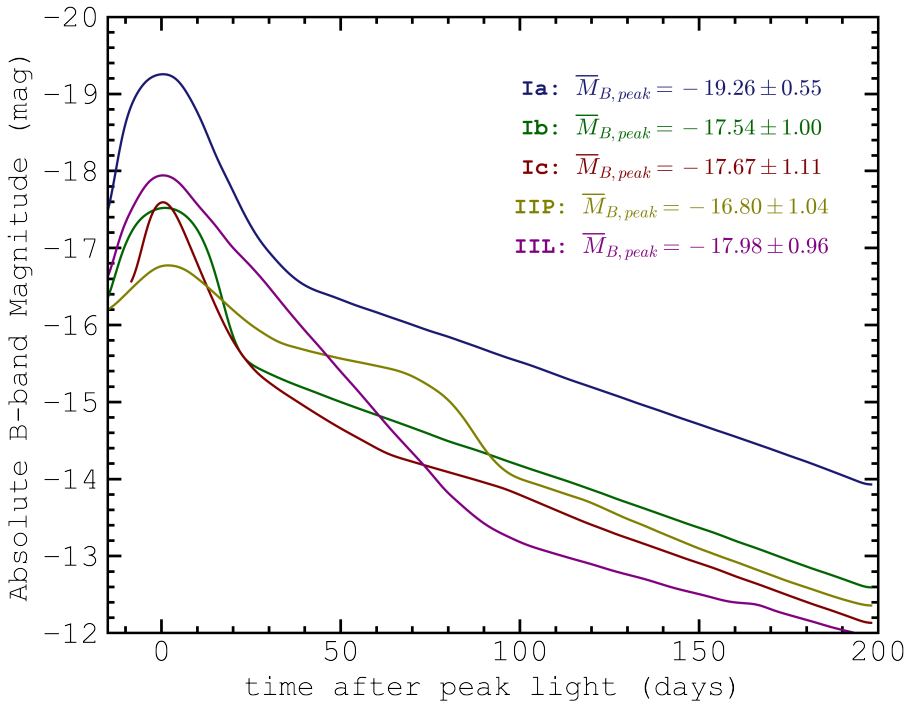

FIGURE 1.2: Schematic light curves of various SN types, adapted from Wheeler & Harkness (1990) and re-scaled such that peak B-band magnitudes match those estimated by Richardson et al. (2014) (i.e. the values inset within the figure, along with their standard deviation within volume limited samples of each SN type.)

2. **The Star Formation Rates of Elliptical Galaxies**

3. **The Hubble Tension**

Chapter 2 attempts to address Problems **1** & **2**, using CCSNe as probes of star formation and galaxy number density. Chapter 3 lends its focus to Problem **3**, in which Type Ia SNe are used as standard candle distance indicators to study the current rate of expansion of our Universe, or the Hubble Constant. More specifically, the relationship between the environment of the SNe and measurements of the Hubble Constant will be explored in detail. Finally, Chapter 4 presents a summary of the findings of this thesis, outlines the potential solutions to the aforementioned problems with our understanding of the hierarchical formation and the Λ-CDM model, and suggests how the next generation of SN and galaxy surveys coupled with the methods of this thesis might lead to a deeper understanding of our Universe.

Chapter 2

Core-Collapse Supernovae as Tracers of Galaxy Evolution

2.1 The Galaxy Stellar Mass Function and Low Surface Brightness Galaxies from Core-Collapse Supernovae

2.1.1 The Sub-Structure Problem

The GSMF is a direct probe of galaxy evolution, as mass is known to be a primary driver of differences in galaxy evolution. For example, Kauffmann et al. (2003) find galaxy colours, star-formation rates and internal structure all correlate strongly with stellar mass. It is argued by Thomas et al. (2010) that early-type galaxy formation is independent of environment and controlled solely by self-regulation processes, which depend only on intrinsic galaxy properties including mass. Pasquali et al. (2009) demonstrate that star-formation and AGN activity show the strongest correlations with stellar mass. Past attempts to measure the low-redshift GSMF have established clear evidence of a low-mass upturn in galaxy counts, indicating that low mass galaxies dominate the galaxy population by number at current epochs (Baldry et al. 2012; see also Cole et al. 2001; Bell et al. 2003; Baldry et al. 2008; Li & White 2009; Kelvin et al. 2014)

The majority of cosmological simulations today invoke a Λ-CDM description of our Universe, due to its ability to simultaneously reproduce various observable properties of the Universe (Perlmutter et al., 1999; Bennett et al., 2013). Despite these successes, a major challenge to the Λ-CDM model today is the 'sub-structure problem'. Numbers of dwarf galaxies as predicted by straightforward simulations are significantly larger

than those observed, and as a consequence, so too is the overall number of galaxies on cosmological scales (Moore et al., 1999). This discrepancy in dwarf galaxy counts is reflected in the form of the GSMF.

The observed number density of dwarf galaxies increases down to $\sim 10^8$ $M_\odot$, below which the form of the GSMF is uncertain due to the incompleteness of low surface brightness galaxy counts (e.g. Bell et al., 2003; Baldry et al., 2008; Drory et al., 2009; Baldry et al., 2012; Tomczak et al., 2014; Wright et al., 2017). The related uncertainties on the low mass counts mean that one cannot rule out a turn-down in number density which would indicate the need to deviate from a Λ-CDM cosmology.

The majority of state-of-the-art cosmological simulations of galaxy evolution such as EAGLE (Schaye et al., 2015; Crain et al., 2015) and ILLUSTRIS (Genel et al., 2014) hint towards a power law rise to galaxy number counts in the dwarf regime, but these are indeed only hints, as such a calculation pushes these simulations to the limits of their resolution (See, e.g. Schaye et al. 2015). An accurate observational assessment of the GSMF at low masses will be crucial for the next generation of cosmological simulations, many of which will be intentionally tailored to dwarf galaxy science similar to Dubois et al. (2020), who have recently utilised a 34-parsec resolution, 16 Mpc^3 box, evolved from a much larger 1 Gpc^3 box to begin to study the dwarf galaxy regime as well as the clumpiness of star formation in galaxies and the nature of the interstellar medium. As increased resolution and box size becomes less computationally expensive, such simulations will require an improved observational benchmark, as the only information currently available on dwarf galaxy counts are upper limits.

Almost all galaxy surveys suffer from a combination of magnitude and surface brightness constraints (Cross & Driver, 2002; Wright et al., 2017). Most dwarf systems (typically $\lesssim 10^8 M_\odot$, Kirby et al. 2013) have intrinsically lower surface brightnesses than their higher mass counterparts, and consequently, the lower mass end of the GSMF may be underestimated due to sample incompleteness, with lower surface brightness galaxies more likely to be missed by galaxy surveys. The current observed number densities of low mass galaxies can be treated as a lower limit when constraining evolutionary models (Baldry et al., 2008).

Knowing the precise form of the GSMF is clearly crucial should one wish to use it as a diagnostic of galaxy evolution. Developing techniques to increase completeness of the low mass end of the GSMF must be the focus should one wish to use it to assess the nature of the physics which controls this evolution.

In this section, one such technique is developed and implemented, using the SDSS-II SUPERNOVA SURVEY (Sako et al., 2018a) to produce a sample of galaxies located at the positions of core-collapse supernovae (CCSNe). As CCSNe peak at luminosities of 10^8 – 10^9 $L_\odot$, they can be used as pointers to their host galaxies, which may have been missed from previous galaxy surveys due to their low surface brightness: The Palomar Transient Factory (Law et al., 2009) located low surface brightness galaxies (LSBGs) when combining SN positions with imaging taken pre-supernova or long after SN peak epoch (Perley et al., 2016). As well as aiding the identification of LSBGs, a galaxy selection using a complete sample of supernovae may significantly reduce surface brightness and magnitude biases if the host galaxy is identified for each SN in a sample.

As detailed in Chapter 1, CCSNe are perhaps the most direct and indisputable tracers of star formation available, due to the fact that their short lifetimes, relative to the timescales of galaxy evolution, yield a tight link between the rates of star birth and star death. Several studies have made use of CCSNe as an indicator of star formation in the local Universe. On the most local scales, both Botticella et al. (2012) and Xiao & Eldridge (2015) have compared CCSN rates and integrated star formation rates within a spherical volume of radius 11 Mpc centred on the Milky Way, finding good agreement between observed and predicted numbers of SNe. A similar conclusion was also reached by Cappellaro et al. (1999), looking at a rather more extended (mean distance ∼40 Mpc) sample of SNe and host galaxies. Other studies have used CCSNe to probe star formation at intermediate redshifts, e.g. Dahlen et al. (2004) who investigated the increase in the cosmic star-formation rate out to redshift ∼0.7, and Botticella et al. (2017) whose sample of 50 SNe mainly occurred in host galaxies in the redshift range 0.3 – 1.0. Pushing to still higher redshifts, Strolger et al. (2015) have investigated the cosmic SF history out to z∼2.5 using CCSNe within galaxies from the CANDELS (Grogin et al., 2011) and CLASH (Postman et al., 2012) surveys.

Supernovae have also been used to investigate SF in different environments and types of galaxies, e.g. in starbursts (Miluzio et al., 2013) and galaxies with Active Galactic Nuclei (Wang et al., 2010), and to determine the metallicity dependence of the local SF rate (Stoll et al., 2013).

By selecting galaxies using CCSNe and measuring galaxy stellar masses, the resultant number densities as a function of mass imply CCSN-rate densities as a function of mass (ρ_{CCSN}) in units of $\mathrm{yr}^{-1}\mathrm{Mpc}^{-3}$, under the assumption that the CCSN sample itself is complete. By assuming a relationship between core-collapse supernova rate and star-formation rate, the star-formation rate density (SFRD; $\mathrm{M}_\odot\mathrm{yr}^{-1}\mathrm{Mpc}^{-3}$) can be traced.

The well-established star-forming galaxy main sequence (Noeske et al., 2007a; Davies et al., 2016; McGaugh et al., 2017; Pearson et al., 2018) can then be used to determine typical star-formation levels expected for a given stellar mass, to infer star-forming galaxy number densities (Mpc^{-3}) as a function of galaxy stellar mass (the GSMF), such that $\rho_{CCSN} \rightarrow \rho_{SFR} \rightarrow$ GSMF.

A programme similar to that in the present section was proposed by Conroy & Bullock (2015) who suggested that SNe detected by the Large Synoptic Survey Telescope from 2021 could be used as a statistical probe of the numbers and stellar masses of dwarf galaxies. The present section can be seen as a precursor to such a study.

The structure of the present section is as follows. Section 2.1.2 outlines in further detail the connections between CCSN-rate density, star-formation rate density, and the galaxy stellar mass function, along with the assumptions required to form them. In Section 2.1.3 the relevant data sets are presented. Sections 2.1.4 and 2.1.5 presents a methodology for drawing from these complete SN and galaxy samples, unbiased by magnitude and surface brightness. Section 2.1.6 discusses the spectroscopic redshifts of galaxies used where available, which are important for their stellar mass calculations. Section 2.1.7 presents 2 original photometric redshift estimators which are used in the absence of spectroscopic redshifts. Sections 2.1.11 and 2.1.12 present SFRD and star-forming GSMF estimates respectively, both obtained via a CCSN host galaxy selection, where comparison is drawn with existing SFRD and GSMF results, both observational and simulated. Finally, Section 2.1.13 presents the relationship between galaxy surface brightness and stellar mass for the sample of CCSN hosts. Therein, this relationship is compared with predictions from recent hydrodynamical simulations to test the compatibility of observations with the Λ-CDM framework.

2.1.2 The Relationship Between Core Collapse Supernova Rate Density and the Star-Forming Galaxy Stellar Mass Function

In this section, the relationship between the CCSN-rate density, the SFRD, and the GSMF is represented mathematically. This shows how one is able to arrive at an estimate for the GSMF beginning with a measurement of the CCSN-rate density as a function of host galaxy stellar mass ($\mathcal{M}$).

For a volume-limited sample of galaxies, the binned GSMF is defined by

$$\Phi(\mathcal{M}) = \frac{1}{\Delta \log \mathcal{M}} \frac{N(\mathcal{M})}{V} \tag{2.1}$$

over a mass bin of width $\Delta \log \mathcal{M}$, where N is the number of galaxies in the bin, and V is the volume. In other words, the GSMF is the number of galaxies, per unit volume, per logarithmic bin of galaxy stellar mass.

The SFRD is often estimated for the entire galaxy population, particularly as a function of redshift (Madau & Dickinson, 2014), but it can also be determined as a function of galaxy mass (Gilbank et al., 2010). This can then be given by

$$\rho_{\rm SFR}(\mathcal{M}) \;=\; \frac{1}{\Delta \log \mathcal{M}} \frac{\sum_{i=1}^{N} \mathcal{S}_i \, \mathcal{M}_i}{V} \tag{2.2}$$

where $\mathcal{S}_i$ is the *specific* star-formation rate (SSFR) for each of the N galaxies in a bin. In other words, the SFRD is the summed star-formation rate, per unit volume, per logarithmic bin of stellar mass.

The SFRD can then be approximated by considering that the majority of star formation in the Universe occurs on the galaxy main sequence (Noeske et al., 2007a; Davies et al., 2016; McGaugh et al., 2017). This sequence represents the relation, and its scatter, of SFR versus mass for typical star-forming galaxies. The SFRD can then be given by

$$\rho_{\rm SFR}(\mathcal{M}) \;=\; \frac{1}{\Delta \log \mathcal{M}} \frac{\overline{\mathcal{S}}(\mathcal{M}) \, \mathcal{M} \, N_{\rm SF}(\mathcal{M})}{V} \tag{2.3}$$

where $N_{\rm SF}$ is number of star-forming galaxies in the bin, $\mathcal{M}$ is the mid-point mass (assuming $\Delta \log \mathcal{M} \ll 1$), and $\overline{\mathcal{S}}$ is the mean SSFR for star-forming galaxies.

A 'star-forming galaxy', here refers to all galaxies that are not permanently quenched or virtually quenched with minimal residual star formation. In other words, these are the galaxies that are represented by the cosmological SFRD as a function of mass. Note that in the estimate of the mean $\mathcal{S}$, one should include galaxies that are in a quiescent phase but are otherwise representative of the typical star-forming population, and the CCSN-host galaxy selection method presented in this chapter naturally leads to an appropriate contribution from such galaxies. This is relevant for low-mass galaxies that undergo more variation in their SFR with time (see, e.g. Skillman, 2005; Stinson et al., 2007). The mean $\mathcal{S}$ should represent an average over duty cycles in this regime.

Comparing with Eq. 2.1, it is noted that the SFRD can be rewritten in terms of the GSMF of star-forming galaxies $\Phi_{\rm SF}$ as follows

$$\rho_{\rm SFR}(\mathcal{M}) \;=\; \overline{\mathcal{S}}(\mathcal{M}) \, \mathcal{M} \, \Phi_{\rm SF}(\mathcal{M}) \tag{2.4}$$

By using a parameterisation of SSFR with galaxy stellar mass, (e.g. Noeske et al., 2007a;

Speagle et al., 2014), it is possible to estimate the GSMF for star-forming galaxies from the SFRD or vice versa.

The observed CCSN-rate density is next considered, which is defined as the rate of CCSNe observed over a defined volume of space (redshift and solid angle limited), per unit volume, per logarithmic bin of galaxy stellar mass. From a non-targeted supernova survey, like that of SDSS (Frieman et al., 2008; Sako et al., 2018a), this is given by

$$\rho_{\mathrm{CCSN,obs}}(\mathcal{M}) \;=\; \frac{1}{\Delta \log \mathcal{M}} \, \frac{n_{\mathrm{CCSN,obs}}(\mathcal{M})}{\tau \, V} \tag{2.5}$$

where $n_{\mathrm{CCSN,obs}}$ is the number of observed CCSNe associated with galaxies in the bin, and τ is the effective rest-frame time over which CCSNe could be identified. The time period of the supernova survey, in the average frame of the host galaxies (τ), is shorter than that in the observed frame (t), such that τ = t / (1+$\overline{z}$).

The relationship between the CCSN rate and SFRD is then given by

$$\rho_{\mathrm{CCSN,obs}}(\mathcal{M}) \;=\; \rho_{\mathrm{SFR}}(\mathcal{M}) \, \overline{\epsilon}(\mathcal{M}) \, \overline{\mathcal{R}}(\mathcal{M}) \tag{2.6}$$

where $\overline{\mathcal{R}}$ is the mean ratio of CCSN rate to SFR, which is equivalent to the number of core-collapse supernovae per mass of stars formed; and $\overline{\epsilon}$ is the mean efficiency of detecting supernovae. For an apparent-magnitude limited supernova survey, the latter function accounts for varying brightnesses and types of supernova occurring in star-forming galaxies of a given stellar mass, and the variation in extinction along different lines of sight to the supernovae.

By combining these relations one arrives at

$$\Phi_{\mathrm{SF}} \;=\; \frac{\rho_{\mathrm{CCSN,obs}}}{\overline{\epsilon} \, \overline{\mathcal{R}} \, \overline{\mathcal{S}} \, \mathcal{M}} \tag{2.7}$$

which explicitly relates CCSN-rate density to the star-forming GSMF. The connection is given in terms of three functions of galaxy stellar mass: $\overline{\mathcal{S}}$ is the SSFR relation of the galaxy main sequence; $\overline{\mathcal{R}}$ is the number of CCSNe per unit mass of stars formed; and $\overline{\epsilon}$ is the efficiency of detecting CCSNe, which depends on their luminosity function, and also non-intrinsic effects of sample selection and survey strategy, in particular, the limiting CCSN detection magnitude. The basic premise is that these should be a weak function of galaxy stellar mass. The effects of varying ϵ on the CCSN-rate density is investigated in Section 2.1.10. The effects of varying $\overline{\mathcal{S}}$ on the GSMF are shown in Section 2.1.12.

2.1.3 Relevant Data Sets

The present section makes use of 3 data sets, all of which are data products of the SLOAN DIGITAL SKY SURVEY (SDSS). SDSS is a large-area imaging survey of mainly the north Galactic cap, with spectroscopy of $\sim 10^6$ galaxies and stars, and $\sim 10^5$ quasars (York et al., 2000). The survey uses a dedicated, wide-field, 2.5 m telescope (Gunn et al., 2006) at Apache Point Observatory, New Mexico. A 142 megapixel camera, using a drift-scan mode (Gunn et al., 2006), gathers data in 5 optical SLOAN broad band filters, *ugriz*, approximately spanning the range from 3000 to 10,000 Å, on nights of good seeing. Images are processed using the software of Lupton et al. (2001) and Stoughton et al. (2002). Astrometric calibrations are achieved by Pier et al. (2003). Photometric calibrations are achieved using methods described by Hogg et al. (2001) and Tucker et al. (2006) via observations of primary standard stars observed on a neighbouring 0.5m telescope (Smith et al., 2002).

This chapter makes use of data associated with the STRIPE 82 Region, a 275 sq. degree equatorial region of sky (Baldry et al., 2005). The region spans roughly $20^{\rm h} <$ R.A. $< 4^{\rm h}$ and $-1.26° <$ Decl. $< 1.26°$. Between 1998 and 2004, the region was scanned $\sim$80 times. A further $\sim$200 images were taken between 2005 and 2007, as part of the SDSS-II SUPERNOVA SURVEY (Frieman et al., 2008; Sako et al., 2018a).

The SDSS-II SUPERNOVA SURVEY data release outlined in Sako et al. (2018a) forms the basis of the supernova sample used in this chapter. 10258 transient sources were identified using repeat *ugriz* imaging of the region, with light curves and follow-up spectra used for transient classifications, all of which are utilised in this chapter to produce a SN sample, with great care taken to ensure its completeness and the removal of non-SN transients.

One aims to produce a galaxy sample selected via the SNe which they host. Host galaxies for many of the transient sources were already identified as part of the Supernova Survey. However, in the present section, host-galaxy identification is revisited for 2 reasons: i) There is now access to deeper, coadded SDSS imaging with which to search for the host galaxy. ii) There is often a natural bias towards assigning a transient to a higher surface brightness galaxy when one or more lower surface brightness galaxy is nearby. The method of transient-galaxy matching presented in this section is specifically designed to address this bias.

To form this galaxy sample, both single epoch imaging and multiple epoch SDSS imaging are utilised. Single epoch imaging published as part of SDSS-IV DR14 forms the initial

galaxy sample (often referred to in the present section as the SDSS sample for simplicity), and the sample of stars used for the removal of variable stars from the SN sample, as outlined in Sections 2.1.4.1 and 2.1.5.1 respectively. Galaxy and star classification is described in Section 4.4.6 of Stoughton et al. (2002).

Next, coadds of multiple epoch imaging are utilised. The IAC STRIPE 82 LEGACY project (Fliri & Trujillo, 2016) performed median stacking of existing STRIPE 82 LEGACY data, with additional complex sky-subtraction routines applied thereafter, in order to reach the extremely faint limits of the data ($\sim$28.5 mag arcsec^2 to 3σ for 10$\times$10 arcsec^2). The IAC STRIPE 82 LEGACY catalogue hence forms a deeper sample of objects used in this section. Approximately 100 single epoch images are median stacked per SN region, to produce the deeper imaging crucial for LSBG detection. From this coadded imaging the aim is to identify additional low-surface brightness galaxies not found by the SDSS sample. IAC STRIPE 82 image mosaicking and postage stamp creation about the positions of SNe, crucial for host galaxy identifications, are completed using the Cutout and Mosaicking Tool, part of the ARI Survey Imaging Tools. The completeness of the SDSS sample is compared with the sample found by Fliri & Trujillo (2016) from this coadded data, as well as with a `SExtractor` implementation designed as a bespoke search for CCSN host galaxies, using the same data (Section 2.1.5.3), in order to demonstrate the sensitivity of results to sample incompleteness.

Redshift estimates are also required for the SN-galaxy pairs. Approximately 480 of the SN candidates have spectra of their own, from ten sources outlined in Frieman et al. (2008). Host galaxy spectroscopic redshifts for SN-galaxy pairs are only used once the host galaxy has been confidently identified. The galaxy spectra utilised stem from 3 main sources within SDSS. These are the SDSS-II LEGACY (York et al., 2000), SDSS-II SOUTHERN (Baldry et al., 2005), and SDSS-III BOSS/SDSS-IV eBOSS surveys (Dawson et al., 2013, 2016). The latter contains spectroscopy for galaxies identified as the hosts of 3743 of the 10258 SN candidates in Sako et al. (2018a), approximately a third of which are identified as non-supernovae as a result. Supernova redshifts are used in cases where both are available. Photometric redshifts of galaxies are calculated from the coadded photometry in cases where no spectroscopic redshift is available for a SN-galaxy pair, as outlined in Section 2.1.7.1.

2.1.4 Selection of the Supernova Sample

2.1.4.1 Star Removal

In order to produce a sample of core-collapse supernovae (CCSNe), a focus is given to the removal of non-supernovae from the SDSS-II SUPERNOVA SURVEY sample. 10258 transient sources were found by Sako et al. (2018a). Their classification attempts are built upon by firstly removing those transient sources categorised as variable stars (objects detected over multiple observing seasons) and AGN (identified spectroscopically via their broad hydrogen lines).

The main SN classifications of Sako et al. (2018a) are Type II, Type Ib/c, and Type Ia SNe. One wishes to remove Type Ia SNe to obtain a CCSN sample in order to trace star formation rates. However, likely Type Ia SNe are left in the sample at this stage to search for LSBGs and to increase the size of the training sample used for the estimations of galaxy redshifts, as described in Section 2.1.7.1. At this stage, the sample consists of 6127 transients. Of these objects, 1809 are spectroscopically confirmed SNe and a further 2305 are, photometrically, deemed very likely to be supernovae, via a combination of Bayesian, nearest-neighbour and light-curve fit probabilities (see Sako et al. (2018a) for a full description). Those remaining are classified as 'Unknown'. However, these objects may still be supernovae. For several of these objects it may simply be unclear from the photometry what type of supernova is being seen. For instance, if probabilities derived from the 3 aforementioned techniques give a reasonable likelihood for more than 1 of Type Ia, Ib/c or II, the object will be classified as 'Unknown'.

Transient positions are matched with all objects of the SDSS-IV DR14 PHOTOPRIMARY catalogue located in the STRIPE 82 region with Galactic extinction-corrected r-band magnitude < 22.0 (Petrosian, psf or model) ($\sim 10^7$ objects). This is referred to as the SDSS catalogue in the remainder of the present chapter, for simplicity. Additional variable stars are found in the SN sample by computing the separations between SDSS stars and all transients without a spectroscopic SN classification. Variable stars are identified as those objects found within 1" of an SDSS star. This 1" transient – star separation cut-off was chosen following inspection of Figure 2.1.

The counts of non-associated transient–star pairs rise as the square of their separation. Additional counts arise below a separation of approximately 1" due to genuine association between the transient and SDSS object, and the detection is deemed to have arisen from the star. 718 stars are removed from the supernova sample in this manner, leaving a sample of 5549 transients. Most of these transients are likely to be SNe, but some may

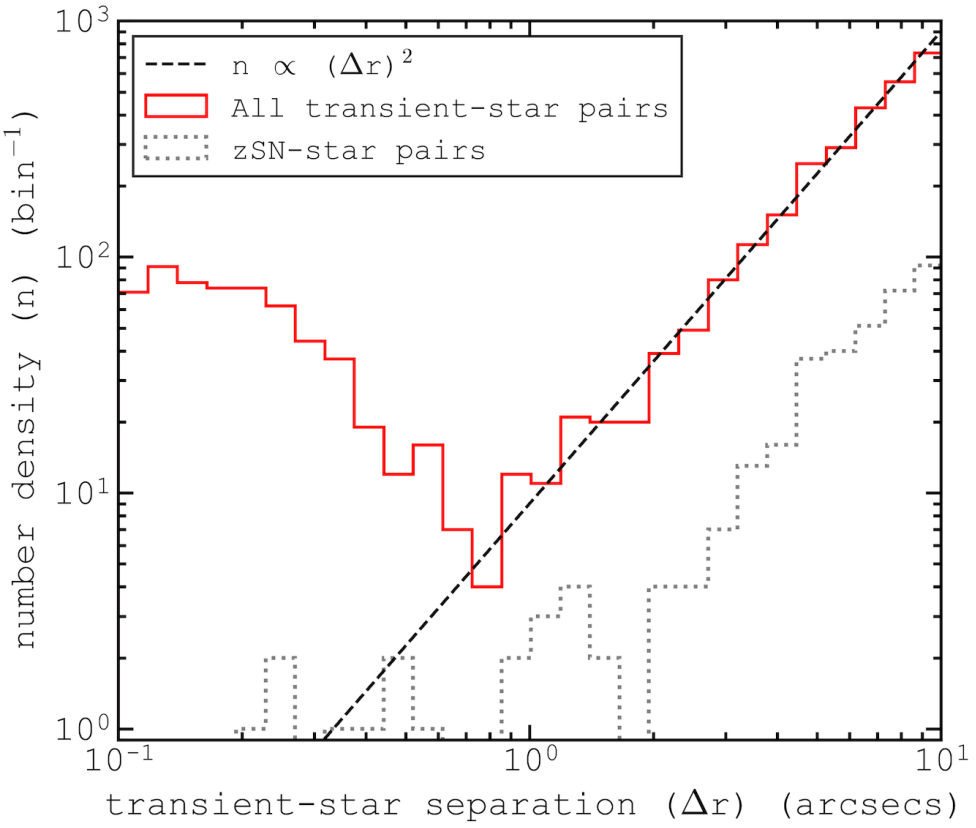

FIGURE 2.1: A histogram of sky separation between each SDSS-II SN survey transient and each star in the SDSS-IV DR14 PHOTOPRIMARY catalogue. The red solid line represents these transient–star pairings. The grey dotted line represents all spectroscopically-confirmed-SN–star pairings. The dashed line shows the n = 2 power-law expected to be followed by unassociated transient-star pairs. For a transient–star separation $\lesssim 1$" transients are likely to be variable light from the nearby star, and not supernovae.

be QSOs. Redshift information helps distinguish SNe and QSOs. However, not all of these transients have spectroscopic redshifts, as outlined in Section 2.1.3. Therefore, all remaining transients are kept in the sample at this stage, until each source is matched to its host galaxy, for which a spectroscopic redshift may be available.

2.1.4.2 SN Apparent Peak Magnitude Cut

With stars removed, attention is turned to the completeness of the sample. The r-band supernova peak-magnitude ($r_{SN,peak}$) distribution is found to follow a power-law up to $\sim$ 21.8, beyond which the slope decreases, as shown in Figure 2.2. A power-law increase to counts is expected due to the increased volume sampled as mean SN

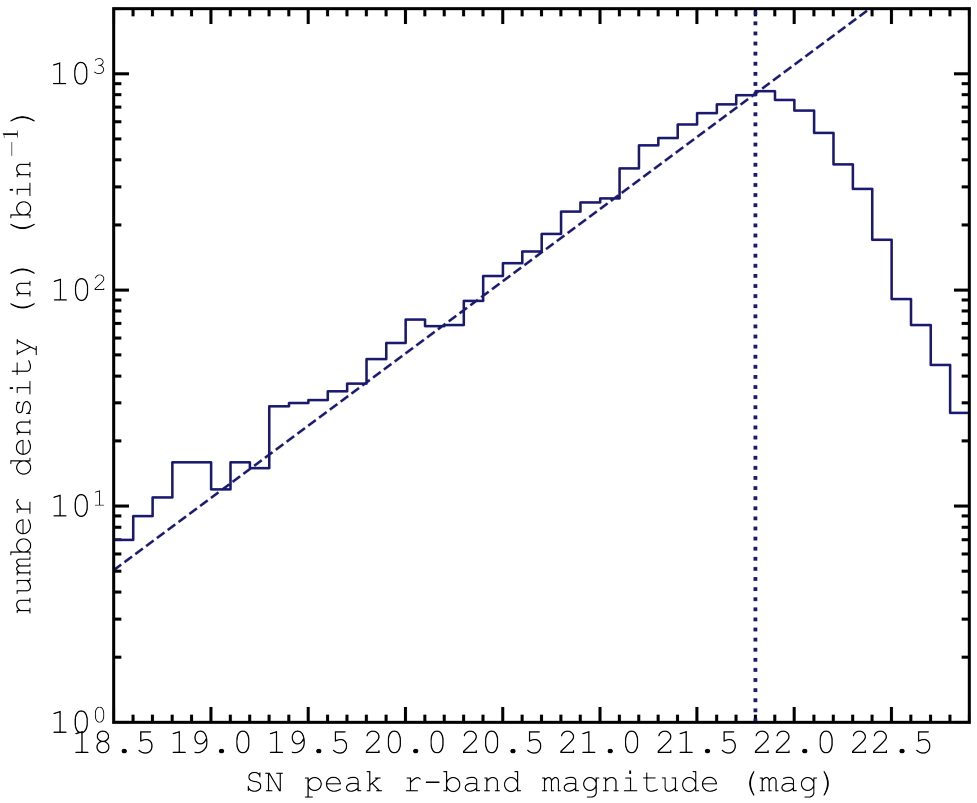

FIGURE 2.2: The r-band supernova peak-magnitude distribution of all supernova candidates in the SDSS-II Supernovae Survey following star and AGN removal. The dashed line shows the power law fit to the SN number density for $19.8 < r_{SN,peak} < 21.8$. The vertical dotted line corresponds to $r_{SN,peak} = 21.8$.

apparent magnitude becomes fainter. A deviation from this power-law for $r_{SN,peak} > 21.8$ hence indicates incompleteness. Henceforth, a cut is implemented to include only supernovae brighter than $r_{SN,peak} = 21.8$. Approximately 25% of the aforementioned removed stars are brighter than this cut. Table 2.1 shows the SN sample sizes following the removal of stars and spectroscopically confirmed AGN. SN counts are also given as a function of SN type. The $r_{SN,peak} = 21.8$ SN apparent magnitude cut reduces the sample to 2931 SNe.

TABLE 2.1: Transient counts as a function of type, built from the SDSS-II SUPERNOVA SURVEY sample of 10258 transients. Counts are divided into: i) those rejected by a magnitude cut, $r_{SN,peak} > 21.8$, because of sample incompleteness for fainter transients; ii) those brighter than $r_{SN,peak} < 21.8$ but rejected as variable stars or AGN; and iii) those that are selected for the SN sample in this section. Variable star counts are shown as the summation of those classified by Sako et al. (2018a), by host matching to single-epoch SDSS imaging, and to IAC STRIPE 82 LEGACY coadded imaging. AGN counts are shown as the summation of those classified by Sako et al. (2018a), by host matching to single-epoch SDSS imaging, and from redshifts that indicate the host is a QSO (See Sections 2.1.5.1 to 2.1.5.3). Counts are also subdivided into those classified using spectroscopy and those using photometry.

	transient type	spec	phot	total
$r_{SN,peak} > 21.8$ (5257)	Ia	301	302	603
	Ib/c	17	12	29
	II	149	813	962
	SL	0	0	0
	Unknown	0	884	884
	Variable Star	0	2416	2416
	AGN	363	0	363
$r_{SN,peak} < 21.8$ rejected (2545)	Variable Star	0	1342 + 185 + 294	1821
	AGN	543 + 98 + 83	0	724
$r_{SN,peak} < 21.8$ selected (2456)	Ia	966	267	1233
	Ib/c	51	7	58
	II	274	207	481
	SL	3	0	3
	Unknown	0	681	681
Total	-	2848	7410	10258

2.1.5 Supernova Host Galaxy Identification

2.1.5.1 The SDSS Catalogue

Following supernova sample completeness checks, one aims to determine the correct host galaxy for each supernova. Firstly, similar to the aforementioned transient–star matching, for each supernova the separation from each SDSS galaxy within a 130" radius is found. This separation is then normalised to be in units of the galaxy's Petrosian radius. To do this, the following steps are taken:

1. **Flag unreliable radii:** Galaxy Petrosian radii calculations are deemed reliable if *all* of the following SDSS flag criteria (Lupton et al., 2001) are met:
   a) `NOPETRO = 0`;
   b) `petroradErr_r` > 0;
   c) `clean = 1`;
   d) `petroR90Err_r`/`petroR90_r` < 1.

2. **Winsorize Petrosian Radii:** Winsorization is the limiting of extreme values to reduce the effects of potentially spurious outliers (Hastings et al., 1947). A

minimum radius of 2" is set, and if the radius is flagged as unreliable, a maximum radius of 10" is set. This maximum prevents a galaxy with an non-physically large radius measurement from being matched to a distant, unassociated supernova. The radius minimum ensures SN-galaxy matches are not missed due to an underestimation of radius. 2" is chosen as a minimum as it approximates the radius of the lowest stellar mass galaxies known to be in SDSS STRIPE 82 at the lowest redshifts in the sample (see Section 2.1.6), whereas the maximum of 10" corresponds to the 90th percentile of radius in the SDSS STRIPE 82 galaxy sample.

3. **Account for galaxy eccentricity:** Axis ratio b/a from an exponential fit is Winsorized to $b/a > 0.5$. From axis ratio and Petrosian radius, $r_{gal,proj}$ is calculated: this is the length on the sky, projected from the galaxy centre to the edge of the galaxy ellipse, in the direction of the supernova, as shown schematically in Figure 2.3.

SN-galaxy separation is then normalised to units of this projected galaxy radius, and for each SN, the 3 galaxies with the lowest normalised separations are taken as the 3 most likely host candidates. The Petrosian radius is chosen for this method due to the robustness of measurements over a large redshift range (Stoughton et al., 2002). To improve confidence in the most likely host galaxy for each SN, the following 3 factors are considered:

1. **Is the normalised separation reasonable?** A separation of < 1.25 galaxy radii is deemed as a likely association, based on a similar analysis as seen in Figure 2.1. If no galaxy lies within 1.25 radii of the SNe, the host is flagged as ambiguous.

2. **Are SN and galaxy redshift compatible?** The 10th and 90th percentiles of expected SN absolute magnitude, drawn from Richardson et al. (2014), are used. Different distributions are used for each SN type. A range of possible redshifts is then draw from these and the observed SN apparent magnitude. Should the SN and galaxy redshift appear inconsistent, the host is ambiguous.

3. **Is the Petrosian radius reliable?** (see above).

Each SN region is inspected using IAC STRIPE 82 LEGACY coadded *gri* imaging (Fliri & Trujillo, 2016), with the above flags used to aid the search for a host galaxy. Figure 2.4 shows example *gri* imaging used for inspection, with supernova position and host galaxy candidates labelled. At this stage, SNe are only assigned to galaxies in the single-epoch

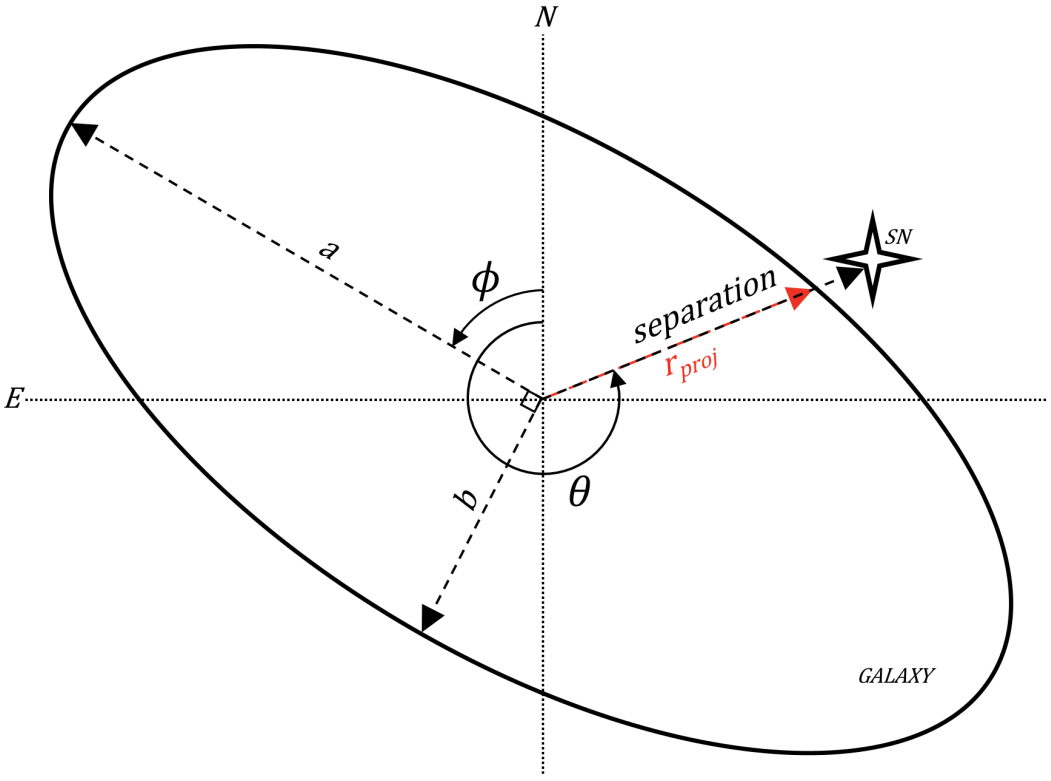

FIGURE 2.3: A schematic representation of host galaxy radius as projected in the direction of its SN, $r_{gal,proj}$, where θ is the angle from galaxy centre to SN, ϕ is position angle of the galaxy (both in degrees, from N to E), and where a and b are the galaxy semi-major and semi-minor axes, respectively. The quantity of SN-galaxy separation, normalised by $r_{gal,proj}$, is the main criterion for deciding the most likely host galaxy for each SN. See text for details.

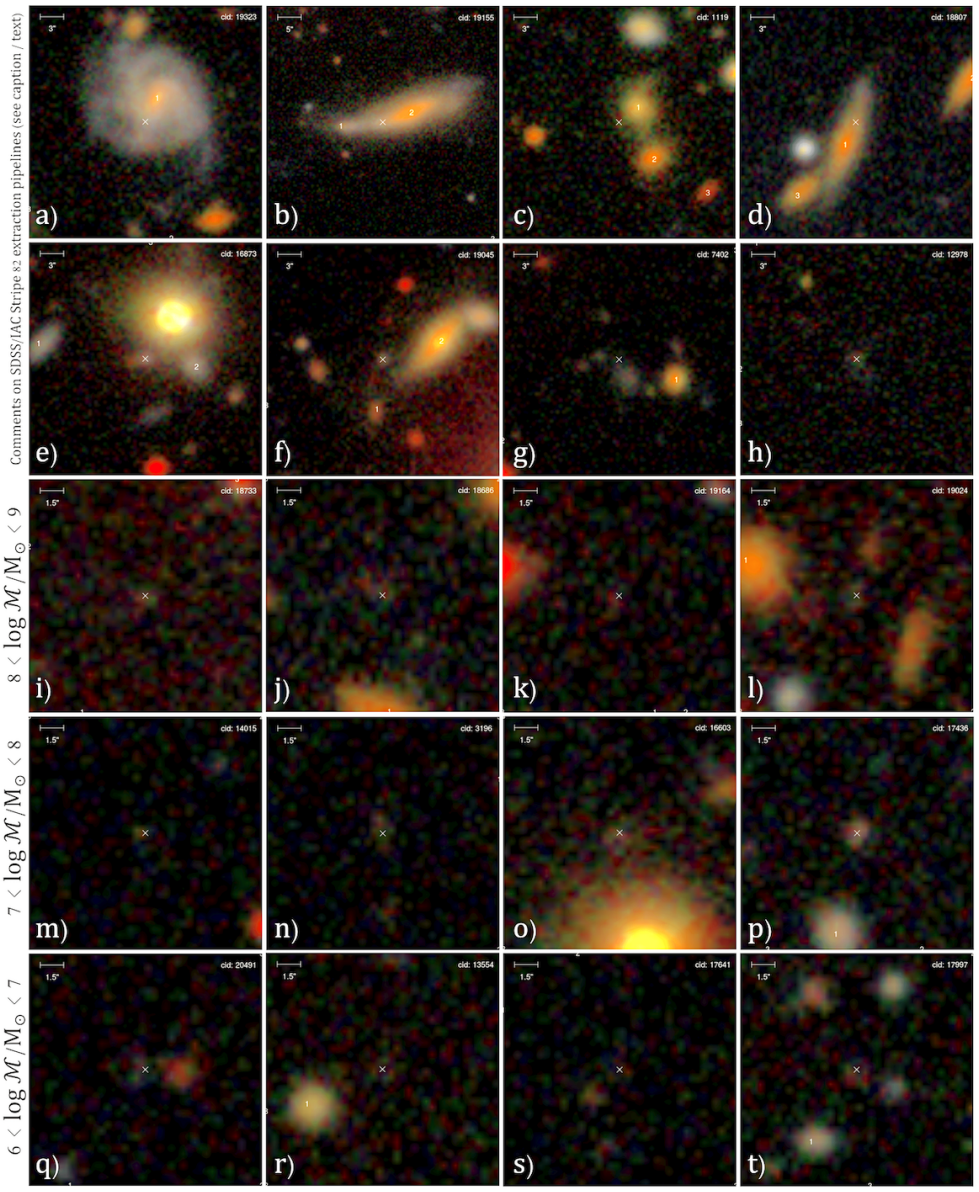

FIGURE 2.4: Example postage stamps of IAC STRIPE 82 LEGACY coadded imaging, centred on SN positions, used to inspect each SN region to identify its host galaxy. SN catalogue ID, as listed in the SDSS-II SUPERNOVA SURVEY is indicated. Labels 1, 2 & 3 in each stamp indicate the central positions of the 3 normalised-nearest SDSS galaxies to the SN. **Row 1:** chosen to show a) a straightforward SN-galaxy match, b) the successful resolution of satellite galaxies from their primaries, as well as a particularly ambiguous case, c) resolved galaxies in group environments, and d) a case involving extreme morphology. For a) to d), the normalised-nearest galaxy is chosen as the host galaxy. **Row 2**: example SNe associated with newly identified LSBGs in IAC imaging. Uncatalogued SN hosts are missed by the SDSS and IAC catalogues due to: g) and h) low-surface-brightness alone; f) being a close-in satellite or the lower-luminosity constituent of a merger; or e) a bright neighbour. **Rows 3-5:** Examples of newly identified LSBGs. Rows bin by mean galaxy stellar mass from a Monte Carlo technique (see Section 2.1.8).

imaging based SDSS catalogue, such as to test the performance of the single-epoch imaging for the task of host identification.

Following manual inspection of the coadded *gri* imaging, the above procedure finds that 86% of $r_{SN,peak} < 21.8$ supernovae are matched to an $r < 22.0$ SDSS galaxy. 96% of these are ultimately assigned to their normalised-nearest galaxy. When deciding the normalised nearest galaxy to each SN without accounting for galaxy ellipticity, this fraction is reduced to ∼94%. Approximately 2% are matched to the second normalised-nearest. Reasons why the normalised-nearest galaxy is not the SN host include that fact that the galaxy extraction pipeline of SDSS sometimes catalogues a galaxy's star-forming region or the galaxy bulge as a galaxy in its own right. Another reason comes in cases of extreme galaxy eccentricities or irregular galaxy morphologies. Only ∼0.1% of SNe are assigned to the third normalised-nearest galaxy. The remaining ∼2% are assigned to another $r < 22.0$ SDSS galaxy outside of the 3 normalised-nearest galaxies. The most common reason for this is again the case of bright galaxies with well-resolved stellar/dust components, and in particular, where a bright bulge was catalogued as the galaxy, and the disk was missed by the extraction pipeline altogether.

The importance of taking the described precautions before assigning SNe to host galaxies is emphasised, as it is more likely that SNe belonging to dwarf or satellite galaxies are assigned to the wrong host. Matching without caution would almost certainly cause a biased selection towards brighter galaxies which would ultimately reflect in the GSMF.

In cases where a transient was not a spectroscopically confirmed supernova, and was matched within 0.5 $r_{gal,proj}$ of an SDSS galaxy with a previously classified QSO, the AGN was assumed to be the source of the transient. This was the case for 98 objects. Removing these leaves at this stage 2422 SN candidates with hosts found in single epoch SDSS imaging.

2.1.5.2 The IAC STRIPE 82 LEGACY Catalogue

To find the host galaxy for the remaining 14% of SNe, attention is turned to the deeper IAC STRIPE 82 LEGACY Catalogue (Fliri & Trujillo, 2016), extracted from the same coadded *gri* imaging used for the above manual inspection. Data are formed from the median stacks of ∼100 images per supernova region, with individual epoch imaging stemming from both the SDSS-main data release (Stoughton et al., 2002) and from repeat visits of the supernova regions between 2005 and 2007 as part of the SDSS SN survey (Sako et al., 2018a). Both the median stacks and SN peak-magnitude-epoch

imaging are inspected to ensure that the point sources are not visible in the former, and are visible in the latter, such that neither supernova nor host galaxy are spurious detections.

The increased signal-to-noise achieved by the coadded imaging showed that 294 of the objects matched to SN candidates which were classified by the single epoch imaging as galaxies were more likely to be stars. The corresponding SN candidates were removed accordingly, leaving at this stage 2128 galaxies identified from single-epoch imaging in the SN host sample.

The SDSS and IAC catalogues were linked, by matching their objects within 2". Removing objects in common, the previous matching procedure is repeated using Kron-based magnitudes and radii in the place of Petrosian measurements, due to the increased flexibility of Kron-based magnitudes in capturing a large fraction of the object flux (Kron, 1980). Note that these objects have photometry only, and do not have redshift estimates. Therefore, in these cases the possible redshift range and the trustworthiness of the radius measurement are not considered in the matching procedure.

Nevertheless, ∼1% and ∼64% of the previously unmatched supernovae candidates are matched to a star or to a galaxy from the IAC catalogue, respectively. This still leaves 146 supernovae not matched to either a galaxy or a star in either catalogue. A bespoke `SExtractor` procedure is therefore turned to, which is applied to the same coadded imaging to attempt to locate the remaining host galaxies.

2.1.5.3 Bespoke LSBG Identification

Care is taken to obtain photometry for the remaining host galaxies, whilst simultaneously obtaining photometry for the previously matched objects which is consistent with that found by SDSS and IAC. To do this, several `SExtractor` parameter setups are considered (Bertin & Arnouts, 1996a), using different detection thresholds, minimum aperture sizes, and smoothing filters, as shown in Table 2.2. *ugriz* magnitudes are calculated using a fixed r-band defined, elliptical Kron aperture for all bands.

Each of these `SExtractor` setups is more prone to extracting spurious objects than the last, due to its increasingly generous extraction threshold. However, as only detections corresponding to the likely supernova host are kept, and as the supernova's presence is confirmed by visual inspection, the spurious detections are not deemed problematic.

TABLE 2.2: `SExtractor` configurations used for a bespoke search for LSBGs. Parameters shown are the only parameters varied for each configuration, from the setup of Fliri & Trujillo (2016) (here labelled IAC_S82). 2391 identified galaxies using the setup IAC_S82 are matched to the SN catalogue. `SExtractor` configurations are implemented in the order 1) to 6), and photometry from the first configuration to detect the galaxy is used. Additional SN-galaxy matches with successive configurations are indicated.

`SExtractor` Config.	DETECT_MINAREA (sq. pix)	DETECT_THRESH	FILTER_NAME	DEBLEND_NTHRESH	DEBLEND_MINCONT	Additional detections
1) IAC_S82	4	2	default	16	0.002	0
2) default_3.0	3	1	default	32	0.001	63
3) tophat_2.5	3	1	tophat_2.5_3x3	64	0.0001	28
4) mexhat_2.5	3	1	mexhat_2.5_7x7	64	0.0001	23
5) tophat_1.5	3	1	tophat_1.5_3x3	64	0.0001	18
6) gauss_1.5	2	0.5	gauss_1.5_3x3	64	0.0001	9

To maximise the reliability of photometry and to minimise the number of these false detections, a galaxy catalogue is first generated using the first `SExtractor` setup, i.e. the most reliable. This was the setup used by Fliri & Trujillo (2016), and their catalogue is successfully reproduced. The aforementioned SN-galaxy matching procedure is then completed using this catalogue. If the host galaxy is not found, the next `SExtractor` setup is turned to, in order to create a catalogue of the previously missed objects, and so on, for each setup, until a galaxy match is found for each SN. In the case of 5 SN, none of the described `SExtractor` setups could automatically detect the galaxy host. In these cases the presence of a host galaxy is still assumed, and a 2.5" circular aperture is used for the galaxy's photometry, centred on the r-band SN position. Indeed, these 5 galaxies, along with their supernovae, may be spurious, but can still be used to assess uncertainties on the form of the GSMF.

Using the above procedure, the photometry of the host galaxy is the photometry derived from the `SExtractor` setup which first located it. The galaxies which required several extraction attempts are therefore subject to the largest uncertainties. However, these uncertainties are folded into results and can help constrain the form of the galaxy stellar mass function considerably.

In the case that the object is detected in the r-band but is not detected in another band, the magnitude is set to 3 times the sky noise in the aperture for that band. However, using these magnitudes is avoided wherever possible. Only in the case of 6 galaxies is one forced to use these magnitudes, due to the lack of reliable photometry in other bands.

Row 2 of Figure 2.4 shows example IAC STRIPE 82 LEGACY coadded imaging in which

the supernova is centred on a newly identified LSBG from the bespoke search. Uncatalogued SN hosts were missed by the SDSS and IAC catalogues due to i) low-surface-brightness alone; ii) a bright neighbour; or iii) being a close-in satellite or the lower-luminosity constituent of a merger.

The different `SExtractor` setups shown in Table 2.2 were found to overcome different problems faced by the SDSS/IAC extraction pipelines. For instance, a 'Mexican hat'-type smoothing filter was particularly useful for identifying dwarf satellite galaxies close to brighter companions.

2.1.5.4 A Summary of Data Products

For the same reasons given for a galaxy being missed by the SDSS and IAC catalogues, it was found that ∼2% of hosts were incorrectly identified by Sako et al. (2018a). The vast majority of galaxies constituting this 2% are more massive than the true SN host, and thus their inclusion in the galaxy sample would have caused an underestimation of dwarf galaxy counts.

Figure 2.5 shows the galaxy magnitude distributions of the 3 SN-matched catalogues presented in this section, giving a clear comparison of their depth. Recall that the SDSS sample was selected to include only $r < 22.0$ (extinction corrected) galaxies. Thus, the most direct comparison of r-band magnitude depth is between the IAC data set and that of the full sample produced in the present section. The (90th,99th) percentiles of galaxy counts come at r-band magnitudes of (22.0,23.8) for the IAC sample and (22.8,25.3) for the bespoke sample, respectively.

One is able to test the success of the galaxy matching by using the relationship between Galactic extinction-corrected SN peak apparent magnitude ($r_{SN,peak}$) and redshift. Figure 2.6 shows this relationship for those SNe matched to a galaxy for which spectroscopic redshift (z_{spec}) is known. Redshift is plotted as $\zeta = \ln(1+z)$ (Baldry, 2018). For Type Ia SNe, there is an approximate maximum SN redshift as a function of SN peak apparent magnitude. CCSNe do not exhibit a relationship that is sufficiently sharp to set a strict maximum redshift, but still follow the same underlying distribution in $r_{SN,peak}$–ζ space. One can hence test if a galaxy match is reasonable by verifying that the galaxy spectroscopic redshift lies below the maximum redshift expected for that supernova.

For all host galaxies with redshifts exceeding their predicted maximum, given by the red demarcation line in Figure 2.6), Further inspection of the coadded imaging is performed,

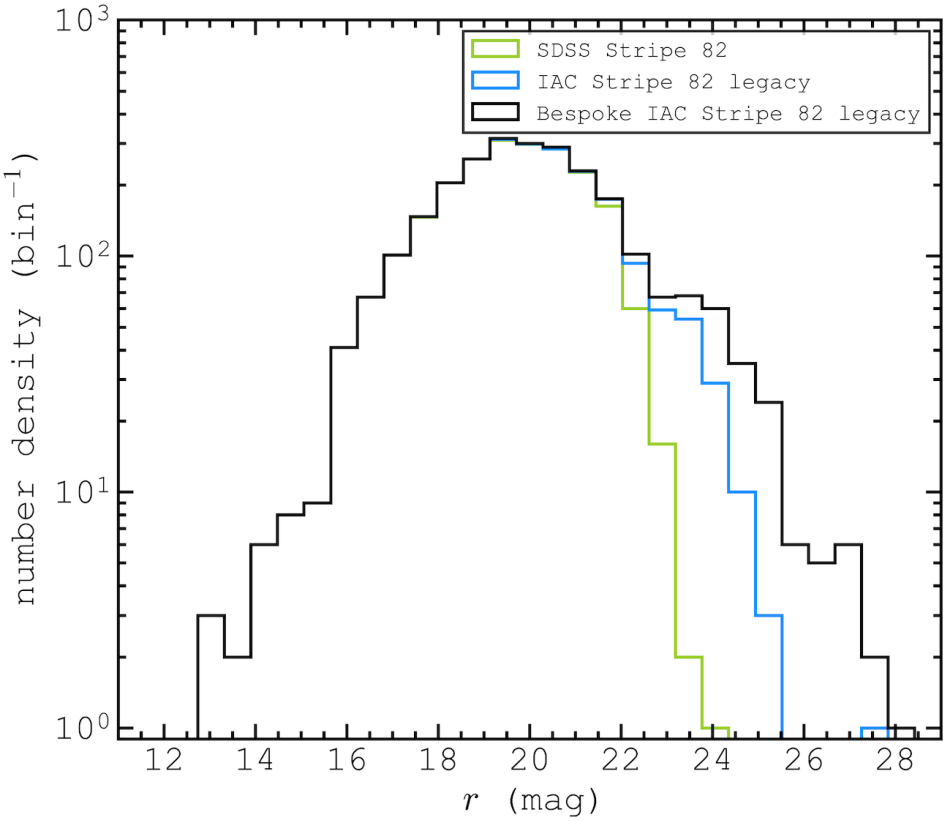

FIGURE 2.5: Galaxy number densities as a function of Kron r-band magnitude calculated from a bespoke search of IAC STRIPE 82 LEGACY coadded imaging for SN host galaxies. All SN host galaxies are shown in black; in blue, only those host galaxies known from the IAC STRIPE 82 LEGACY catalogue; in green, only those known from the SDSS PHOTOPRIMARY catalogue.

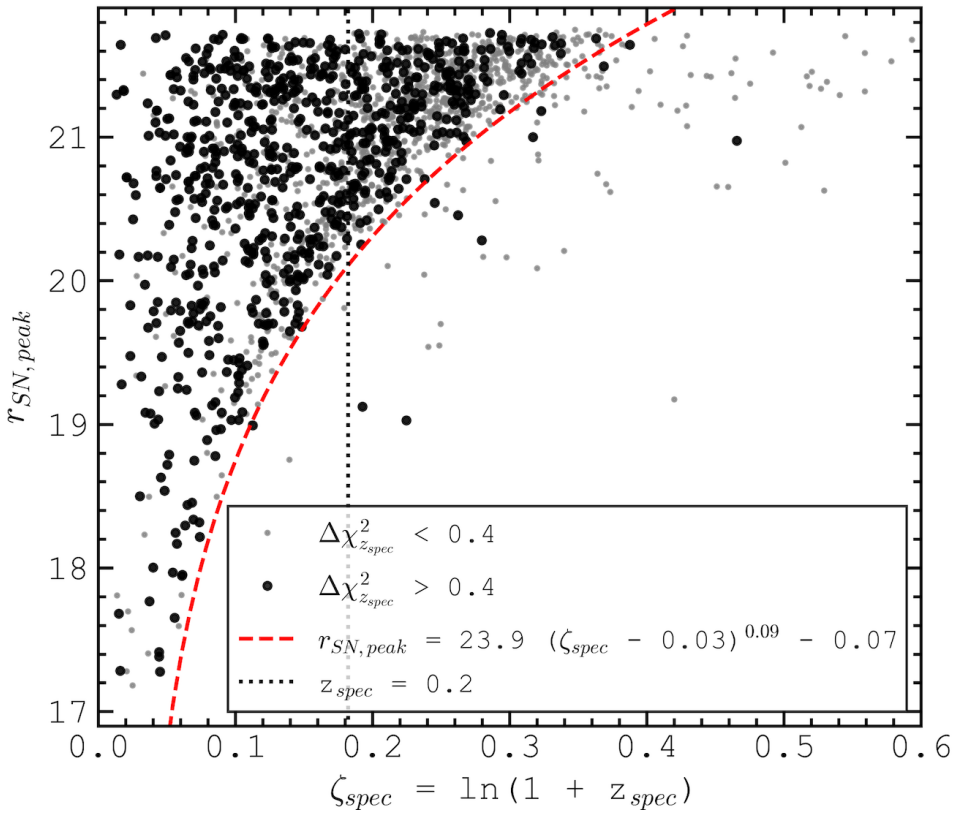

FIGURE 2.6: SN host galaxy spectroscopic redshift, expressed as $\zeta_{spec} = \ln(1+z_{spec})$, versus supernova peak r-band apparent magnitude ($r_{SN,peak}$), corrected for Galactic extinction. Black circles represent host galaxies with $\Delta\chi^2_{z_{spec}} > 0.4$, representing more confident redshift estimates. Grey circles represent host galaxies with spectroscopic redshifts not satisfying this criterion. The dashed red line is the inferred line of maximum redshift as a function of $r_{SN,peak}$, used to assess the validity of host galaxy identification.

to check for incorrect identification of SN hosts. However, in no case is a more sensible host galaxy found according to this extra criterion.

Not only can Figure 2.6 be used to test galaxy matches, it can also be used as a further check that all remaining transient objects are indeed SNe. The demarcation line implies that the maximum redshift for the faintest SNe in the bespoke sample, at $r_{SN,peak} = 21.8$, is $z = 0.48$. This is hence the maximum trustworthy redshift for SNe in the sample. Bolton et al. (2012) classify objects as QSOs from their spectra. Cross-matching classifications with host galaxies, a sudden rise in QSO classification is found at $z = 0.48$, with $\gtrsim 80\%$ of $z > 0.48$ galaxies classified as QSOs. 83 transients assigned to a galaxy with $z_{spec} > 0.48$ are thus removed, citing the fact that the transient is AGN in nature and not a SN, leaving a final sample of 2456 host galaxies for CCSNe or Type Ia SNe.

Figure 2.7 shows SN-Galaxy separation in arcseconds plotted against Kron galaxy magnitude. The same overall distribution is followed for each of the 3 galaxy subsamples: SDSS galaxies, IAC galaxies, and newly identified LSBGs. SN-galaxy separation increases towards brighter magnitudes due to the correlation of galaxy radius with galaxy magnitude. Normalising separation by galaxy radius, no correlation is found between magnitude and separation. This helps confirm that the SN-galaxy separations found for the LSBGs are reasonable.

To summarise, the host galaxy for each supernovae in the sample has been located, with great care taken to ensure the correct host is chosen. Following several steps taken to remove contamination to the SN sample from AGN and variable stars, a sample of 2456 SN host galaxies is obtained. These galaxies were identified from single-epoch SDSS imaging (2046), the standard pipeline of multi-epoch IAC STRIPE 82 LEGACY imaging (262), and from a bespoke search for the hosts within the multi-epoch imaging (148). The resultant galaxy sample, free of incompleteness, can now be used for the remainder of this section.

2.1.6 Spectroscopic Redshifts

Following the determination of the sample one now requires galaxy stellar masses, in order to calculate CCSN-rate densities, star-formation rate densities, and star-forming galaxy number densities as a function of galaxy stellar mass. It is often useful to define an approximate stellar mass that can be obtained from absolute magnitudes and colours (Bell et al., 2003). This works reasonably well because of the correlation between

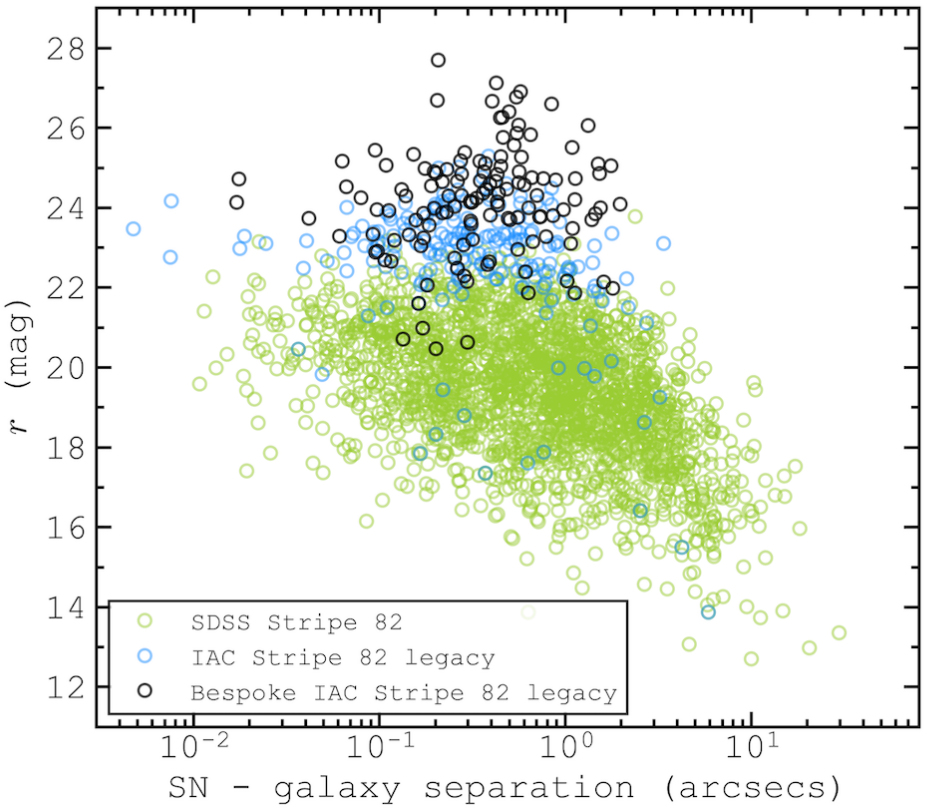

FIGURE 2.7: SN–galaxy separation in arcseconds versus galaxy Kron r-band magnitude calculated from a bespoke search of IAC STRIPE 82 LEGACY coadded imaging for SN host galaxies. In black is shown galaxies found using the bespoke SN-host search only; in blue, those found by the IAC STRIPE 82 LEGACY survey; and in green, those found by the SDSS survey in the STRIPE 82 region.

mass-to-light ratio and rest-frame color (Taylor et al., 2011). Following Bryant et al. (2015), one can also effectively fold in the k-correction, and estimate a stellar mass from distances and observed magnitudes as follows:

$$\log \mathcal{M} = -0.4i + 0.4\mathcal{D} + f(\mathrm{z}) + g(\mathrm{z})(g-i)_{\mathrm{obs}} \tag{2.8}$$

where $\mathcal{D}$ is the distance modulus, and f and g are two functions to be determined.

To calibrate the observed-magnitude-$\mathcal{M}$ relation, the GAMA stellar masses that were determined by spectral-energy-distribution fitting (Taylor et al., 2011; Baldry et al., 2018) are utilised. The data are binned in redshift over the range $0.002 < z < 0.35$, in 18 regular intervals of redshift. The values for f and g are determined for each bin, and finally $f(\mathrm{z})$ and $g(\mathrm{z})$ are fitted by polynomials. The coefficients obtained are (1.104, –1.687, 9.193, –15.15) for f and (0.8237, 0.5908, –12.84, 26.40) for g, with the constant terms first. Note because these are cubic functions, they cannot be reliably extrapolated to $z > 0.35$.

Clearly, this prescription requires a galaxy redshift in order to calculate stellar mass. Where available, the most reliable redshift for each galaxies is spectroscopic. The order of preference for the spectroscopic redshift (z_{spec}) used is as follows:

1. Galaxy redshifts obtained by either the SDSS-II LEGACY (York et al., 2000), SDSS-II SOUTHERN (Baldry et al., 2005), or SDSS-III BOSS/SDSS-IV eBOSS surveys (Dawson et al., 2013, 2016), and derived via a χ^2 minimisation method described in Bolton et al. (2012) ($\sim 60\%$ of the galaxy sample).

2. In the absence of galaxy spectra, supernova spectroscopic redshifts are used, derived from the various sources outlined in Sako et al. (2018a) (a further $\sim 8\%$ of the sample).

3. With neither available, in cases where one is confident that the host galaxy which was missed by SDSS is tidally interacting with a galaxy possessing a spectroscopic redshift, the redshift of the interacting galaxy is used ($\sim 1\%$ of the sample).

Approximately 70% of the galaxy sample have some form of spectroscopic redshift. For the remaining galaxies, photometric redshift estimates are turned to, as described in Section 2.1.7.1.

2.1.7 Photometric Redshifts

Approximately 65% of the photometry-only galaxies have SDSS KF-method (kd-tree nearest-neighbour fitted) photometric redshift (z_{phot}) estimates (Csabai et al., 2007; Beck et al., 2016). However, for galaxies only found in the IAC catalogue or from the bespoke `SExtractor` implementation, no galaxy redshift is available. A supernova photometric redshift is only known for ∼50% of these galaxies. The aim is to calculate galaxy photometric redshifts for the remainder of the sample using 2 new empirical method presented in this section. It is ultimately found that these methods are the most reliable photometric redshift estimator of the four, and so these new methods are used to calculate photometric redshifts for all photometry-only galaxies. Comparisons are made between the performance of the 2 new methods throughout this section.

2.1.7.1 Photometric Redshifts from *z*MEDIC

For the first photometric redshift determination, IAC STRIPE 82 LEGACY imaging (Fliri & Trujillo, 2016) is used along with all available spectroscopic redshifts in STRIPE 82. 2.5" circular-aperture-derived *ugriz* colours (used to maximise signal to noise) and their errors are utilised for the method, corrected for Galactic extinction as a function of position, using the extinction maps of Schlegel et al. (1998).

A training set of galaxies is used to calculate an empirical relationship between galaxy colours and redshift. The training set consists of a random 50% of galaxies for which all of the following conditions are met:

1. SDSS/BOSS spectroscopic galaxy redshift is known.
2. The difference between the χ^2 values of the most likely and second most likely redshift, i.e. $\Delta\chi^2$, is > 0.4. The most likely redshifts were determined from best-fit redshift templates (Dawson et al., 2013).
3. Galaxy 2.5" aperture magnitudes have S/N > 10 in each of the optical SLOAN filters, corresponding to colour errors of $\lesssim$0.15 magnitudes.

Conditions (ii) to (iii) ensure the spectroscopic redshifts and colours that the colour-z relation is trained on are reliable. The resulting training and validation sets each consist of ∼22000 galaxies

Equation 2.9 (below) is used to relate galaxy colours to redshift, giving each colour a coefficient. The optimal coefficients are those which yield an output z_{phot} which

resembles the known z_{spec} for the training sample galaxy. The coefficients k_1 and k_2 in Equation 2.9 are used as scaling values, to normalise and linearise the relationship between colours and z_{phot}. This code is named *z*MEDIC (***z*** **Me**asure**d** via **I**teration of **C**oefficients).

$$\zeta_{phot} = (c_1(u-g) + c_2(g-r) + c_3(r-i) + c_4(i-z) + k_1)^{k_2} \tag{2.9}$$

Optimal coefficients are found by producing random sets of numbers to iteratively approach the set which minimises the ζ_{spec} root-mean-square (rms) deviation, given by Equation 2.10.

$$\sigma = \sqrt{\frac{\sum_{i=1}^{n} w_i(\zeta_{phot} - \zeta_{spec})^2}{\sum_{i=1}^{n} w_i}} \tag{2.10}$$

The weights w_i are chosen to give larger weight to confident z_{spec} measurements and more precise colours, and to even out weighting across redshift space. To ensure the latter, the data are divided into ζ bins of width 0.05, normalising weights with a value, $\mathcal{F}_{bin}$, different for each bin, such that the sum of weights is the same in each bin. Thus, the final form of the weights w_i is $1/(\chi^2_{z_{spec}}\mathcal{F}_{bin}\Delta(i-z))$. Due to the observed upper limit to redshift as a function of SN apparent magnitude, given by the red demarcation line in Figure 2.6, a constraint is added such that the set of coefficients do not result in more than 10% of the sample lying above this redshift limit.

Figure 2.8 shows ζ_{spec} vs ζ_{phot} for each r-band magnitude bin, and the corresponding values of σ for the validation set. The best-fit coefficients of Equation 2.9 are shown in Table 2.3. Note that this colour-z relation is trained on both star-forming and quiescent galaxies. Removing quiescent galaxies from the training set to better reflect the SN hosts, no significant change is found to the optimal coefficients. Furthermore, training instead on only the SN sample of host galaxies for which the above training set selection criteria are met (∼400 galaxies), coefficients are similarly unaffected. The effect of binning galaxies by r-band apparent magnitude is also tested, to check for potential improvements to σ. No benefit to σ is found when dividing the large training sample of ∼22000 galaxies into magnitude bins, but for the much smaller sample of ∼400 CCSN-host galaxies, binning by magnitude is found to reduce σ for the $r \leq 19.5$ galaxies by ∼20%.

The redshift parameterisation of Equation 2.9 can be modified to deal with non-detections. The optimal coefficients are calculated with every possible combination of colours. For

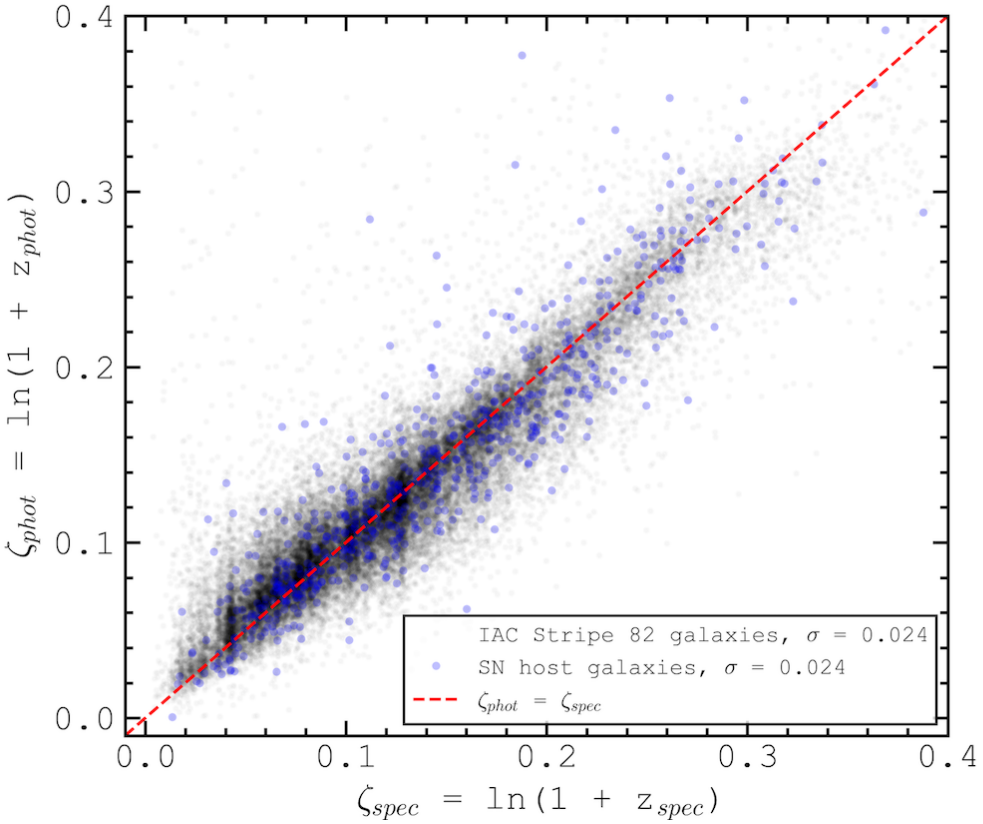

FIGURE 2.8: Spectroscopic versus photometric redshift estimates from *z*MEDIC, derived using 2.5" circular aperture-derived optical galaxy colours. Redshifts are represented as $\zeta = \ln(1+z)$. The validation set of ∼22000 galaxies from the IAC STRIPE 82 LEGACY catalogue is shown as black circles. The validation set of ∼400 SN host galaxies found from a bespoke search of the same IAC coadded imaging is shown as cyan circles. All redshifts are calculated using the *z*MEDIC coefficients found from the training set of ∼22000 galaxies. Weighted root-mean-square (rms) deviations (σ) in ζ are indicated.

TABLE 2.3: Best-fit values for the coefficients in Equation 2.9, as inferred from a training set of ∼22000 galaxies, with coefficients calculated separately for 3 bins of r-band galaxy magnitude, and for the entire training sample (labelled 'All').

	c_1	c_2	c_3	c_4	k_1	k_2
All	–0.21	0.32	–0.11	–0.03	0.18	0.90
$r \leq 17.5$	–0.17	0.55	0.13	–0.38	0.18	1.97
$17.5 < r \leq 19.5$	–0.15	0.35	–0.22	–0.12	0.13	0.74
$r > 19.5$	–0.19	0.38	–0.07	0.06	0.12	0.87

instance, if a non-detection is found for a galaxy in the g-band only, one is able to use the optimal coefficients associated with the colours $(u-r)$, $(r-i)$ and $(i-z)$, in order to infer photometric redshift. The most common filter with non-detections for the host galaxies is the u-band. Removing $(u-g)$ colour increases σ by ∼20% and ∼2% for $r \leq 19.5$ and $r > 19.5$.

The method works over the redshift range of $0 < z < 0.4$. Beyond this upper limit, there are too few reliable spectroscopic redshifts in the sample for an assessment, and the chosen relationship for all galaxies may be expected to break down due to evolutionary effects and more complex k-corrections.

To emphasise, it is found that Equation 2.9 yields its most accurate redshift estimates when using galaxy colours alone. The coefficients used are specific to 2.5" circular aperture colours. The rms deviation values between photometric and spectroscopic redshifts for this method are comparable to those using the SDSS KF-method (Csabai et al., 2007; Beck et al., 2016), and are substantially better than rms deviations using a SN light-curve method (Guy et al., 2007).

2.1.7.2 Photometric Redshifts from SCALED FLUX MATCHING

The second photometric redshift technique introduced and utilised in this section is named SCALED FLUX MATCHING (SFM). The is an empirical method that specifically works in linear flux space (unlike e.g. Beck et al. 2016 that uses colours and magnitudes) and requires a matching set of galaxies with reliable spec-z's. The matching set were chosen to have the SDSS flag ZWARNING $= 0$, $0.002 < z < 1.226$, reasonable S/N and reasonable measured colours for the redshift range. (S/N$>$ 10 in r and i bands, and S/N$>$ 5 in g and z bands, colours in the range $-0.1 < u-g < 3.5$, $-0.1 < g-r < 2.2$, $-0.1 < r-i < 1.5$, $-0.1 < i-z < 1.0$.) The matching set consisted of 103 376 galaxies out of a total sample of 117 690 (STRIPE 82 catalogue with SDSS redshifts and SN hosts, removing duplicates).

For each source (i), the fluxes were fitted to matching-set galaxy (j) fluxes with χ^2 defined as:

$$\chi^2_{i,j} = \sum_k \frac{(f_{i,k} - n_{i,j} f_{j,k})^2}{\sigma^2_{i,k}} \tag{2.11}$$

where $n_{i,j}$ is the best-fit normalisation and the summation is over all the photometric bands (k). The photometric errors $\sigma_{i,k}$ were taken to be the linear flux errors from SExtractor added in quadrature to fractional errors: $0.02 f_{i,k}$ for g, r, i, z and $0.05 f_{i,k}$ for the u-band. Note aperture fluxes with radius $2.4''$ were used.

The reliability weight of the match is then given by:

$$w_{i,j} = \exp(-\chi^2_{i,j}/2)\, W_j \tag{2.12}$$

where W_j is the bin weight assigned to galaxy j of the matching set. This was obtained by binning by 0.002 in $\zeta = \ln(1+z)$ (over the range 0.002–0.8) and with galaxies in a bin given a weight of $1/n_{\rm bin}$ with a maximum weight of 1/25. Note also that $w_{i,j}$ is set to zero where i and j refer to the same galaxy for calibration purposes.

The weighted mean of ζ, for the best-estimate photo-z, is given by:

$$\zeta_{i,\rm phot} = \frac{\sum_j w_{i,j} \zeta_{j,\rm spec}}{\sum_j w_{i,j}} \tag{2.13}$$

where ζ is the appropriate quantity to use when dealing with redshift measurements and errors (Baldry et al., 2018). The initial estimate of the uncertainty (or the nominal error) is given by:

$$\zeta^2_{i,\rm err} = \left(\frac{\sum_j w_{i,j} \zeta^2_{j,\rm spec}}{\sum_j w_{i,j}} - \zeta^2_{i,\rm phot} \right) \frac{N_{i,\rm eff}}{N_{i,\rm eff} - 1} \tag{2.14}$$

which is the weighted standard deviation multiplied by a correction factor to obtain the sample standard deviation, and $N_{i,\rm eff}$ is the effective number of measurements for reliability weights.

For the zMEDIC photometric redshift method outlined in Section 2.1.7.1, the matching set of galaxies was sub-divided by photo-z into bins of width 0.025, before the spec-z distribution was determined for each bin. This yields a set of redshift probability density functions (PDFs) which can be drawn from a Monte Carlo (MC) technique for a given photo-z input, in order to calculate galaxy stellar masses and volume-limit the sample ($z < 0.2$) for each iteration. A benefit of this technique is that it can account for any systematic offsets between photo-z and spec-z, and PDFs need not be Gaussian.

A shortcoming of the technique is that it does not account for errors on a galaxy-by-galaxy basis. To mitigate against this problem, the SCALED FLUX MATCHING method is modified as follows:

1. For each photo-z bin, galaxies are ranked by their nominal error estimated from the SFM technique.
2. spec-z distributions are determined using galaxies from the 0th to 20th percentile, and from the 80th to 100th percentile. These distributions are denoted $\mathcal{P}_{10}(z)$ and $\mathcal{P}_{90}(z)$, respectively, which are normalised to integrate to unity.
3. If a galaxy (i) has a mean nominal SFM redshift error at the $(j)^{th}$ percentile of the SFM error-ranked spectroscopic sample, then the PDF, $P_i(z)$, used as the galaxy's input into the MC-technique is given by:

$$P_i(z) = \frac{100-j}{100}\mathcal{P}_{10}(z) + \frac{j}{100}\mathcal{P}_{90}(z) \tag{2.15}$$

This improvement to the method accounts for changes in photo-z vs spec-z space with the SFM nominal error. This modified version of SCALED FLUX MATCHING is referred to as 'SFM + an advanced error analysis (AEA)'.

A summary of how results for the SFRD and the GSMF depend on the choice of photo-z technique is given in Section 2.1.13. However, unless stated, zMEDIC photometric redshifts are utilised in this chapter.

With redshifts estimated, likely Type Ia supernovae are removed from the sample to leave only likely CCSNe. In Section 2.1.9 the effects of assumptions for the nature of the unknown-type SNe are examined. It is likely that the unknown-type fraction of the sample consists of both CCSNe and Type Ia SNe, and it is discussed how attempts are made to circumvent this problem.

2.1.8 A Monte Carlo Assessment of Uncertainties

The CCSN-rate densities, star-formation rate densities and hence galaxy stellar mass functions that will be derived in this section are sensitive to redshift estimates in 2 ways: i) galaxy stellar masses are estimated using redshifts (see Equation 2.8); ii) incompleteness of the sample is a function of redshift. Redshifts are required to volume limit the sample. As small numbers of $\log(\mathcal{M}/\mathrm{M}_{\odot}) \lesssim 8.0$ galaxies can significantly change the form of the SFRD, and hence the GSMF, care msu be taken when utilising photometric redshifts.

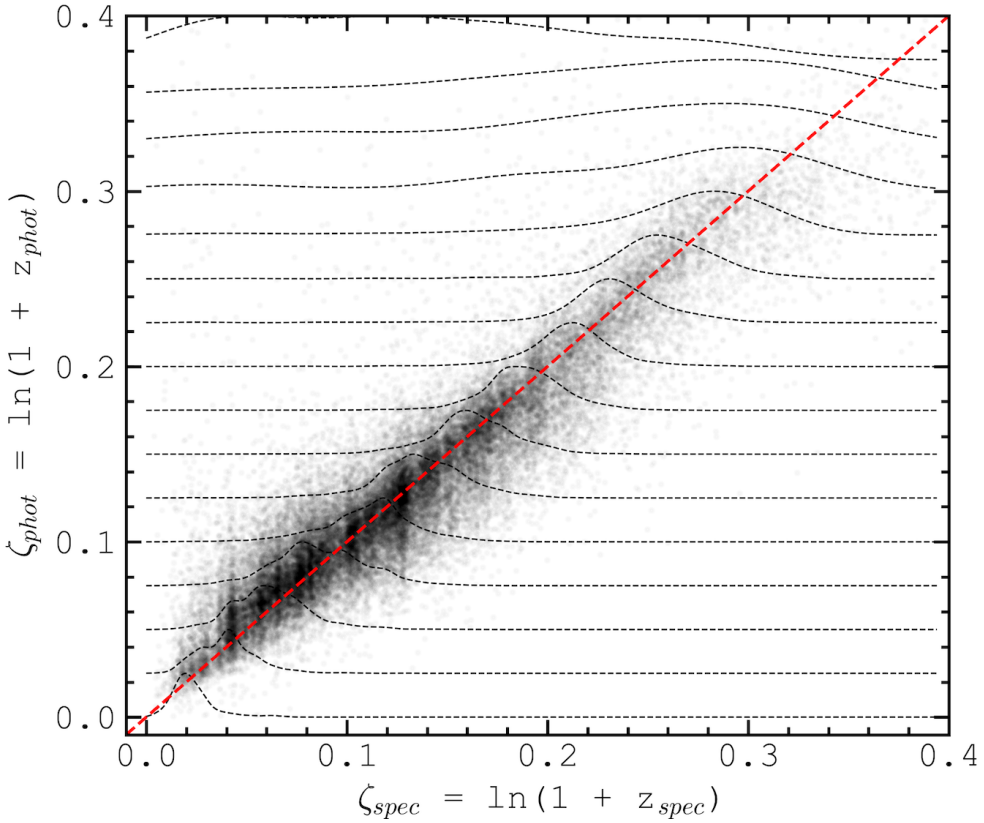

FIGURE 2.9: As in Figure 2.8, but showing only the validation set of approximately ∼22000 IAC STRIPE 82 LEGACY galaxies. Probability density functions (PDFs) of spectroscopic redshift as a function of photometric redshift are superimposed; these were used to model photometric redshift uncertainties. PDFs are calculated from a multi-Gaussian kernel-density-estimation, in ζ_{phot} bins of width 0.025. Redshift PDFs as a function of photometric redshift estimation are implemented into a 1000-iteration Monte Carlo method to assess galaxy stellar mass uncertainties.

To circumvent this problem, a Monte Carlo technique is turned to. Firstly, to assess the uncertainty in photometric redshifts, the ζ_{spec} vs ζ_{phot} space is divided into bins along the ζ_{phot} axis. A histogram of counts along the ζ_{spec} axis is produced for each ζ_{phot} bin, smoothed via a multi-Gaussian kernel-density estimation (kde) (Parzen, 1962). As such, the ζ_{spec} distribution is obtained as a function of ζ_{phot}. Each kde can be used as a probability density function (PDF) for a particular ζ_{spec} distribution as a function of the ζ_{phot} input. These distributions are shown superimposed onto the combined ζ_{spec} vs ζ_{phot} distribution in Figure 2.9. ζ_{phot} is found to be systematically greater than ζ_{spec} at the highest values ($\zeta_{phot} \gtrsim 0.3$). The PDF is designed to statistically account for this systematic when implemented into the Monte Carlo technique.

A 1000-iteration Monte Carlo code is then ran, where each photometric-galaxy's redshift

is replaced by a value drawn from the probability density functions of redshift shown in Figure 2.9. For spectroscopic galaxies, the spectroscopic redshift is used, and varied for each Monte Carlo iteration according to its error. For each iteration a galaxy's z-estimate is converted to a luminosity distance assuming an $h = 0.7$, $\Omega_m = 0.3$, $\Omega_\Lambda = 0.7$, flat cosmology. g and i 2.5" circular-aperture-derived magnitudes, as well as elliptical Kron-aperture-derived i-band magnitude, are varied with each iteration in accordance with their uncertainties. This allows an estimate of the galaxy's stellar mass for each iteration using Equation 2.8.

To volume limit the sample to obtain a SFRD, a $z < 0.2$ cut is made following each Monte Carlo iteration. This cut is chosen to limit the effects of galaxy evolution at higher redshifts, to match to the redshift cut of Gilbank et al. (2010), for the most direct comparison of SFRDs, and to limit the effects of extinction on SN counts. At higher redshifts, more SNe are near the detection limit of the survey, where a small amount of extinction can make the SNe undetectable. Limiting the number of SN detections sensitive to extinction decreases the reliance of results on the extinction model. Using this cut, the number density of CCSNe as a function of host galaxy mass is estimated, with galaxy stellar mass bins 0.2 dex in width. The mean of bin counts and the standard deviation of bin counts is then taken over the 1000 iterations, for each bin.

2.1.9 Observed Core Collapse Supernova Rate Densities

Using Equation 2.5, one can convert number statistics of CCSNe as a function of host galaxy stellar mass into volumetric CCSN-rate densities, given effective SN rest frame survey time τ and survey volume V. CCSN-rate densities are corrected for cosmological time dilation effects on survey time period as a function of redshift.

Figure 2.10 shows volumetric $z < 0.2$ CCSN number densities as a function of host galaxy mass, derived from a Monte Carlo technique. Based on the redshift cut, sky coverage and the effective span of the SDSS-II SUPERNOVA SURVEY [$\tau \sim 270/(1+\bar{z})$ days], $\sim 10^{-7}$ CCSN yr^{-1}Mpc^{-3}h$_{70}^{3}$ corresponds to 1 observed CCSN. Densities below log $(\mathcal{M}/\mathrm{M}_\odot) = 6.4$ are not assessed, as below this mass the mean number counts per bin descend below 1 for the full sample of galaxies found from a bespoke search for SN hosts in IAC STRIPE 82 LEGACY imaging. For this sample, CCSN number densities are found to decrease as a power-law for $\log(\mathcal{M}/\mathrm{M}_\odot) \lesssim 9.0$. To show the effects of selection bias, CCSN number densities are also calculated using only those CCSNe assigned to hosts in the SDSS and IAC galaxy catalogues. As expected, consistency is found at higher masses, whilst a deviation in CCSN counts is found at lower host galaxy masses

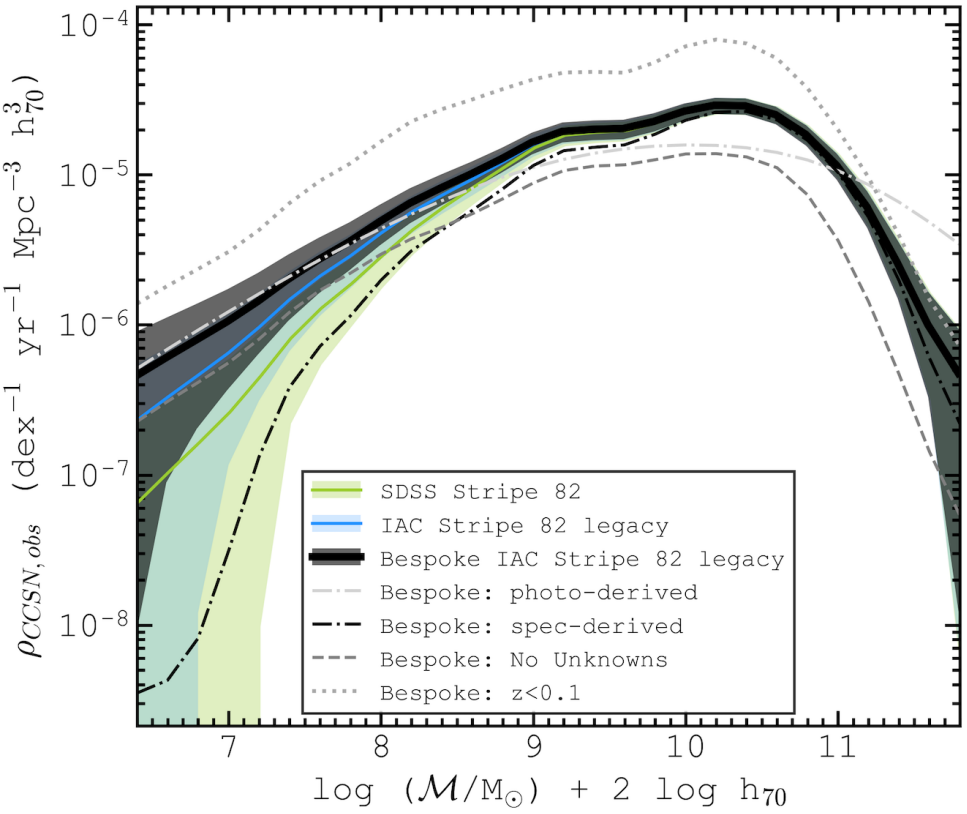

FIGURE 2.10: Volumetric CCSN-rate densities ($z < 0.2$) as a function of host galaxy stellar mass. The black solid line shows galaxies derived from a bespoke search for CCSN host galaxies in IAC STRIPE 82 LEGACY imaging. The blue line shows CCSN host galaxies known from the IAC STRIPE 82 LEGACY galaxy catalogue. The green line shows CCSN host galaxies known from the SDSS STRIPE 82 galaxy catalogue. Shaded regions indicate the 1σ of standard deviation from a Monte Carlo method and Poisson errors. The dot-dashed grey line shows the bespoke sample but with all galaxy masses derived using photometric redshifts, while the black dot-dashed line shows all galaxy masses derived using spectroscopic redshifts (with galaxies omitted where spectroscopic redshifts are unavailable). The grey dashed line shows the bespoke sample but with all unknown-type SNe removed. The grey dotted line shows the bespoke sample but with a redshift cut of $z < 0.1$.

($\log(\mathcal{M}/\mathrm{M}_\odot) < 9.0$) due to decreased sample completeness. A double peak in number density is observed, consisting of a primary peak at $\log(\mathcal{M}/\mathrm{M}_\odot) \sim 10.8$ and a secondary peak at $\log(\mathcal{M}/\mathrm{M}_\odot) \sim 9.4$. Using the alternative stellar mass prescription of Gilbank et al. (2010) in the Monte Carlo method, a modification of the prescription introduced by Kauffmann et al. (2003), this double-peak is found to persist.

Error bars incorporate the uncertainties in redshift and in the stellar mass parameterisation, as well as the uncertainty in the nature of the unknown-type transients. The work of Sako et al. (2018a) has here been built upon to deduce that these unknown-types are very likely to be supernovae. However, each of these objects could be either a CC or a Type Ia SN. Volume-limited SN number statistics, calculated by Richardson et al. (2014), are used to derive a ratio of CCSNe to Type Ia SNe. This gives a predicted percentage of unknown-type SNe that are Type Ia, and for each Monte Carlo iteration, this percentage of unknown-type SNe, selected at random, are removed from the sample.

Figure 2.10 shows the effect of removing this fraction of unknown-type SNe from the sample. Comparing with the full sample, no strong correlation is found .between the percentage of SNe that are unknown-type and galaxy stellar mass. As such, a removal of a percentage of unknown-type SNe to attempt to remove Type Ia's effectively corrects number densities by a constant amount, rather than modifying the CCSN-rate density distribution with mass. Changing the percentage of unknown-type SNe removed does not affect the presence of the double-peak in CCSN-rate density.

Also shown is the sub-sample of galaxies for which spectroscopic redshift is known. Lower-mass galaxies are less likely to have been selected for spectroscopic analysis. The low-mass limit of the CCSN-rate density is therefore dominated by galaxies with photometric redshifts.

To test the performance of *z*MEDIC in producing reliable redshift estimates, the effect of calculating *all* galaxy masses using *z*MEDIC photometric redshifts is observed. It is seen in Figure 2.10 that *z*MEDIC-derived redshifts, depicted by the grey dot-dashed series, are able to reproduce the fundamental shape of the CCSN number densities as a function of mass, but that fine features such as the double-peak are not reproduced.

Also plotted in Figure 2.10 is the bespoke sample's CCSN-rate densities using a redshift cut of $z < 0.1$. CCSN-rate densities are increased when using this cut, by a factor of $\sim$3. This is because a truly volume limited sample has not been obtained, due to the supernova magnitude cut. This draws one's attention to the need for corrections for

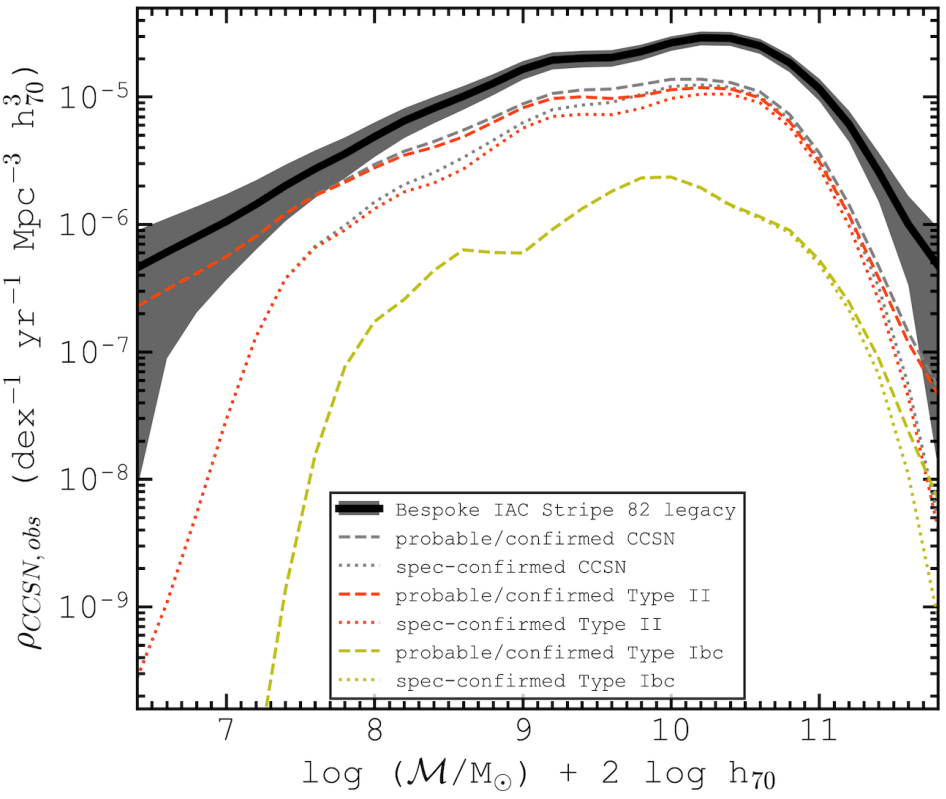

FIGURE 2.11: As Figure 2.10, but also showing the full CCSN host sample subdivided into probable/confirmed CCSNe (grey dashed) and confirmed CCSNe only (grey dotted), where probable indicates those classified via photometry only, and where confirmed indicates those classified via spectroscopy. These series are subdivided further by SN type: probable/confirmed and confirmed Type II SN (red dashed, red dotted) and probable/confirmed and confirmed Type Ib/c SN (yellow dashed, yellow dotted).

SN-detection efficiency, ϵ, as discussed in Section 2.1.10.

To test if the double-peak in observed CCSN-rate density as a function of galaxy mass arises due to a particular SN type, Figure 2.11 is plotted, separating the CCSN sample into Type II and Type Ib/c SN. Those with spectroscopically confirmed SN types are also plotted in isolation. For all SN types and for probable and confirmed SNe-types, the double-peak remains, with or without a Monte Carlo variation of masses.

2.1.10 Volume-Limited Core Collapse Supernova Rate Densities

In Section 2.1.4.2, it was found that it is unlikely that any $r_{SN,peak} < 21.8$ SNe are missed by the instrumentation described in Sako et al. (2018a) over the observing seasons, and that by locating the host galaxy for each of these SNe, surface brightness/mass biases

are significantly reduced. However, the magnitude $r_{SN,peak}$, which controls whether a SN is contained in the sample, may be a function of redshift, the type of core-collapse supernova that is observed, and, most importantly for this analysis, host galaxy stellar mass.

1. **In the case of galaxy mass**, higher mass galaxies may contain more dust than lower mass galaxies. Gilbank et al. (2010) uses the Balmer decrement to estimate the dependency of $A_{H\alpha}$ on galaxy stellar mass. The assumption that rest frame r-band extinction for a SN line-of-sight in its host galaxy follows the same extinction-mass relation as the Hα line. Alternatively, extinction in CCSN environments within these galaxies may not be so strongly dependent on the extinction inferred from the Balmer decrement. In the present sample, mean CCSN colours at peak epoch do not show any notable correlation with host mass. For Type Ia SNe, which are known to peak at approximately the same (B–V) colour (Nugent et al., 2002), there is no correlation between colour and host mass (although environments may differ for Type Ia and CCSNe).

2. **In the case of redshift**, CCSNe will be fainter with distance due to inverse square dimming to flux. They will also generally experience additional dimming to r-band magnitude with redshift, in the low redshift regime, due to the shape of their spectra. k-corrections are therefore necessary to represent the higher redshift portion of the sample correctly. CCSN k-corrections are estimated using a Type IIP template spectrum from Gilliland et al. (1999) at peak magnitude for all SNe in the present sample, and following Equation 1 of Kim et al. (1996).

To investigate these effects, the way in which SN detection efficiency depends on host galaxy mass and redshift is considered. Using absolute r-band magnitude distributions of SNe as a function of SN type, one can estimate the probability that each SN is brighter than $r_{SN,peak} = 21.8$, given its redshift and extinction. These probabilities lead to detection efficiencies, ϵ. Each CCSN contributes $1/\epsilon$ counts to the number density within its galaxy stellar mass bin, leading to corrected CCSN-rate densities. Detection efficiencies are calculated for each Monte Carlo iteration to account for the uncertainties in redshift, mass and SN type that efficiencies depend on.

In order to estimate detection efficiency, an assumption concerning SN absolute magnitudes is first required. The distributions used are derived from the volume-limited distributions calculated by Richardson et al. (2014), who observe approximately Gaussian distributions for each SN type. These SN types are finer classifications than made

in Sako et al. (2018a): a Type II SN as classified by Sako et al. (2018a) could be any one of IIP, IIL, IIn or IIb in Richardson et al. (2014). Therefore if each of the 4 sub-types follow different Gaussian distributions in absolute magnitude, one can utilise an absolute magnitude distribution for all Type II SNe which is the sum of these 4 Gaussians, whilst preserving the relative counts for each sub-type. This is done similarly for Type Ib and type Ic SNe, which come under 'Type Ib/c' in Sako et al. (2018a). The r-band absolute magnitude distributions used are derived from the B-band distributions of Richardson et al. (2014), converted using the prescription of Jester et al. (2005) for stars with R_c – $I_c < 1.15$. Assuming $(B–V) = 0.0$, as found to be typical for Type Ia SNe at peak magnitude by Nugent et al. (2002), it is estimated that $M_r \sim M_B + 0.1$ on average for the CCSNe.

If the absolute magnitude distribution of a SN type can be approximated as a Gaussian with a mean $\overline{M}$ (and standard deviation σ), then for an individual SN of that type, the mean apparent magnitude $\overline{m}$ as a function of redshift and extinction is given by Equation 2.16, where k_{rr} is the r-band k-correction for the SNe, $\mathrm{A}_{r,h}$ is the host galaxy r-band extinction and $\mathrm{A}_{r,MW}$ is the Galactic r-band extinction along the line-of-sight.

$$\overline{m} = \overline{M} + 5\log d_L(\mathrm{z}) + k_{rr} + A_{r,h} + A_{r,MW} \tag{2.16}$$

Again, the sum of the Gaussian distributions is taken to obtain distributions for Type Ib/c and Type II SNe. By integrating under the summed Gaussian distributions, the efficiency of detection, ϵ, as a function of redshift and extinction, correcting for the effects of a SN peak magnitude cut at $r_{SN,peak} = 21.8$ is then estimated by Equation 2.17, where N_i are the predicted relative numbers of each SN type, used to weight the sum of the n Gaussians.

$$\epsilon = \frac{1}{2} - \frac{1}{2\sum_i^n N_i} \sum_i^n N_i \,\mathrm{erf}\left(\frac{\overline{m_i} - 21.8}{\sqrt{2}\sigma_i}\right) \tag{2.17}$$

Detection efficiency is clearly a function of SN type. Therefore, the effects of bias in the SN classifications of Sako et al. (2018a) by varying the ratio of Type Ia, Ib/c and II SNe in the unknown-type fraction of the sample are tested. However, it is found that any effects are of second-order importance. Therefore, it is simply assumed that the unknown-type SNe follow the volume-limited type ratios of Richardson et al. (2014).

For each Monte Carlo iteration, unknown-type SNe are reassigned a SN type, and are thus either removed from the sample as a Type Ia, or are given an absolute magnitude

drawn from the distribution associated with either a Type Ib/c or Type II SN, which enables an estimate of their detection efficiency for each iteration.

Equations 2.16 and 2.17 are sensitive to assumptions for host galaxy extinction, $A_{r,h}$. Significant uncertainty exists around the relationship between CCSN extinction and host galaxy mass. Figure 2.12 shows corrected CCSN-rate density vs redshift, for different values of $A_{r,h}$. In comparison to the observed values, clearly there are larger corrections at higher redshift and with higher assumed $A_{r,h}$.

Also shown in Figure 2.12 is the inferred CCSN-rate density derived from the star-formation history of Madau & Dickinson (2014), assuming different values for $\mathcal{R}$, the expected number of stars that explode as CCSNe per unit mass of stars formed. Madau & Dickinson (2014) assume a Salpeter (Salpeter, 1955) initial mass function (IMF) for the star formation history. Using this IMF with initial masses 0.1 – 100 $M_\odot$ and assuming that all stars with initial masses 8 – 40 $M_\odot$ result in CCSNe, then $\log \mathcal{R} = -2.17$. It is found that using values of $A_{r,h}$ from ~ 0.3 to 0.6 reproduces the evolution of CCSN density with redshift, with $\log \mathcal{R}$ in the range -2.2 to -1.8. $\log \mathcal{R} = -1.9$ is adopted.

Note though that the measured $z < 0.05$ rate is higher than expected. it is found there is a significant excess of SNe with very faint peak r-band absolute magnitudes ($M_{r,sn} > -15$), only found for this redshift bin. Richardson et al. (2014) predict the fraction of CCSNe with $M_{r,sn} > -15$ to be negligible. One explanation for this excess could be a contamination of the SN sample at these lowest redshifts from outbursts of Luminous Blue Variables, which can exhibit similar light curve properties to Type IIn supernovae (see, e.g. Goodrich et al., 1989; Van Dyk et al., 2000). The red point of Figure 2.12 shows the effect of removing objects inferred to have $M_{r,sn} > -15$ on the $z < 0.05$ CCSN counts. This corrected value is in agreement with Li et al. (2011a) and Taylor et al. (2014).

The effects of corrections for SN detection bias on CCSN number densities as a function of galaxy stellar mass are shown in Figure 2.13 (with $A_{r,h} = 0.5$). CCSN-rate densities ($z < 0.2$) are now higher than the uncorrected values by a factor of ~ 2 at the low-mass limit, and by a factor of ~ 3 at $\log(\mathcal{M}/M_\odot) = 10.6$, the position of the primary peak. Even though host galaxy extinction is set constant with galaxy stellar mass, this larger factor at higher masses indicates the effects of a weak SN-type dependence on galaxy stellar mass.

The uncertainties take account of the efficiency corrections in Figure 2.13. Even with

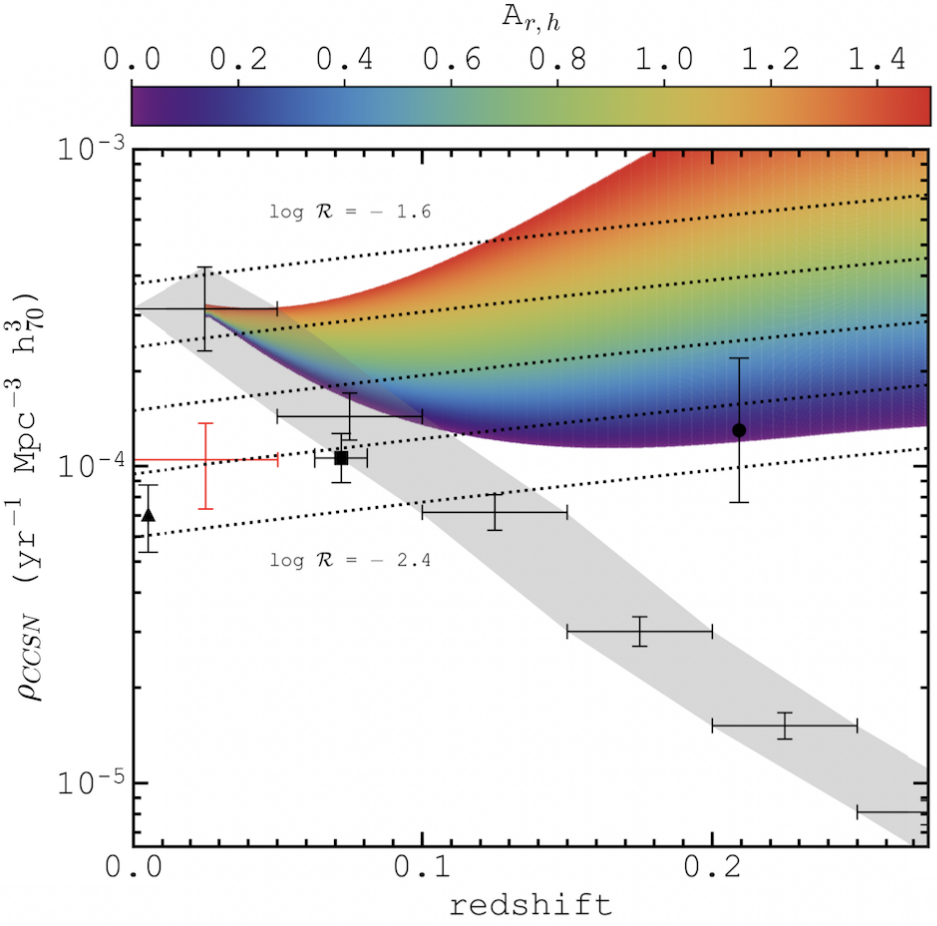

FIGURE 2.12: Volumetric CCSN-rate density versus redshift, calculated in redshift bins of 0.05, and as a function of SN detection efficiency corrections. The grey shaded region depicts observed CCSN-rate densities from the CCSN sample, uncorrected for SN detection efficiencies, bounded by 1σ Poisson+Monte Carlo+Cosmic Variance errors. Colour-shaded density values are corrected for SN detection efficiency. The colour bar represents the different corrected CCSN-rates obtained when assuming different values of CCSN host galaxy extinction, $A_{r,h}$. Dashed lines represent expected CCSN-rate histories derived from the star-formation history of Madau & Dickinson (2014), assuming different values of log $\mathcal{R}$ in the range –1.6 to –2.4 (see text). Triangular, square and circular points represent CCSN-rate densities obtained by Li et al. (2011a), Taylor et al. (2014) and Botticella et al. (2008), respectively. The red point shows how observed $z < 0.05$ SN counts are reduced when objects inferred to have r-band peak absolute magnitudes > -15 are discounted as CCSNe.

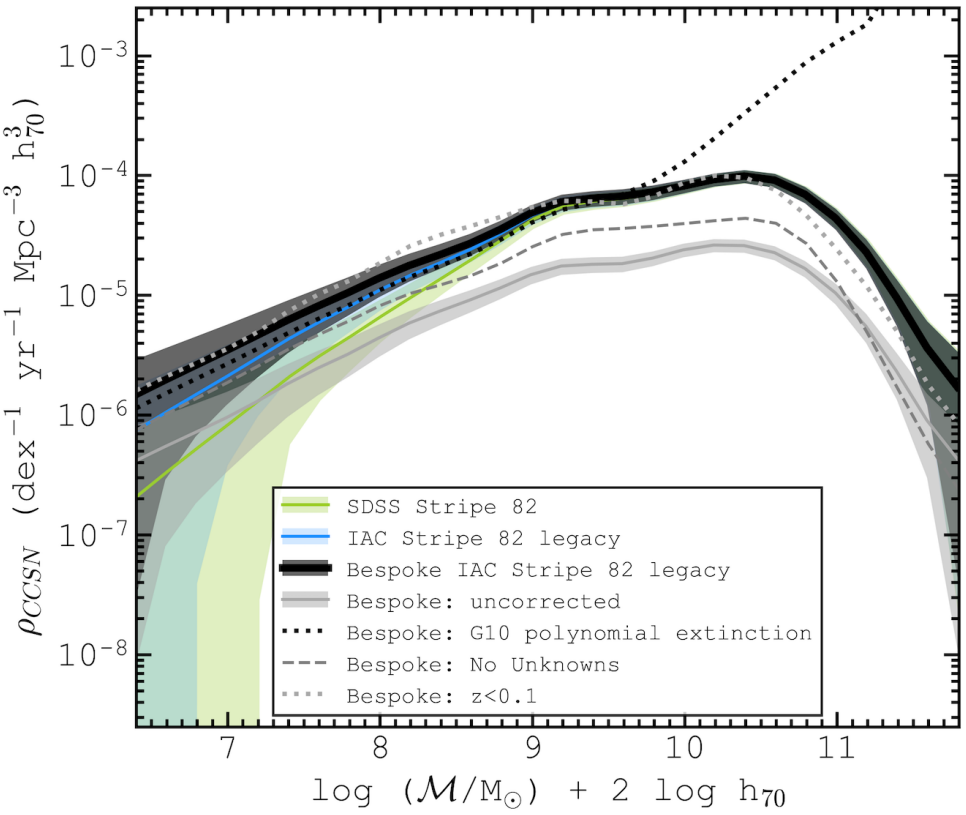

FIGURE 2.13: Volumetric $z < 0.2$ CCSN-rate densities as a function of host galaxy stellar mass, corrected for the effects of SN detection efficiencies. All series are as described in Figure 2.10. All results assume constant host galaxy extinction with mass, $A_{r,h}$=0.5 mag, except the black dotted line which assumes polynomially increasing host galaxy extinction with mass (as in Gilbank et al. (2010)). The grey solid line and shaded region represent CCSN-rate densities uncorrected for SN detection efficiencies and their 1σ errors, respectively.

these uncertainties, corrected CCSN-rate densities using the full sample of CCSN hosts show a power-law decrease with decreasing stellar mass, down to the low-mass limit of the sample. This is not evident from the samples that do not use the bespoke LSBG detections. The 1σ levels indicated by the shaded regions suggest non-zero number densities from single-epoch SDSS imaging only down to $\log(\mathcal{M}/\mathrm{M}_\odot) = 7.2$, and down to $\log(\mathcal{M}/\mathrm{M}_\odot) = 6.8$ for IAC STRIPE 82 coadded imaging. The $z < 0.1$ densities now approximate the $z < 0.2$ densities across the mass range, indicating the validity of corrections.

The black dotted line of Figure 2.13 shows CCSN-rate densities assuming increasing extinction with mass as in Gilbank et al. (2010). High mass counts appear to be significantly overestimated compared to predictions for the star-formation rate density (see

Section 2.1.11). This discrepancy is not surprising because Gilbank et al. (2010) uses the Balmer decrement and one expects this to be an overestimate of typical CCSN extinction for two reasons: (i) Balmer line production is weighted towards higher luminosity stars, and therefore younger phases of star clusters ($\sim$ 1–5 Myr, Gilbank et al. 2010); (ii) SNe occur at the end of a star's life, counts are weighted by number in the IMF, and therefore SNe typically occur later in the life of star clusters ($\sim$ 10–40 Myr). While some increase to extinction with host galaxy mass may be expected, due to the inter-stellar medium, the extinction in the *specific supernova regions* may not scale in an identical manner, and so for simplicity we assume a constant extinction with mass for the remaining results of the present thesis.

2.1.11 Star-Formation Rate Density

To convert CCSN-rate densities into star-formation rate densities, an assumption for the CCSN rate per unit of star formation, $\mathcal{R}$, is required, as discussed in Section 2.1.2. Using a value of $\log \mathcal{R} = -1.9$, the star-formation-rate densities plotted in Figure 2.14 are obtained as a function of galaxy stellar mass. The resultant SFRD is consistent with the 'SFR_{tot}' result of Gilbank et al. (2010) for $9.0 < \log(\mathcal{M}/\mathrm{M}_{\odot}) < 11.0$, the stellar mass range for which the Gilbank et al. (2010) galaxy sample is expected to be complete.

Using a bespoke search for the CCSN hosts in IAC STRIPE 82 LEGACY imaging, results are sufficiently constrained to deduce a power-law decrease to star-formation rate densities with decreasing galaxy stellar mass, down to the low mass limit. The methods presented in this section allow for an estimation of star-formation rates 1.6 dex lower in stellar mass than achieved by Gilbank et al. (2010) who calculated star formation rates directly from galaxy emission lines.

2.1.12 The Star-Forming Galaxy Stellar Mass Function

For the previous results of the present section, no assumptions are required for the volumetric numbers of galaxies at each stellar mass. On the contrary, by making assumptions about specific star formation rate levels with mass, volumetric galaxy number densities as a function of mass can be estimated.

The star-forming GSMF can be derived from CCSN-rate densities using Equation 2.7, requiring an assumption for mean specific CCSN-rate variation with galaxy stellar mass ($\mathcal{M}$). Specific CCSN-rates are expected to trace $\mathcal{S}$ irrespective of $\mathcal{M}$ (See Section 2.1.1).

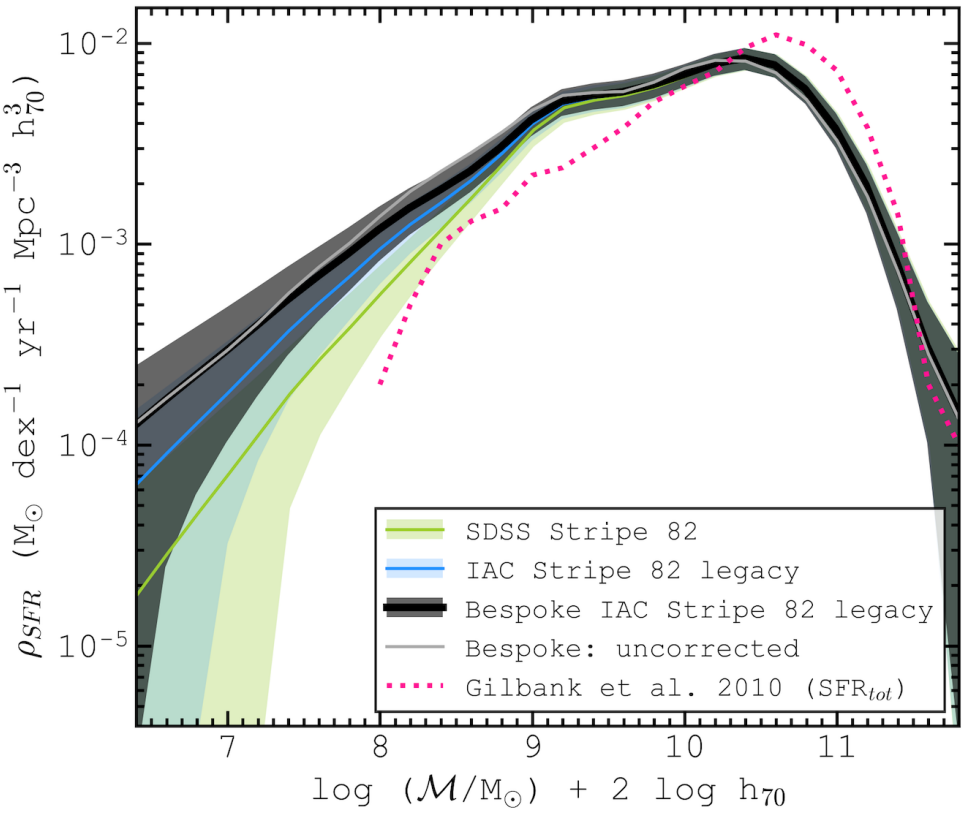

FIGURE 2.14: Volumetric $z < 0.2$ star-formation rate densities as a function of host galaxy stellar mass. The black line depicts galaxies selected from a bespoke search for CCSN host galaxies in IAC STRIPE 82 LEGACY imaging. The blue line shows galaxies from the IAC STRIPE 82 LEGACY galaxy catalogue. The green line shows galaxies from the SDSS STRIPE 82 galaxy catalogue. Shaded regions indicate 1σ of standard deviation from Monte Carlo, Poisson and cosmic variance errors. The grey line depicts the same as the black solid line but uncorrected for SN detection efficiencies. The magenta dotted line indicates Gilbank et al. (2010) 'SFR$_{tot}$' star-formation rate densities.

CCSN-rates may in fact be the most direct tracers of star formation rates. Studies which attempt to measure both $\mathcal{S}$ and specific CCSN rates find consistent slopes with $\mathcal{M}$ (see, e.g. Graur et al., 2015a). This gives confidence in the adopted assumption of a constant $\mathcal{R}$ value with $\mathcal{M}$ used to estimate star-formation rate densities in Section 2.1.11. With this similar trend in mind, one can use the numerous studies of $\mathcal{S}$ vs $\mathcal{M}$ to suggest the sensible range of assumptions for specific CCSN-rate vs mass, required to derive the star-forming GSMF.

There exist conflicting results in the literature for the variation of $\mathcal{S}$ vs $\mathcal{M}$. Whilst some studies find much higher efficiencies towards lower masses (Zheng et al., 2007; Li et al., 2011a; Karim et al., 2011; Graur et al., 2015a), where typically $\mathcal{S} \propto \mathcal{M}^{-0.5}$, others find much shallower trends consistent with a constant $\mathcal{S}$ (see, e.g. James et al. 2008; Bell et al. 2007; Wuyts et al. 2011 and most notably Sako et al. 2018a).

The majority of these studies do not probe down to the masses studied in the present section. Uncertainty exists around whether the $\mathcal{S}$ vs $\mathcal{M}$ relations found for massive galaxies apply to the dwarf regime down to $\log(\mathcal{M}/\mathrm{M}_{\odot}) = 6.4$. McGaugh et al. (2017) find a distinct star forming main sequence for $7 \lesssim \log(\mathcal{M}/\mathrm{M}_{\odot}) \lesssim 10.0$, with results consistent with a constant $\mathcal{S}$. Rate simulations of Graur et al. (2015a) predict a tanh-like function to specific CCSN-rate with galaxy mass, with constant specific rates in the dwarf regime and at the highest galaxy masses ($>10^{11}$), and with decreasing $\mathcal{S}$ with increasing mass for the masses in between.

One of the key results of the present section is the shape of the galaxy stellar mass function in the dwarf regime. High mass ($\log(\mathcal{M}/\mathrm{M}_{\odot}) \gtrsim 9.0$) galaxy counts in this chapter are subject to uncertainties related to the modelling of host galaxy extinction in massive galaxies, and the star-forming GSMF is already well constrained at high masses by several independent works finding consistent number densities (e.g. Baldry et al., 2008; Li & White, 2009; Kelvin et al., 2014). Consider instead the mass range of $8.0 < \log(\mathcal{M}/\mathrm{M}_{\odot}) < 9.0$. The variation of SF galaxy counts with mass in this range is also well constrained, yet the effects of varying assumptions for host galaxy extinction with mass are significantly smaller than at higher masses. Hence one expects that the $\mathcal{S}$ vs $\mathcal{M}$ relation which produces a slope consistent with well-constrained number densities from previous studies is the most reliable relation.

The best fit $\mathcal{S}$ vs $\mathcal{M}$ log-log relation for $8.0 < \log(\mathcal{M}/\mathrm{M}_{\odot}) < 9.0$ to Baldry et al. (2012) star-forming galaxy number densities (computed from GAMA data, Driver et al. 2011) is found to exhibit a slope of $-0.08^{+0.08}_{-0.10}$. Equation 2.7 can be expressed in the following

form:

$$\phi_{SF} \propto \rho_{CCSN} \mathcal{M}^{-\gamma} \quad . \tag{2.18}$$

For a constant ratio of CCSN-rate to SF-rate with mass, the best-fit $\mathcal{S}$ vs $\mathcal{M}$ slope leads to $\gamma = 0.92^{+0.08}_{-0.10}$. A constant value of γ with mass is found to give good agreement with Baldry et al. (2012) star-forming galaxy number densities, across their full range of masses. The effects of different values of γ on the derived star-forming galaxy stellar mass function are shown in Figure 2.15. This displays the typical range of $\mathcal{S}$ vs $\mathcal{M}$ values found in the literature.

Given this section's focus on low-mass galaxies, a constant value of $\mathcal{S}$ with mass ($\gamma = 1.0$) is assumed, and number densities are normalised to those of Baldry et al. (2012) in the mass range $8.0 < \log(\mathcal{M}/\mathrm{M}_{\odot}) < 9.0$, to derive the star-forming galaxy number densities (Mpc^{-3} dex^{-1}) for $6.4 < \log(\mathcal{M}/\mathrm{M}_{\odot}) < 11.8$. This is shown in Figure 2.16 with the Monte Carlo, Poisson and cosmic variance uncertainties. The results derived using the 3 galaxy samples derived using SDSS STRIPE 82 galaxies, IAC STRIPE 82 LEGACY galaxies, and those from a bespoke SN host search of IAC STRIPE 82 LEGACY imaging.

Using the full sample of CCSN host galaxies, a continuation of a power-law rise in galaxy number density with decreasing mass is observed. When selecting host galaxies from the IAC and SDSS catalogues, incompleteness is found below masses of $\log(\mathcal{M}/\mathrm{M}_{\odot}) \sim 9.0$, and zero number densities cannot be ruled out below masses of $\log(\mathcal{M}/\mathrm{M}_{\odot}) = 6.8$ and $\log(\mathcal{M}/\mathrm{M}_{\odot}) = 7.2$, respectively.

It is found that the GSMF result from the full SN host sample is consistent with the Schechter function fit to Baldry et al. (2012) star-forming galaxy number densities, when extrapolating the fit below $\log(\mathcal{M}/\mathrm{M}_{\odot}) = 8.0$. Baldry et al. (2012) use a fit with parameters [$\log\ (\mathcal{M}/\mathrm{M}_{\odot})$, $\phi^*/10^{-3}$ $\mathrm{dex}^{-1}\mathrm{Mpc}^{-3}$, α] = [10.72, 0.71, –1.45], which is plotted in Figure 2.16. From the method of the present section, and using $\gamma = 1.0$, the best-fit parameters are found to be [10.54, 1.32, –1.41], obtained using a Levenberg-Marquardt algorithm applied to the full mass range shown in Figure 2.16.

The GSMF result is also compared to that derived from the SFRD of Gilbank et al. (2010) assuming a constant specific star-formation rate with galaxy mass. Between $8.4 < \log(\mathcal{M}/\mathrm{M}_{\odot}) < 11.0$ the gradient of number densities with mass is consistent with the Baldry et al. (2012) equivalent, giving support to this assumption.

Although the star-forming galaxy stellar mass function is shown, rather than that of all galaxies, it is expected that the low-mass population is dominated by star-forming

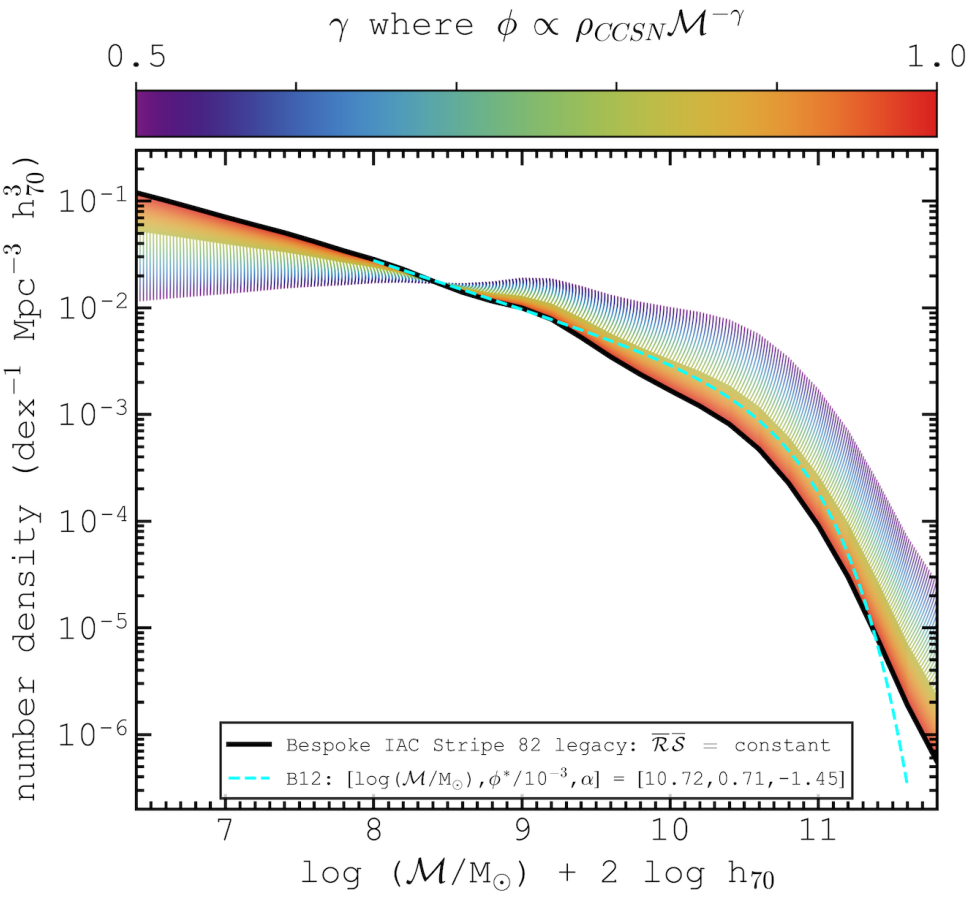

FIGURE 2.15: The $z < 0.2$ star-forming galaxy stellar mass function, as a function of the parameter $\gamma(\mathcal{R}, \mathcal{S})$. The black line shows the GSMF derived assuming constant specific CCSN-rate with stellar mass, i.e. $\gamma = 1.0$. The solid region shows star-forming galaxy number densities corresponding to the 1σ uncertainty level on the best fit value of γ to the Baldry et al. (2012) star-forming GSMF (the cyan dashed line) in the range $8.0 < \log(\mathcal{M}/\mathrm{M}_\odot) < 9.0$. The hatched region shows number densities derived using lower values of γ.

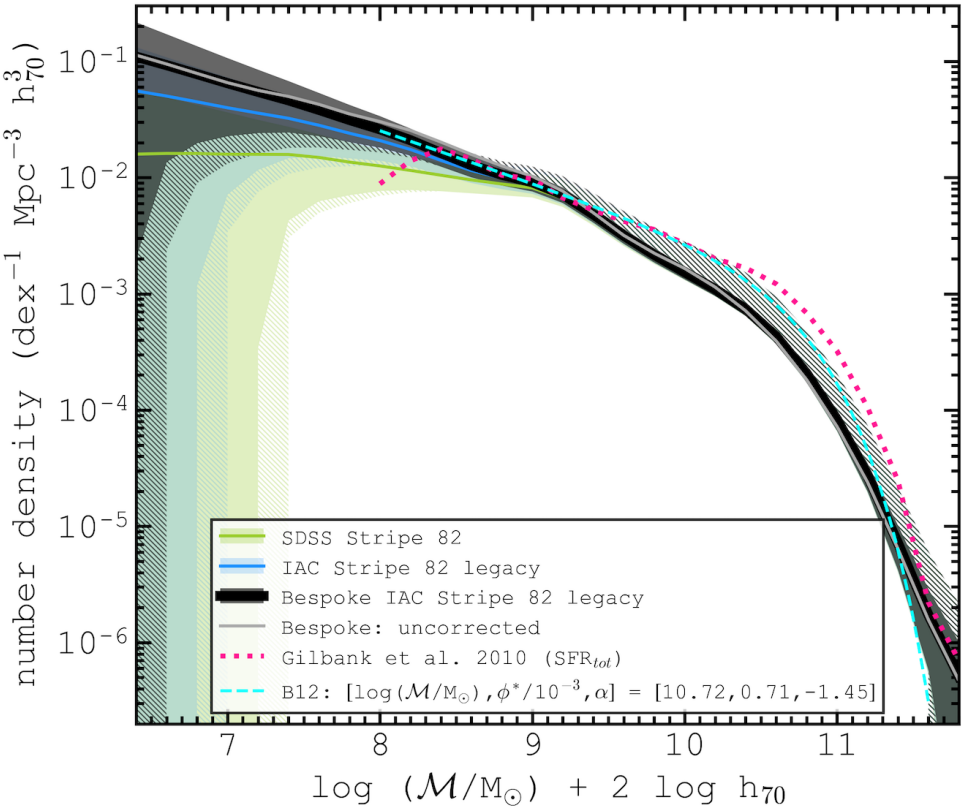

FIGURE 2.16: The $z < 0.2$ star-forming galaxy stellar mass function: star-forming galaxy number densities as a function of stellar mass, in logarithmic units of solar mass, as derived from corresponding star-formation rate densities (see Figure 2.14). The cyan dashed line represents the Schechter-fit to star-forming galaxy number densities obtained by Baldry et al. (2012). Hatched regions represent additional uncertainties on top of observational uncertainties concerning the optimal model of specific star formation rate vs galaxy mass (see Figure 2.15).

galaxies (Baldry et al., 2012). Therefore, by constraining the low-mass end of the star-forming GSMF one places strong constraints on the form of the total GSMF. The low-mass number densities derived using the methods of the present section are found to be consistent with those from the EAGLE simulation (Schaye et al., 2015) assuming a standard Λ-CDM cosmology. Given that a GSMF with incompleteness in the dwarf regime could be mistaken as evidence for tension with the standard cosmology, it is clear that surface brightness and stellar mass biases which have been overcame in this section using SNe are crucial for an assessment of the sub-structure problem. Consistency is also found with the low-mass galaxy number densities of Wright et al. (2017), derived from a method used to estimate and correct for surface brightness incompleteness. An upper limit of 0.1 $\mathrm{dex}^{-1}\mathrm{Mpc}^{-3}$ is found at 10^7 $\mathrm{M}_{\odot}$, which is on the low end of their results, which do not distinguish between star-forming and quenched galaxies.

2.1.13 Improved Constraints Using SCALED FLUX MATCHING

Improved estimates of photo-z's and their uncertainties are in particular crucial for the constraining of CCSN-rates, star-formation-rates, and star-forming galaxy number densities of low stellar mass galaxies. This is firstly because high surface brightness objects, and therefore typically higher stellar mass objects are more typically the focus of spectroscopic analyses, and secondly because only 27 of 140 low-surface-brightness SN-host galaxies discovered in the present section have associated spectroscopy (those which do use SN spec-z).

Using different photo-z implementations, CCSN-rate densities are calculated as a function of galaxy stellar mass (corrected for the SN survey flux-limit). These results are shown in the top-panel of Figure 2.17. All errors shown are the quadrature sum of MC + Poisson + cosmic variance errors. The result presented in Sections 2.1.11 and 2.1.12, using the zMEDIC photo-z method are shown in black. Using SFM to derive photo-z's, shown in blue, the uncertainties on CCSN-rates in the dwarf galaxy regime of mass are significantly reduced. A slight increase to mean estimates of CCSN-rates in each bin over MC iterations is found below masses of $\log(\mathcal{M}/\mathrm{M}_{\odot}) \lesssim 8.0$. Accounting for nominal redshift error estimates from the SFM method, note the additional reduction to CCSN-rate density uncertainties at low masses, shown in yellow (SFM + AEA). This result gives further evidence for a power-law decrease to volumetric CCSN-rate densities with decreasing galaxy stellar mass. One is also able to probe 0.2 dex lower in galaxy stellar mass using the SFM technique compared to zMEDIC.

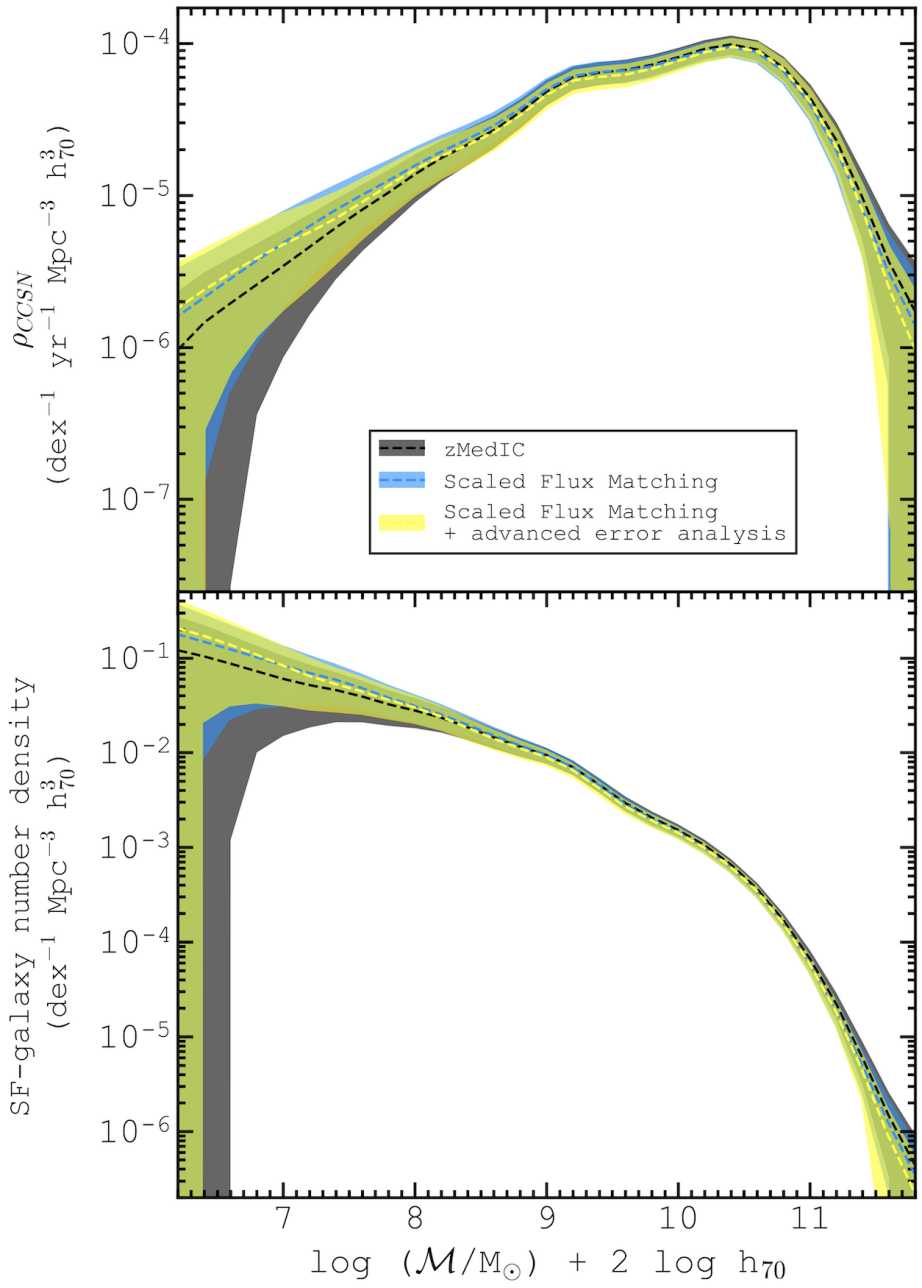

FIGURE 2.17: Top: Volumetric $z < 0.2$ CCSN-rate densities as a function of galaxy stellar mass. Bottom: The $z < 0.2$ star-forming GSMF; using different photo-z techniques: zMEDIC (shown in black); SCALED FLUX MATCHING (SFM), shown in blue; and a modification of SFM where Monte Carlo errors on photo-z are calculated using redshift PDFs dependant on the nominal redshift error estimate from SFM, shown in yellow).

Using the assumption of a constant sSFR, volume-integrated CCSN-rate estimates as a function of mass are used to estimate the SF-GSMF. Binned CCSN statistics are divided by their host galaxy mass.

Values are then normalised to the Baldry et al. (2012) SF-galaxy number densities over the range $8 < \log(\mathcal{M}/\mathrm{M}_{\odot}) < 9$ to yield estimates of the SF-GSMF from CCSNe, shown in the bottom panel of Figure 2.17.

The significant improvement to constraints of densities in the dwarf galaxy mass regime when moving from *z*MEDIC (shown in black) to SFM (shown in blue) is highlighted once more, with the fractional error on the number density a factor of ~ 3 smaller at $\log(\mathcal{M}/\mathrm{M}_{\odot}) = 7.0$. This improvement is likely due to the fact that *z*MEDIC requires a single relationship between galaxy colours and redshift whereas SFM is flexible to spectral variety in the galaxy population and does not require a knowledge of the optimal parameterisation of colour versus redshift.

Further constraints using the SFM + AEA approach are shown in yellow. Whilst these additional improvements are less significant, the lower limit on the number density is a factor of ~ 3 higher at the low mass limit of $\log\ (\mathcal{M}/\mathrm{M}_{\odot}) = 6.2$. The trend is consistent with a power-law rise to SF-galaxy number densities continuing deep into the dwarf regime of mass.

This lack of deviation from a power law below $\log(\mathcal{M}/\mathrm{M}_{\odot}) \sim 9.0$ implies there is no evidence for any truncation to galaxy formation processes down to at least $\log\ (\mathcal{M}/\mathrm{M}_{\odot}) = 6.2$. In Section 2.1.14, implications for galaxy formation processes, in light of trends of galaxy surface brightness with stellar mass, are discussed further.

2.1.14 The Galaxy Surface Brightness – Stellar Mass Relation

Star-forming galaxies exhibit a well-established trend of surface brightness with stellar mass (see, e.g. Baldry et al., 2012), indicating that surface brightness scales with stellar mass. A break from this relation with decreasing mass could imply that star-formation is constrained by different processes below a certain mass.

The effective absolute r-band surface brightness of a CCSN host galaxy is computed using Equation 2.19, where $A_{r,50}$ denotes the area in arcsec^2 enclosing half the total galaxy flux, $m_{r,auto}$ is the Galactic extinction-corrected r-band AUTO apparent magnitude from SExtractor, $K_{rr}(z)$ is the k-correction using the prescription of Chilingarian et al.

(2010), and the final term is the cosmic surface-brightness-dimming correction.

$$\langle\mu\rangle_{e,r} = m_{r,auto} + 2.5\log(A_{r,50}) + 2.5\log(2) - K_{rr}(z) - 10\log(1+z) \tag{2.19}$$

Figure 2.18 shows (in blue) the observed trend of effective surface brightness vs galaxy stellar mass. Shown are all galaxies hosting SNe classified as CCSNe or 'Unknown' by Sako et al. (2018b) which have a mean redshift from the SFM+AEA method of $z < 0.2$ over 1000 MC iterations. The mean galaxy stellar mass over these iterations is utilised. The surface brightness vs mass relation is observed to be linear for the full range of galaxy masses, with the regression line taking the form $\langle\mu\rangle_{e,r} \simeq -1.35\log(\mathcal{M}/10^9\mathrm{M}_\odot) + 22$. This result implies no phase change in galaxy evolution or star-formation processes down to $\log(\mathcal{M}/\mathrm{M}_\odot) = 6.2$, in concordance with the GSMF results shown in Section 2.1.13.

The predicted surface brightness-mass plane found in the NewHorizon hydrodynamical simulation (Jackson et al., 2021) is well-suited to a comparison with the observational results of the present section due to the simulation's unrivalled stellar mass and spatial resolution of resolution of only $10^4 M_\odot$ and 40 parsecs, respectively.

The NewHorizon simulation (Dubois et al., 2020) is a high-resolution zoom of an average-density region of the horizon-agn simulation (Dubois et al., 2016). Both simulations are evolved down to a redshift $z = 0.25$, and so while results are not at an identical epoch to that of the present work (the mean redshift in the observed $z < 0.2$ sample is $z = 0.11$), the simulations still offer a valuable comparative tool.

In NewHorizon, the hydrodynamics determine the 2-dimensional positions of baryons, which in turn determine the surface brightness of the simulated galaxies: Firstly, a mock magnitude is inferred for each particle using full spectral energy distributions from the simple stellar population templates of Bruzual & Charlot (2003). These are then redshifted and weighted by particle mass to yield mock total galaxy magnitudes. Finally, the flux-weighted second-moment of the stellar particle distribution is used to infer surface brightness (Bernstein & Jarvis, 2002).

The surface brightness versus mass relation for *all* NewHorizon galaxies is shown in red in Figure 2.18. As with the observations, a power law is observed for the relation. However, as the simulation is not subject to the signal to noise limitations of observational surveys, they can give a prediction for the relation down to lower masses than can be observed with sdss. The power law continues down to at least $\sim 10^6 M_\odot$ in the simulation, suggesting that according to a Λ-CDM framework, surface brightness and

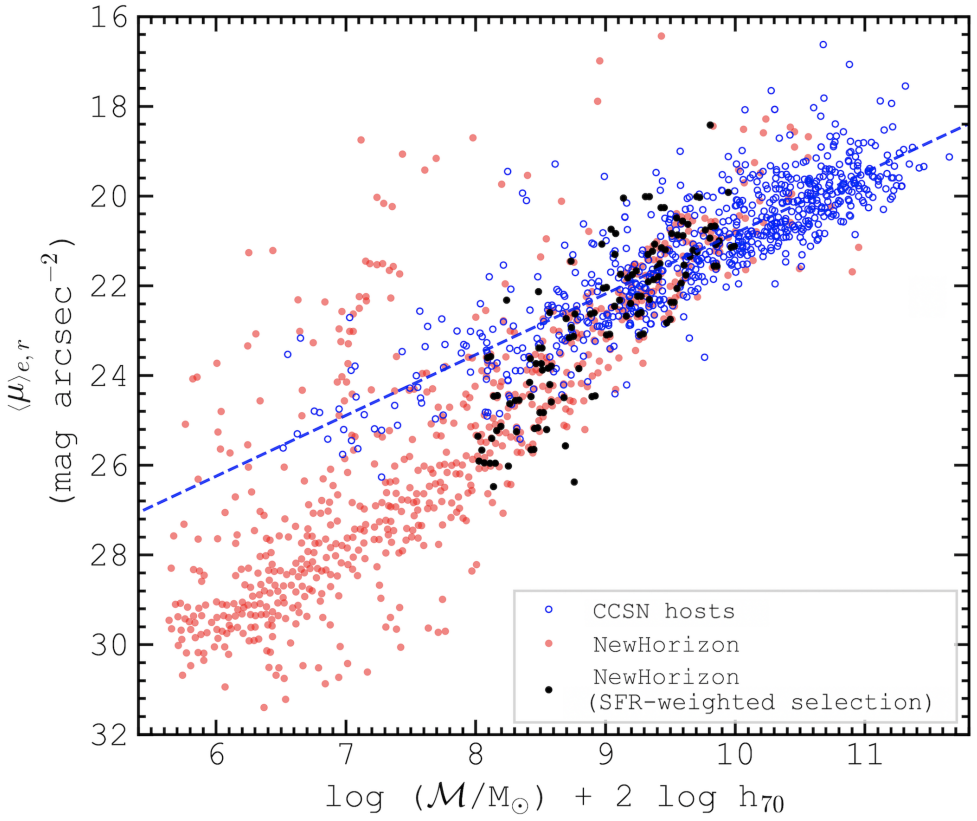

FIGURE 2.18: Galaxy effective r-band surface brightness of CCSN host galaxies as a function of stellar mass (shown in blue). A least-squares regression-line fit to observational data is shown as the dashed line. The counterpart distribution for all galaxies from the $z = 0.25$ snapshot of the NEWHORIZON simulation is shown in red. Black points depict a sub-sample of NEWHORIZON galaxies selected randomly with a weight proportional to the normalised probability distribution in star formation rate, such as to match the selection function of core-collapse supernovae.

mass are expected to obey the same simple scaling relation seen at higher masses.

What is perhaps most profound about the similarity between the observed and simulated surface brightness versus mass plane is that stellar feedback, AGN feedback and merger histories are in no way calibrated on the low mass galaxy population, nor is surface brightness tuned in any way, and yet the observed relation is reproduced.

It should be stressed that the observed result only relates to the sub-population of star-forming galaxies, whereas the simulations show the surface brightness – mass relation for the *total* galaxy population. However, the observed selection function of galaxies can be reproduced easily with the simulations by selecting galaxies at random weighted only by their star formation rate. As has already been established in this thesis, this replicates a core-collapse supernova selection.

The selected sub-sample is shown in black in Figure 2.18. This series offers an expectation for the surface brightness – mass plane were the simulations subject to detection limitations. Once again, the observed distribution is followed to first order.

It could be argued that the slope of surface brightness with mass is steeper than that in the observations at the low mass end in the simulation, however it is possible that the regression line on the observations, shown in blue, is subject to over-fitting due to a low number of galaxies below $10^9 M_\odot$.

Only with the next generation of surveys, with improved surface brightness depth and SN detection capabilities, will we be able to test the precise slope of the observed surface brightness – mass relation below masses of $\sim 10^9 M_\odot$. At present however, there is no evidence of a tension between the observed surface brightness – mass relation and that resulting from the most advanced hydrodynamical applications of Λ-CDM physics.

2.1.15 Summary

Using a SNe sample (Sako et al., 2018a) as pointers to their host galaxies, approximately 150 newly identified LSBGs have been located in IAC STRIPE 82 LEGACY coadded imaging (Figure 2.4). A galaxy selection using a complete sample of CCSNe removes surface-brightness bias.

In order to estimate stellar masses of host galaxies without spectroscopic redshifts, a colour-based photo-z method is introduced and utilised. This method, named zMEDIC,

uses the strong correlation between SLOAN *ugriz* colours and redshift. The parameterisation used is shown to work for a sample containing both star-forming and quiescent galaxies at $z < 0.4$ (Figure 2.8).

In order to assess uncertainties on CCSN-rate densities as a function of galaxy stellar mass, A Monte Carlo method is employed to fold in errors on photometric redshift (Figure 2.9) and *ugriz* photometry. The observed CCSN-rate densities as a function of mass are shown to peak at $\sim 10^{10.5}\mathrm{M}_{\odot}$ and drop by a factor of ~ 100 down to $10^{6.5}\mathrm{M}_{\odot}$ (Figure 2.10).

A model is used to correct CCSN-rate densities for SN detection efficiencies (ϵ) that depend on host galaxy extinction, Galactic extinction, SN type (Richardson et al., 2014) and redshift. Corrected CCSN-rate densities are consistent with expectations derived from the cosmic star-formation history (Madau & Dickinson, 2014) assuming $\log \mathcal{R} \simeq -2$ (Figure 2.12), where $\mathcal{R}$ is the expected number of stars that explode as CCSNe per solar mass of stars formed.

By assuming a value for $\mathcal{R}$, the corrected CCSN-rate density as a function of stellar mass (Figure 2.13) can then be scaled to the SFRD (Figure 2.14). The SFRD is consistent with the emission-line derived SFRD at high masses (Gilbank et al., 2010) but the SN-based method of the present section extends these measurements to lower masses. By assuming a constant specific star formation rate ($\mathcal{S}$), and scaling appropriately (to Baldry et al. 2012), the SFRD is converted to the star-forming GSMF (Figure 2.16). Derived star-forming galaxy number densities are found to rise as a power-law with decreasing galaxy stellar mass down to the lowest assessed masses of $\log(\mathcal{M}/\mathrm{M}_{\odot}) = 6.4$; and even at the lower limits of each bin there is no turnover in the number density of star-forming galaxies per unit log mass at least down to $\log(\mathcal{M}/\mathrm{M}_{\odot}) \sim 7$.

This section has also presented the 'SCALED FLUX MATCHING' technique for the calculation of photo-z's. It is found that relative to results using the zMEDIC technique, SCALED FLUX MATCHING produces improved galaxy stellar mass estimates of CCSN host galaxies, leading to tighter constraints on trends of volumetric CCSN-rates, star-formation-rates and star-forming galaxy number densities with stellar mass.

These improved constraints imply a lack of truncation to galaxy formation processes down to at least $\log(\mathcal{M}/\mathrm{M}_{\odot}) = 6.2$. Further evidence for this conclusion is found from trends of surface brightness with galaxy stellar mass, with no break from the higher mass relation observed down to the low-mass limits of this study. Such a power-law continuation to the galaxy surface brightness – mass relation deep into the dwarf

mass regime is found by the NewHorizon simulations to be consistent with a Λ-CDM framework.

The demonstrated CCSN-based method has been shown to significantly reduce the tension between observations and the simulated predictions of galaxy number densities derived via a standard Λ-CDM cosmology.

2.1.16 List of Assumptions

- Volumetric core-collapse supernova rates directly trace recent volumetric star formation rates.
- All SDSS-II Supernova Survey transients with $z < 0.2$ and $r_{sn,peak} < 21.8$ are authentic SNe, provided that they are > 2.5" in separation from a known star or AGN.
- 'Unknown'-type SNe are either Ia, Ib/c or II. That is, they are not spurious and are not an obscure SN type e.g. Super-luminous supernovae.
- Redshifts can be accurately converted to luminosity distances via the adoption of an $h = 0.7$, $\Omega_m = 0.3$, $\Omega_\Lambda = 0.7$ cosmology.
- $M_r \sim M_B + 0.1$ on average for the CCSNe, allowing for the estimation of r-band magnitude probability distributions for various SN types, adapted from Richardson et al. (2014).
- 'Unknown'-type SNe follow the volume-limited type ratios of Richardson et al. (2014).
- $\log \mathcal{R} = -1.9$ as an average across the cosmological volume.
- Host galaxy r-band extinction is constant with mass at $A_{r,h} = 0.5$ mag, as this yields the best consistency with the well-constrained star formation history whern adopting $\log \mathcal{R} = -1.9$.
- Specific star-formation rate is constant with galaxy mass, at least for $\log (\mathcal{M}/M_\odot) \lesssim 9.0$.

2.2 The Star Formation Rates of Elliptical Galaxies from Core-Collapse Supernovae

2.2.1 An Introduction to Elliptical Galaxies

Elliptical galaxies dominate the high-mass end of the stellar mass function at late epochs (e.g. Kelvin et al., 2014), making them essential probes of our structure formation paradigm. The stellar mass growth of these systems is tightly linked to their star formation rates over cosmic time. The classical hypothesis of a 'monolithic collapse' (Eggen et al., 1962; Larson, 1974; Chiosi & Carraro, 2002) suggests that the stellar populations of early-type galaxies formed at high redshifts ($z \gtrsim 2$), and that these galaxies have since evolved passively.

Optical properties of ellipticals appear to obey simple scaling relations which indicate that the majority of star formation in ellipticals galaxies did indeed occur at high redshift. For instance, both rest-frame optical colours and the 'Fundamental Plane' of ellipticals (Jorgensen et al., 1996; Saglia et al., 1997) exhibit only a small scatter, and do not appear to have evolved significantly for several Gyrs (e.g. Bower et al., 1992a; Franx, 1993; Van Dyk et al., 2000; Peebles, 2002).

Problematically, a monolithic star formation history cannot be aligned with the currently widely-accepted Λ-CDM framework, which in both semi-analytical models (e.g. Cole et al., 2000; Khochfar & Burkert, 2003) and in hydrodynamical simulations predicts ongoing contributions to early-type galaxy stellar mass from merger and interaction driven star formation (Mihos & Hernquist, 1994; Kaviraj et al., 2009; Naab et al., 2009; Martin et al., 2017). Therefore, an accurate quantification of the star formation levels in ellipticals has ramifications for our knowledge of both early-type galaxy evolution and cosmology, as such results can be used to anchor the physics of the simulations.

The star-formation rates of early-type galaxies can be estimated observationally via several means. UV emission is a widely utilised indicator, as it exhibits the signal of photospheric light from the very youngest, most massive stars (e.g. Salim et al., 2007; Bouwens et al., 2009). A less direct indicator is mid and far IR emission, which captures the heating of dust due to young stellar populations (e.g. Calzetti et al., 2000; Inoue et al., 2000). Specific nebular recombination lines are also widely utilised, most notably, Hα, which has contributions to its flux from hot, luminous, young stars (e.g. Glazebrook et al., 1999; Erb et al., 2006).

However, each of these diagnostics can have their signal contaminated by other mechanisms. For example, post-AGB stars see their outer envelopes, in the process of being ejected, illuminated by core UV emission (Greggio & Renzini, 1990). In Horizontal Branch stars, the intense temperatures of core-helium burning can also cause UV emission in these stars' optically thin regions. In the case of both phenomena, strong emission lines such as Hα can also be generated; lines which are typically associated with the presence of young stars (Preston et al., 2006). Other mechanisms which could be misinterpreted as star formation without careful investigation include the ionisation of gas due to active galactic nuclei (AGN; Groves et al., 2006), or due to shocks, with the collision of gas clouds (Oparin & Moiseev, 2018).

In the case of galaxies residing on the star forming main sequence (Noeske et al., 2007b), such as most spiral galaxies, the contributions from these contaminants make up a small fraction of the star formation signal, and can be largely ignored. However, for galaxies below the main sequence, such as ellipticals, these contaminants present a serious boundary to studies of their star formation rates.

A consequence of this issue is some degree of debate over the precise level of star formation typical in ellipticals, which in turn perpetuates the debate over our pictures of early-type galaxy mass assembly and cosmology. Whilst some studies conclude practically zero levels, (e.g. Jura, 1977; Kennicutt, 1998),

More recent work suggests that low-level star formation persists in ellipticals over at least the latter half of cosmic time. For instance, Kaviraj et al. (2007) find that, while they are a homogeneous population in optical colours (Bower et al., 1992b), elliptical galaxies show more than 6 mags of colour spread in the NUV, which is a much wider range than can be produced from old stellar populations (e.g. Yi, 2003). They conclude that at least 30% of local elliptical galaxies have NUV colours indicative of recent star formation within the last Gyr, and at $z \lesssim 0.1$, elliptical galaxies have $1\% - 3\%$ of their stellar mass in stars produced within such a time-frame.

Interestingly, for ellipticals at intermediate redshift ($0.5 < z < 1$), i.e. epochs at which the Universe is effectively too young for old stellar populations to exist, the characteristics of NUV colours remain the same (Kaviraj et al., 2008; Martin et al., 2018). This implies that this observed low-level star formation persists in early-type galaxies over at least the latter half of cosmic time. There also exists a strong correspondence between the presence of disturbed morphologies and blue UV colours (Kaviraj et al., 2011) indicating that the star formation is merger driven (Schweizer et al., 1990; Schweizer & Seitzer, 1992). Furthermore, the frequency of these morphological disturbances is

larger than can be accounted for by the major-merger rate alone (Kaviraj et al., 2011), suggesting that minor mergers (i.e. mergers between ellipticals and gas-rich satellites) are likely to drive much of the elliptical star formation seen in the NUV, at least at late epochs (Kaviraj et al., 2009), with $\sim$ 14% of the total cosmic star formation budget residing in the elliptical population in the low-redshift Universe (Kaviraj, 2014a,b).

Broad-wavelength SED-based derivations, such as those from Salim et al. (2016), offer arguably the most sensitive treatment to sub-main sequence star formation rates to date, due to the ability to better identify sources of contamination to the star formation signal from the broad view of spectral information spanning from the UV to the IR. However, even these estimates are only reported as upper limits on the level of star formation in ellipticals.

It is common to try to distinguish signatures of true star formation from those of AGN or old stellar populations using galaxy emission line ratios, such as Hα/[NII] and $H\beta$/[OIII] (e.g. Kauffmann et al., 2003). However, there is scatter in these relations, and if ellipticals do exhibit some level of star formation, they are unlikely to occupy the main locus as blue star-forming galaxies. As such, the issue is turned on its head, and low-level star formation could easily be misattributed to AGN activity and/or old stellar emission in a discrete treatment, such as that seen with the BPT diagram (e.g. Baldwin et al., 1981; Veilleux & Osterbrock, 1987). Additionally, there are not an abundance of models which can predict these ratios from first principles.

Recent sophisticated simulation suites such as EAGLE (Schaye et al., 2015), HORIZON-AGN (Dubois et al., 2016; Kaviraj et al., 2017) and ILLUSTRIS-TNG (Pillepich et al., 2018) support the suggestion that minor mergers could generate a persistent low-level of star formation. This would not only make them a phenomenon crucial to the evolution of ellipticals, but would also point further towards the hierarchical evolution now widely accepted under a Λ-CDM paradigm.

There are other ways in which simulations can manipulate galaxy star formation rates, aside from merging and other environmental processes. AGN accretion prescriptions and black hole feedback can respectively enhance or suppress star formation (Somerville & Davé, 2015). Irrespectively, observational results are crucial to constraints on each of these physical processes.

Such simulations also implement sub-grid star formation recipes as well as feedback mechanisms which can remove cold gas and quench star formation. Since these sub-grid recipes are often calibrated and benchmarked against a number of observed properties

and relations (including star formation rate densities; e.g. Pillepich et al., 2018), any biases or systematic uncertainties in these quantities can produce unrealistic sub-grid physics and degrade the predictive power of the simulations.

If the observed elliptical morphology and colour are reproduced organically via 'dry' mergers as a consequence of quenching through feedback, both merger rates (minor and major) and feedback mechanisms could be better constrained in light of accurate and unbiased tracers of elliptical star formation rates. Furthermore, since many of these simulations now aim to replicate the star formation rate density (SFRD) of main-sequence galaxies as standard, a natural progression would be to test model physics using the observed star formation rates of the early-type population.

There are other mechanisms which may also drive star formation in ellipticals. For example, galaxies of all morphological types are surrounded by significant reservoirs of cold gas (Chen et al., 2010; Thom et al., 2012), which may fuel low levels of star formation even in apparently dead ellipticals (Tumlinson et al., 2017). In hydrodynamical simulations, the structure and physical properties of the CGM are found to depend strongly on factors such as resolution, feedback and the presence of magnetic fields and cosmic rays (Hummels et al., 2019; Butsky et al., 2020). Therefore, accurate measurements of the level of star formation in elliptical galaxies are an important clue for understanding the connection between galaxy evolution and the CGM. In more sophisticated simulations, which incorporate magnetic fields and cosmic ray heating in addition to stellar and AGN feedback processes, observations like these will be important for placing constraints on the recipes used to model these processes.

For each of the described reasons, one is encouraged to search for an independent diagnostic of star formation which is not subject to the aforementioned uncertainties. Core-collapse supernovae (CCSNe) are unambiguous indicators of recent star formation. The short ($\sim$ 6-40 Myr; Smartt, 2009; Botticella et al., 2017) lifetimes of their progenitor stars, relative to the timescales of galaxy evolution, mean that the presence of CCSNe in the low-z elliptical population would offer explicit evidence of recent low-level star formation within them.

These transients also provide a more thorough analysis of star formation in the shape of the volumetric SFRD ($\rho_{\rm SFR}$) as a function of galaxy stellar mass, $\mathcal{M}$. It was shown in Section 2.1 that the SFRD of low-surface brightness galaxies can be accurately traced from the volume's CCSN rates, $\rho_{\rm CCSN}$, as measured by the untargeted, high-cadence, SDSS-II SUPERNOVA SURVEY (Sako et al., 2018b), by matching CCSNe to their host galaxies. This connection is shown via Equation 2.20, where $\overline{\mathcal{R}}$ is the mean ratio of

CCSN events to mass of stars formed.

$$\rho_{\rm SFR}(\mathcal{M}) \;=\; \frac{\rho_{\rm CCSN}(\mathcal{M})}{\overline{\mathcal{R}}} \tag{2.20}$$

In the case of low surface brightness galaxies (LSBGs), CCSNe not only helped locate galaxies which would have been missed using traditional galaxy extraction pipelines, by acting as signposts towards them, but they also allowed the population's star formation to be quantified in situations where spectral and broad-band photometry-based derivations would be subject to large uncertainties related to low signal-to-noise. It is this latter point which particularly encourages the extension of a similar method to elliptical galaxies.

The SFRD would allow constraints to be placed on the elliptical contribution to the cosmic star formation budget. As well as the SFRD, one may also be able to assess the mean *specific* star formation rate (SSFR; $\overline{\mathcal{S}}$) of ellipticals, both as a function of mass, and for the total population. This is due to the connection between the SFRD, the galaxy stellar mass function (GSMF) and ($\overline{\mathcal{S}}$), demonstrated via Equation 2.21, where ϕ is the number density of galaxies in a cosmological volume.

$$\overline{\mathcal{S}}(\mathcal{M}) \;=\; \frac{\rho_{\rm SFR}(\mathcal{M})}{\Phi(\mathcal{M})\,\mathcal{M}} \tag{2.21}$$

In Section 2.1, the SFRD was first found from CCSNe, before the GSMF was determined using a re-arrangement of Equation 2.21 from the assumption that $\overline{\mathcal{S}}$ is constant with mass for low-surface brightness galaxies, due to their residence on the star forming main sequence (McGaugh et al., 2017). In the case of massive ellipticals, however, the GSMF is already well-constrained via various experiments (Franceschini et al., 2006; Vulcani et al., 2011; Kelvin et al., 2014), and it is instead $\overline{\mathcal{S}}$ which is unknown. Whilst this section will utilise Equation 2.21 to measure the mean SSFR of ellipticals, the relation can be applied to any well-defined galaxy population for which any two of $\rho_{\rm SFR}$, ϕ and $\overline{\mathcal{S}}$ are known.

The structure of the present section is summarised as follows: Sections 2.2.2 and 2.2.3 summarise the definition of the CCSN and elliptical samples, respectively along with summaries of the data sets used. Section 2.2.4 gives measurements of the volumetric star formation rate density of ellipticals. Section 2.2.5 shows results for the galaxy stellar mass function and mean specific star formation rate of ellipticals. Section 2.2.6 compares the spectra of CCSN-hosting ellipticals to that of a control sample of standard

ellipticals. Finally, Section 2.2.7 summarises each finding in the context of early-type galaxy evolution.

2.2.2 A Recap of the Core Collapse Supernova Sample

We begin with the SN sample utilised in Section 2.1. This was formed from the SDSS-II Supernovae Sample (Sako et al., 2018b), cross matched with the IAC STRIPE 82 LEGACY sample (Fliri & Trujillo, 2016). A more detailed discussion of this cross-matching is given in Section 2.1, which describes the careful assignment of host galaxies, and the rejection of variable stars and AGN. This sample was cut to exclude SN of r-band peak brightness > 21.8 magnitudes, fainter than which the sample is estimated to be incomplete (as also described in the aforementioned section). This initial sample consists of 2528 $r_{peak} < 21.8$ mag SNe and their hosts, following variable star/AGN removal.

The best redshift estimate available is utilised for each SN/host pair: this is spectroscopic, from either SN (taking preference) or host galaxy, the latter from either SDSS-II LEGACY (York et al., 2000), SDSS-II SOUTHERN (Baldry et al., 2005), SDSS-III BOSS (Dawson et al., 2013) or SDSS-IV eBOSS (Dawson et al., 2016), or in the absence of spectra, photometric, from *ugriz* STRIPE 82 legacy survey galaxy fluxes, using the 'SCALED FLUX MATCHING' technique. The SN sample is then cut to $z < 0.2$, leaving 1070 SNe, 845 of which have a spectroscopic redshift.

In the present section, SN classifications are treated differently than in Section 2.1. Sako et al. (2018b) attempted to classify each of these SNe as either a Type Ia, Type Ib/c, or Type II. As a brief summary, 2 main sets of probabilities were calculated for each SN:

The first was a set of Bayesian probabilities of belonging to each of the 3 SN classes, obtained by analysing observed light curves with the Photometric SN IDentification (PSNID) software (Sako et al., 2011), using a grid of Type Ia, Type Ib/c and Type II SN light curve templates.

The second was a set of Bayesian + nearest-neighbour (NN) probabilities, the improvement being that with the NN extension, probabilities account for differences in the distributions of extinction, light curve shape and redshift seen for each of the 3 SN types. Synthetic SNe of each type were considered a 'near-neighbour' to an observed SN if within a threshold Cartesian distance in a 3-dimensional parameter space consisting of the above 3 parameters. The NN probability of the candidate being a Type II SN, for instance, was then the fraction of NN simulated SNe which were Type II's. In the present section, the NN probability, $P_{\rm NN}$ is utilised if there are at least 20 near-neighbours for

the transient, which is the case for 738 $z < 0.2$ SNe, and in the 332 remaining cases the Bayesian-only probability, $P_{\rm Bayes}$ is used. The best probabilities available are denoted as $P_{\rm Ia}$, $P_{\rm Ibc}$ and $P_{\rm II}$. Though there is some spread in the $P_{\rm NN} - P_{\rm Bayes}$ distributions, with a standard deviation of 0.22 for the $z < 0.2$ Type Ia probabilities, for example, the mean difference of $P_{\rm NN} - P_{\rm Bayes}$ for Type Ia SNe is very close to zero, implying a consistency between the 2 methods on a statistical level.

Elliptical galaxies are more traditionally associated with Type Ia SNe than with CCSNe (e.g. Gallagher et al., 2008). To ensure Type Ia interlopers do not cause an overestimate of star-formation properties, it is therefore required that $P_{\rm Ia} < 0.05$ for the SN to be included in the CCSN sample. Removing those with $P_{\rm Ia} > 0.05$, one is left with 360 confidently classified $z < 0.2$ CCSNe. This sub-sample is used for all main CCSN-based results in the present section. However, analyses will be repeated including an additional 61 $0.05 < P_{\rm Ia} < 0.5$ objects, to test for the sensitivity of results to Type Ia contamination. Note that these numbers suggest the CCSN probabilities are largely bi-modal. Put differently, $\sim 93\%$ of all $z < 0.2$ SNe have either $P_{\rm Ia} < 0.05$ or $P_{\rm Ia} > 0.95$.

The ratio of likely Type Ib/c SNe to likely Type II SNe is also approximately in line with expectations from the literature (e.g. Hakobyan, 2008), with 24 ± 1 (Poisson error) % having $P_{\rm Ibc} > P_{\rm II}$. Furthermore, it is far more common to misclassify a Type Ia as a Type Ic rather than as a Type II SN, due to the similar light curve shapes of Type Ia and Type Ic supernovae (lack of plateau), and due to their similar spectra (Clocchiatti & Wheeler, 1997). As a result, if the core-collapse sample had significant contamination from Type Ia supernovae, one would expect a higher ratio of Type Ib/c to Type II supernovae than is observed. These points increase confidence that the Bayesian SN-type classifications are fully trustworthy.

Other tests for the sensitivity of forthcoming results to contamination include a repeating of results with SN type probabilities re-scaled to account for the efficiency and purity estimates in each SN class. These values were estimated from a set of simulated SNe by Sako et al. (2018b). The effect of simply using Bayesian-only probabilities for all SNe is also tested for. As might be expected given the aforementioned mean of the $P_{\rm NN} - P_{\rm Bayes}$ distribution, and the bi-modality of the CCSN probabilities, respectively, it is found for both tests that the forthcoming results do not change notably. Furthermore, it is seen in Figure 2.19 that the extinction-corrected absolute r-band magnitude distributions of $P_{\rm cc} > 0.5$ and $P_{\rm Ia} > 0.5$ supernovae match well the counterpart distributions for spectroscopically confirmed core-collapse and Type Ia supernovae, which in turn match the volume-limited magnitude distributions of Richardson et al. (2014). These factors

further increase confidence that the Bayesian-classified core-collapse supernovae found in ellipticals are genuinely core-collapse in nature.

As a final point, there may also be a small contamination from SN1991bg-like objects in the $P_{\rm cc} > 0.5$ sample as this subclass of Type Ia supernovae are 1-2 magnitudes fainter than typical Type Ia's (Taubenberger, 2017). However, the decay time of the light curves of 91bg-like objects is significantly more rapid than that of Type II and Type Ib/c supernovae, which would affect the Bayesian probabilities when compared to template light curves of core-collapse supernovae (Taubenberger et al., 2008). Furthermore, the frequency of these objects is small compared to core-collapse rates (Silverman et al., 2012), and as such they are not expected to constitute a significant fraction of the $P_{\rm cc} > 0.5$ sample. In conclusion, the CCSNe are classified from their light curves with sufficient confidence that the sample selection is stable to the fine tuning of the SN classification procedure.

2.2.3 Defining Elliptical Galaxies

It must next be determined which hosts galaxies are ellipticals, and as quantitatively as possible. For this, the wider sample of galaxies in IAC STRIPE 82 LEGACY coadded imaging is turned to.

Using estimates by Fliri & Trujillo (2016) from simulated de Vaucouleurs profiles, one can expect 95% of all $z < 0.2$ bulge-dominated galaxies in the LEGACY coadded imaging to have at least 95% of their light recovered at $r_{\rm AUTO} = 20$ mag, where AUTO denotes the near-total light 'Kron' elliptical aperture (Kron, 1980; Bertin & Arnouts, 1996b). This magnitude cut is therefore imposed, leaving a sample of 113239 galaxies. Note that this cut is not applied to the SN hosts, as it is the SN light which determines their detection. Nonetheless, 70% of all $z < 0.2$ SN hosts in the sample have $r < 20$ mag, and this rises to 98% for $\mathcal{M} > 10^{10.0}{\rm M}_{\odot}$, masses below which one expects few ellipticals.

The most common and straightforward way to attempt to isolate ellipticals is to use a cut on galaxy morphology. For example, Kelvin et al. (2014) define ellipticals as all single-component, bulge-dominated galaxies. A useful parameter to quantitatively represent 'bulge dominance', available for all SDSS galaxies, is the 'de Vaucouleurs fraction' ($f_{\rm deV}$). In SDSS, the composite model r-band flux for a galaxy, $F_{\rm comp}$, is calculated by taking a best-fit linear combination of flux in a de Vaucouleurs profile with that in an exponential profile, such that $F_{\rm comp} = f_{\rm deV}F_{\rm deV} + (1 - f_{\rm deV})F_{\rm exp}$, i.e. $F_{\rm comp} = F_{\rm deV}$ and $f_{\rm deV} = 1$ for the most bulge dominated cases.

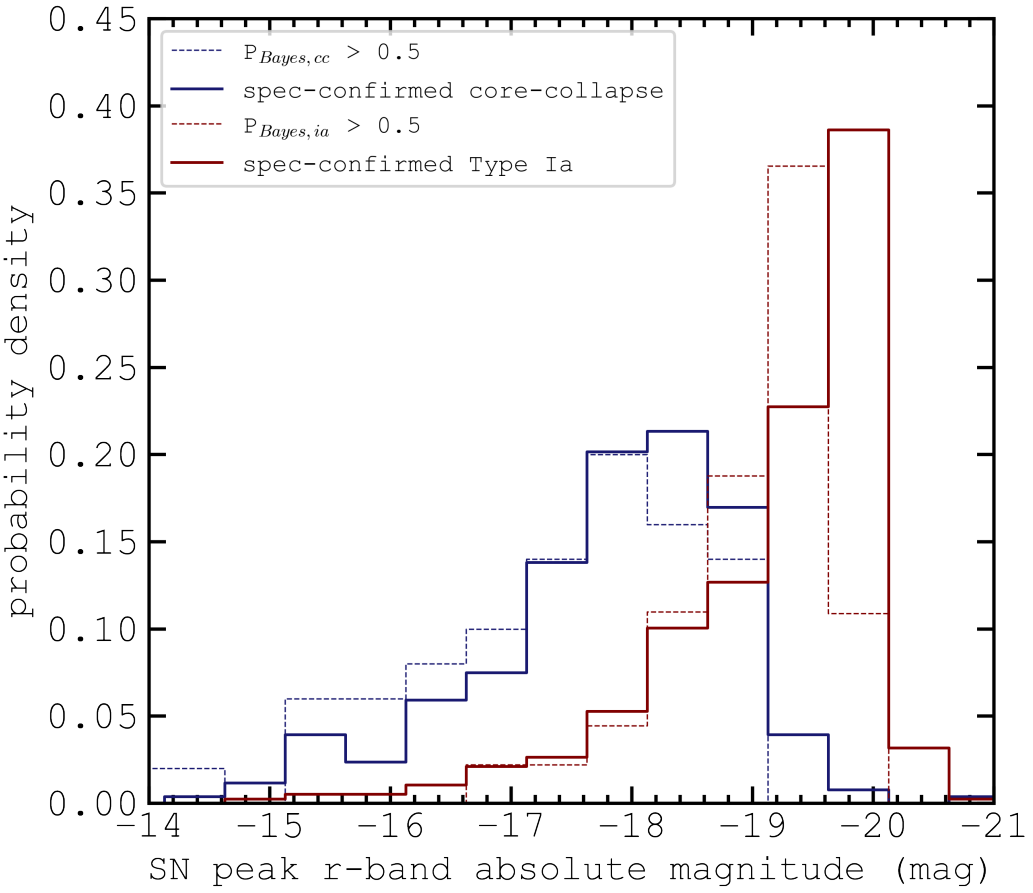

FIGURE 2.19: Extinction-corrected absolute peak r-band magnitude distributions of various supernovae. Solid red and blue lines depict $z < 0.2$, $r_{sn,peak} < 21.8$, spectroscopically confirmed Type Ia and core-collapse Supernovae respectively. Red and blue Dashed lines depict $P_{\rm Ia} > 0.5$ and $P_{\rm cc} > 0.5$ supernovae respectively (with $z < 0.2$ and $r_{sn,peak} < 21.8$ and with spectroscopically confirmed supernovae removed).

Whilst defining ellipticals based on this parameter alone is sufficient for most applications, if one is to estimate the typical star formation of ellipticals, then particular care must be taken to avoid any contamination from non-ellipticals, which could have a significant weighting on such calculations.

To estimate the contamination when classifying on $f_{\rm deV}$ alone, the galaxy sample is cross-matched, within 2.5", to GALAXY ZOO 1 (combined main and bias studies; Lintott et al., 2011). Next, those $z < 0.2$, $r < 20$ mag galaxies (although most have $r < 18$ mag) with $P_{\rm E,GZ} > 0.8$ (4692 galaxies) and those $z < 0.2$, $r < 20$ mag galaxies with $P_{\rm E,GZ} < 0.2$ (3874 galaxies) are isolated. Here, $P_{\rm E,GZ}$ is the fraction of votes for an elliptical classification within the GALAXY ZOO Project.

Of those confidently classified galaxies with either $P_{\rm E,GZ} > 0.8$ or $P_{\rm E,GZ} < 0.2$, it is found that 20% of galaxies with $f_{\rm deV} > 0.5$ have $P_{\rm E,GZ} < 0.2$. Imagine this interloping 20% possess (a maybe even conservative) 10 times the star formation rate of the genuine ellipticals in the sample: Suddenly, ~ 70 of all CCSNe (and star formation) within this sample would stem from interlopers.

A naive solution would be to inspect the ~ 45000 $z < 0.2$, $r < 20$ mag, $f_{\rm deV} > 0.5$ galaxies manually to remove non-ellipticals. A consistent inspection of this number of galaxies is not only impractical but it is also found that an over-reliance on manual inspection results in a significant redshift bias towards the selection of nearby objects, due to the better resolution of galaxy structure at lower redshifts.

One instead finds that a Bayesian classification method, effectively based on distributions of colour and morphology, yields a near-complete sample of ellipticals, whilst removing contaminants effectively, and minimising redshift selection biases.

The previously obtained samples of $P_{\rm E,GZ} > 0.8$ and $P_{\rm E,GZ} < 0.2$ galaxies are treated as respective reference samples of ellipticals and non-ellipticals. Redshift-debiased values of $P_{\rm E,GZ}$ from the GALAXY ZOO project's spectroscopic sample are utilised where available. In the absence of such a value, the raw classification fractions from their photometric sample are utilised. Note, however, that for the low redshift range pertaining to the present section, the median change to classification fraction is small, at $\sim 5\%$ for $0.15 < z < 0.2$, $r < 20$ mag galaxies.

One next arrives at an elliptical classification confidence level, $P_{\rm E,Bayes}$, using a range of variables $i, i+1, i+2, ..., n$. Let $P(E \mid i)$ correspond to the probability that a galaxy would belong to the $P_{\rm E,GZ} > 0.8$ sub-sample, given the galaxy's value for a variable i. Likewise, let $P(N \mid i)$ denote the probability that the galaxy would belong to the

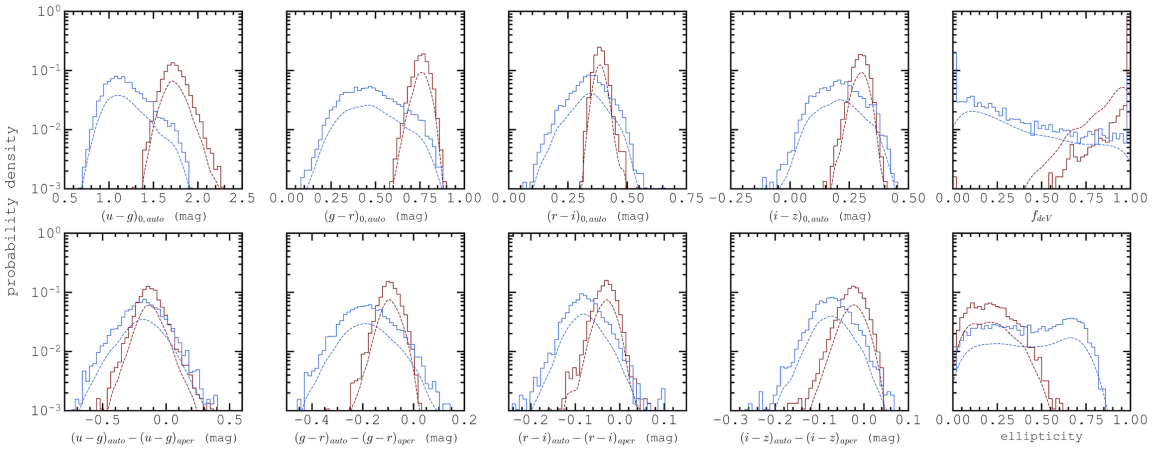

FIGURE 2.20: The 10 sets of probability density functions used to classify elliptical galaxies (see text for details). Dark-red series denote the training sample of $P_{\mathrm{E,GZ}} > 0.8$ $z < 0.2$ $r < 20$ mag galaxies in the STRIPE 82 region. Blue series show the same but with instead $P_{\mathrm{E,GZ}} < 0.2$. Gaussian KDEs are fitted to the distributions. For a given galaxy, the ratios of the KDE heights at a given value for each variable are used to calculate $P_{\mathrm{E,Bayes}}$.

$P_{\mathrm{E,GZ}} < 0.2$ sub-sample given this input. According to Bayesian statistics, the odds ratio $P(E \mid i)/P(N \mid i)$ is then given by Equation 2.22, where $P(E)/P(N)$ is the odds ratio prior to the consideration of the variable i. Crucially, $P(i \mid E)/P(i \mid N)$ equates to the ratio of probability density function heights at the value for i.

$$\frac{P(E \mid i)}{P(N \mid i)} = \frac{P(i \mid E)}{P(i \mid N)} \frac{P(E)}{P(N)} \tag{2.22}$$

It is assumed as an initial prior that $P(E)/P(N) = 1$. As the odds ratio becomes the new prior when combining information from successive variables, it follows that a galaxy's elliptical classification confidence level is given directly from the product of several PDF height ratios, as shown by Equation 2.23.

$$P_{\mathrm{E,Bayes}} = \left[\left(\prod_{i}^{n} \frac{P(i \mid E)}{P(i \mid N)} \right)^{-1} + 1 \right]^{-1} \tag{2.23}$$

In total, 10 variables are used to calculate $P_{\mathrm{E,Bayes}}$, as shown in Figure 2.20. The PDFs used as inputs for Equation 2.23 equate to Gaussian kernels fitted to each variable's distribution, each smoothed empirically to avoid non-physical discontinuities.

Firstly, rest-frame *ugriz* colours within elliptical AUTO apertures are utilised, which are corrected for Galactic extinction using the maps of Schlegel et al. (1998) and k-corrected

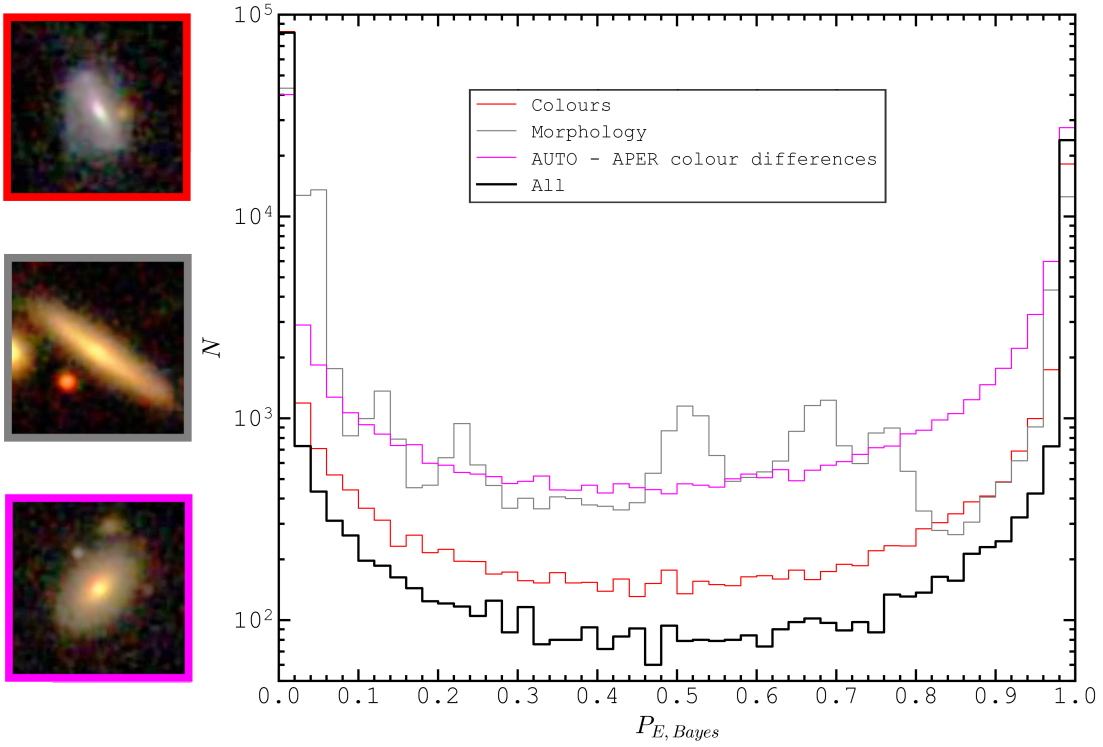

FIGURE 2.21: Distributions of $P_{\rm E,Bayes}$ values for the sample of $\sim 10^5$ $z < 0.2$ $r < 20$ mag STRIPE 82 galaxies. In black: the final $P_{\rm E,Bayes}$ values using all 10 variables in unison. In red, grey, and magenta: $P_{\rm E,Bayes}$ values from galaxy colours, morphology (ellipticity and $f_{\rm deV}$), and AUTO-APER colour differences alone, respectively. Adjacent images show examples of galaxies with final values of $P_{\rm E,Bayes} < 0.5$, but which would have had $P_{\rm E,Bayes} > 0.5$ were it not for a single set of variables, where image border colour denotes the set of variables which caused the crucial reduction to $P_{\rm E,Bayes}$.

with the prescription of Chilingarian et al. (2010). These primarily help isolate 'red sequence' galaxies from the star-forming 'blue cloud' (see, e.g. Baldry et al., 2004).

The next variable used is the difference between AUTO aperture colours and those within 2.5" radius circular apertures (denoted APER, Bertin & Arnouts, 1996b). Late-type galaxies typically feature disks which are bluer than their bulges, due to the higher star formation levels in the former regions. Conversely, ellipticals display relatively radially consistent colours. As a result, the wider spread about a null colour difference seen for the non-elliptical reference sample helps one to exclude disk galaxies.

Finally, 2 measures of morphology are utilised. The first is the apparent ellipticity, measured in the r-band. The second is $f_{\rm deV}$. These 2 morphological parameters primarily aid the exclusion of dusty, red, star-formers.

The distribution of final $P_{\rm E,Bayes}$ values found from the 10 sets of input PDFs in unison is shown as the black series in Figure 2.21. Approximately 95% of all $z < 0.2$, $r < 20$

mag galaxies have $P_{\rm E,Bayes} > 0.95$ or $P_{\rm E,Bayes} < 0.05$. This includes all galaxies, not just the training sample.

Also shown are the distributions of $P_{\rm E,Bayes}$ values resulting from the parameters used in isolation. It can be seen that galaxy colours are the most crucial parameters for a confident elliptical classification, with $\sim 90\%$ of $z < 0.2$, $r < 20$ mag galaxies having $P_{\rm E,Bayes} > 0.95$ or $P_{\rm E,Bayes} < 0.05$ from colour alone. Morphology ($f_{\rm deV}$ and ellipticity) and AUTO-APER colour differences are of secondary and comparable importance for classification confidence.

Of course, confidence is not always a reflection of the accuracy of classifications: Each of the parameters helps remove a different sort of contaminating object, and must be used in unison for an effective isolation of ellipticals. This is emphasised with the IAC STRIPE 82 LEGACY coadded images included in Figure 2.21, which show galaxies that would have been assigned $P_{\rm E,Bayes} > 0.5$ were it not for a given criterion.

The top image shows a nearby irregular galaxy which exhibits similar morphological properties to a massive elliptical, but was rejected after a consideration of its optical colours. The central image shows an edge-on, dusty, star-forming galaxy which is consistent in colour with an elliptical, but was rejected due to $f_{\rm deV}$ and ellipticity. The bottom image shows either a poorly resolved spiral or a lenticular disk, consistent in both colour and morphology with an elliptical, yet rejected due to its AUTO-APER colour differences.

Of a total of 113239 $z < 0.2$, $r < 20$ mag galaxies, 27940 ($\sim 25\%$) have $P_{\rm E,Bayes} > 0.5$, and it is these galaxies which define the elliptical sample, to be used in successive sections of the present section.

Manual inspection of these objects reveals little to no contamination from any obvious non-ellipticals, nor any obvious evidence of LSBGs along the line-of-sight to these ellipticals which could have instead housed the observed CCSNe. Figure 2.22 shows 2 more quantitative tests for the validity of classifications. The left-hand panel shows k-corrected r-band absolute magnitude versus rest-frame $(g-r)$ colour, where all magnitudes are in AUTO apertures, with the aperture defined in the r-band. Contour levels are 10% to 90% of the peak number density in steps of 10%. The fact that the dashed-red and dashed-blue contours overlap shows that, much like a rudimentary cut on $f_{\rm deV}$, a 'hard' cut on colour would not be able to remove non-ellipticals without also removing a significant number of ellipticals.

It can be seen that the sample of ellipticals resulting from the Bayesian classification

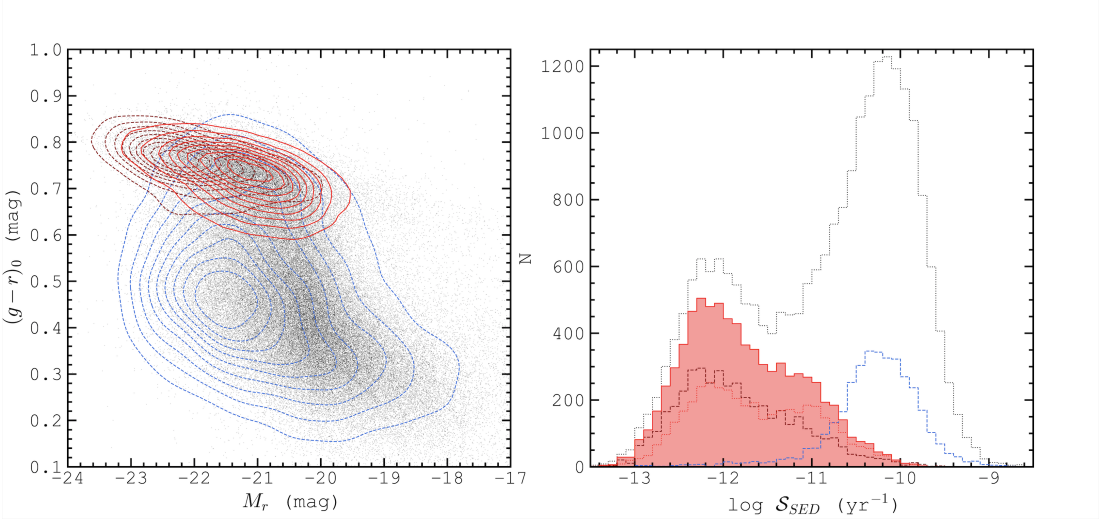

FIGURE 2.22: Left: Rest-frame r-band absolute magnitude versus rest-frame $(g-r)$ colour, where all magnitudes are those within elliptical AUTO ('Kron') apertures and are corrected for Galactic extinction. Contour levels are 10% to 90% of the peak number density in steps of 10%. Dashed-dark-red and dashed-blue contours depict the training samples of $P_{\rm E,GZ} > 0.8$ and $P_{\rm E,GZ} < 0.2$ galaxies, respectively. The solid-red contours represent the sample of ellipticals resulting from the Bayesian classification method presented in this section. Black points show the distribution of all $z < 0.2$, $r < 20$ mag STRIPE 82 galaxies. Right: Galaxy counts as a function of specific-star formation rate as measured by GSWLC-2. The dashed-dark-red, dashed-blue, red-filled and black-dotted series represent the same respective sub-samples, described for the left-hand panel. The red-dotted series depicts the same sample as shown by the red-filled series, but excluding the training set of $P_{\rm E,GZ} > 0.8$ galaxies.

method (solid-red) follows a similar distribution to the training set of $P_{\rm E,GZ} > 0.8$ galaxies (dashed-dark-red), with the only notable difference being an offset in absolute magnitude of ~ 1 mag between the peak density of the 2 distributions. This is due to the bias of having more confident manual classifications in GALAXY ZOO for brighter galaxies. This is also clear from the fact that the magnitude at which one finds a peak number density in the $P_{\rm E,GZ} < 0.2$ sample (dashed-blue) does not correspond the magnitude at which peak density is seen for all galaxies (black points).

To test the CCSN-derived star formation results of the present section, a comparison will be repeatedly made with star formation rates derived from UV/Optical SED fitting applied to the second edition of the GALEX-SDSS-WISE LEGACY CATALOGUE (GSWLC-2; Salim et al., 2016, 2018).

In the present section, 23009 out of 113239 $z < 0.2$ $r < 20$ mag galaxies are matched with the GSWLC-2 sample within 2.5". These matches are $r_{\rm petro} < 18$ mag galaxies with a spectroscopic redshift in the range $0.03 < z < 0.2$, which lie within the GALEX footprint (Martin et al., 2005; Morrissey et al., 2007).

Star formation properties of these galaxies were estimated using SED fitting with the Code Investigating GALaxy Emission (CIGALE; Noll et al., 2009; Boquien et al., 2019). Excellent summaries of the SED fitting technique are given in Salim et al. (2018) and Turner et al. (2021), but in short: Synthetic spectra, generated using the simple stellar population templates of Bruzual & Charlot (2003), based on a Chabrier (2003) initial mass function and covering a wide range of metallicities ($\log(Z) = -2.4$ to -1.3), are fitted to the observed UV-to-Optical photometry.

Templates were then combined with Myr-resolution star formation histories. The library of these histories were built using exponentials with various decay times for an old stellar population, with a relatively flat burst superimposed (at least 100 Myr ago) to represent a younger population. The SED estimates of star formation rate were additionally constrained by the galaxy IR luminosity, itself calculated by matching the energy absorbed by a galaxy's dust with the energy it re-emits. Other properties derived in this fitting procedure include (but are not limited to) galaxy stellar masses, stellar ages, stellar metallicities, absolute magnitudes and colour excess. In the present section, what is utilised is the SFR derived using the deepest photometry available for each galaxy (catalogue GSWLC-X2).

The right-hand panel of Figure 2.22 shows the matched distribution of SED-derived SSFRs ($\mathcal{S}_{\rm SED}$). It is seen that the peak value of $\mathcal{S}_{\rm SED}$ comes at $\sim 10^{-12.0}$ yr^{-1} for both the training sample and Bayesian-classified sample of ellipticals. A notable difference between the final elliptical sample and the GALAXY ZOO training sample is that the former exhibits a secondary peak at $\mathcal{S}_{\rm SED} \sim 10^{-11.0}$ yr^{-1}. However, no significant difference is found in the appearance of the galaxies classified as ellipticals at these 2 different levels of star formation, and so the origin of this secondary peak remains unexplained.

According to the classifications presented in this section, 74% of $\mathcal{S}_{\rm SED} < 10^{-11.0}$ yr^{-1} are classified as ellipticals. This number rises to 80% for $\mathcal{S}_{\rm SED} < 10^{-12.0}$ yr^{-1}. Ellipticals become the dominant class for $\mathcal{S}_{\rm SED} \lesssim 10^{-10.8}$ yr^{-1}.

In summary, this Bayesian method is able to isolate a near-complete sample of $z < 0.2$, $r < 20$ mag elliptical galaxies in the STRIPE 82 region. In theory, this method could be extended to efficiently classify several species of galaxies over wide-field survey footprints, in a manner consistent over redshift.

2.2.4 The Star Formation Rate Density in Ellipticals

As CCSN hosts were classified simultaneously with the larger galaxy sample, they are subject to identical classification criteria as in the previous sub-section. Of the sample of 421 likely CCSN hosts ($P_{\rm Ia} < 0.5$), 36 are classified as ellipticals using the described Bayesian procedure. 27 of these have $P_{\rm Ia} < 0.05$.

Co-added STRIPE 82 images of these 36 galaxies are shown in Figure 2.23. These host galaxies can now be used to estimate the contribution to the cosmic star-formation density from ellipticals. One can utilise Equation 2.26 to estimate the CCSN-rate density per unit volume V in ellipticals using the sample of elliptical CCSN host galaxies (see also Section 2.1). Galaxy stellar masses are first calculated using the same prescription as in Section 2.1; a k-correction inclusive prescription based on i-band AUTO mag, $(g-i)$ observed colour (in 2.5" circular apertures) and redshift.

To correct for the fact that the SN sample is flux-limited but what is instead desired are volume-limited CCSN statistics, a statistical correction identical to that used in Section 2.1 is implemented. This is similar to a $1/V_{\rm max}$ method, but where the SN light is the determining factor in detection, not the host galaxy light. The volume-limited absolute magnitude distributions of Richardson et al. (2014) are employed for Type Ib/c and Type II SNe. For each SN, i, in the sample, the mean of the absolute magnitude distribution for its SN type j, is used. This is denoted $\overline{M}_j$. One can then compute the mean *expected* apparent magnitude, $\overline{m}_i$, for a SN, as a function of its redshift (z_i), Galactic extinction ($A_{r,\rm MW,i}$), host-galaxy extinction ($A_{r,\rm h,i}$) and k-correction ($k_{r,i}$), as shown by Equation 2.24.

$$\overline{m}_i = \overline{M}_j + 5\log d_L(\rm z_i) + k_{r,i} + A_{r,\rm h,i} + A_{r,\rm MW,i} \tag{2.24}$$

Using the standard deviation in the relevant absolute magnitude distribution, σ_j, one can estimate the detectable fraction, ϵ_i, of SNe that would have $r < 21.8$ mag, for the redshift, extinction and k-correction of a SN, using Equation 2.25. The inverse of the fraction ϵ_i is the SN's (and hence its host's) weight of contribution to the volumetric number density.

$$\epsilon_i = \frac{1}{2} - \frac{1}{2}\,\mathrm{erf}\left(\frac{\overline{m_i} - 21.8}{\sqrt{2}\sigma_j}\right) \tag{2.25}$$

$$\rho_{\rm CCSN}(\mathcal{M}) \;=\; \frac{1}{\Delta\log\mathcal{M}}\,\frac{\sum_i 1/\epsilon_i(\mathcal{M})}{\tau\,V} \tag{2.26}$$

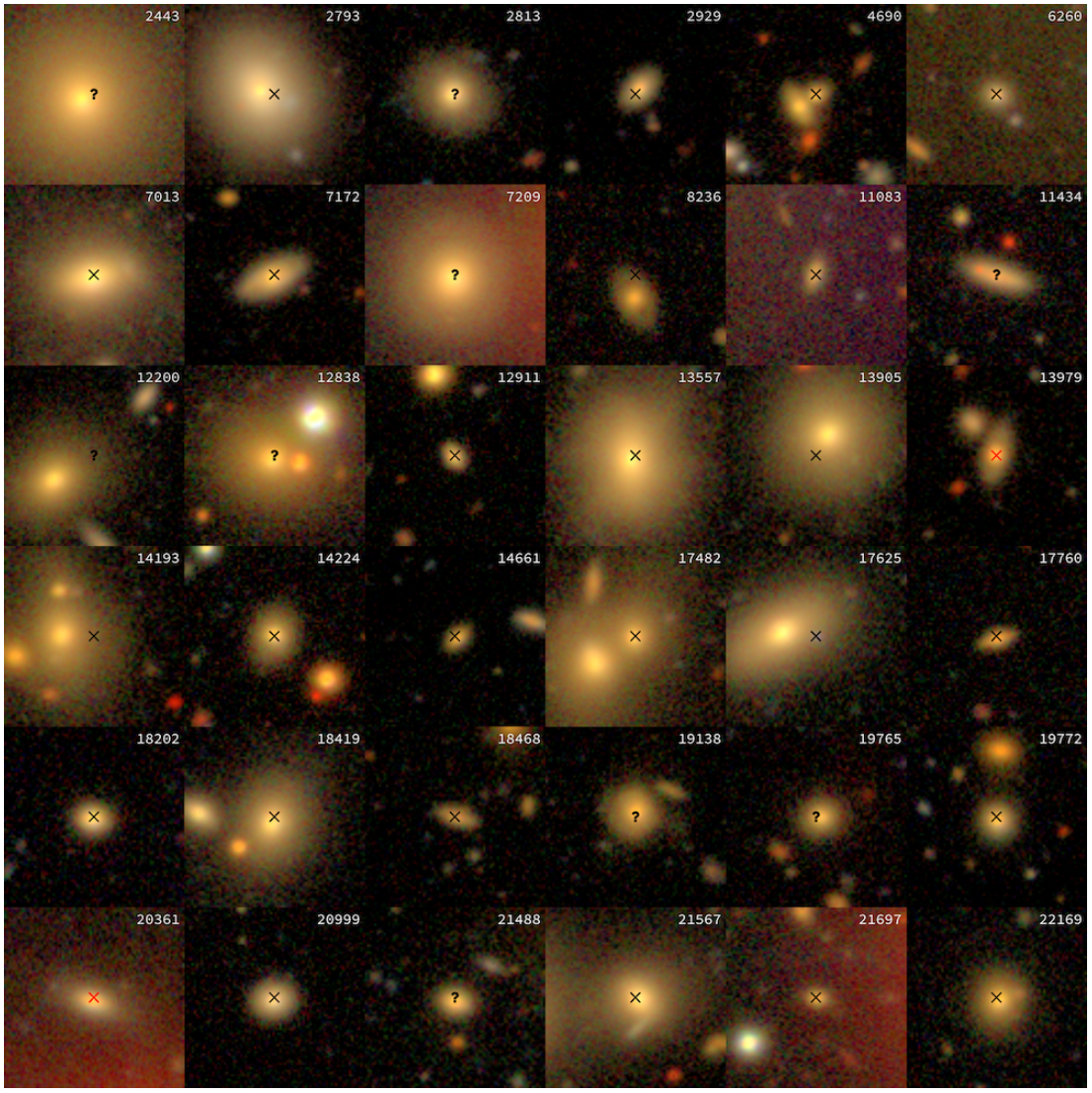

FIGURE 2.23: 36 $z < 0.2$ elliptical galaxies found to host $r_{peak} < 21.8$ CCSNe from the SDSS-II SUPERNOVA SURVEY , as shown in 30" x 30" coadded images from the IAC STRIPE 82 LEGACY SURVEY. Crosses (question marks) denote the locations of CCSNe with $P_{\rm Ia} < 0.05$ ($0.05 < P_{\rm Ia} < 0.5$). Black (red) symbols denote those with (without) spectra. Numbers indicate SN catalogue IDs from the SDSS-II SUPERNOVA SURVEY .

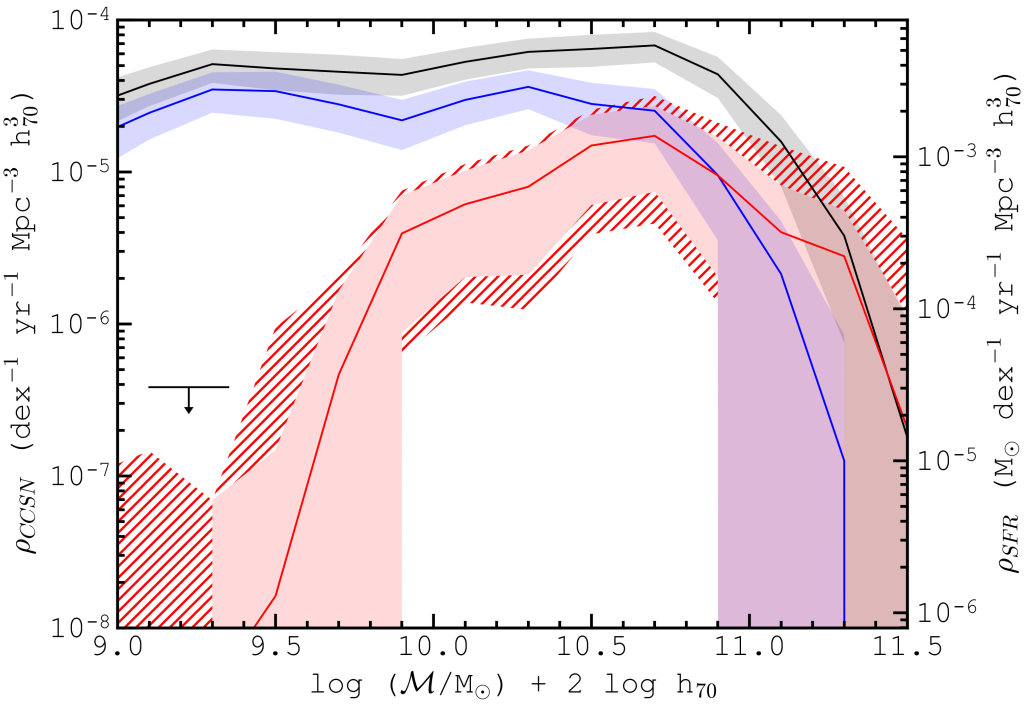

FIGURE 2.24: The core-collapse supernova rate density (left-hand vertical axis) and the implied star formation rate density (right-hand vertical axis), as a function of galaxy stellar mass. The red solid line depicts the contribution to these densities from elliptical galaxies. The solid filled red region depicts the associated statistical uncertainty, which is the quadrature sum of MC + Poisson + Cosmic Variance errors. Hatched red regions depict systematic errors, from the treatment of $0.05 < P_{\rm Ia} < 0.5$ objects (positive error) and from the dust extinction assumed for the elliptical hosts (negative error). The blue (black) line and filled region shows the CCSN-rate and SF-rate as a function of mass for blue star-forming disk galaxies (all galaxies). The black arrow shows the upper-limit at $10^{9.0} - 10^{9.5}$M$_\odot$ at which number counts are consistent with zero (see text).

Equation 2.26 shows that summing over a mass bin of width $\Delta \log \mathcal{M}$, the quantity $\sum_i 1/\epsilon_i(\mathcal{M})$ leads to the volume-corrected number of CCSNe associated with galaxies for each bin. τ is the effective rest-frame time over which CCSNe could be identified by the survey. This is shorter than the observed time-frame of the un-targeted supernova survey, t, such that τ = t / (1+$\overline{z}$). The observable volume, V, is derived from the sky coverage of the STRIPE 82 region and the imposed $z < 0.2$ limit. The relationship between the CCSN rate and SFRD is then given by Equation 2.6. As derived in Section 2.1, $\log \overline{\mathcal{R}} = -1.9$ is adopted.

A 10^3 iteration Monte Carlo (MC) technique is utilised to account for uncertainties in redshift, galaxy magnitudes and the resultant stellar masses which all feed into the calculation of the CCSN-rate density and SFRD as a function of galaxy stellar mass,

the results for which are shown in Figure 2.24. The statistical errors (labelled 'stat') on these densities are represented by the filled regions, and equate to the quadrature sum of MC errors (standard deviation of the densities over MC iterations), Poisson errors and the cosmic variance, the latter estimated given the volume of the STRIPE 82 region out to $z = 0.2$ (Driver & Robotham, 2010). The red series denotes the estimate of CCSN-rate and star formation rate density in ellipticals as a function of mass.

The black arrow shows the approximate upper limit to counts for $10^{9.0} - 10^{9.5}$M$_\odot$. This is the appropriate one-sided 1σ error on bins with zero counts (Gehrels, 1986), normalised for the SN survey coverage, $\tau \times V$, as well as the mean detection efficiency and redshift for the aforementioned mass range.

Additionally there are 2 main sources of systematic uncertainty on this result. The first relates to uncertainties in SN classifications within the SN Sample: The CCSN-rate density described above is formed from the SN sample excluding those with $P_{\rm Ia} > 0.05$. The positive systematic uncertainty equates to the increase to densities found when including $0.05 < P_{\rm Ia} < 0.5$ CCSNe.

A second systematic relates to the dust extinction assumed within the host galaxies, or more specifically, the dust screen in the region of the SNe. Equations 2.24 and 2.25 rely on an estimate of this extinction level. From the full CCSN sample of Section 2.1, the mean r-band extinction in the SN regions was estimated at 0.5 mag. Therefore, a mean extinction of 0.5 mag is also assumed for elliptical hosts in the present section. However, as the sample in Section 2.1 consisted mostly of star-forming galaxies, which can be abundant in dusty star-forming regions, the level of dust attenuation in elliptical hosts may be lower. Indeed. the median Galactic-extinction corrected absolute r-band magnitude of $P_{\rm Ia} < 0.05$ CCSNe at peak light is -17.70 mag in ellipticals, compared with -17.39 mag in blue disks. This implies a median r-band extinction of ~ 0.2 mag in ellipticals. For comparison, a difference of 0.16 mag is found in the median A_v estimate when moving from blue disk Type Ia SN hosts (median of $A_v = 0.38$ mag) to elliptical Type Ia SN hosts (median of $A_v = 0.22$ mag), where V-band extinction values were estimated by Sako et al. (2018b) from a MLCS2K2 SN light curve fitting technique (Jha et al., 2007). Despite these numbers, a more conservative negative systematic uncertainty on the elliptical SFRD is used, which represents the decrease to densities assuming **zero** extinction in the SN regions. Systematic uncertainties, (labelled 'sys') are shown as the hatched regions in Figure 2.24.

The SFRD in ellipticals is constrained above zero for a mass range $10^{9.8}$ - $10^{11.2}$ M$_\odot$. The peak contribution most likely comes between $10^{10.6}$ - $10^{10.8}$ M$_\odot$, where ellipticals

contribute 1.6±0.8 (stat) $^{+0.3}_{-0.7}$ (sys) $\times 10^{-5}$ CCSNe yr^{-1} Mpc^{-3} dex^{-1} h$^{3}_{70}$, corresponding to an SFRD of 1.3 ± 0.6 (stat) $^{+0.2}_{-0.6}$ (sys) $\times 10^{-3}$ M$_{\odot}$ yr^{-1} Mpc^{-3} dex^{-1} h$^{3}_{70}$ at these masses. All the results of the present section are derived using a 737 cosmology ($h = 0.7$, $\Omega_{\rm m} = 0.3$, $\Omega_{\Lambda} = 0.7$).

There is a narrow range of masses which contribute non-negligibly to the SFRD in ellipticals, with ∼50% of the contribution coming for $10^{10.4}$ - $10^{10.8}$ M$_{\odot}$, and ∼90% of the contribution found between $10^{10.0}$ - $10^{11.2}$ M$_{\odot}$. The integrated density above $10^{10.0}$ M$_{\odot}$, corresponding to what is effectively the total elliptical population, is found to be 1.3 ± 0.3 (stat) $^{+0.4}_{-0.5}$ (sys) $\times 10^{-5}$ CCSNe yr^{-1} Mpc^{-3} h$^{3}_{70}$, equating to 1.0 ± 0.3 (stat) $^{+0.3}_{-0.4}$ (stat) $\times 10^{-3}$ M$_{\odot}$ yr^{-1} Mpc^{-3} h$^{3}_{70}$.

For a comparison with the elliptical SFRD, the result from the sample of CCSNe found in star-forming 'blue disk' galaxies is shown (in blue in Figure 2.24 and in successive figures), which are here defined as those $z < 0.2$ galaxies which have $(g - r)_0 < 0.65$ mag, $f_{\rm deV} < 0.5$, and were found to be non-ellipticals using the classification procedure presented in this section. These galaxies are expected to be the dominant constituents of the star-forming main sequence.

The SFRD in blue disks as integrated above $10^{10.0}$ M$_{\odot}$ is a factor 2.1 ± 0.7 (stat) $^{+1.3}_{-0.5}$ (sys) times that in ellipticals. The SFRD of ellipticals most likely surpasses that in blue star-forming disks above $10^{10.9}$ M$_{\odot}$, due mainly to the domination of the total galaxy number density from ellipticals at the highest galaxy masses.

Also shown, in black, is the total SFRD as determined from the SDSS-II SN Sample. Note that the red and blue series do not sum to give the total SFRD: There will be additional contributions from lenticular galaxies, irregular galaxies and dusty star-forming galaxies, which fall in to neither the elliptical or blue disk groups. These results imply that elliptical galaxies contribute 11.2 ± 3.1 (stat) $^{+3.0}_{-4.2}$ (sys) % of the total star-formation budget at present epochs. This rises to 20.2 ± 6.0 (stat) $^{+5.7}_{-7.7}$ (sys) % for masses above $10^{10.0}$ M$_{\odot}$. Both values are consistent with that of Kaviraj (2014a), who find that 14% pertains to early-type galaxies. It is concluded that ellipticals contribute a non-negligible fraction of the total star-formation budget to the present-day cosmic volume.

2.2.5 The Specific Star Formation Rates of Ellipticals

Equation 2.21 demonstrates that the mean SSFR of ellipticals can be derived using the result for the SFRD if one also has a calculation of the GSMF of ellipticals. To calculate

the required GSMF, a $1/V_{\rm max}$ method is used, applied to the sample of 27940 Bayesian classified ellipticals with $z < 0.2$ and $r < 20$ mag. The maximum luminosity distance, $D_{L,max}$, within which each galaxy would remain brighter than the flux limit of $r = 20$ mag is given by

$$5\log(D_{L,max}) = 5\log(D_{L,obs}) + 20 - r_{\rm AUTO} + dK \ , \tag{2.27}$$

where dK is the k-correction for a galaxy at the observed redshift, minus that at the maximum redshift, and where the required maximum redshift is iteratively inferred starting from the value of $D_{L,max}$ with $dK = 0$. Finally $D_{L,max}$ values are clipped to lie at or below the inferred luminosity distance at $z = 0.2$. $D_{L,max}$ leads to $1/V_{\rm max}$, the values for which act as weights on galaxy number densities in $\log(\mathcal{M}/{\rm M}_\odot)$ bins of width 0.2 dex, yielding volume-limited results. The GSMF of blue disks within our redshift and magnitude limits (a total of 66288 blue disk galaxies) is calculated, as is that of all $z < 0.2$, $r < 20$ mag galaxies (a total of 113239 galaxies), using the same approach.

Corresponding results are shown in Figure 2.25. Similar to the masses at which the peak of CCSN production is observed, the number density of $z < 0.2$ ellipticals peaks between galaxy stellar masses of $10^{10.4}$ and $10^{10.8}$ ${\rm M}_\odot$, at $2.11 \pm 0.03 \times 10^{-3}$ dex^{-1} Mpc^{-3} h$_{70}^3$. Ellipticals dominate the total $z < 0.2$ galaxy number density for masses $> 10^{10.8}$ ${\rm M}_\odot$.

Figure 2.26 shows (with the red solid line and filled regions) the mean SSFR of ellipticals as a function of mass, derived from the results for the volumetric SFRD and the GSMF. Using an inverse-square-error weighting on each mass bin, it is found that the mean SSFR of ellipticals as a function of mass is well represented by the following regression line for masses $> 10^{10.0}{\rm M}_\odot$:

$$\log(\overline{\mathcal{S}}(\mathcal{M})/{\rm yr}) = -\ (0.80\ \pm\ 0.59)\ \log(\mathcal{M}/10^{10.5}{\rm M}_\odot)\ -10.83\ \pm\ 0.18\ . \tag{2.28}$$

The uncertainty on the gradient for this regression line implies there is an 18% chance that $\overline{\mathcal{S}}$ is constant with mass for ellipticals. In relation to this uncertainty, it is noted that although the estimate of mean SSFR in ellipticals approaches that of main sequence galaxies at $\log(\mathcal{M}/{\rm M}_\odot) \sim 10.0$, the uncertainty on the result for individual bins is such that $\overline{\mathcal{S}}$ at $\log(\mathcal{M}/{\rm M}_\odot) = 10.0$ could be as low as $10^{-11.0}$ yr^{-1} within 1σ errors, in line with the mean for the elliptical population.

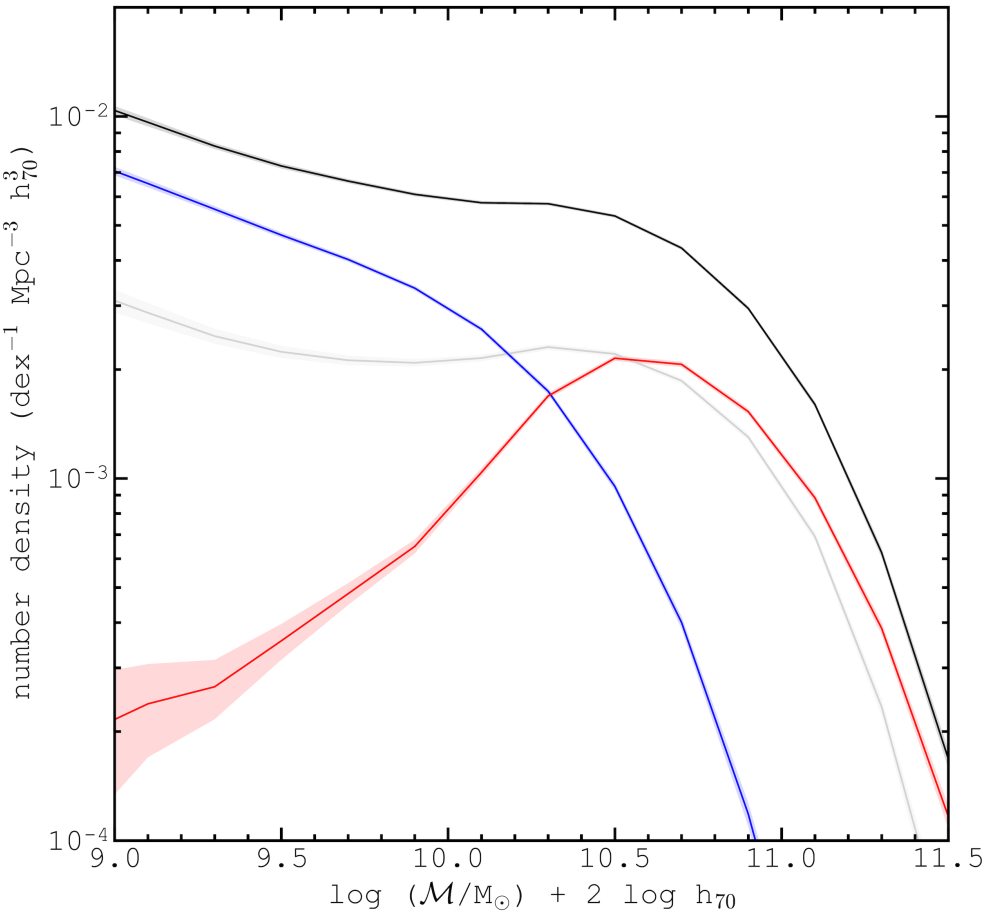

FIGURE 2.25: The $z < 0.2$ galaxy stellar mass function of elliptical galaxies (red), star-forming disk galaxies (blue), and the total galaxy population (black) from a $1/V_{\rm max}$ method, using $r < 20$ mag galaxies. Solid lines and filled regions show galaxy number densities, and their 1 σ MC+Poisson+Cosmic Variance errors, respectively.

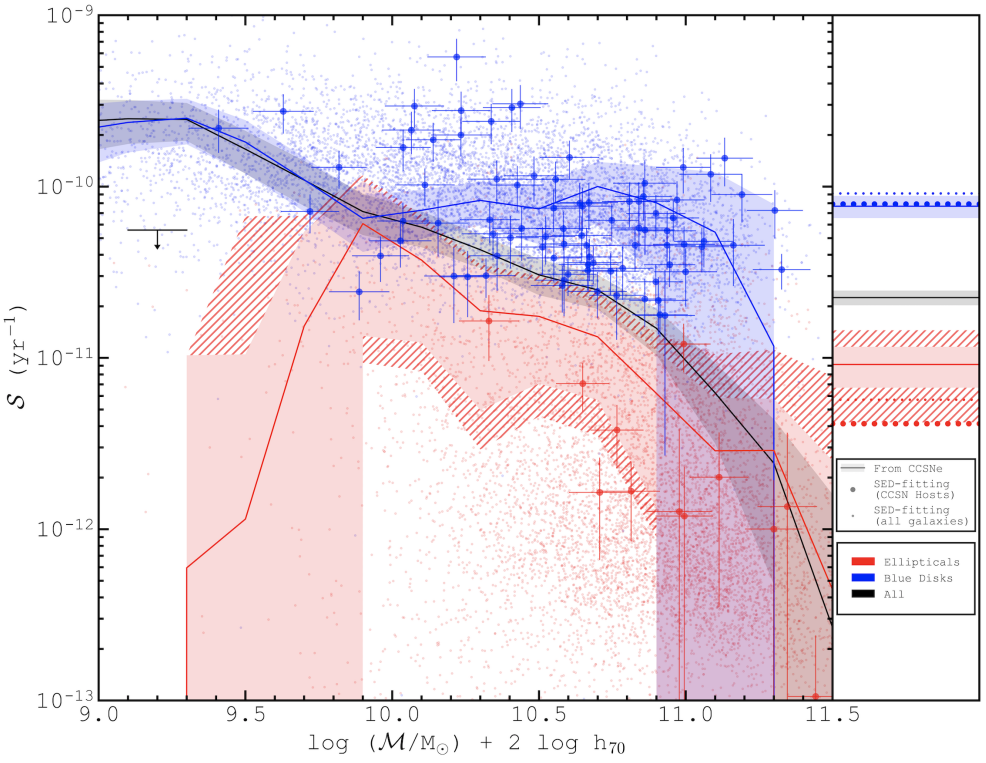

FIGURE 2.26: Left: The specific star formation rate as a function of galaxy stellar mass (via multiple means). The red solid line and filled region denote the mean and 1 σ uncertainty (MC + Poisson + Cosmic Variance) on the specific star formation rate in elliptical galaxies at $z < 0.2$. Hatched-regions depict additional systematic uncertainties described in the caption of Figure 2.24. Small-red points depict the SED-derived specific star formation rates of those *individual* elliptical galaxies cross-matched with GSWLC-X2 data. Large-red points denote cross-matched elliptical CCSN hosts, with error bars showing 1 σ errors from SED-fitting. The blue series depict the same but for blue star forming galaxies. The black series shows the mean specific star formation rate as a function of mass for all galaxies. The black arrow shows the upper-limit at $10^{9.0} - 10^{9.5} M_\odot$ at which SN counts are consistent with zero (see text). Right: The same results as the left-hand panel but derived using the SFRD and GSMF both integrated over galaxy masses $> 10^{10.0}$ $M_\odot$.

Given uncertainties on the SSFR for 'blue disks', which effectively define the star-forming main sequence, it is unclear whether the result shows a step function at $\mathcal{M} \sim 10^{9.5}\mathrm{M}_{\odot}$ and is then flat for higher masses, or whether the SSFR instead exhibits a more gradual negative slope with mass. A slope of some form is likely, given that more massive star-forming galaxies formed earlier and a longer time has passed since the peak of their star formation (see, e.g. Gallazzi et al., 2005).

There may however be reason to expect a step function in SSFR. For instance, McGaugh et al. (2017) find a distinct star forming main sequence for $8.0 < \log(\mathcal{M}/\mathrm{M}_{\odot}) < 10.0$ compared to higher masses, with results consistent with constant $\overline{\mathcal{S}}$ in this mass regime. Type II SN-rate models of Graur et al. (2015b), which build on the work of Li et al. (2011b), imply a step function in $\overline{\mathcal{S}}$ vs mass centred on $\log(\mathcal{M}/\mathrm{M}_{\odot}) \sim 9.5$. Furthermore, it was found in Section 2.1 that assuming a constant SSFR for masses $\lesssim 10^{9.0}\mathrm{M}_{\odot}$ yields the best consistency between the GSMF from CCSNe and that from a $1/V_{\mathrm{max}}$ method. Future larger samples of SNe utilised with these SN-based methods will allow a conclusion to be reached for the presence of a step function in $\overline{\mathcal{S}}$ versus mass for main-sequence galaxies (e.g. Ivezić et al., 2019).

The value of $\overline{\mathcal{S}}(\mathcal{M})$ for the total galaxy population could be argued to follow a Schechter parameterisation (Schechter, 1976). Fitting for $\mathcal{M} > 10^{10.0}\mathrm{M}_{\odot}$, one finds best-fit parameters of $[\log(\mathcal{M}^*/\mathrm{M}_{\odot}), \overline{\mathcal{S}^*}/10^{11.0}\ \mathrm{yr}, \alpha] =$
$[10.90 \pm 0.08,\ \ 7.94 \pm 2.54,\ \ -1.41 \pm 0.03]$.

Similar to Figure 2.24, the black arrow shows the 1σ upper-limit on $\overline{\mathcal{S}}$ for $10^{9.0}-10^{9.5}\mathrm{M}_{\odot}$ ellipticals. This value is derived from the one-sided 1σ error on bins shown in Figure 2.24, and adopting the average galaxy number density and mass in the aforementioned mass range for the conversion in Equation 2.21. This upper limit shows that, because of the form of Equation 2.21, a fractionally large Poisson error on host galaxy counts leads to a particularly large error on the SSFR at low elliptical masses, spanning several dex. To assess $\overline{\mathcal{S}}$ in ellipticals using CCSNe for $\mathcal{M} < 10^{9.5}\mathrm{M}_{\odot}$ would require future data from SN surveys of longer time-span and/or larger sky coverage (e.g. Ivezić et al., 2019) than those currently available.

Points in Figure 2.26 show independent SSFRs for *individual* galaxies derived from UV/Optical SED fitting applied to the GSWLC-2 sample. 7714 of 27940 (8502 of 49641) ellipticals (blue disks) are matched with GSWLC. 12 of 27 (83 of 174) elliptical CCSN hosts (blue disk CCSN hosts) are matched with GSWLC-2, where CCSN hosts are here defined as those with $P_{\mathrm{Ia}} < 0.05$. Hosts are shown as larger points, with their 1σ errors on $\mathcal{S}_{\mathrm{SED}}$.

It is found that there are no significant differences in the optical colour distributions of the GSWLC-matched samples compared with the full samples of ellipticals and blue disks. This is interpreted as a lack of evidence for a bias towards the selection of higher $\mathcal{S}_{\rm SED}$ galaxies in the GSWLC-matched sample. As such, a comparison of the CCSN-derived and SED-derived results is constructive.

$\mathcal{S}_{\rm SED}$ values are qualitatively consistent with $\overline{\mathcal{S}}(\mathcal{M})$ derived from CCSNe, with 10 of the 12 GSWLC-matched elliptical CCSN hosts having a measurement of $\mathcal{S}_{\rm SED}$ within the 1σ uncertainties on the SN-derived $\overline{\mathcal{S}}(\mathcal{M})$, and with the running mean of all GSWLC-matched ellipticals lying within a 1σ separation from the SN-derived mean as a function of mass, as shown in Figure 2.27. Interestingly, the running mean value of $\mathcal{S}_{\rm SED}$ for the main sequence shows no evidence for the aforementioned step function about $\mathcal{M} = 10^{9.5}{\rm M}_{\odot}$. Furthermore, the gradient of $\mathcal{S}_{\rm SED}$ with mass is comparable for both ellipticals and blue disks, which may be in contrast to the findings of the present section using CCSNe.

Integrating the volumetric SFRD and the GSMF for $\mathcal{M} > 10^{10.0}{\rm M}_{\odot}$ (separately) leads to the mean SSFR over this galaxy mass range. Mean values are indicated in the right-hand panel of Figure 2.26. From a CCSN technique, a value of $\overline{\mathcal{S}} = 9.2 \pm 2.4$ (stat) $^{+2.7}_{-2.3}$ (sys) $\times 10^{-12}$ yr^{-1} is obtained for $\mathcal{M} > 10^{10.0}{\rm M}_{\odot}$ elliptical galaxies.

Also shown is the counterpart value of $\overline{\mathcal{S}}_{\rm SED}$, taken as the average SED estimate (in linear space) for all GSWLC-matched ellipticals with $\mathcal{M} > 10^{10.0}{\rm M}_{\odot}$. What is found is that $\overline{\mathcal{S}}_{\rm SED} = 5.7 \times 10^{-12}$ yr^{-1} for all GSWLC-matched ellipticals, and $\overline{\mathcal{S}}_{\rm SED} = 4.1 \times 10^{-12}$ yr^{-1} for the sub-sample of GSWLC-matched elliptical CCSN hosts. Assuming an average dust extinction in hosts of $A_r = 0.5$ mag, these results are in 1.4σ tension, and 2.1σ tension, respectively, with the value of $\overline{\mathcal{S}}$ measured using a CCSNe. Assuming instead zero dust extinction in elliptical hosts, respective discrepancies of 0.5σ and 1.1σ are found.

The mean SSFR result for $\mathcal{M} > 10^{10.0}{\rm M}_{\odot}$ blue disks, derived using a CCSN-based method comes to $\overline{\mathcal{S}} = 7.8 \pm 1.3 \times 10^{-11}$ yr^{-1}. This is in $< 1\sigma$ tension with SED-based measurements, found to be $\overline{\mathcal{S}}_{\rm SED} = 9.1 \times 10^{-11}$ yr^{-1} for all GSWLC-matched blue disks, and $\overline{\mathcal{S}}_{\rm SED} = 7.9 \times 10^{-11}$ yr^{-1} for all matched blue disk CCSN hosts. This consistency reassures one's faith in the elliptical result, given that the mean SSFR of the main sequence is well-defined from SED-based measurements (and other methods) within the literature (see, e.g. Noeske et al., 2007b; Speagle et al., 2014). The CCSN-derived measurement of $\overline{\mathcal{S}}$ for $\mathcal{M} > 10^{10.0}{\rm M}_{\odot}$ main sequence galaxies implies that ellipticals have a mean SSFR which is 11.8 ± 3.7 (stat) $^{+3.5}_{-2.9}$ (sys) % of that on the star-forming

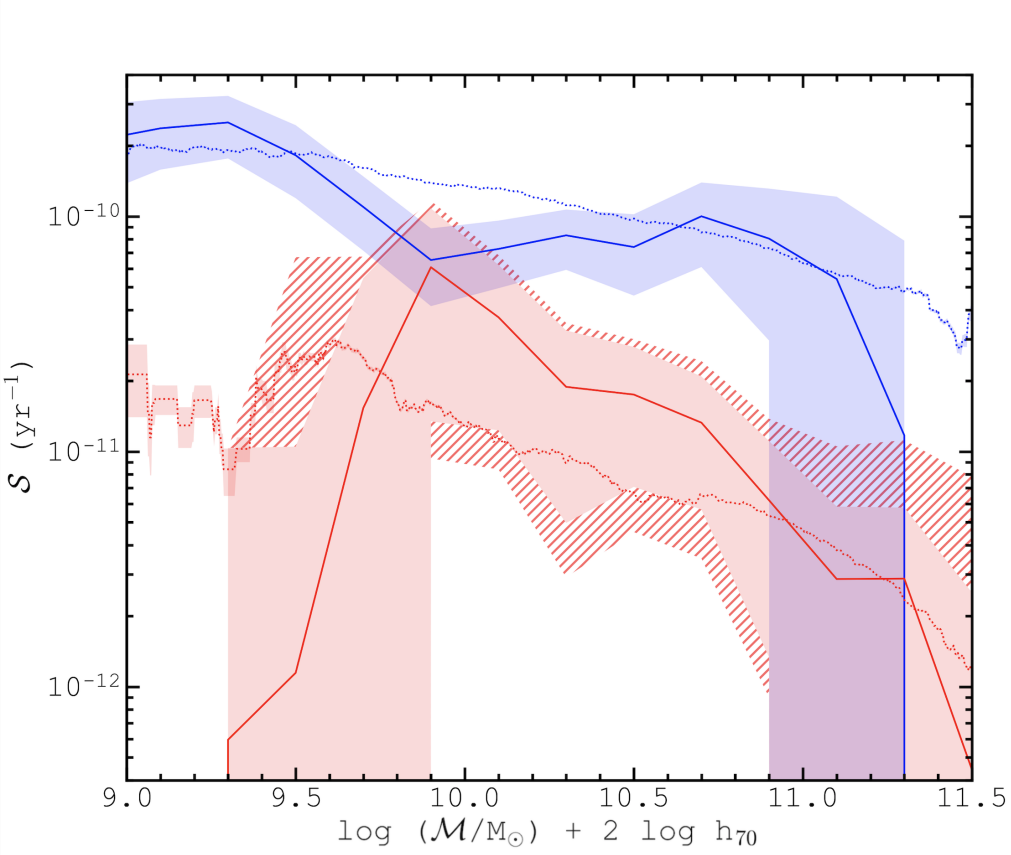

FIGURE 2.27: The specific star formation rate as a function of galaxy stellar mass (via multiple means). The red and blue solid lines and surrounding filled regions denote the CCSN-derived results and their uncertainties for elliptical galaxies and blue disk galaxies, respectively, as described in Figure 2.26. The red and blue dotted lines show the running mean of specific star formation rates from SED fitting (derived by Salim et al. 2018), for elliptical and blue disks, respectively, averaged over 0.1 dex in mass. Surrounding filled regions show the corresponding standard error of these means.

main sequence.

2.2.6 The Median Spectrum of Elliptical Core Collapse Supernova Hosts

Note that the SED result averaged over elliptical CCSN hosts is comparable to that averaged over all ellipticals. This implies that whilst CCSNe hosts are indeed probabilistically determined by their star formation rates, the selection function is not so extreme that one is simply tracing the very highest star formation rate ellipticals. This increases confidence that the measurement of $\overline{\mathcal{S}}$ via CCSNe is well-representative of the mean star formation level over the total elliptical population.

Of course, SED-based measurements of star formation rates for ellipticals are subject to uncertainty; which is indeed a major motivation for the present section. An analysis of the 25 elliptical CCSN host galaxy's coadded spectra is therefore turned to, to test whether these hosts exhibit spectral properties typical of the average elliptical.

Although SED measurements are derived in part from this spectral information, one can observe a more detailed picture of the star formation properties from the direct spectra, and can look at information free of fitting dependencies.

The median spectrum of the $P_{\rm Ia} < 0.05$ elliptical CCSN host galaxies for which spectra are available is first computed, i.e. for those 25 galaxies labelled with black crosses in Figure 2.23. To do this, each galaxy's rest-frame spectrum is normalised to equal unity when integrated over wavelengths of 4000 and 8000, before the sample's median normalised flux is taken as a function of wavelength axis at intervals of 0.1. The 1 σ error on the median flux is calculated from the $16^{\rm th}$ and $84^{\rm th}$ percentiles as a function of wavelength. This uncertainty is shown in each panel except the top main panel, where it is omitted for clarity.

Similarly computed is the median spectrum of a control sample of non-hosting ellipticals matched in galaxy stellar mass and redshift to the CCSN hosts. For each host, the separation with non-hosts in a Cartesian mass-redshift space is found, where separations along each axis are normalised by the median separation of random pairs, such that mass and redshift carry comparable weight in the matching procedure. The nearest 5 matches for each host elliptical are found, yielding a control sample of 125 galaxies.

As the Balmer lines are notable signatures star-formation properties, a particular focus is given to the strengths of Hα and Hβ. The ratios of these lines with the respectively

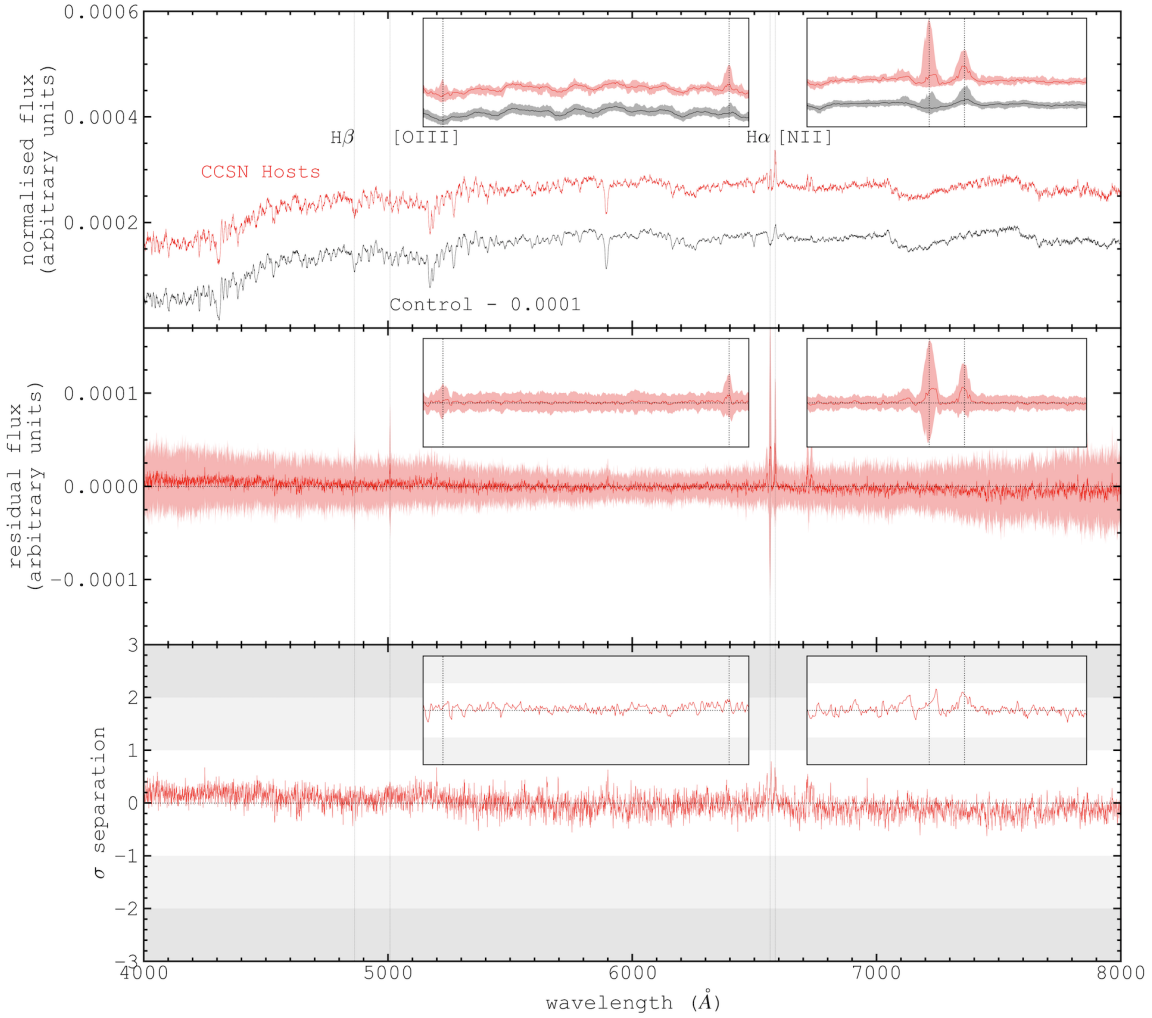

FIGURE 2.28: Top panel: The median spectrum of elliptical CCSN hosts (red) vs that of a control sample of (non-hosting) elliptical galaxies (see text). Inset plots show zoomed in wavelength ranges about the Hβ and Hα lines. Upper and lower bounds on the median normalised flux are signified by filled regions and correspond to the 84^{th} and 16^{th} percentiles, respectively. These are omitted in the top main panel, for clarity. Middle panel: The residual spectrum (host - control). Bottom panel: The statistical significance of the difference between the median spectra as a function of wavelength.

nearby [NII]λ6583 and [OIII]λ5007 lines are also investigated, in order to disentangle flux contributions to the Balmer lines from star formation with those from nuclear activity (Kauffmann et al., 2003).

As shown in the bottom panel of Figure 2.28, no statistically significant difference is found in Hα or Hβ line strength between the SN host sample and control sample. Furthermore, no statistical difference is found between the median strengths of [OIII]λ5007 or [NII]λ6583. In fact, not one optical emission line is found to differ in its median strength over the 2 samples, within the errors shown.

Moreover, no difference in the median line ratios [OIII]λ5007/Hβ or [NII]λ6583/Hα is found, implying a similar level of both star formation and nuclear activity for the host sample and control sample. The equivalent width of these 4 emission lines is also consistent across the 2 samples.

These line ratios are finally used to consider the positions of the 25 elliptical CCSN hosts on the BPT diagram (Baldwin et al., 1981). It is found that all 25 of these galaxies lie comfortably on the AGN/Passive side of the Kauffmann et al. (2003) demarcation. This implies that these line ratios are incompatible with high-levels of star-formation and instead that the majority contribution to the aforementioned lines is coming from old stellar populations and/or AGN (which would be Type-II AGN in the majority of cases, given the lack of broad lines seen in Figure 2.28).

Each of these results implies once more that the elliptical CCSN hosts have typical levels of star formation when compared to the average (or classical interpretation of an) elliptical, and as such, what has been derived in this section is an accurate measure of the mean SSFR of all elliptical galaxies, directly from CCSNe. The consistency between the spectral properties of the CCSN hosts with the remaining elliptical population may also imply that the star formation in ellipticals is not particularly bursty in nature.

2.2.7 Summary

This section has seen the classification all $z < 0.2$, $r < 20$ mag STRIPE 82 galaxies using a Bayesian method, trained on the colour and morphology properties of manually-classified samples of ellipticals and non-ellipticals from GALAXY ZOO 1 (Figure 2.20).

A sample of 421 $r < 21.8$ mag, $z < 0.2$ likely CCSNe, originating from the SDSS-II SUPERNOVA SURVEY have been isolated. From their light curves, these SNe each had a Bayesian confidence ($P_{\rm CC}$) $> 50\%$ of being a CCSN. 360 ($\sim 86\%$) of these had a

Bayesian confidence $> 95\%$, making this a reliable sample of CCSNe. $24 \pm 1\%$ of these CCSNe are likely to be of Type Ib/c, in line with expectations for the ratio of those of Type Ib/c to Type II. As it is far more common to misclassify Type Ia SNe as Type Ic SNe (lack of light curve plateau and similar spectral properties) rather than as Type II SNe, this reasonable ratio of Type Ib/c SNe to Type II SNe increases one's faith in the SN classification procedure. In Section 2.1, these SNe were carefully matched to their host galaxies, meaning that those CCSNe residing in ellipticals could be isolated. 36 CCSNe (27 with $P_{\rm CC} > 0.95$) were found to occur in such galaxies (Figure 2.23).

The $z < 0.2$ volumetric star formation rate density (SFRD; Figure 2.24) in elliptical galaxies was calculated from the CCSN rate as a function of host galaxy stellar mass, assuming a ratio between core-collapse events and star formation of $\overline{\mathcal{R}} = 10^{-1.9}\ {\rm M}_{\odot}^{-1}$. The elliptical SFRD result was constrained above zero for $9.8 < \log(\mathcal{M}/{\rm M}_{\odot}) < 11.2$, with the peak star formation contribution from ellipticals coming at $10.4 < \log(\mathcal{M}/{\rm M}_{\odot}) < 10.8$. Ellipticals were found to dominate the present-day star formation budget for $\log(\mathcal{M}/{\rm M}_{\odot}) > 10.9$.

Ellipticals were found to contribute 11.2 ± 3.1 (stat) $^{+3.0}_{-4.2}$ (sys) % of the total star-formation budget. This rises to 20.2 ± 6.0 (stat) $^{+5.7}_{-7.7}$ (sys) % for $\log(\mathcal{M}/{\rm M}_{\odot}) > 10.0$. These results are consistent with recent studies of star formation in ellipticals using galaxy emission, such as the UV-optical study of (Kaviraj, 2014a). As CCSN statistics cannot be misconstrued as anything but signatures of recent star formation, the methods presented in this section have definitively demonstrated that *ellipticals contribute a non-negligible level of star formation to the present-day cosmic budget.*

The mean specific star formation rate (SSFR; Figure 2.26) of ellipticals was calculated as a function of mass, via the combined information of the previous SFRD result and the galaxy stellar mass function (Figure 2.16). The mean elliptical SSFR most likely exhibits a slope, with a regression line well-representative for galaxy masses $> 10^{10.0}{\rm M}_{\odot}$, such that $\log(\overline{\mathcal{S}}(\mathcal{M})/{\rm yr}) = -\ (0.80 \pm 0.59)\ \log(\mathcal{M}/10^{10.5}{\rm M}_{\odot})\ -10.83 \pm 0.18$. However, these errors show there is still an 18% chance the SSFR is constant with mass in ellipticals. The mean SSFR for all $\log(\mathcal{M}/{\rm M}_{\odot}) > 10.0$ ellipticals was found to be $\overline{\mathcal{S}} = 9.2 \pm 2.4$ (stat) $^{+2.7}_{-2.3}$ (sys) $\times 10^{-12}\ {\rm yr}^{-1}$. This is 11.8 ± 3.7 (stat) $^{+3.5}_{-2.9}$ (sys) % of the average SSFR on the star-forming main sequence.

An independent mean SSFR in ellipticals derived from GSWLC-2 SED fitting is found to be $\overline{\mathcal{S}}_{\rm SED} = 5.7 \times 10^{-12}\ {\rm yr}^{-1}$, which is moderately consistent with the SN-derived result (a 1.4σ tension). Assuming zero dust extinction in elliptical CCSN hosts this tension drops to only 0.5σ. This indicates the SED-derived results put forward as upper limits

by (Salim et al., 2018) are likely close to the true levels of star formation for these objects (See Figure 2.27).

The median optical spectrum of the 27 $P_{\rm Ia} < 0.05$ CCSN hosts is finally computed. This is compared with that of a control sample of non-hosting ellipticals matched in galaxy stellar mass and redshift (Figure 2.28). No statistically significant difference in the median strengths of emission lines is found for these 2 samples, including various commonly associated with star formation (Hα, Hβ, [OIII]λ5007 and [NII]λ6583). This result implies elliptical CCSN hosts have typical levels of star formation compared to the average elliptical. This in turn signifies that the CCSN-derived results of the present section are an accurate representation for the total elliptical population at current epochs. These results are consistent with the hierarchical evolution widely accepted under a Λ-CDM paradigm, in which low-level star formation is expected to continue in ellipticals out to current epochs, likely due to the influence of galaxy mergers and/or a slow-rate of gas cooling.

2.2.8 List of Assumptions

Section 2.2 has made use of the same assumptions as in Section 2.1 with the exception that zero-dust extinction is appropriate for elliptical CCSN hosts, and assuming that, for the Bayesian scheme for the classification of ellipticals from their photometry it is accurate to assume no initial prior.

Chapter 3

The Effects of Peculiar Velocities in Type Ia Supernova Environments on Local Estimates of the Hubble Constant

3.1 The Hubble Tension

The Hubble Constant at the present-epoch (H_0) parameterises the current rate of expansion of the Universe. A knowledge of the precise value of H_0 is crucial to Λ-CDM simulations and their extensions, to our description of the present-day Universe and to predictions of its ultimate fate.

A key problem in modern day cosmology is the persistent tension between measurements of H_0 when probed on different scales. Using measurements of anisotropies in the cosmic microwave background (CMB) and calibrating using a Λ-CDM cosmology, the Planck Collaboration et al. (2018), obtain the most stringent estimate of H_0 from the physics of the sound horizon to date, finding $H_0 = 67.36 \pm 0.54$ km s^{-1} Mpc^{-1}. Alternatively, measurements of H_0 on local scales of our Universe find larger values of H_0 (Riess et al., 2016, 2018b). Riess et al. (2019), using Large Magellanic Cloud (LMC) Cepheids to calibrate SNIa photometry, give an estimate of $H_0 = 74.03 \pm 1.42$ km s^{-1} Mpc^{-1}, a result which lies in 4.4σ tension with that of Planck Collaboration et al. (2018).

Increasing numbers of works in the literature cite physical effects as the cause of the

Hubble tension (see, e.g. Di Valentino et al., 2018; Agrawal et al., 2019; Vattis et al., 2019). Indeed, Riess et al. (2019) note that the H_0 discrepancy may point towards a problem for Λ-CDM, given the reliance of sound-horizon-scale results on the assumption of the standard cosmology.

An alternative source of the Hubble tension could instead relate to local systematics: the cosmic distance ladder, utilised on local (typically, $z \lesssim 0.1$) scales (and for example in Riess et al. 2019), offers a direct and largely model-independent measure of H_0. However, a problem faced on these scales is that peculiar velocities, due to the inhomogeneity of the local Universe, are non-negligible when compared to recession velocities. The component of an object's velocity due to cosmic expansion must be sufficiently decoupled from peculiar velocity for an accurate calculation of H_0. Peculiar velocities are, on local scales, solely gravitationally induced motions (Peebles & Shaviv, 1982), and as a result, these velocities are expected to be strongly correlated with the galaxy density field.

There exists in the literature debated evidence for a 'Local Void', or under-density at our location in the Universe. The contrast and isotropy of such an under-density has been investigated using various phenomena, including SNeIa (Zehavi et al., 1998; Jha et al., 2007; Conley et al., 2007), clusters (Giovanelli et al., 1999; Hudson et al., 2004; Böhringer et al., 2015) and galaxies (Shanks et al., 1984; Huang et al., 1997; Ratcliffe et al., 1996; Busswell et al., 2004; Keenan et al., 2013) to probe the local density. Whitbourn & Shanks (2014) find a particularly significant galaxy under-density, most prominent in the direction of the 6dFGS South Galactic Cap region (SGC-6dFGS) in which a deficit of ~ 40 % is estimated for $z < 0.05$. This region has been cited as under-dense independently from the galaxy samples of the 6dFGS Redshift Survey (Busswell et al., 2004) and 2MASS (Frith et al., 2003).

The above studies probe the density on a regional basis, and a stem of this debate is whether the local under-density found in numerous works would persist across the full sky (Shanks et al., 2018, 2019; Riess et al., 2018c,a; Kenworthy et al., 2019). Recent work from Böhringer et al. (2019) finds a local X-ray cluster under-density which pertains to the full sky. The existence of such an isotropic void would be expected to induce a bias towards peculiar velocities away from the observer, typically increasing local H_0 estimates away from the true value. Whilst past studies have attempted to calculate the expected error in H_0 estimates from the measured density contrast (see, e.g. Shanks et al., 2019), estimating the offset from the true H_0 often relies on a modelling of the void (Enqvist & Mattsson, 2007; Kenworthy et al., 2019).

In the present chapter, an attempt is made to form an independent, near-full sky picture of the local galaxy density field for comparison with previous studies. A method for the empirical estimation of peculiar velocities using the galaxy density field is then introduced. To bypass assumptions related to the geometry of the Local Void, a direct search for correlations between the density field and SNIa H_0 estimates is performed. In doing so, it is demonstrated that peculiar velocities are more tightly linked to gradients in the density field along the SN LOS, than to the absolute density of the SN region. Ultimately, the fractional effect of the galaxy density field on the local H_0 estimate can be quantified.

The structure of the present chapter is as follows: Section 3.1.1 presents the Hubble constant estimator used in this study. Section 3.2 outlines the data sets used. Section 3.3 presents the methodology for the calculation of the local galaxy density field. Section 3.4 then discusses the application of the aforementioned H_0 prescription to a sample of SNeIa. A density parameter using the galaxy density field, is then introduced. This parameter is designed to act as a proxy for peculiar velocity. Tests for correlations of this parameter with the aforementioned SNIa H_0 estimates are performed in Section 3.6.1. In Section 3.6.2 analyses are repeated using mock data to compute a mock density field where line-of-sight velocities are known, in order to test observational results and assess sources of uncertainty in the observations. This chapter concludes with final estimates of the fractional effect on the local H_0 measurement due to peculiar velocities.

3.1.1 An Estimator for the Hubble Constant

In this chapter, the estimator for the measured Hubble constant is given by

$$H_{0,\mathrm{est}} = H_{0,\mathrm{fid}} \frac{D_{C,\mathrm{fid}}(z_{\mathrm{cmb}})}{D_{C,\mathrm{est}}} = \frac{c \int_0^{z_{\mathrm{cmb}}} [E(z)]^{-1} \, \mathrm{d}z}{D_{C,\mathrm{est}}} \quad , \tag{3.1}$$

where the terms with subscript 'fid' correspond to the fiducial cosmology applied to calculate distances as a function of z_{cmb}, and $D_{C,\mathrm{est}}$ is the estimated comoving distance of the standard candle [$D_C = D_L/(1 + z_{\mathrm{helio}})$ assuming a flat cosmology]. The CMB-frame redshift is given by

$$1 + z_{\mathrm{cmb}} = (1 + z_{\mathrm{helio}})(1 + z_{\mathrm{sun,comp}}) = (1 + z_{\mathrm{cos}})(1 + z_{\mathrm{pec}}) \quad , \tag{3.2}$$

where $z_{\mathrm{sun,comp}}$ is from the component of the Sun's motion toward the source in the CMB frame, with $z_{\mathrm{sun}} = 0.00123$ (Lineweaver et al., 1996; Fixsen, 2009), and the other

subscripts refer to the heliocentric, cosmological and peculiar redshifts of the observed source.

Defining velocity as $v = c\ln(1+z)$ (more useful and accurate than the historical cz, Baldry et al. 2018), a straightforward and transparent approximation for D_C, comoving distance, can be obtained using the usual present-epoch deceleration parameter (q_0).

The Hubble law is often stated such that the recession velocity is equal to the Hubble constant times the distance, with the most common approximation for velocity given by cz. However, a more useful expression for velocity (e.g. Cappellari, 2017; Emsellem et al., 2019) is given by

$$v = c\ln(1+z)\,. \tag{3.3}$$

This is more accurate for pure line-of-sight velocity and means that the peculiar velocity and cosmological terms, and frame corrections, are additive (Baldry et al., 2018). A common misconception is to assume cz terms are additive. Coupled with different distance definitions, there are thus many versions of a Hubble law.

Figure 3.1 shows four different views of the Hubble law using these approximations for velocity with luminosity distance (D_L) and line-of-sight comoving distance (D_C). For each version, curves are shown for three model cosmologies, all with flat geometry and with $H_0 = 70$ km s^{-1} Mpc^{-1}. Two are ΛCDM models, for which the deceleration parameter $q = \Omega_m/2 - \Omega_\Lambda$, while the other is a 'coasting' model with $w = -1/3$. Notably, none of these versions of the Hubble law are accurate except in the case of (d) $v = c\ln(1+z) = H_0\,D_C$ for the coasting model (Sutherland & Rothnie, 2015). Note this exact law also is valid for a non-flat coasting model such as an empty universe [though in this case, $D_L \neq (1+z)D_C$]. Shown below is a derivation of a second-order Hubble law that is natural in this view with a transparent dependence on q_0.

For demonstrative purposes, one considers a flat universe with a single type of fluid with equation of state w such that:

$$q = \frac{1+3w}{2} \quad \text{and} \quad E(z) = (1+z)^{q+1} \quad . \tag{3.4}$$

The comoving distance is then given by

$$D_{\rm C} = \frac{c}{H_0}\int_0^z \frac{{\rm d}z}{E(z)} = \frac{c}{H_0}\int_0^z \frac{{\rm d}z}{(1+z)^{q+1}} \quad . \tag{3.5}$$

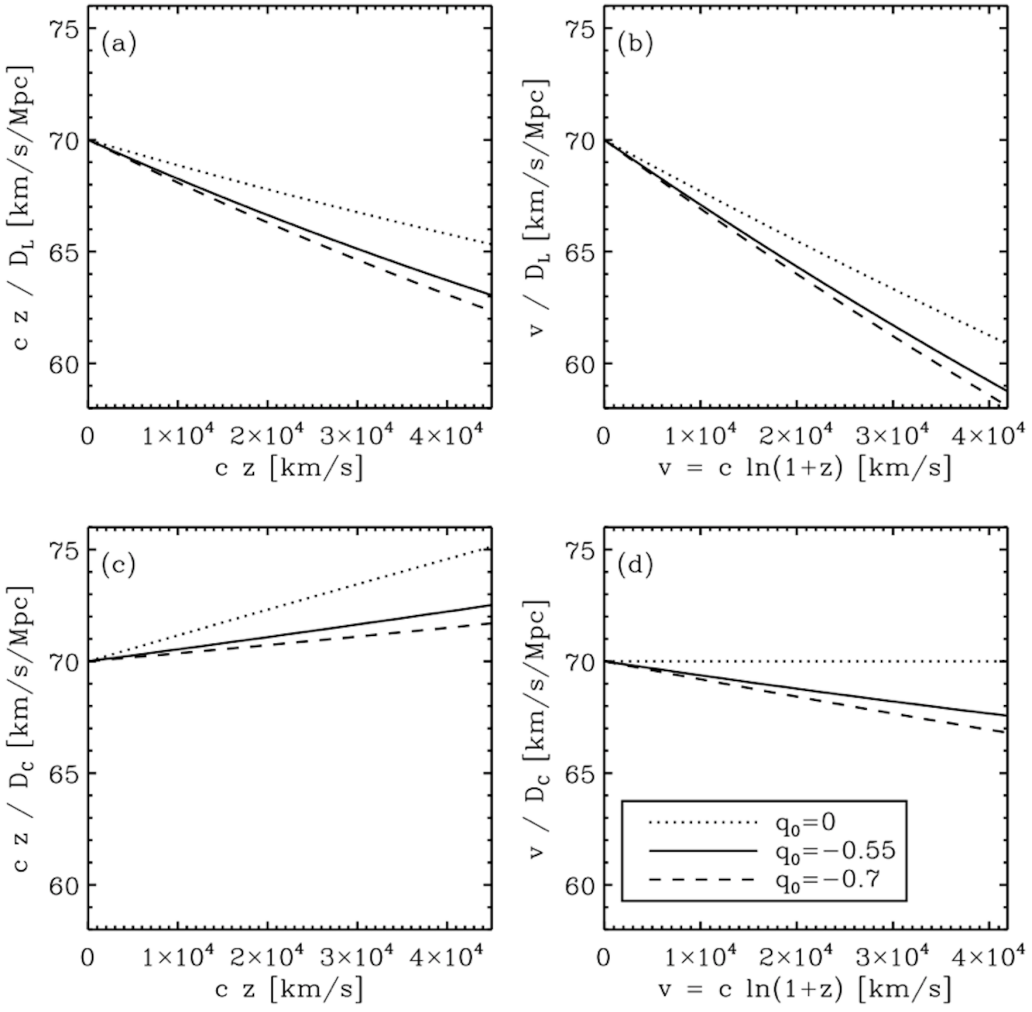

FIGURE 3.1: Different views of the Hubble law. The relations shown are for: a coasting cosmological model ($q_0 = 0$), a flat $\Omega_{m,0} = 0.3$ model ($q_0 = -0.55$), and a flat $\Omega_{m,0} = 0.2$ model ($q_0 = -0.7$).

Using the logarithmic shift $\zeta = \ln(1+z)$, this becomes

$$D_{\rm C} \;=\; \frac{c}{H_0}\int_0^{\zeta}\frac{(1+z)}{E(z)}{\rm d}\zeta \;=\; \frac{c}{H_0}\int_0^{\zeta} e^{-q\zeta}\,{\rm d}\zeta \quad ; \tag{3.6}$$

and after integrating ($q \neq 0$),

$$D_{\rm C} \;=\; \frac{c}{H_0}\left[\frac{1}{q}(1-e^{-q\zeta})\right] \quad . \tag{3.7}$$

For a non-constant q, the above result is valid only over a small change in ζ. For small $\zeta = v/c$, using a second-order Taylor series expansion, a second-order Hubble law is obtained:

$$D_{\rm C} \;\simeq\; \frac{c}{H_0}\,\zeta\left(1-\frac{q_0\zeta}{2}\right) \;=\; \frac{v}{H_0}\left(1-\frac{q_0 v}{2c}\right) \quad . \tag{3.8}$$

This form tends to the exact law with $q_0 \to 0$, and the right-hand term $[1-(q_0/2)(v/c)]$ represents an average of $(1+z)/E(z)$ assuming constant acceleration (c.f. the quadratic fitting function given by Sutherland & Rothnie (2015) for improved precision).

For ΛCDM cosmologies, the approximation is accurate to within 0.1% at $z \lesssim 0.1$. Note that regardless of the accuracy of the Hubble law, v accurately represents the integral of the velocity differences along the line-of-sight, precisely in the case of fundamental observers. This is evident from the additive nature of terms in ζ or v (Baldry et al., 2018).

From Eqs. 3.1 and 3.8, an accurate approximation for the Hubble constant estimator is given by

$$H_{0,\rm est} \;\simeq\; \frac{v_{\rm cmb}}{D_{C,\rm est}}\left(1-\frac{q_{0,\rm fid}v_{\rm cmb}}{2c}\right) \quad , \tag{3.9}$$

with $v_{\rm cmb} = v_{\rm cos} + v_{\rm pec}$. From this equation, the effect of peculiar velocities and choice of fiducial cosmology on the estimated Hubble constant is evident. The effects of cosmological assumptions on the results of the present chapter are shown in Section 3.7.

Sources of uncertainty for estimating the Hubble constant include: (i) calibration of the standard candle scale, (ii) photometric measurements, (iii) bandshifts (k corrections), (iv) evolution, (v) differences between the true cosmology and the fiducial cosmology, and (vi) peculiar velocities. Any systematic uncertainty from the first two is generally independent of redshift, while the uncertainty from the cosmology (or bandshift or evolution) increases approximately proportional to $v_{\rm cmb}$. The uncertainties from peculiar velocities are approximately proportional to $1/v_{\rm cos}$ because $v_{\rm cmb} = v_{\rm cos}(1 + v_{\rm pec}/v_{\rm cos})$.

Figure 3.2 illustrates the differences in the H_0 estimate arising from redshift-dependent

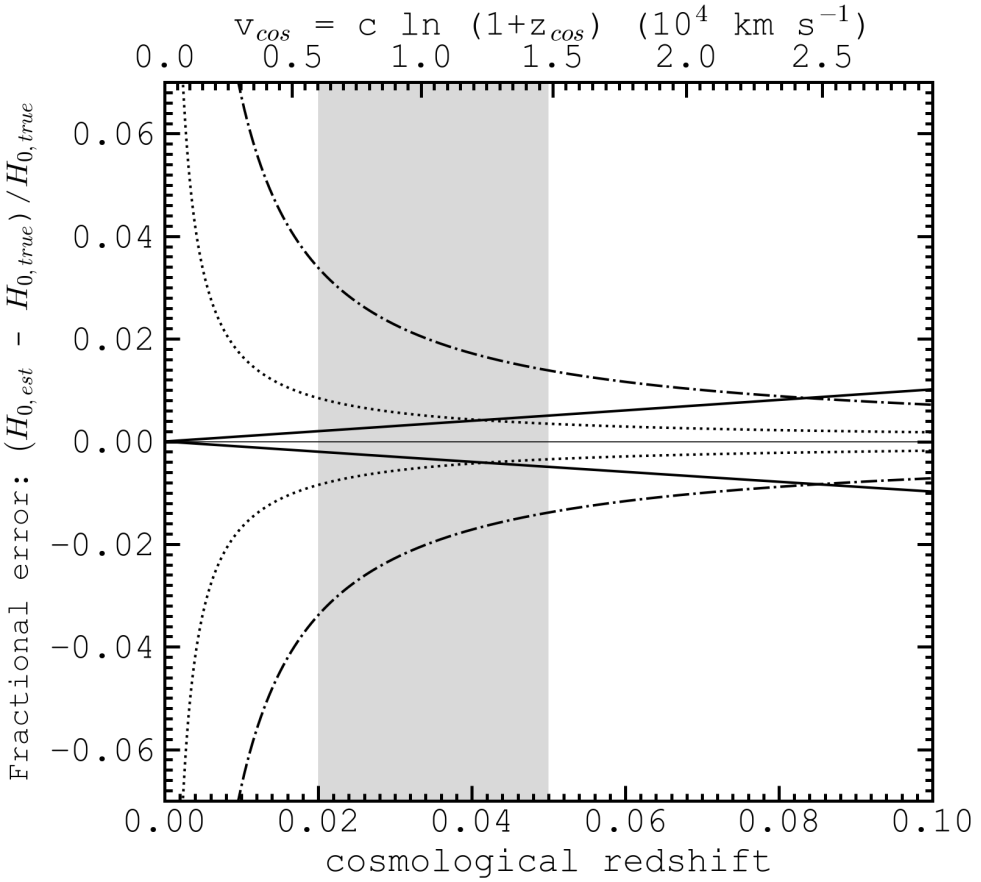

FIGURE 3.2: The fractional error in the estimated Hubble constant due to peculiar velocities and erroneous cosmological assumptions. The solid lines show the fractional error with a 0.2 offset in q_0 between the true and fiducial cosmologies. The dot-dashed lines show the fractional error for systematic offsets of 200 km/s between CMB-frame velocities and cosmological recession velocities, while the dotted lines show the same with a reduced systematic offset of 50 km/s. The shaded region depicts $0.02 < z < 0.05$ which is ultimately the focus for H_0 estimates in the present chapter.

uncertainties. The impact of peculiar velocities, in particular any non-zero average, pushes one to measure H_0 at $v_{cos} > 20000$ km/s. However, in order to limit the degeneracy with q_0 and uncertainties that scale proportional to v_{cos}, it would be useful to measure H_0 at lower recessional velocities. Either way, it is important to control for any systematic peculiar velocity offsets in the standard candle sample. It is the aim of this chapter to test and account for peculiar velocity biases.

3.2 Relevant Data Sets

In order to quantify the effects of the galaxy density field on SNIa peculiar velocities, and hence on local H_0 measurements, 3 key data sources are utilised:

1. **The 2MASS REDSHIFT SURVEY:** the galaxy sample with which to measure the galaxy density field must have redshifts and cover a large solid angle on the sky, in order to minimise biases due to cosmic variance. As such the 2MASS REDSHIFT SURVEY (2MRS) from Huchra et al. (2012) is utilised, built from the Extended Source Catalogue (XSC) of the 2-MICRON ALL-SKY SURVEY (2MASS) (Skrutskie et al., 2006). The result is a galaxy redshift sample of 44,599 galaxies with $m_K \leq 11.75$ mag (henceforth, the K-band magnitude refers to the extinction-corrected 2MASS isophotal Vega magnitude measured in an elliptical aperture defined at 20 mag/sq.arcsec) and with $|b| \geq 5°$ ($|b| \geq 8°$ for $330° < l \leq 30°$, i.e. towards the Galactic bulge), giving 97.6% completeness within these limits (Huchra et al., 2012), i.e. away from the Zone of Avoidance (ZoA). This high completeness coupled with redshift information allows the construction of a 3-dimensional picture of the local galaxy density field.

2. **The PANTHEON SNIa Sample:** to test for correlations of the local galaxy density field with H_0 measurements from SNeIa, the PANTHEON SNIa Sample (Scolnic et al., 2018) is made use of. This sample compiles photometry and spectroscopic redshifts for 1048 SNeIa. In the present chapter, 88 SNeIa are utilised. These are those which overlap with the 2MRS footprint, are at least 50 Mpc from the ZoA in 3-dimensional Cartesian space, and occupy the redshift range $0.02 < z < 0.05$; the range for which the 2MRS galaxy density field is best constrained. This is in order to produce the most reliable H_0 estimates or fractional H_0 error when corrected for peculiar velocities, as discussed in Section 3.6.1.

3. **The MDPL2-GALACTICUS Simulation:** to test for the effects of sample volume, sample size, and cosmic variance on the strength of correlations of SNIa H_0 estimates with the density field, the analyses in this chapter will be repeated using the mock data products of MDPL2-GALACTICUS (Knebe et al., 2018), produced by running the Galacticus semi-analytical code (Benson, 2012) on the MultiDark Planck 2 (MDPL2) hydrodynamical simulation (Klypin et al., 2016). Details are described in Stoppacher et al. (2019) and in the above works, but to summarise: the result is a 1 h^{-3} Gpc^3 box containing 3840^3 Dark Matter particles, whose SDSS *ugriz* luminosities are traced over cosmic time. The methods in this chapter make use of the $z = 0$ redshift snapshot, using corresponding z-band galaxy luminosities to impose a detection-limit on the galaxy sample, in order to construct mock galaxy density fields, used for comparison with the 2MRS K-band observational counterpart. These simulations will also be used to test for the cosmic variance

on results, and to estimate how common the observed local density structure is within a Λ-CDM framework.

3.3 Measuring the 2MRS Galaxy Density Field

As discussed in Section 3.1, the aim of this chapter is to quantify the effects of the galaxy density field on SNIa peculiar velocities, and hence, on the local estimate of H_0. The next step is to construct the required galaxy density field from the 2MRS Galaxy Catalogue.

This catalogue is flux-limited at $m_K \leq 11.75$. As a result, a knowledge of the galaxy luminosity function is required, from which to estimate the completeness of the sample as a function of redshift. Correcting for this completeness above a chosen luminosity value yields estimates of volume-limited number densities with redshift. This minimum luminosity boundary is chosen to be $L_K = 10.5$ (where L_K here and henceforth refers to the luminosity in logarithmic units of the solar K-band luminosity quoted by Cohen et al., 2003). This gives volume-limited number densities for $z \lesssim 0.02$, and is chosen as a trade-off between the maximisation of statistics whilst limiting reliance on the completeness estimation method which will be outlined. The K-band luminosity distribution of the sample as a function of redshift is shown in Figure 3.3.

To improve the accuracy of the nearby galaxy density field, for which peculiar velocity is most troublesome for the determination of galaxy distance, the 2MRS redshift is replaced in 2 cases: Firstly, if the galaxy is matched within $5'$ (on the sky) and 150 km s^{-1} of a galaxy from the Updated Nearby Galaxy Catalogue of Karachentsev et al. (2013), this catalogue distance is utilised. Secondly, if galaxies are matched within $0.5'$ of a member of the Extended Virgo Cluster Catalogue (EVCC) (Kim et al., 2014), a distance of 16.5 Mpc is assumed. If either case applies, the redshift implied from the comoving distance via a 737 cosmology ($H_0 = 70$, $\Omega_\mathrm{m} = 0.3$, $\Omega_\Lambda = 0.7$) is utilised. Henceforth, the 'fiducial cosmology' means 737 unless explicitly noted.

Galaxy K-band luminosities are calculated using Equation 3.10, where $M_{K,\odot}$ is the solar K-band Vega-mag absolute magnitude of 3.28, and $k(z)$ is the k-correction computed as $k(z) = -6.0\log(1+z_{hel})$ following Kochanek et al. (2001).

$$L_K = \frac{5\log(D_{L,fid}(z_\mathrm{cmb})/10\,\mathrm{pc}) + \mathrm{M_{K,\odot}} - \mathrm{m_K} + \mathrm{k(z)}}{2.5} \tag{3.10}$$

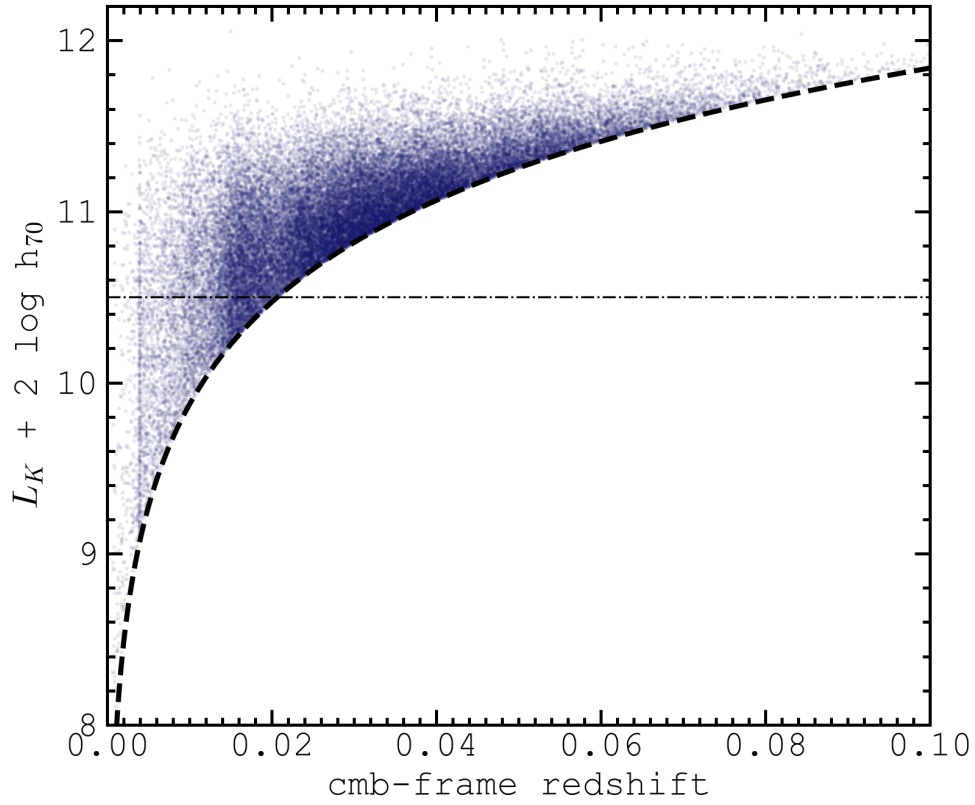

FIGURE 3.3: 2MRS galaxy K-band luminosities versus CMB-frame redshift. The dashed line indicates the flux limit as a function of redshift. Number densities as a function of redshift will be corrected to the number expected with $L_K > 10.5$ (see text for details). $L_K = 10.5$ is marked with the dot-dashed horizontal line.

To estimate the K-band luminosity function, the parametric maximum-likelihood method of Sandage et al. (1979, henceforth, the STY method) is employed. The method is well-described in the literature, (see, e.g. Loveday et al., 1992), but in short, it is first assumed that the galaxy luminosity distribution is well-described by a single-Schechter function (Schechter, 1976). The probability of observing a galaxy of a given luminosity at a given redshift is estimated. The single-set of Schechter function parameters L^* (the 'knee') and α (the faint-end slope), which maximises the product of these probabilities over the entire galaxy sample is the best maximum-likelihood estimate.

The best-fit Schechter function is then used to estimate the completeness of galaxy number density at a given redshift. This is achieved by computing the ratio between the number density integrated above the flux limit corresponding to this redshift, and the integrated number density brighter than the reference luminosity of $L_K = 10.5$. For demonstrative purposes, Figure 3.4 shows the luminosity distribution for the broad redshift range of $0.02 < z < 0.05$, as well as the maximum-likelihood Schechter function fit. For this redshift range, the STY method finds that the likelihood is maximised using parameters $[L^*, \alpha] = [11.02, -0.91]$. Next, the best-fit Schechter parameters in smaller redshift bins is assessed, in order to quantify any parameter evolution.

Figure 3.5 shows the redshift evolution of these best-fit parameters. In redshift bins of width 0.01, likelihood values as a fraction of the maximum likelihood for each bin are assessed as a function of L^* and α. 1.8σ and 1.9σ separations in L^* and α, respectively, are found for $0 < z < 0.01$ when compared with $0.01 < z < 0.02$. Comparing the latter bin with the $0.02 < z < 0.03$ result, separations of 0.35σ and 1.08σ are found. It is concluded that consistency is found within 2σ for the parameter values and hence a fixed α value for the full redshift range is adopted. The value corresponding to the inverse-squared error weighted (henceforth, error-weighted) mean over all redshift bins out to $z = 0.1$ is adopted, equating to $\alpha = -0.99$.

A correct assessment of luminosity versus redshift is crucial to analyses of the local density field. A lack of correction for this effect may result in an over-estimation of galaxy number densities which would worsen with increasing redshift. Such a slope to galaxy number density could lead to an over-estimate of the local outflow, which would lead to an under-estimation in local H_0 estimates.

Galaxy luminosities may be expected to evolve since $z = 0.1$, primarily due to changes in mass-to-light ratio. The faint-end slope of the LF, α, is not expected to evolve as significantly in this redshift range (see, e.g. Madau & Dickinson, 2014). Irrespective of any α evolution, however, one can use the fact that L^* and α are somewhat degenerate

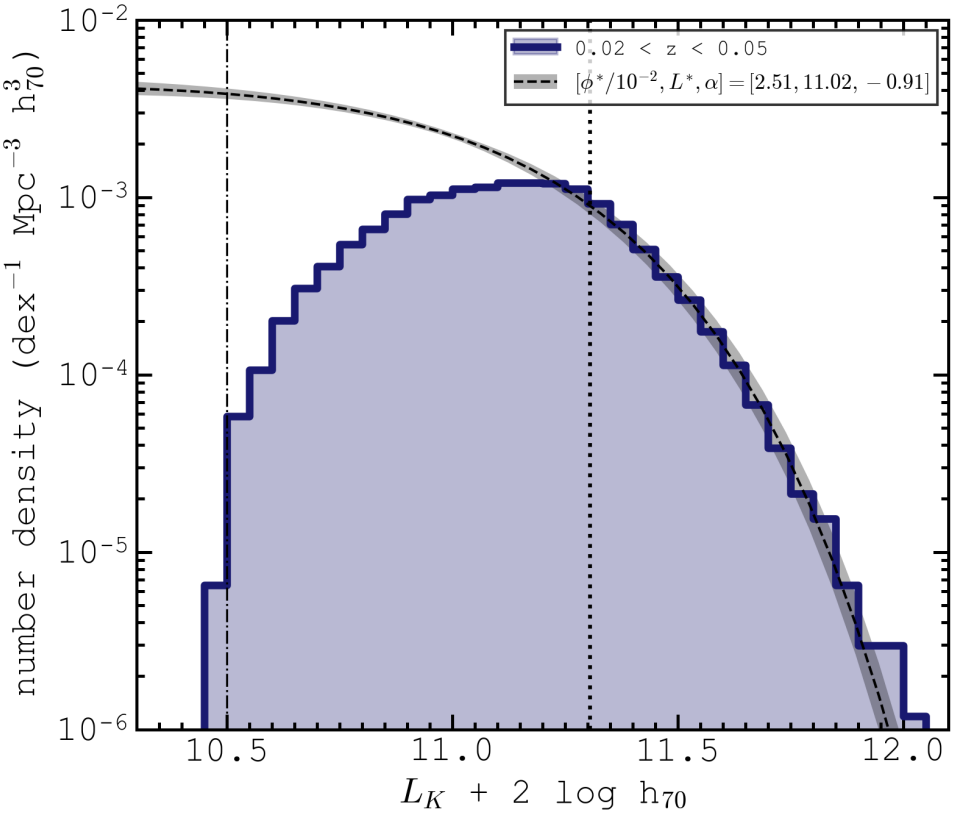

FIGURE 3.4: In blue: a histogram of the observed $0.02 < z < 0.05$ K-band luminosity distribution of 2MRS galaxies. The dashed line shows the maximum-likelihood single-Schechter fit determined using the STY method. The dotted line shows the luminosity limit for $z = 0.05$. The dot-dashed line corresponds to $L_K = 10.5$.

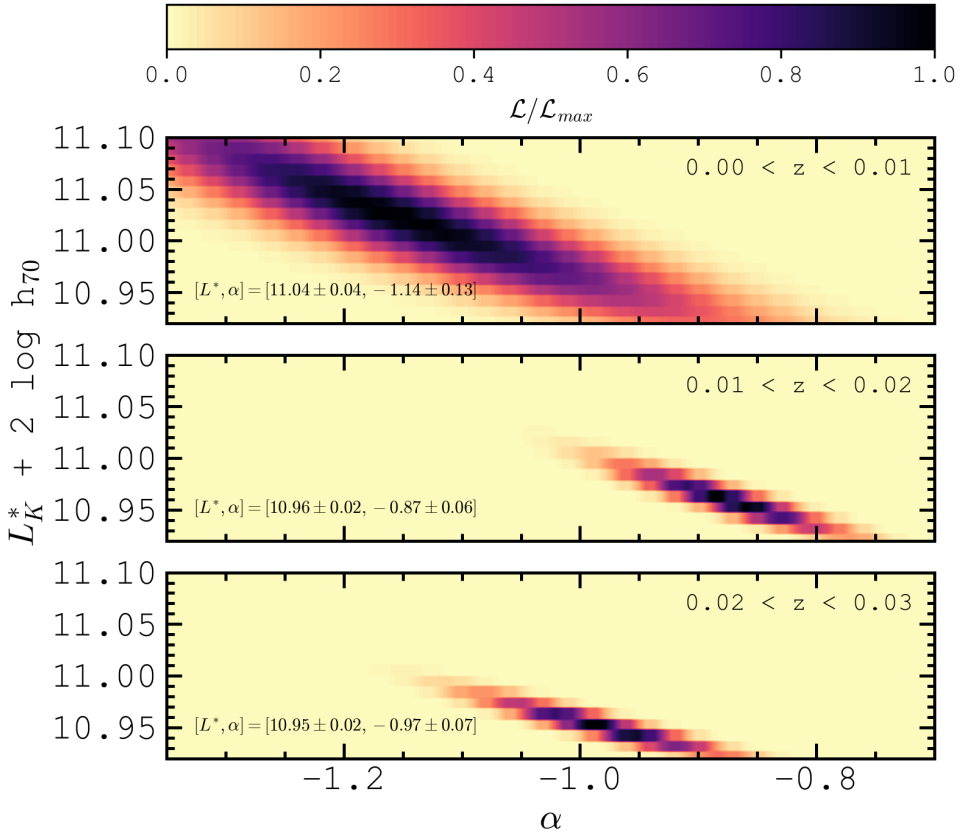

FIGURE 3.5: Likelihood values for combinations of the single-Schechter function parameters α and L^*, from the STY method applied to the 2MRS K-band luminosities. Likelihood values are in units of the maximum likelihood in each panel. The three panels show 3 different CMB-frame redshift ranges of width 0.01, as indicated.

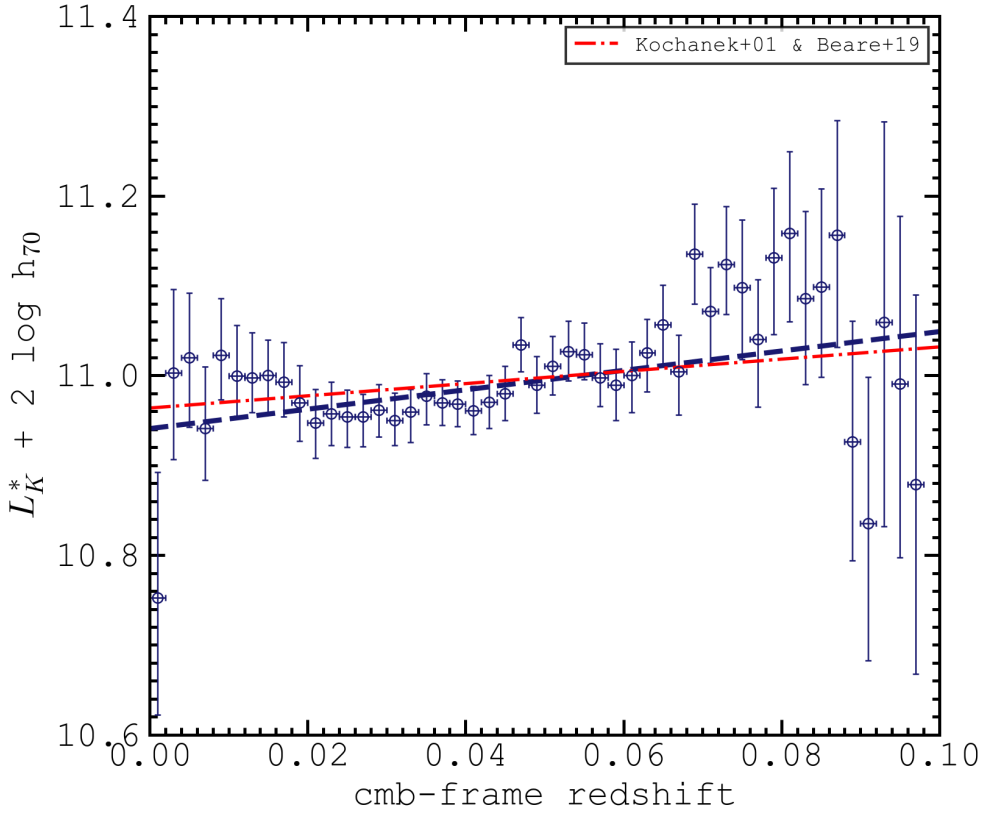

FIGURE 3.6: The inferred maximum-likelihood values of the single-Schechter parameter L^* as a function of CMB-frame redshift, when using a fixed $\alpha = -0.99$ value. L^* is computed in redshift bins of width 0.002. The error-weighted best-fit line is shown as the dashed blue line. The slope is consistent with that expected due to luminosity evolution, shown by the red dot-dashed line, made by connecting the L^* values of Kochanek et al. (2001) and Beare et al. (2019) (see text).

in order to treat any evolution as purely in luminosity, and as such this likely wraps-in changes to α. (Furthermore, it is found in Section 3.5 that the choice of α does not affect results significantly.) Repeating the Schechter fit determination as a function of redshift but with a fixed α value, a positive trend of L^* with redshift is quantified, shown in Figure 3.6. The blue-dashed line shows the error-weighted regression fit, equating to $L^* = 1.080(z - 0.03) + 10.973$, which has a Spearman rank correlation coefficient (r_s) of 0.558 and a p-value (p) of 0.001.

An indication of expected luminosity evolution is shown as the red dashed line by connecting the inferred K-band L^* value of Kochanek et al. (2001) ($z < 0.01$) with the $z = 0.3$ value of Beare et al. (2019) who adopt $\alpha = -1.00$. The observed trend of L^* with redshift is consistent with estimates of luminosity evolution found in the literature.

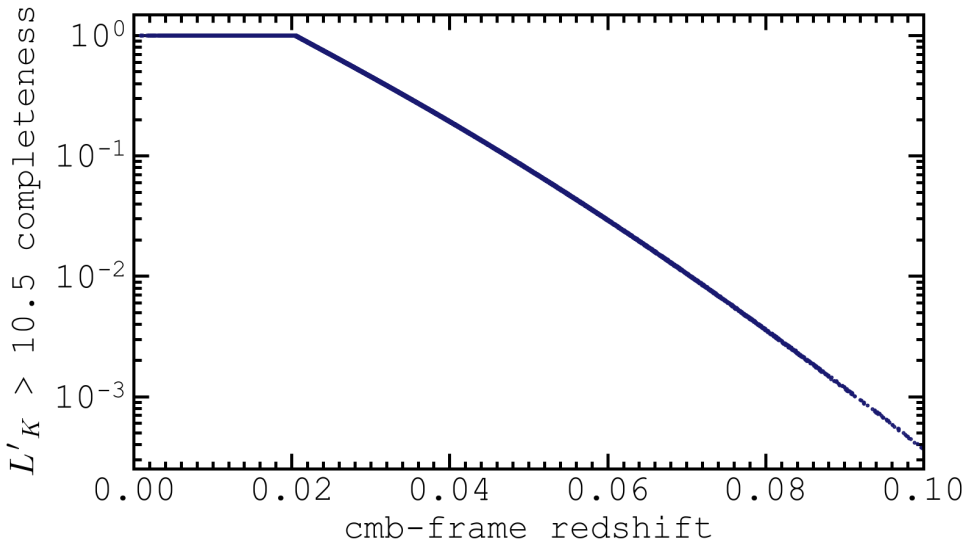

FIGURE 3.7: Estimated completeness of $L'_K > 10.5$ galaxy number statistics in the 2MRS galaxy sample, as a function of CMB-frame redshift.

Galaxy luminosities are next corrected for evolution as a function of CMB-frame redshift, such that the evolution-corrected luminosity, L'_K, is given by $L'_K = L_K + \delta_L$, where $\delta_L = -1.080(z - 0.03)$. The sample is now re-selected with $L'_K > 10.5$.

With galaxy luminosities corrected for evolutionary effects, the luminosity function is well-approximated by the same single-Schechter function for the full redshift range $(0 < z < 0.1)$, with parameters $[L^*, \alpha] = [10.97, -0.99]$. The sample completeness above $L'_K = 10.5$ as a function of redshift, $\mathcal{C}(z)$, is estimated using Equation 3.11, where L'_{min} is the maximum of 10.5 and $L_K + (m_K - 11.75)/2.5 + \delta_L$. Completeness as a function of redshift is shown in Figure 3.7. Galaxy counts are weighted by the inverse of $\mathcal{C}(z)$ where:

$$\mathcal{C}(z) = \frac{\int_{L'_{min}}^{\infty} \phi(L')dL'}{\int_{10.5}^{\infty} \phi(L')dL'} \quad . \tag{3.11}$$

The volume-limited number density of galaxies in a redshift shell is estimated using Equation 3.12 where $\sum w_N$ is the sum of weights corresponding to galaxies within the shell, and V is the shell volume, dependent on the solid angle spanned by the survey region:

$$\phi(z') = \frac{\sum w_N}{V} \tag{3.12}$$

3.4 A Proxy for Peculiar Velocity from the Galaxy Density Field

Equation 3.1 shows that the local H_0 estimate inferred from a standard candle depends directly on the velocity of the object in the frame of the CMB. This velocity is the sum of components due to the expansion of the Universe (v_{cos}), and any peculiar velocities (v_{pec}). Hence, local H_0 estimates depend not only on cosmological expansion but also on v_{pec} as demonstrated in Figure 3.2.

In Section 3.5, galaxy number densities as a function of redshift will be presented, but for the successive stages of this chapter's analysis, a knowledge of the 3-dimensional galaxy density field will be required. As mentioned in Section 3.1, the observed peculiar velocity is the line-of-sight (LOS) component of solely gravitationally induced motions on these scales. However, it is not only the absolute density in a SNIa region that determines its peculiar velocity, but also the density gradient along the LOS (see, e.g. Peebles, 1980; Lahav et al., 1991).

A density parameter which captures this LOS density gradient is required. This is achieved by measuring the density around the SN region in 2 hemispheres: the density of galaxies in a hemisphere between the SN and observer is denoted ϕ_-, and the density of galaxies in a hemisphere beyond the SN is denoted ϕ_+. The parameter $\Delta\phi_{+-}$ is then the LOS density gradient in a SN environment, and can be written as:

$$\Delta\phi_{+-} = \frac{\phi_+ - \phi_-}{\phi_+ + \phi_-} \quad . \tag{3.13}$$

To determine the contributions of galaxies to $\Delta\phi_{+-}$, galaxy and SN positions are first converted into 3-dimensional Cartesian coordinates using RA, Dec, and comoving distance derived from CMB-frame redshift, using the fiducial cosmology. The angle made between the LOS and the SN-galaxy directional vector is then measured. Let a function η_i be defined. If the cosine of this angle is positive, $\eta_i = 1$, and a galaxy i contributes to ϕ_+. Otherwise $\eta_i = -1$ and the contribution is to ϕ_-. $\Delta\phi_{+-}$ can now be re-written as:

$$\Delta\phi_{+-} = \frac{\sum_i \eta_i w_{N,i} \exp\left(-|\vec{r}_{gal,i} - \vec{r}_{sn}|^2/2\sigma^2\right)}{\sum_i w_{N,i} \exp\left(-|\vec{r}_{gal,i} - \vec{r}_{sn}|^2/2\sigma^2\right)} \quad . \tag{3.14}$$

Here, $w_{N,i}$ are the weights on contributions from each galaxy, i, determined previously

with the STY method for the previous density vs redshift analysis. $\vec{r}_{gal,i}$ is the LOS vector from observer to each galaxy, and $\vec{r}_{sn}$ is the LOS vector from observer to SN. The parameter σ controls how sharply contributions to $\Delta\phi_{+-}$ decrease as a Gaussian with SN-galaxy separation. This parameter will be referred to throughout the present chapter, along with another parameter, R, which represents the sphere radius out to which density contributions are considered.

The parameters R and σ are highlighted because one aims to test for correlations for H_0 with $\Delta\phi_{+-}$. It will be investigated whether particular values of R and/or σ maximise the strength of correlations, and in doing so, the aim is to reveal the scales of density structure which control peculiar velocities in SN environments.

The method of estimating a proxy for peculiar velocity directly from the galaxy density field produces an independent test for the effects of density flows on H_0 estimates without the use of flow models, often utilised in the literature (e.g. Hudson et al., 2004; Scolnic et al., 2018; Neill et al., 2007). One is able to assess the effects of peculiar velocity with no assumptions for the geometry of any density structure, and the impact of structure can be assessed on a wide variety of scales.

3.5 Regional 2MRS Galaxy Densities

The top panel of Figure 3.9 shows galaxy number densities as a function of CMB-frame redshift for the sky coverage of 2MRS, equating to a $\sim 91\%$ coverage of the sky (see Section 3.2). Number densities are quoted in logarithmic units of the global density, ϕ_{global}, itself calculated in the present chapter as the error-weighted mean density for $0 < z < 0.1$, with a value of $10^{-2.49}$ Mpc^{-3} bin^{-1}. Densities are given for redshift bins of width 0.002. Poisson errors are shown, demonstrating the well-constrained nature of density structure out to at least $z \sim 0.08$. For the full 2MRS coverage, the $z < 0.05$ integrated under-density equates to only $6 \pm 1\%$. As such, although a strong statement cannot be made for redshifts exceeding those of the 2MRS galaxy survey, no evidence for a void pertaining to the full sky is found out to at least $z = 0.1$.

As a comparison with previous studies of the galaxy density field, densities for the regions of NGC-SDSS ($150° < \text{RA} < 220°$, $0° < \text{dec} < 50°$) and SGC-6DFGS ($330° < \text{RA} < 50°$, $-50° < \text{dec} < 0°$) are calculated. These are regions of focus in Whitbourn & Shanks (2014), who also utilise 2MASS photometry, coupled with redshifts from SDSS and 6DFGS for the 2 regions, respectively. Their densities are plotted as the grey filled regions in

the bottom 2 panels of Figure 3.9, along with the results of the present chapter. Also plotted are the REFLEX-II/CLASSIX cluster densities from Böhringer et al. (2015, 2019).

A comparison with Whitbourn & Shanks (2014) shows consistency for densities in the NGC-SDSS region. An integrated $z < 0.05$ under-density of $8 \pm 3\%$ is obtained for this region. Whitbourn & Shanks (2014) found their largest under-densities in the SGC-6DFGS region. Calculating the integrated number density for $z < 0.05$, they obtain a $40 \pm 5\%$ under-density in this region. In the present chapter, an equivalent under-density of $27 \pm 2\%$ (Poisson error only) is found for this region, which equates to a 2.4σ tension.

In light of this discrepancy, density measurements are tested for the effects of the assumptions for the luminosity function used to correct for $L_K > 10.5$ galaxy incompleteness beyond $z \sim 0.02$. It is found that a deviation in the Schechter function slope of $\alpha = 0.1$ either side of the adopted $\alpha = -0.99$ produces a 3% deviation to the $z < 0.05$ integrated density, and as such cannot be the main source of the discrepancy. Note also that Figure 3.9 shows the SGC-6DFGS result deviates most from that of Whitbourn & Shanks (2014) for $z < 0.02$, the redshift range for which the sample of the present chapter is complete for $L_K > 10.5$, i.e. where no completeness corrections are required. Furthermore, sample completeness is here estimated using an evolving LF for $z \gtrsim 0.02$, whereas Whitbourn & Shanks (2014) use a fixed LF to model completeness for the full redshift range of $0 < z < 0.1$. It is worth noting, however, that Whitbourn & Shanks (2016) still find a significant local under-density, consistent with their previous analysis, when instead using a LF fitted simultaneously with the galaxy density distribution, albeit with a steeper faint-end slope to their LF than found in the present chapter..

Comparing to other recent results in the literature, Jasche & Lavaux (2019) use physical Bayesian modelling of the non-linear matter distribution and find no clear evidence for an under-density in the direction of the SGC-6DFGS region, with an under-density of $3 \pm 11\%$. Böhringer et al. (2015) find a REFLEX-II cluster under-density in the SGC-6DFGS region of $55 \pm 10\%$. Cluster bias is well-known to exaggerate voids and this is clear from Figure 3.9. Correcting for cluster bias they deduce a $z < 0.05$ under-density comparable with that of the present chapter, of $20 \pm 8\%$. In Section 3.5.1 the SGC-6DFGS under-density is investigated in more detail, using simulations to estimate how common such under-densities are in the Universe.

3.5.1 Studying the SGC Local Under-density via Simulations

In Section 3.5, it was concluded that no evidence for a 'Local Void' which pertains to the

full sky was found, out to the $z = 0.1$ limit of the 2MRS survey. However, a significant under-density in the direction of the SGC-6DFGS region was found which was $27 \pm 2\%$ under-dense relative to the global density when integrated below $z < 0.05$.

In Section 3.6.2, a useful property of the MDPL2-GALACTICUS simulations will be demonstrated: one is able to estimate the cosmic variance of peculiar velocity effects on H_0 estimates by mimicking the observational analysis from a variety of mock observer positions. Using a similar method, one can test how 'common' the SGC-6DFGS under-density is, by examining how often an under-density of this amplitude is observed at different observer positions in the simulation. Here, the observer is placed at 10^6 random positions in the 1 h^{-3} Gpc^3 box.

Figure 3.8 re-iterates that the main contribution to SGC-6DFGS under-density occurs at $z \sim 0.05$. For integrated densities out to $z \sim 0.03$, the percentage of mock observed positions which produce a density at least as under-dense as found in SGC-6DFGS is approximately 40%. This implies such an under-density is common-place at many positions in the universe at current-epochs.

However, what is striking about the results of Figure 3.8 is that the SGC-6DFGS under-density at $z \sim 0.05$ is extremely unlikely to arise from the vast majority of mock observer positions: The number of the 10^6 positions finding such an integrated underdensity out to $z = 0.05$ is of the order 100, or 0.01%. This either implies that our position in the Universe is particularly special, that the large scale structure in the simulation is unrealistic, or that there is an unknown observational systematic in the direction of SGC-6DFGS. Given that several more studies, including Whitbourn & Shanks (2014), find the $z = 0.05$ SGC-6DFGS under-density to be of notably high-amplitude, a quantification of such a systematic in future work would be of great interest. However, it is noted that the correspondence with the X-ray REFLEX-II clusters result argues against it being a systematic associated with the galaxy surveys. The tension between measurements of the local under-density and the current cosmological model highlights the great potential in future work using deeper and more complete extra-galactic samples with new facilities such as eROSITA.

To summarise, no evidence for a significant void which pertains to the full sky is found, out to the $z = 0.1$ limit of the 2MRS galaxy survey. However, Figure 3.9 shows that regional density structures found by Whitbourn & Shanks (2014) are reproduced well, albeit with different amplitudes of the under-density of certain structures on scales of $z < 0.05$. Notable density structures reproduced in this thesis include the void in the direction of NGC-SDSS centred on $z \sim 0.015$, for which a density of $\sim 0.5\phi_{global}$ is

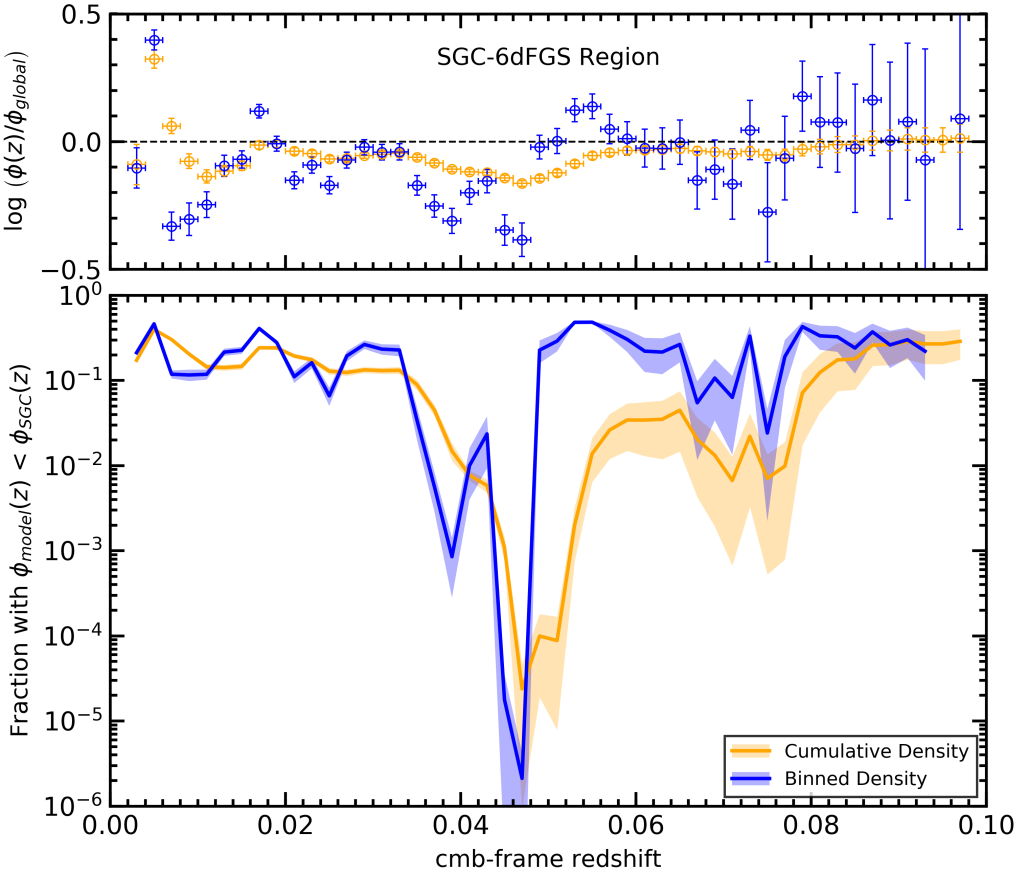

FIGURE 3.8: Top: local galaxy densities as a function of redshift in the SGC-6DFGS region, in logarithmic units of the global density. In blue is the binned density at z. In yellow is the cumulative (integrated) density out to z. Redshift bins are of width 0.002. Bottom: the fraction of 10^6 SGC-6DFGS-sized regions from the MDPL2-GALACTICUS simulation, which have a density less than that observed in SGC-6DFGS, as a function of redshift. The simulated densities use a mock detection limit matching the observations, and observer position is randomised for each iteration.

obtained, as well as the over-density on smaller scales ($z \sim 0.004$) in the same sky direction, of order 10 times that of the global density. Such density structures would be expected to be consequential for the peculiar velocities of SNeIa in these regions (see, e.g. Peebles, 1980; Clutton-Brock & Peebles, 1981). As such, quantifying and correcting for these effects is the main focus for the remainder of the present chapter.

3.6 Correlations of the Hubble constant with the Galaxy Density Field

3.6.1 PANTHEON SNe in the Galaxy Density Field

One can estimate H_0 from individual SNeIa based on their redshifts and distance moduli (found by Scolnic et al. 2018), using Equation 3.1. Note that this estimator is not sensitive to the fiducial value of H_0 assumed, and only slightly sensitive to differences in the assumption for q_0: as quantified in Section 3.7. However, since the goal of this chapter is to determine the effects of peculiar velocity, the majority of results will be presented in terms of the *fractional change* in H_0, which is not sensitive to the well-documented issue of SNIa distance calibration. The only exception is in Section 3.7, where for completeness, absolute H_0 estimates are given, found by calibrating SNIa distance moduli on the BAO-derived cosmic distance scale (Anderson et al., 2014).

The fractional error in H_0 from the zero peculiar velocity case is calculated by performing an error-weighted linear fit of $\Delta\phi_{+-}$ to H_0. The fractional error in H_0 is then given as $(H_0 - c)/c$, where c is the $\Delta\phi_{+-} = 0$ intercept of the regression line. SNe with redshifts in the range $0.02 < z < 0.05$ are utilised for this fit, as this range meets several useful criteria for these analyses: a trade off is seen between uncertainties due to peculiar velocity and due to q_0 (See Figure 3.2); both the galaxy and SN statistics are high; the best-fit Schechter function parameters required to infer the density field are best-constrained; and it may be interesting to examine the effects of well-defined structures on peculiar velocities, found in this range (e.g. in NGC-SDSS and SGC-6DFGS). In short, this redshift range will produce the most reliable estimates of fractional H_0 error due to peculiar velocity. 111 of the 1048 PANTHEON SNe are found in this range.

For each SN, if the nearest path to the edge of the 2MRS survey (i.e. to the ZoA) is shorter than R, the SN is removed from the sample to prevent edge effects. Also removed are galaxies within 10 Mpc of the SN position. This is because the typical galaxy group velocity dispersion is a continuous scale from 10s of km s^{-1} (for groups of

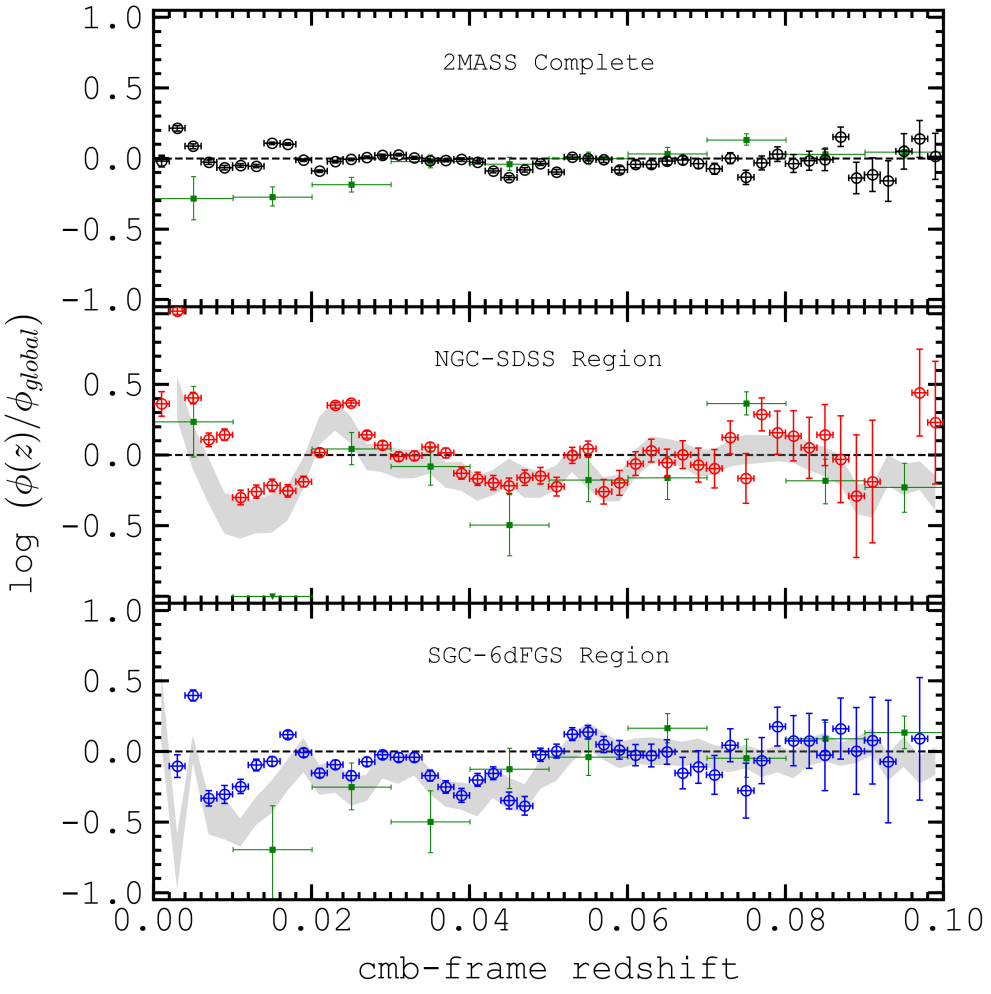

FIGURE 3.9: Galaxy number densities as a function of CMB-frame redshift in logarithmic units of the global density. Black, red and blue circles depict densities for the full 2MRS survey region, the NGC-SDSS region and SGC-6DFGS region, respectively. Shown as green points are $|b| > 20°$ CLASSIX cluster densities (top), CLASSIX cluster densities in the NGC-SDSS region (middle) (Böhringer et al., 2019), and REFLEX-II cluster densities (Böhringer et al., 2015) in the SGC-6DFGS region. Grey-filled regions depict number densities found by Whitbourn & Shanks (2014).

a few dwarf galaxies) to 1000s of km s^{-1} (for the richest clusters). Hence, the inferred line-of-sight group radius is of the order ∼10 Mpc for large groups. The positions of these galaxies relative to the SN are uncertain. Indeed, if included, these galaxies would also carry the most weight in the density prescription.

In Figure 3.10, the 6 panels show the differing strength of correlation of fractional H_0 error due to peculiar velocity with $\Delta\phi_{+-}$, as the sphere radius, R, and the density smoothing length, σ, are varied. In each panel, the correlation is found to be roughly linear, and so an error-weighted regression line is calculated. The corresponding Spearman rank correlation coefficient (r_s) and p-value (p) are shown in each panel. It is found that the maximum significance of correlation between H_0 estimates and $\Delta\phi_{+-}$ (maximum r_s and minimum p) arises for $[R, \sigma] = [50 \text{ Mpc}, 50 \text{ Mpc}]$.

The results shown adopt the cut within 10 Mpc of the SN, as discussed. This cut was found to reduce the p-value of the H_0 vs $\Delta\phi_{+-}$ fit by $\sim 5\%$. Using instead a 5 Mpc or 20 Mpc cut, one sees in both cases a $\sim 10\%$ rise to the p-value when compared to the preferred 10 Mpc cut.

For the $0.02 < z < 0.05$ PANTHEON sample, 88 out of 111 SNe are sufficiently far from the galaxy survey edge to assess the density within 50 Mpc of the SNe. For these 88 SNe one finds $[r_s, p] = [0.2739, 0.0016]$. Therefore, for the remainder of the present chapter, when referring to $\Delta\phi_{+-}$, what is utilised for calculations is $[R, \sigma] = [50 \text{ Mpc}, 50 \text{ Mpc}]$. This result suggests that peculiar velocities are driven primarily by supercluster scale structure. In Section 3.6.2 this suggestion is investigated and discussed in more detail.

Alternative prescriptions for $\Delta\phi_{+-}$ are also investigated. Firstly, the change to the correlation of H_0 with $\Delta\phi_{+-}$ is examined when galaxies within 10 Mpc of the SNe are instead included in the density measurements. Secondly, the change to correlations when using an inverse-squared weighting with separation is tested: The observed peculiar velocity results from the net line-of-sight component of the gravitational force, and so an inverse squared weighting is expected to be most appropriate. Thirdly, tests for the effects of modifying the density weights to also account for the luminosity of the galaxies are performed. This modification assumes that luminosity traces the galaxy mass.

With each of these prescriptions, $\Delta\phi_{+-}$ is found to correlate more weakly with fractional H_0 error than a Gaussian-smoothed number-density based calculation, albeit, marginally in the case of the 10 Mpc cut. For the remaining tests, this is likely due to the uncertainty in estimating the total (stellar + halo) galaxy mass from the luminosity. An over-weighting of individual galaxies can lead to a catastrophic miscalculation of the

peculiar velocity proxy.

It was highlighted in Section 3.4 that over- or under-density alone does not always result in significant peculiar velocities, and that galaxies at a density peak or trough, may experience a small *net* force upon them and hence a small peculiar velocity. This is demonstrated using $\Delta\phi_{+-}$ (using $[R, \sigma] = [50$ Mpc, 50 Mpc$]$), in Figure 3.11, which shows the parameter as a function of sky position in Galactic co-ordinates. In each panel, the same process for calculating $\Delta\phi_{+-}$ around SNIa positions is applied to the whole sky, for different tomographic slices through the density field, at various steps of $v_{cmb} = c\ln(1 + z_{cmb})$.

Referring back to Figure 3.9, a significant under-density was seen centred on $z_{cmb} \sim 0.015$, in the NGC-SDSS region. This redshift corresponds to a recession velocity in the CMB-frame of ~ 4000 km s^{-1}. Note then, that in Figure 3.11, $\Delta\phi_{+-}$ is close to zero in the $v_{cmb} = 4000$ km s^{-1} panel. On the other-hand, at the redshifts corresponding to the 2000 km s^{-1} and 6000 km s^{-1} velocity slices, (0.007 and 0.020, respectively), objects are expected to be flowing away from the trough of under-density towards the over-dense peaks at $z \sim 0.003$ and $z \sim 0.024$. This causes measurable effects on the values of $\Delta\phi_{+-}$ in the NGC-SDSS region, seen in Figure 3.11, with significant blueshift and redshift in the $v_{cmb} = 2000$ and $v_{cmb} = 4000$ km s^{-1} panels, respectively. This demonstrates how $\Delta\phi_{+-}$ is able to capture expected peculiar velocity information due to density gradients.

Another notable structural influence is the Perseus Cluster, situated at $[l, b, z_{cmb}, v_{cmb}]$ $\sim [150°, -13°, 0.017, 5000$ km s$^{-1}]$ (Piffaretti et al., 2011): in-fall to the cluster is seen to cause positive $\Delta\phi_{+-}$ (peculiar-velocity induced redshift) for the $v_{cmb} = 4000$ km s^{-1} slice, and negative $\Delta\phi_{+-}$ (peculiar-velocity induced blueshift) for the $v_{cmb} = 6000$ km s^{-1} slice.

3.6.2 Mock Data from MDPL2-GALACTICUS

Note that in Figure 3.10, the mean value of $\Delta\phi_{+-}$ lies close to zero, implying that the $0.02 < z < 0.05$ PANTHEON SN sample is minimally biased in the sign of peculiar velocities. It was also seen that $\Delta\phi_{+-}$ correlates with locally-inferred fractional H_0 error estimates. One can turn to mock data from the MDPL2-GALACTICUS simulation (Knebe et al., 2018) in order to test, firstly, whether trends of fractional H_0 error with $\Delta\phi_{+-}$ are consistent with the observations; secondly, whether the strength of correlation is limited by the ability of $\Delta\phi_{+-}$ to capture peculiar velocity information, or instead by observational photometric uncertainties, not present in the models; and thirdly, what

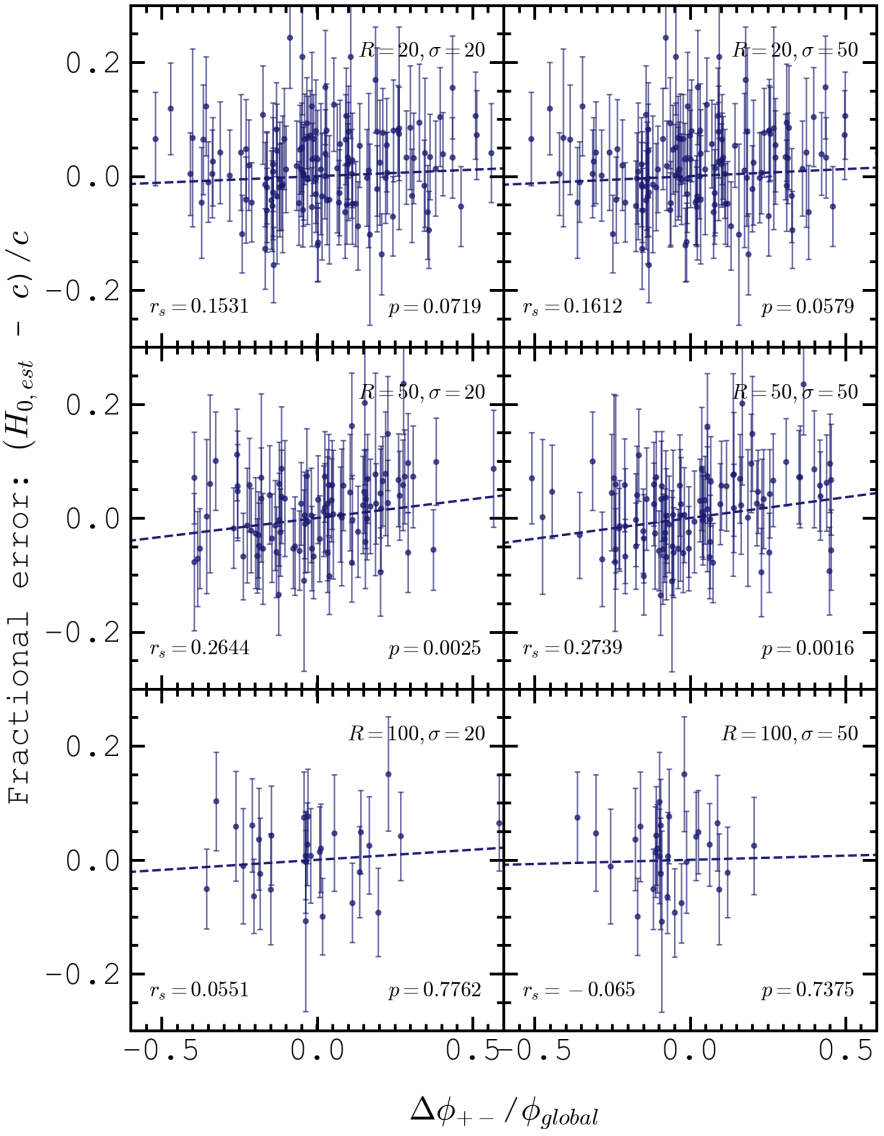

FIGURE 3.10: Estimates of fractional error in H_0 for $0.02 < z < 0.05$ PANTHEON SNe as a function of $\Delta\phi_{+-}$. In each panel, $\Delta\phi_{+-}$ is computed with different values for the Gaussian smoothing scale of density, around the SN (σ), and of the maximum separation from the SN considered in the density calculation (R). The error-weighted line-of-best fit to the data is shown for each σ-R combination, as well as the Spearman's rank correlation coefficient (r_s) and p-value (p).

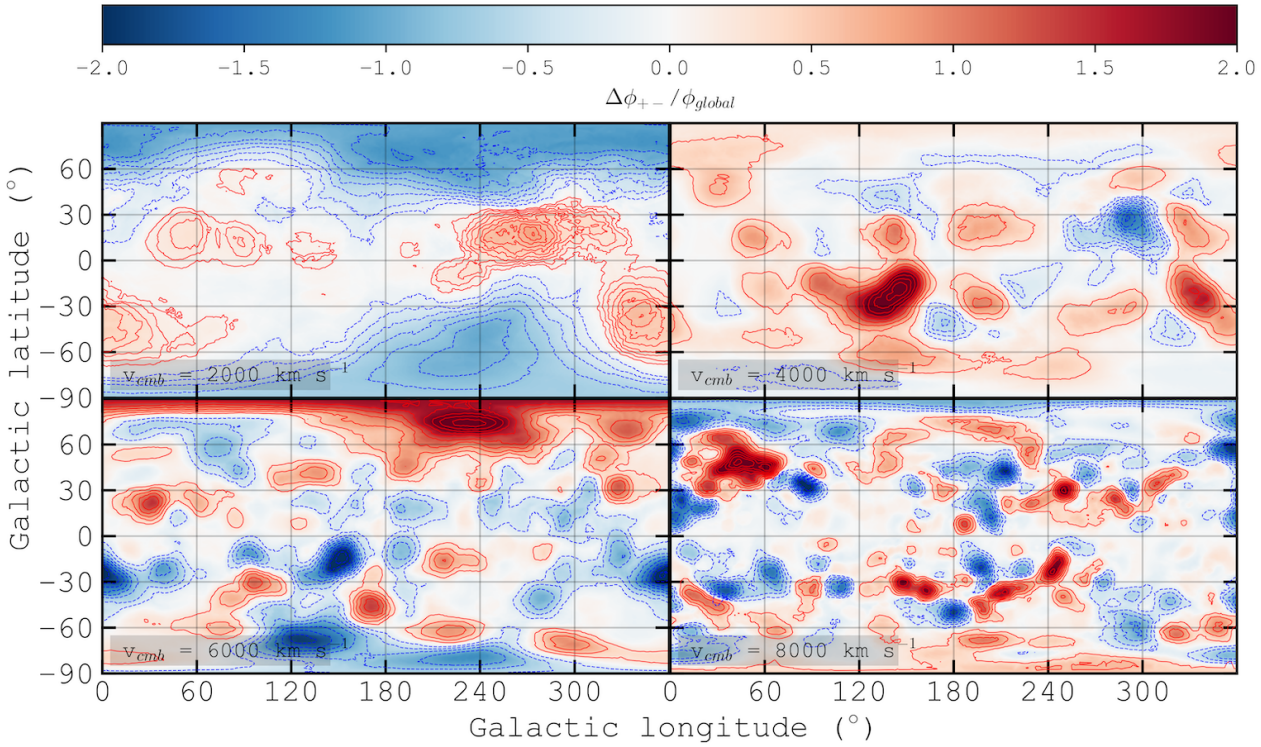

FIGURE 3.11: The density parameter $\Delta\phi_{+-}$ (see text), plotted as a function of sky position, in Galactic coordinates. The parameter is assessed at 4 velocities in steps of 2000 km s^{-1}, where $v = c \ln(1 + z)$, and approximately corresponding to distances from the observer. Objects in regions with $\Delta\phi_{+-} > 0$ are expected to flow away from the observer faster than the Hubble flow, and slower than the Hubble flow when $\Delta\phi_{+-} < 0$.

the cosmic variance is in the $\Delta\phi_{+-}$ distribution, given an access to arbitrary observer positions. This cosmic variance result gives one an estimate of the error on observational peculiar velocity corrections.

As discussed in Section 3.2, a 1 h^{-3} Gpc^3 box is utilised, with 3840^3 dark matter particles traced to the current epoch, using the $z = 0$ redshift snapshot. Each particle has 3-dimensional positions ($\vec{r}$) and velocities ($\vec{v}$). The particles' mock z-band stellar luminosities are used to impose a detection-limit. L_z is here defined as the logarithm of the luminosity in units of 4.4659e13 W Hz^{-1}. The limit is then set to $L_z = 8.843$ such that global 'galaxy' density matches the global $L_K > 10.5$ density found for the 2MRS galaxy sample.

To calculate $\Delta\phi_{+-}$ and local fractional H_0 errors from the mock data, the observer's position in the 1 h^{-3} Gpc^3 box is randomised, and the particle coordinates are redefined such that the observer lies at the origin. Next, galaxies lying at redshifts $0.02 < z < 0.05$ from the observer, are selected at random as SNIa hosts.

Peculiar velocities relative to the observer for all galaxies above the mock flux limit, including the SN hosts, are calculated as follows:

$$v_{pec} = \frac{\vec{r} \cdot \vec{v}}{|\vec{r}|} \quad . \tag{3.15}$$

Galaxy redshifts due to cosmic expansion (z_{cos}) are inferred using the comoving distances $D_C = |\vec{r}|$ associated via the fiducial cosmology. Mock observed redshifts (z_{cmb}) are then calculated using:

$$\ln\left(1 + z_{cmb}\right) \;=\; \ln\left(1 + z_{cos}\right) + \frac{v_{pec}}{c} \quad . \tag{3.16}$$

Fractional H_0 errors from the SNe are obtained using a modification of Equation 3.1:

$$H_{0,\mathrm{est}} \;=\; H_{0,\mathrm{fid}} \frac{D_{C,\mathrm{fid}}(z_{cmb})}{D_{C,\mathrm{fid}}(z_{cos})} \quad . \tag{3.17}$$

$\Delta\phi_{+-}$ is finally calculated about the CMB-frame redshift-inferred SN positions, as was the observational data, using the resultant mock density field. Figure 3.12 shows r_s values corresponding to linear fits of H_0 to $\Delta\phi_{+-}$, where each fit is to 1000 random SN positions from the simulation. Values of $10 < R < 200$ Mpc are sampled, in equal logarithmic steps.

In black, mock-observed galaxy redshifts were used to produce the galaxy density field,

to test for the effects of redshift space distortions on correlations. SNe with $0.02 < z < 0.05$ were chosen to match the observations. r_s is shown as a function of sphere size, R, within which $\Delta\phi_{+-}$ is calculated. The solid black line shows $\Delta\phi_{+-}$ when all galaxies contribute equally to the density. it is observed that the maximum correlation of fractional H_0 error vs $\Delta\phi_{+-}$ comes for $R \sim 50$ Mpc. When using a weighting of density contributions such that $\sigma = 50$ Mpc, one sees that r_s rises significantly as scales of 50 Mpc are approached, and then improves marginally as this sphere size is increased further.

A benefit of the simulations is that these tests can be repeated using the *real-space* positions of galaxies, as shown in blue. A peak at $R = 50$ Mpc is observed once again in the unweighted case, but the most-significant correlation comes when $[R,\ \sigma] = [200$ Mpc, 50 Mpc$]$. r_s is increased using real-space galaxy positions. As would be expected, the real-space and redshift-space results differ most when considering the density on small scales.

The effects of the $0.02 < z < 0.05$ SN selection are tested for by instead including $z < 0.02$ SNe. The galaxy luminosity cut is also alleviated to $L_z > 7.0$ to test for the effects of increasing the number of tracers of the density field. These results are shown in yellow and magenta, respectively. In both cases, no significant change to the amplitude of r_s as a function of $\Delta\phi_{+-}$ is found. In the case of including $z < 0.02$ SNe, this implies that although one is forced to omit these lowest-redshift SNe in the observations due to uncertainties in peculiar velocity, they are not crucial for an assessment of $\Delta\phi_{+-}$. In the case of the increased number of tracers, this implies that the density field is already sufficiently sampled for $L_z > 8.843$, and hence, so too is the 2MRS sample.

It was seen that using a finite value of σ increased values of r_s for large sphere radii, R. As such, tests are made for the effects of fixing $R = 200$ Mpc, and instead varying σ between 10 and 200 Mpc. The result, shown in green in Figure 3.12, reveals that a density weighting corresponding to $\sigma \sim 40$ Mpc produces the maximum significance of correlation between fractional H_0 error and $\Delta\phi_{+-}$. Note that qualitatively identical conclusions are drawn to those found in Figure 3.12 when plotting the p-value associated with a correlation against R and σ.

The underlying result of these analyses is that density gradients on super-cluster scales ~ 50 Mpc are most strongly correlated with estimates of fractional H_0 error. This result is in concordance with expectations from the well-known $J_3(r)$ integral (see, e.g. Peebles, 1981). The 2-point correlation function of galaxies together with linear theory predicts that the largest contribution to peculiar velocities comes from density

structures on these scales (Clutton-Brock & Peebles, 1981). It is also noted that this scale size is established to maximise angular diameter distance biases via gravitational deflection (Kaiser & Peacock, 2016), which is albeit a small gravitational lensing effect. These factors support conclusions that the correlations between density structure on supercluster scales and H_0 are in fact due to real gravitational effects.

It is noted that a sphere size of $R = 200$ Mpc is not appropriate for the case of the observations, as a large fraction of the $0.02 < z < 0.05$ PANTHEON SNe lie within 200 Mpc of the ZoA. In the observations, as spheres around SNe which overlap the survey edge may produce unreliable $\Delta\phi_{+-}$ measurements, one may expect that this is why the prescription $[R, \sigma] = [50$ Mpc, 50 Mpc$]$ was instead found to be optimal. It is reiterated, however, that in the z-space simulations, r_s flattens out for $R > 50$ Mpc, suggesting that the trend of fractional H_0 error with $\Delta\phi_{+-}$ would not improve significantly in the observations, was one able to access a greater volume. As a result, it is expected that the methods already presented in this chapter have found close to the maximum coherence of fractional H_0 error with $\Delta\phi_{+-}$ with the $[R, \sigma] = [50$ Mpc, 50 Mpc$]$ prescription.

For the next stage of this chapter's analysis, the mock redshift-space galaxy density fields is utilised once more, using $[R, \sigma] = [50$ Mpc, 50 Mpc$]$. For 100 random observer positions in the box, 88 mock SNe are each time drawn from the simulation, in order to match to the number of PANTHEON SNe which are observed at $0.02 < z < 0.05$ and at least 50 Mpc from the ZoA. This enables tests for the effects of sample size on the H_0 vs $\Delta\phi_{+-}$ correlation.

For each iteration, a linear fit of fractional H_0 error to $\Delta\phi_{+-}$ is taken. Figure 3.13 shows with red dashed line the mean gradient and intercept values, averaged over the 100 iterations. The intercept is allowed to vary for each iteration, but the mean intercept over iterations is set to 0 at $\Delta\phi_{+-} = 0$. The red filled region shows the standard deviation in the regression line parameters over the iterations. The 88 $0.02 < z < 0.05$ PANTHEON SNe are shown as blue points, and the blue dashed line depicts the regression line to the data seen in Figure 3.10. The observational and simulated results show excellent consistency for the slope of local fractional H_0 error with $\Delta\phi_{+-}$. Note that a 737 cosmology was also assumed when calculating fractional H_0 errors in the models. However, once again, the results are not sensitive to the fiducial H_0 assumed.

The mean slope for the simulations, of $\overline{\mathcal{S}} = 0.061 \pm 0.021$, implies with 3σ confidence that the observer will find a positive trend of H_0 estimates with $\Delta\phi_{+-}$ at a random observer position in the Universe when using a SN sample of matching statistics to the PANTHEON sample. This is consistent with the observation slope of $\overline{\mathcal{S}} = 0.065$.

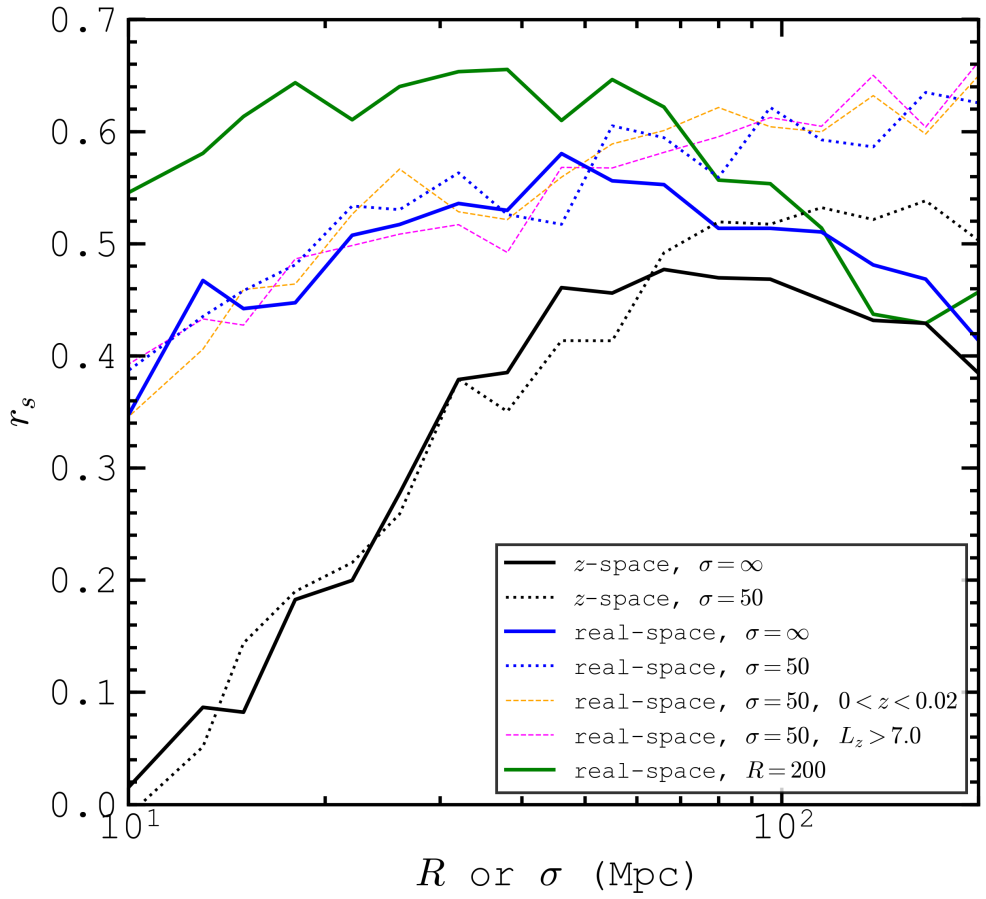

FIGURE 3.12: Spearman rank correlation coefficients, r_s, corresponding to linear fits of fractional H_0 error to $\Delta\phi_{+-}$ for mock SNe positions in the $z = 0$ snapshot of the MDPL2-GALACTICUS simulation, as a function of the density smoothing parameters R and σ, in Mpc (used to calculate $\Delta\phi_{+-}$). r_s is shown as a function of R with the exception of the green solid line, where r_s is shown as a function of σ. Unless stated, SNe are drawn from the simulation at redshifts $0.02 < z < 0.05$ and the galaxy sample is luminosity limited at $L_z > 8.843$ (see text for details).

Although separate from the analysis of fractional H_0 offset due to peculiar velocity, note that the mean intercept in the simulations is found to be $\bar{c} = 69.99$ km s^{-1} Mpc, with a root mean square (rms) deviation from the fiducial $H_0 = 70$ km s^{-1} Mpc^{-1} of 0.26 km s^{-1} Mpc^{-1}, showing that a regression fit reproduces the fiducial H_0 at $\Delta\phi_{+-} = 0$, and hence, when there is zero peculiar velocity. The rms error from the model is an estimate of the cosmic variance in the trend of H_0 estimates with $\Delta\phi_{+-}$. The mean values of r_s and p are 0.4010 and 0.0006, respectively.

In the simulations one is free from uncertainties from SN photometry and from light-curve fitting techniques, which result in the larger spread in observational fractional H_0 errors compared with results from the model. This highlights the fact that uncertainty in the SN photometry is what limits the significance of the observed correlation to $r_s = 0.2739$, rather than the ability of $\Delta\phi_{+-}$ to capture peculiar velocity information.

Recalling that the mock sample used for these calculations is luminosity limited, tests are repeated for the trend of fractional H_0 error vs $\Delta\phi_{+-}$, but with a flux-limit and corresponding galaxy weighting procedure employed, as seen in Section 3.5, to test for the effects of galaxy weighting on observational correlations. The mock flux limit is chosen to be at a magnitude of $m_z = 15.89$, such that the galaxy sample starts to become incomplete at a redshift $z = 0.0202$, as found for the observations. No significant change is found to the slope of fractional H_0 error vs $\Delta\phi_{+-}$ when using a mock flux limit, nor does the cosmic variance on the intercept increase. This implies that the weighting of galaxy statistics as a function of redshift, required for observational density calculations, has a negligible effect on the magnitude and uncertainty of H_0 estimate corrections.

Reverting to the luminosity-limited sample, $\Delta\phi_{+-}$ vs fractional H_0 error for 2000 simulated SNe is also shown in Figure 3.13, as the red points. Here, the observer's position is changed for each observation. These data follow tightly the mean regression line found for the mock data using $N_{sn} = 88$. The bottom panel shows the probability distribution of the 2000 $\Delta\phi_{+-}$ values in red, showing that the mean $\Delta\phi_{+-}$ value over all observer positions is close to zero. The blue probability function shows that the distribution of $\Delta\phi_{+-}$ values from PANTHEON SNe is consistent with the model distribution, within the Poisson errors shown.

One can use a knowledge of SNIa peculiar velocities in the mock data to relate this velocity to its proxy, $\Delta\phi_{+-}$. For the 2000 randomly selected SNe, it is found that the regression line $v_{pec} = 618.5\Delta\phi_{+-}$ best approximates the relation. Using this scaling, an estimate of peculiar velocity is plotted as a secondary x-axis in the top panel of Figure 3.13. This scaling, coupled with the $\Delta\phi_{+-}$ distribution shown in the bottom panel

of Figure 3.13 implies that the 1σ deviation from zero peculiar velocity is ~ 120 km s^{-1}, i.e. 68% of SN positions are estimated to have an absolute peculiar velocity less than this value. From this scaling, the observational SN positions are estimated to have a mean absolute peculiar velocity of ~ 100 km s^{-1}, with a standard deviation of ~ 75 km s^{-1}.

In conclusion, reassuring consistency has be found for the trend of fractional H_0 error estimates vs $\Delta\phi_{+-}$ using the MDPL2-GALACTICUS simulation when compared with observational results from the PANTHEON SN sample and 2MRS galaxies. These simulations have been used to compute the expected cosmic variance in the trend of fractional H_0 error with $\Delta\phi_{+-}$, giving an indication of uncertainty on any observational H_0 estimates when corrected for density effects.

The error-weighted mean value of fractional H_0 error for the 88 PANTHEON SNe is found to be 6×10^{-4}. Given that the fractional error is defined to be zero at $\phi_{+-} = 0$, this means that in the case of this SN sample, peculiar velocities affect the mean estimate of H_0 by $< 0.1\%$. This result shows that with a large number of SNe and sufficient sky coverage, the net effect of peculiar velocities on the mean H_0 estimate from SNe is negligible.

3.7 Calibration of Type Ia Supernova Distance Moduli & An Estimate of the Hubble Constant

The main focus of this chapter has been the fractional effect on H_0 measurements from peculiar velocities. However, for completeness, an H_0 value is estimated from the $0.02 < z < 0.05$ sample of PANTHEON SNe.

To estimate H_0 with Equation 3.1, the accuracy of SN distance moduli is relied upon. To calibrate the distance moduli, the $z = 0.57$ angular diameter distance (D_A) result of Anderson et al. (2014) is relied upon. This was derived from detections of baryon acoustic oscillations (BAO) in the clustering of galaxies. D_A can be represented as 1421 ± 20 Mpc $(r_d/r_{d,fid})$ where $r_{d,fid} = 149.28$ Mpc is the fiducial sound horizon scale used by Anderson et al. (2014). This can be converted to an equivalent distance modulus using $D_L = D_A(1+z)^2$, leading to $\mu = (42.72 \pm 0.03) + 5\log(r_d/r_{d,fid})$ mag.

A higher redshift portion of the PANTHEON sample is next turned to, in order to have a sample covering the redshift of the BAO result. To avoid an assumption for $M_{B,fid}$ (the fiducial stretch and colour corrected SNIa absolute magnitude) which is degenerate with H_0, a linear fit of the corrected apparent magnitude $(\mu_B + M_{B,fid})$ against the

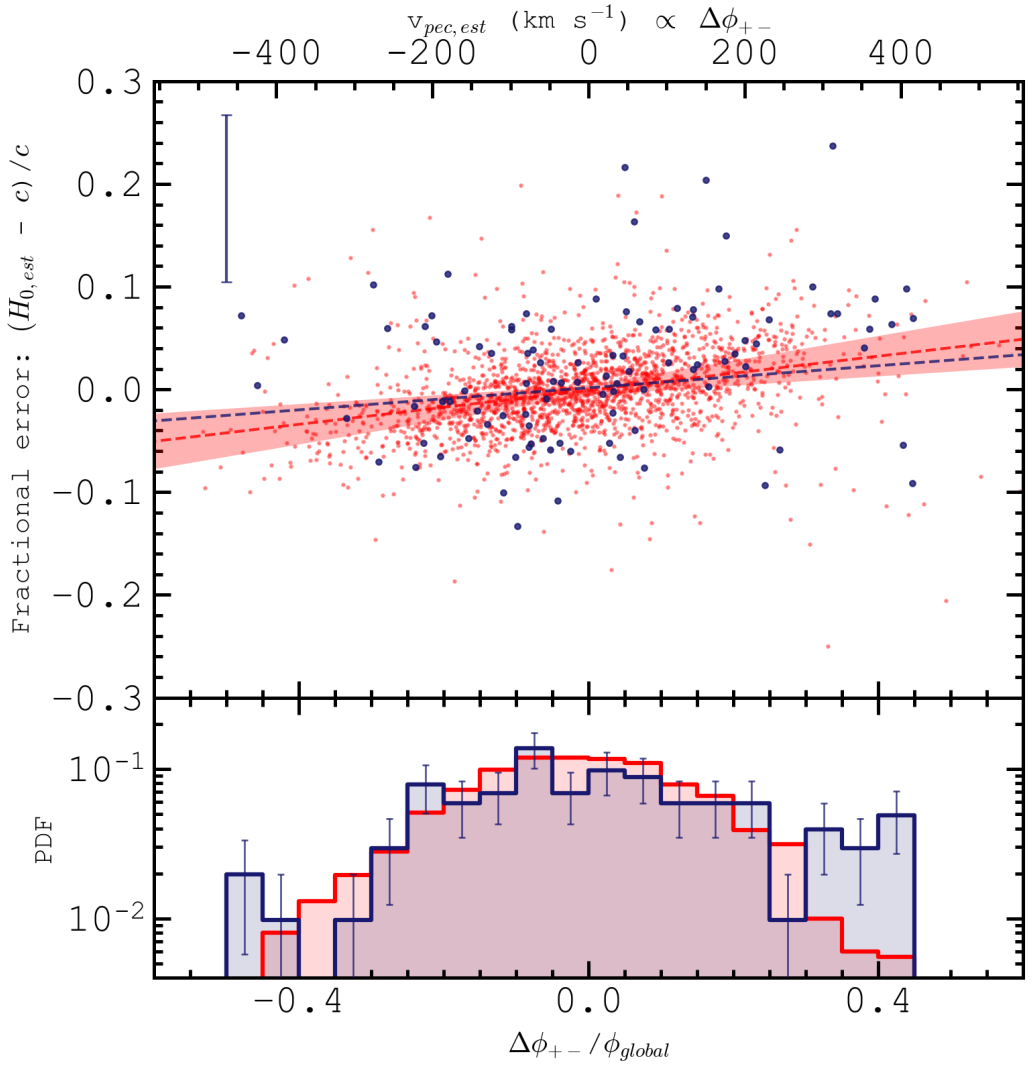

FIGURE 3.13: Top: fractional H_0 errors for $0.02 < z < 0.05$ SNe as a function of $\Delta\phi_{+-}$, using $[\sigma,R]$=[50 Mpc, 50 Mpc] (see text & Figure 3.10). Blue points show 88 observed PANTHEON SNe, where the median uncertainty on fractional H_0 error is shown as the blue error bar at the top-left of the panel. Red points represent 2000 mock SNe from the MDPL2-GALACTICUS model, each viewed from a random observer position. The blue dashed line shows the error-weighted line of best fit to the observational data. The red dashed line and filled region depict the mean and standard deviation in the best-fit line, respectively, to the mock data when matching the observational sample size of $N_{sn} = 88$, averaged over 100 Monte Carlo iterations and observer positions. The secondary x-axis (top) shows estimates of v_{pec} as a function of $(\Delta\phi_{+-})$, inferred from the gradient of the linear fit of v_{pec} to $\Delta\phi_{+-}$ in the mock data. Bottom: Probability distributions of $\Delta\phi_{+-}$ for 2000 simulated SNe (red) and 88 PANTHEON SNe (blue). Poisson errors on the observed result are shown as blue error bars.

logarithm of CMB-frame redshift is performed, for 118 SNe in the redshift range $0.45 < z < 0.70$. The offset to $\mu_B + M_{B,fid}$ required for this fit to intercept the BAO-derived distance modulus at $z = 0.57$ is then determined. It is found that that $\mu_B + M_{B,fid} + 19.45 \pm 0.04 + 5\log(r_d/r_{d,fid})$ coincides with the BAO result, and so correct the lower redshift SN distance moduli accordingly. This calibrates the SNe distance moduli using the BAO scale with negligible dependence on cosmology or peculiar velocities since the $z = 0.57$ BAO result is interpolated using only data from $0.45 < z < 0.70$.

Returning to the now calibrated $0.02 < z < 0.05$ sub-sample, from Equation 3.1, the set of H_0 estimates uncorrected for peculiar velocities can be found. The error-weighted mean value of H_0 before peculiar velocity correction is $H_0 = (67.47 \pm 1.00) \times (r_{d,fid}/r_d)$ km s^{-1} Mpc^{-1}.

In Section 3.6.1 the observational slope, $\mathcal{S}$, of fractional H_0 error vs $\Delta\phi_{+-}$ was estimated, and in Section 3.6.2, so too was the uncertainty in this result due to cosmic variance, given SN sample size. Converting $\mathcal{S}$ to units of km s^{-1} Mpc^{-1}, one can calculate individual peculiar-velocity corrected values as $H_{0,corr} = H_0 - \mathcal{S}\Delta\phi_{+-}$. The error-weighted mean H_0 measurement over the SN sample is the best estimate for the present-day value of the Hubble parameter.

A 10^4 iteration MC technique is utilised to compute the best-estimate and its uncertainty. The density-corrected SN H_0 measurements are varied for each iteration given uncertainties in the slope, $\mathcal{S}$, estimated from the simulations. Uncertainties in the SN photometry and in the re-calibration of SN distance moduli to the BAO-inferred distance scale are also folded in to the final errors. The error-weighted mean of the 88 individual H_0 estimates is calculated for each iteration. The best estimate of H_0 in this chapter is then given by the mean and standard deviation of this average over the iterations.

It is inferred that $H_0 = (67.41 \pm 1.02) \times (r_{d,fid}/r_d)$ km s^{-1} Mpc^{-1}, as shown by the solid blue range in Figure 3.14. This result is consistent with that obtained by Planck Collaboration et al. (2018), who find $H_0 = 67.40 \pm 0.50$ km s^{-1} Mpc^{-1}. Conversely, the result of the present chapter lies in 3.8 σ tension with the result of Riess et al. (2019), who find $H_0 = 74.03 \pm 1.42$ km s^{-1} Mpc^{-1}, using LMC Cepheid standards to calibrate the distance scale and constrain distance moduli of SNeIa residing in Cepheid hosts. It is concluded that the PANTHEON SN sample is large enough and surveys a large enough volume that the sign of peculiar velocities is unbiased, and therefore that accounting for estimated peculiar velocities of PANTHEON SNe does not resolve the Hubble tension.

The corrected H_0 distribution for the individual SNe is also shown, as the filled histogram. It is once again clear from comparison with the uncorrected distribution that the net effect of peculiar velocities on the average H_0 estimate is small when averaged over a large number of SNe at different sky positions, with a negligible reduction to the mean H_0 value of only 0.06 $\times$ $(r_{d,fid}/r_d)$ mag via this correction.

The component of the error in the H_0 estimate due to peculiar velocity corrections has a magnitude of 0.26 $\times$ $(r_{d,fid}/r_d)$ km s^{-1} Mpc^{-1} when accounting for the model-estimated cosmic variance in the slope of H_0 vs $\Delta\phi_{+-}$. The vast majority of this error is found to stem from noise in the v_{pec} vs $\Delta\phi_{+-}$ relation, which introduces error in the H_0 estimate vs $\Delta\phi_{+-}$ relation. Variations in the H_0 distribution over observer positions are found to have a relatively negligible contribution to the error.

The resultant error in the best H_0 estimate using PANTHEON SNe is the quadrature sum of: i) an error of 0.95 $\times$ $(r_{d,fid}/r_d)$ km s^{-1} Mpc^{-1} from BAO-based calibrations of SN distance moduli; ii) an error of 0.33 $\times$ $(r_{d,fid}/r_d)$ km s^{-1} Mpc^{-1} from SN photometric uncertainties; and iii) an error of 0.26 $\times$ $(r_{d,fid}/r_d)$ km s^{-1} Mpc^{-1} from corrections of the H_0 estimates for peculiar velocity effects. Thus, for comparable SN samples and for future samples with larger statistics and coverage, density effects are not expected to be the main cause of the Hubble tension. Instead, the majority of the uncertainty on the local H_0 estimate stems from uncertainties in the calibration of SNIa photometry.

All the results discussed have adopted $[q_0,\ \Omega_m,\ \Omega_\Lambda] = [-0.55,\ 0.7,\ 0.3]$. For comparison, using instead $[q_0,\ \Omega_m,\ \Omega_\Lambda] = [0,\ 0.67,\ 0.33]$ causes a 0.68 $\times$ $(r_{d,fid}/r_d)$ km s^{-1} Mpc^{-1} drop in the present best-estimate of H_0 to 66.73 km s^{-1} Mpc^{-1}. Adopting $[q_0,\ \Omega_m,\ \Omega_\Lambda] = [-0.7,\ 0.2,\ 0.8]$ causes a 0.42 $\times$ $(r_{d,fid}/r_d)$ km s^{-1} Mpc^{-1} rise, giving $H_0 = 67.83 \times (r_{d,fid}/r_d)$ km s^{-1} Mpc^{-1}. These results are shown as the blue dotted and dashed ranges in the top panel of Figure 3.14, respectively, and demonstrate that errors from SN distance calibration dominate the error budget as opposed to errors associated with the fiducial cosmology at these low redshifts.

It is also emphasised that even though the SNe are calibrated on the inverse distance ladder, the same relative effects on the result due to peculiar velocities would be evident were the SNe calibrated on the local distance ladder.

Figure 3.14 shows, in black, some notable H_0 estimates since the millennium which have not yet been discussed in this chapter. The HUBBLE SPACE TELESCOPE (HST) KEY PROJECT established an early estimate of H_0 at 72 ± 8 km s^{-1} Mpc^{-1}, from Type Ia supernovae standard candles calibrated with a Cepheid distance to NGC 4258

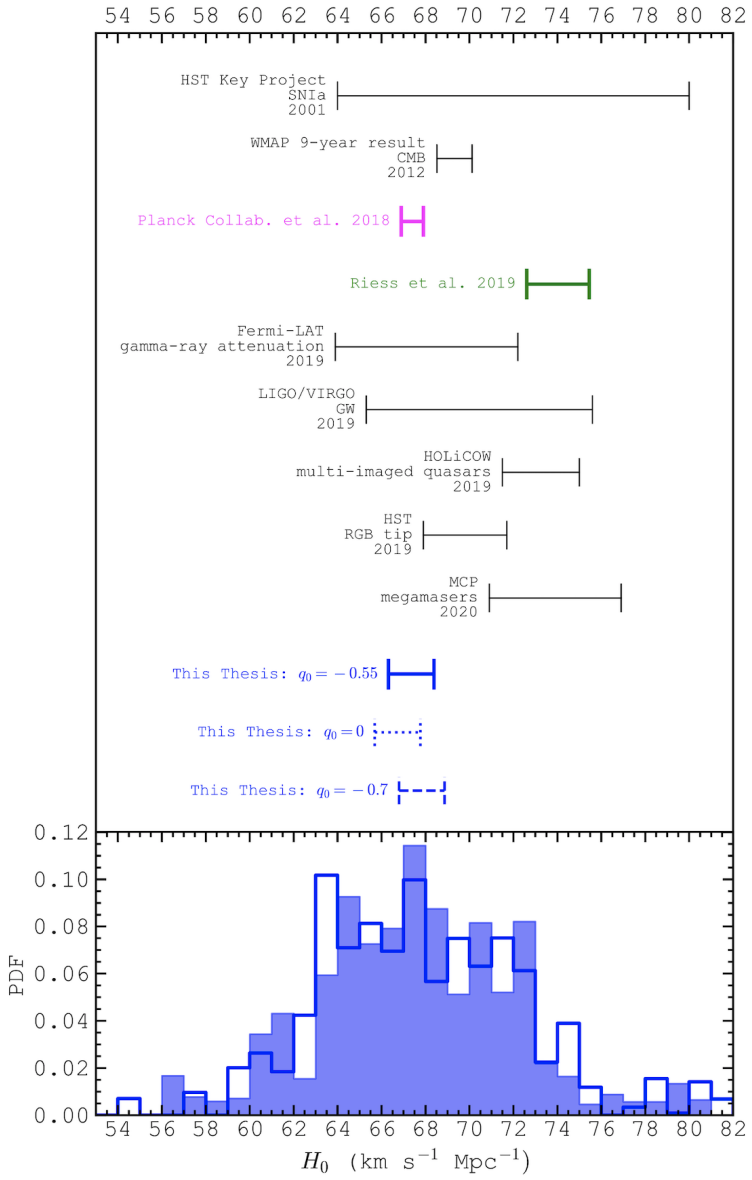

FIGURE 3.14: Top: a comparison of H_0 estimates. In blue: the results of the present chapter derived from SNe with distance moduli calibrated on the BAO-inferred cosmic distance scale (see text), and corrected for peculiar velocity effects. The blue solid range indicates the 1σ uncertainty on the best H_0 estimate from 88 PANTHEON SNe, where errors account for uncertainties in SN photometry, in SN distance calibration, and in the cosmic variance of peculiar velocity effects. This result assumes $q_0 = -0.55$. For comparison, the dotted and dashed ranges depict the change to this result, assuming instead $q_0 = 0$ and $q_0 = -0.7$, respectively. In green: the Riess et al. (2019) H_0 measurement from a combination of LMC DEBs, masers in NGC 4258 and Milky Way parallaxes. In pink: the Planck Collaboration et al. (2018) result from the CMB and Λ-CDM. Bottom: the unfilled (filled) histogram represents the error-weighted probability density function (PDF) of individual H_0 estimates from the SNe using Equation 3.1, before (after) corrections for the effects of peculiar velocities. In black: other notable H_0 results since the millennium. The research team, H_0 indicator and year of publication are listed for each result (see text for references).

(Freedman et al., 2001). The WILKINSON MICROWAVE ANISOTROPY PROBE MISSION (WMAP) presented a map of anisotropies in the cosmic microwave background in Bennett et al. (2013) which lead to a result of $H_0 = 69.32 \pm 0.80$ km s^{-1} Mpc^{-1}.

Although measurements of H_0 from the CMB and Type Ia SNe are the most common avenues to date, there have emerged, in recent years, independent probes of the Hubble constant. The fact that accounting for the effects of peculiar velocities does not bring local H_0 estimates in line with sound horizon-based measurements serves to demonstrate that the solution may lie with alternative probes.

The FERMI-LAT group presented an estimate of $H_0 = 68.0^{+4.2}_{-4.1}$ km s^{-1} Mpc^{-1} from gamma-ray attenuation due to extragalactic light (Domínguez et al., 2019). Later that same year, the team behind the LIGO/VIRGO detectors released a measurement of $H_0 = 70.3^{+5.3}_{-5.0}$ km s^{-1} Mpc^{-1}, based on the superluminal motion of the radio jet associated with the gravitational wave (GW) source GW170817, coupled with electromagnetic and GW information from previous similar events (Hotokezaka et al., 2019).

Other recent novel measurements of H_0 include a multi-imaged quasar result from the HOLiCOW collaboration (Wong et al., 2020), who find $H_0 = 73.3^{+1.7}_{-1.8}$ km s^{-1} Mpc^{-1}, an HST result based on distances to red giant stars from the tip of the red giant branch (Freedman et al., 2019), coming to $H_0 = 69.8 \pm 1.9$ km s^{-1} Mpc^{-1}, and a result from the MEGAMASER COSMOLOGY PROJECT, based on geometric distance measurements to megamaser-hosting galaxies from Pesce et al. (2020), at $H_0 = 73.9 \pm 3.0$ km s^{-1} Mpc^{-1}. Each of the aforementioned results are also shown in Figure 3.14 for a comparison with the results of this thesis.

The errors on the above-mentioned results from alternative methods are not yet constrained enough to solve the ongoing problem of the Hubble tension. The next decade will likely see a focus on reducing the errors from such indicators, in order to put the H_0 debate to rest, and allow a definitive constraining of our Universe's cosmology.

3.8 Summary

Using the $K < 11.75$ flux-limited 2MASS REDSHIFT SURVEY (2MRS) of galaxies (Huchra et al., 2012), and assuming that the K-band luminosity distribution is well-approximated by a Schechter function, the STY maximum-likelihood method (Sandage et al., 1979) is used to infer a best-fit Schechter function to the data with parameters [α, L^*] = [–0.99, 10.97], fitting the data well as a function of redshift when accounting for galaxy luminosity evolution effects. This yields $L_K > 10.5$ sample completeness as a function of

redshift, allowing a reconstruction of the galaxy density field. Whilst region-specific density structure which is qualitatively consistent with the findings of Whitbourn & Shanks (2014) and Böhringer et al. (2019) is found, no strong evidence for a 'Local Void' which pertains to the whole sky is found, out to the $z = 0.1$ redshift limit of the 2MRS galaxy survey, in agreement with Carrick et al. (2015).

This chapter has introduced a density parameter, denoted here as $\Delta\phi_{+-}$, which quantifies density gradients along a LOS. $\Delta\phi_{+-}$ is a proxy for peculiar velocities as a function of location in the local Universe. Using a sample of 88 SNeIa from the PANTHEON sample (Scolnic et al., 2018), in a redshift range $0.02 < z < 0.05$, the clear effects of the density field on H_0 estimates are seen, from trends of fractional H_0 error vs $\Delta\phi_{+-}$. it is found from this empirical method that density gradients on the scale of super-clusters (~ 50 Mpc) have the strongest effects on local fractional H_0 errors.

The present-day snapshot from the MDPL2-GALACTICUS simulation (Knebe et al., 2018) is used to repeat analyses with a mock galaxy density field and SN sample, which is free from photometric uncertainties, and find remarkably consistent results with the observations for the trend of fractional H_0 errors with $\Delta\phi_{+-}$. Maximum coherence between fractional H_0 error and $\Delta\phi_{+-}$ is again found for density structure on the scale of super-clusters (~ 50 Mpc), coincident with expectations from the behaviour of the correlation function of galaxies (see, e.g. Clutton-Brock & Peebles, 1981), increasing confidence that these strong correlations are in fact due to real gravitational effects.

It is found that the $0.02 < z < 0.05$ PANTHEON sample has enough SN statistics and survey volume that the mean peculiar velocity of these SNe lies close to zero. As a consequence, the average offset in H_0 estimates due to galaxy density effects is also close to zero. The simulations are used to estimate the cosmic variance in the peculiar velocity distribution when matching to the sample size and sky coverage of the observations, finding that the mean peculiar velocity for such a sky coverage and sample size lies close to zero over practically all observer positions. However, should one wish to estimate H_0 using local SN surveys which are not all sky, it is noted that these methods would be able to correct for the effects of the density field on H_0 estimates, irrespective of peculiar velocity biases.

3.8.1 List of Assumptions

- An $h = 0.7$, $\Omega_m = 0.3$, $\Omega_\Lambda = 0.7$ cosmology is accurate.
- The Virgo Cluster is at a distance of 16.5 Mpc.

- The galaxy luminosity distribution is well-described by a single-Schechter function.
- The luminosity function parameter L^* varies linearly with redshift, at least between $0 < z < 0.1$.

Chapter 4

Summary & Conclusions

In Chapter 1, it was described that for all the successes of the Λ-CDM model, there are three outstanding problems which have yet to be solved. These three problems were as follows:

1. **The Sub-Structure Problem:** Is the observed surplus of low-mass / dwarf galaxies relative to the number predicted by simulations invoking Λ-CDM genuine ?

2. **The Star Formation Rates of Elliptical Galaxies**: At present epochs, are ellipticals truly quiescent, given that Λ-CDM predicts a low-level of star formation maintained by mergers?

3. **The Hubble Tension:** What is the cause of the persistent discrepancy between local ($z \lesssim 0.1$) estimates of the Hubble Constant (or the current rate of expansion of the Universe) and predictions from sound-horizon physics?

It was explained that in this thesis, these potential problems would be probed in a novel manner: using supernovae as statistical tools.

Chapter 2.1 focused on Problem **1**. A method was presented for producing a galaxy sample unbiased by surface brightness and stellar mass, by selecting star-forming galaxies via the positions of core-collapse supernovae (CCSNe). Whilst matching ∼2400 supernovae from the SDSS-II SUPERNOVA SURVEY to their host galaxies using IAC STRIPE 82 LEGACY coadded imaging, ∼150 previously unidentified low surface brightness galaxies (LSBGs) were discovered.

Using a sub-sample of ∼900 CCSNe, CCSN-rate and star-formation rate densities as a function of galaxy stellar mass, and the star-forming galaxy stellar mass function were inferred. Resultant star-forming galaxy number densities were found to increase following a power-law down to a low mass limit of $\sim 10^{6.2}$ $M_{\odot}$, and as a single Schechter function with a faint-end slope of $\alpha = -1.41$.

Furthermore, no deviation from the high-mass version of the surface brightness – mass relation was found in the dwarf mass regime. These findings implied a lack of truncation to galaxy formation processes at least down to $\sim 10^{6.2}$ $M_{\odot}$. Both of these results are consistent with the predictions of Λ-CDM when invoked in hydrodynamical simulations of galaxy evolution.

In short, using a CCSN-based selection of galaxies, and applying the methods of Chapter 2.1, the tension in the observed dwarf galaxy number density with the predictions of Λ-CDM is entirely alleviated. **It is therefore concluded that overcoming surface brightness and stellar mass biases in galaxy samples is the likely solution to the sub-structure problem.**

Chapter 2.2 was dedicated to Problem **2**. The reason levels of star formation in elliptical galaxies are poorly constrained is the difficulty in quantifying the contamination of flux-based estimates of star formation from unrelated phenomena, such as AGN and old stellar populations. In Chapter 2.2, core-collapse supernovae (CCSNe) were utilised, as unambiguous tracers of recent star formation in ellipticals within a cosmic volume.

A sample of 421 $z < 0.2$, $r < 21.8$ mag CCSNe from the SDSS-II SUPERNOVA SURVEY was first isolated. A Bayesian method for identifying ellipticals via their colours and morphologies was then introduced. This method identified ellipticals in a manner unbiased by redshift and yet consistent with manual classification from GALAXY ZOO 1. It was found that $\sim 25\%$ of $z < 0.2$ $r < 20$ mag galaxies in the STRIPE 82 region are ellipticals (~ 28000 galaxies).

In total, 36 CCSNe were found to reside in ellipticals. It was demonstrated that such early-types contribute a non-negligible fraction of star formation to the present-day cosmic budget, at 11.2 ± 3.1 (stat) $^{+3.0}_{-4.2}$ (sys) %. Coupling this result with the galaxy stellar mass function of ellipticals, the mean specific star formation rate (SSFR; $\overline{\mathcal{S}}$) of these systems was derived. The best-fit slope was given by $\log(\overline{\mathcal{S}}(\mathcal{M})/\mathrm{yr}) = -(0.80 \pm 0.59)\ \log(\mathcal{M}/10^{10.5}\mathrm{M}_{\odot}) - 10.83 \pm 0.18$.

The mean SSFR for all $\log(\mathcal{M}/\mathrm{M}_{\odot}) > 10.0$ ellipticals was found to be $\overline{\mathcal{S}} = 9.2 \pm 2.4$ (stat) $^{+2.7}_{-2.3}$ (sys) $\times 10^{-12}$ yr^{-1}, which is consistent with recent estimates via SED-fitting,

and is 11.8 ± 3.7 (stat) $^{+3.5}_{-2.9}$ (sys) % of the mean SSFR level on the main sequence, as also derived from CCSNe.

It was also found that the median optical spectrum of elliptical CCSN hosts is statistically consistent with that of a control sample of ellipticals that do not host CCSNe, implying that these SN-derived results are well-representative of the total low-z elliptical population. **It can therefore be concluded that elliptical galaxies are not entirely quiescent. Instead, they possess a low, yet non-negligible level of star formation, which may be maintained by minor mergers through cosmic time as is predicted by hydrodynamical simulations invoking Λ-CDM.** As such, a solution to Problem **2** has been reached.

Finally, Problem **3** was of focus in Chapter 3. Peculiar velocities (v_{pec}) of standard candle distance indicators are known to systematically affect local H_0 measurements. In Chapter 3, 2MRS galaxies were first used to measure the local galaxy density field. A notable $z < 0.05$ underdensity was found in the SGC-6DFGS region of 27 ± 2 %. However, no strong evidence for a 'Local Void' pertaining to the full 2MRS sky coverage was found.

Galaxy densities were used to measure a novel density parameter, $\Delta\phi_{+-}$, which was introduced as a proxy for v_{pec} which quantifies density gradients along a SN line-of-sight. $\Delta\phi_{+-}$ was found to correlate with local H_0 estimates from 88 PANTHEON Type Ia SNe ($0.02 < z < 0.05$). Density structures on scales of ~ 50 Mpc were found to correlate strongest with H_0 estimates in both the observational data and in mock data from the MDPL2-GALACTICUS simulation.

Using trends of H_0 with $\Delta\phi_{+-}$, it was made possible to correct for the effects of density structure on local H_0 estimates, even in the presence of biased v_{pec}. However, what was found was that the difference in the inferred H_0 estimate with and without the peculiar velocity correction is limited to < 0.1 %. **It is definitively concluded that accounting for environmentally-induced peculiar velocities of SNIa host galaxies does not resolve the tension between local and CMB-derived H_0 estimates.**

4.1 Future Work

The lower detection limits to galaxy stellar mass for the SN method outlined in Chapter 2.1 depend on the area, surface brightness depth and the observing time-span of

the SN survey. Future high-cadence surveys with improvements to each of these three survey properties will greatly increase the size of CCSN-selected galaxy samples and lead to the detection of vast numbers of dwarf galaxies: Using expectations for these parameters with LSST (Ivezić et al., 2019), and comparing with the specifications and CCSN yield of the SDSS-II SUPERNOVA SURVEY (Sako et al., 2018b), LSST may be expected to identify ~ 25 times more CCSNe in a year for a 5000 deg^2 coverage in rolling cadence regions.

The results of Chapter 2.1 suggest that a similar study with LSST would yield ~ 500 $z < 0.2$ CCSNe yr^{-1} in star-forming galaxies with masses of $\log(\mathcal{M}/\mathrm{M}_{\odot}) < 7.0$, statistics which would undoubtedly give important insights into dwarf galaxy evolution. The co-adding of images is crucial for low-surface brightness host identification. Based on expected exposure times per visit, it is estimated that only 25 LSST images per SN region will be required to match the depth of IAC STRIPE 82 LEGACY imaging. Further co-added imaging will bolster prospects for LSBG detection, help form a more detailed assessment of the functional form of $\mathcal{R}$, ϵ and $\mathcal{S}$, and ultimately help to probe the form of the GSMF to ever lower masses, giving crucial insights into galaxy formation and evolution processes deep into the dwarf regime.

Note that the results of Chapter 2.2 only pertain to massive red ellipticals. This is because CCSNe were only likely to occur in massive red ellipticals given the time-frame of the SDSS-II SUPERNOVA SURVEY, and so Chapter 2.2 cannot reveal information on the star formation properties of lower mass, environmentally quenched galaxies. These may indeed have zero levels of star formation. A relevant investigation may become possible with access to future surveys. Again, LSST data may provide the required capabilities. This survey will greatly increase the size of CCSN-selected galaxy samples, and would also allow for more precise measurements of the SFRD and SSFR in massive ellipticals. A study such as this with LSST may offer up enough CCSN statistics to allow volume-averaged star formation properties to be estimated as a function of redshift, which would shed light on the average star formation history of ellipticals.

It was also seen in Chapter 2.2 that the classification all $z < 0.2$, $r < 20$ mag STRIPE 82 ellipticals was possible using a newly introduced Bayesian method, trained on the colour and morphology properties of manually-classified samples of ellipticals and non-ellipticals from GALAXY ZOO 1. Such a concept could certainly be extended to classify other galaxy types, including spiral, lenticular, and irregular galaxies, efficiently over large surveys. In doing so, the connections between Hubble Type and galaxy evolution could be probed with never-before-seen statistical vigour.

In terms of the methods of Chapter 3, analyses of biases in fractional H_0 error estimates can be built upon with various improvements to assessments of the galaxy density field. These improvements could include: a replacement of 2MRS with 2M++ galaxies (Lavaux & Hudson, 2011); an assessment of the density structure within the 'Zone of Avoidance' (Hubble, 1934); and increased magnitude-depth of all-sky near-IR galaxy surveys from, for example, the UKIRT HEMISPHERE SURVEY (Dye et al., 2018), VISTA HEMISPHERE SURVEY (Sutherland et al., 2015) and, once again, LSST (Ivezić et al., 2019).

Assessments of galaxy cluster densities from deep X-ray surveys such as eROSITA (Merloni et al., 2012) also promise to put state-of-the-art constraints on the local density structure. With the ability to probe the density field over a larger redshift range one can also examine evidence for voids out to cosmological distances for tens of thousands of galaxies or clusters, as well as the relationship of any structure with standard-candle H_0 estimates such as those from supernovae. Note that as advances in photometric precision and distance calibration techniques arrive, studies of the effects of the density field and resultant peculiar velocities will become increasingly important for local measurements of the Hubble constant.

In the coming years, we will also likely need to turn to alternative probes of the Hubble Constant which are independent of both the local distance ladder and the sound-horizon scale inverse distance ladder, in order to reach a conclusion for the true value of H_0. For instance, Chen et al. (2018) predict we could reach a 2 % measurement from GW 'standard sirens' within as little as 2 years, given the progress being made with the detection of GW coalescence events. With such a list of studies on the horizon, we could soon be facing the next major turning point in our understanding of galaxy evolution and cosmology.

Bibliography

Agrawal P., Cyr-Racine F.-Y., Pinner D., Randall L., 2019, arXiv e-prints, p. arXiv:1904.01016

Anderson L., et al., 2014, MNRAS, 441, 24

Baade W., 1943, ApJ, 97, 119

Baade W., Zwicky F., 1934, Proceedings of the National Academy of Science, 20, 254

Baldry I. K., 2018, arXiv:1812.05135,

Baldry I. K., Glazebrook K., Brinkmann J., Ivezić Ž., Lupton R. H., Nichol R. C., Szalay A. S., 2004, ApJ, 600, 681

Baldry I. K., et al., 2005, MNRAS, 358, 441

Baldry I. K., Glazebrook K., Driver S. P., 2008, MNRAS, 388, 945

Baldry I. K., et al., 2012, MNRAS, 421, 621

Baldry I. K., et al., 2018, MNRAS, 474, 3875

Baldwin J. A., Phillips M. M., Terlevich R., 1981, PASP, 93, 5

Beare R., Brown M. J. I., Pimbblet K., Taylor E. N., 2019, ApJ, 873, 78

Beck R., Dobos L., Budavári T., Szalay A. S., Csabai I., 2016, MNRAS, 460, 1371

Bell E. F., McIntosh D. H., Katz N., Weinberg M. D., 2003, ApJS, 149, 289

Bell E. F., Zheng X. Z., Papovich C., Borch A., Wolf C., Meisenheimer K., 2007, ApJ, 663, 834

Bennett C. L., et al., 2013, ApJS, 208, 20

Benson A. J., 2010, Phys. Rep., 495, 33

Benson A. J., 2012, , 17, 175

Bernstein G. M., Jarvis M., 2002, AJ, 123, 583

Bersten M. C., Benvenuto O., Hamuy M., 2011, ApJ, 729, 61

Bertin E., Arnouts S., 1996a, A&AS, 117, 393

Bertin E., Arnouts S., 1996b, A&AS, 117, 393

Bode P., Ostriker J. P., Turok N., 2001, ApJ, 556, 93

Böhringer H., Chon G., Bristow M., Collins C. A., 2015, A&A, 574, A26

Böhringer H., Chon G., Collins C. A., 2019, arXiv e-prints, p. arXiv:1907.12402

Bolton A. S., et al., 2012, AJ, 144, 144

Boquien M., Burgarella D., Roehlly Y., Buat V., Ciesla L., Corre D., Inoue A. K., Salas H., 2019, A&A, 622, A103

Borexino Collaboration Agostini M., et al., 2020, Nature, 587, 577

Botticella M. T., et al., 2008, A&A, 479, 49

Botticella M. T., Smartt S. J., Kennicutt R. C., Cappellaro E., Sereno M., Lee J. C., 2012, A&A, 537, A132

Botticella M. T., et al., 2016, in Napolitano N. R., Longo G., Marconi M., Paolillo M., Iodice E., eds, Vol. 42, The Universe of Digital Sky Surveys. p. 197, doi:10.1007/978-3-319-19330-4_31

Botticella M. T., et al., 2017, A&A, 598, A50

Bouwens R. J., et al., 2009, ApJ, 705, 936

Bower R. G., Lucey J. R., Ellis R. S., 1992a, MNRAS, 254, 589

Bower R. G., Lucey J. R., Ellis R. S., 1992b, MNRAS, 254, 601

Boyle W. S., Smith G. E., 1970, Bell System Technical Journal, 49, 587

Bressan A. G., Chiosi C., Bertelli G., 1981, A&A, 102, 25

Bruzual G., Charlot S., 2003, MNRAS, 344, 1000

Bryant J. J., et al., 2015, MNRAS, 447, 2857

Busswell G. S., Shanks T., Frith W. J., Outram P. J., Metcalfe N., Fong R., 2004, MNRAS, 354, 991

Butsky I. S., Fielding D. B., Hayward C. C., Hummels C. B., Quinn T. R., Werk J. K., 2020, ApJ, 903, 77

Calzetti D., Armus L., Bohlin R. C., Kinney A. L., Koornneef J., Storchi-Bergmann T., 2000, ApJ, 533, 682

Cappellari M., 2017, MNRAS, 466, 798

Cappellaro E., Evans R., Turatto M., 1999, A&A, 351, 459

Carrick J., Turnbull S. J., Lavaux G., Hudson M. J., 2015, MNRAS, 450, 317

Chabrier G., 2003, PASP, 115, 763

Chen H.-W., Helsby J. E., Gauthier J.-R., Shectman S. A., Thompson I. B., Tinker J. L., 2010, ApJ, 714, 1521

Chen H.-Y., Fishbach M., Holz D. E., 2018, Nature, 562, 545

Chilingarian I. V., Melchior A.-L., Zolotukhin I. Y., 2010, MNRAS, 405, 1409

Chiosi C., Carraro G., 2002, MNRAS, 335, 335

Clocchiatti A., Wheeler J. C., 1997, in Ruiz-Lapuente P., Canal R., Isern J., eds, NATO Advanced Study Institute (ASI) Series C Vol. 486, Thermonuclear Supernovae. p. 863 (arXiv:astro-ph/9601023), doi:10.1007/978-94-011-5710-0_53

Clutton-Brock M., Peebles P. J. E., 1981, AJ, 86, 1115

Cohen M., Wheaton W. A., Megeath S. T., 2003, AJ, 126, 1090

Cole S., Lacey C. G., Baugh C. M., Frenk C. S., 2000, MNRAS, 319, 168

Cole S., et al., 2001, MNRAS, 326, 255

Collins George W. I., Claspy W. P., Martin J. C., 1999, PASP, 111, 871

Conley A., Carlberg R. G., Guy J., Howell D. A., Jha S., Riess A. G., Sullivan M., 2007, ApJl, 664, L13

Conroy C., Bullock J. S., 2015, ApJl, 805, L2

Crain R. A., et al., 2015, MNRAS, 450, 1937

Cross N., Driver S. P., 2002, MNRAS, 329, 579

Csabai I., Dobos L., Trencséni M., Herczegh G., Józsa P., Purger N., Budavári T., Szalay A. S., 2007, , 328, 852

Dahlen T., et al., 2004, ApJ, 613, 189

Davies L. J. M., et al., 2016, MNRAS, 461, 458

Dawson K. S., et al., 2013, AJ, 145, 10

Dawson K. S., et al., 2016, AJ, 151, 44

De Vaucouleurs G., Corwin H. G. J., 1985, ApJ, 295, 287

Di Valentino E., Linder E. V., Melchiorri A. r., 2018, Phys. Rev. D, 97, 043528

Doggett J. B., Branch D., 1985, AJ, 90, 2303

Domínguez A., et al., 2019, ApJ, 885, 137

Driver S. P., Robotham A. S. G., 2010, MNRAS, 407, 2131

Driver S. P., et al., 2011, MNRAS, 413, 971

Drory N., et al., 2009, ApJ, 707, 1595

Dubois Y., Peirani S., Pichon C., Devriendt J., Gavazzi R., Welker C., Volonteri M., 2016, MNRAS, 463, 3948

Dubois Y., et al., 2020, arXiv e-prints, p. arXiv:2009.10578

Dye S., et al., 2018, MNRAS, 473, 5113

Eggen O. J., Lynden-Bell D., Sandage A. R., 1962, ApJ, 136, 748

Eggenberger P., Meynet G., Maeder A., Hirschi R., Charbonnel C., Talon S., Ekström S., 2008, Ap&SS, 316, 43

Einstein A., 1916, Annalen der Physik, 354, 769

Emsellem E., et al., 2019, A&A, 625, A76

Enqvist K., Mattsson T., 2007, , 2007, 019

Erb D. K., Steidel C. C., Shapley A. E., Pettini M., Reddy N. A., Adelberger K. L., 2006, ApJ, 647, 128

Fewell M. P., 1995, American Journal of Physics, 63, 653

Filippenko A. V., 1997, ARA&A, 35, 309

Fixsen D. J., 2009, ApJ, 707, 916

Fliri J., Trujillo I., 2016, MNRAS, 456, 1359

Franceschini A., et al., 2006, A&A, 453, 397

Franx M., 1993, PASP, 105, 1058

Freedman W. L., et al., 2001, ApJ, 553, 47

Freedman W. L., et al., 2019, ApJ, 882, 34

Frieman J. A., et al., 2008, AJ, 135, 338

Frith W. J., Busswell G. S., Fong R., Metcalfe N., Shanks T., 2003, MNRAS, 345, 1049

Fryer C. L., New K. C. B., 2011, Living Reviews in Relativity, 14, 1

Gallagher J. S., Garnavich P. M., Caldwell N., Kirshner R. P., Jha S. W., Li W., Ganeshalingam M., Filippenko A. V., 2008, ApJ, 685, 752

Gallazzi A., Charlot S., Brinchmann J., White S. D. M., Tremonti C. A., 2005, MNRAS, 362, 41

Gehrels N., 1986, ApJ, 303, 336

Genel S., et al., 2014, MNRAS, 445, 175

Gilbank D. G., Baldry I. K., Balogh M. L., Glazebrook K., Bower R. G., 2010, MNRAS, 405, 2594 (G10)

Gilliland R. L., Nugent P. E., Phillips M. M., 1999, ApJ, 521, 30

Gilmozzi R., 1987, in European Southern Observatory Conference and Workshop Proceedings. p. 19

Giovanelli R., Dale D. A., Haynes M. P., Hardy E., Campusano L. E., 1999, ApJ, 525, 25

Glazebrook K., Blake C., Economou F., Lilly S., Colless M., 1999, MNRAS, 306, 843

Goodrich R. W., Stringfellow G. S., Penrod G. D., Filippenko A. V., 1989, ApJ, 342, 908

Graur O., Bianco F. B., Modjaz M., 2015a, MNRAS, 450, 905

Graur O., Bianco F. B., Modjaz M., 2015b, MNRAS, 450, 905

Greggio L., 2005, A&A, 441, 1055

Greggio L., Renzini A., 1990, ApJ, 364, 35

Grogin N. A., et al., 2011, ApJS, 197, 35

Groves B. A., Heckman T. M., Kauffmann G., 2006, MNRAS, 371, 1559

Guillochon J., Parrent J., Kelley L. Z., Margutti R., 2017, ApJ, 835, 64

Gunn J. E., et al., 2006, AJ, 131, 2332

Guy J., et al., 2007, A&A, 466, 11

Hakobyan A. A., 2008, Astrophysics, 51, 69

Hamuy M., Phillips M. M., Suntzeff N. B., Schommer R. A., Maza J., Aviles R., 1996, AJ, 112, 2391

Han Z., 1998, MNRAS, 296, 1019

Hastings C., Mosteller F., Tukey J. W., Winsor C. P., 1947, Ann. Math. Statist., 18, 413

Hayakawa T., Iwamoto N., Kajino T., Shizuma T., Umeda H., Nomoto K., 2006, ApJl, 648, L47

Heger A., Fryer C. L., Woosley S. E., Langer N., Hartmann D. H., 2003, ApJ, 591, 288

Heringer E., Pritchet C., Kezwer J., Graham M. L., Sand D., Bildfell C., 2017, ApJ, 834, 15

Heringer E., Pritchet C., van Kerkwijk M. H., 2019, ApJ, 882, 52

Hillebrandt W., Niemeyer J. C., 2000a, ARA&A, 38, 191

Hillebrandt W., Niemeyer J. C., 2000b, ARA&A, 38, 191

Hogg D. W., Finkbeiner D. P., Schlegel D. J., Gunn J. E., 2001, AJ, 122, 2129

Holwerda B. W., Keel W. C., Kenworthy M. A., Mack K. J., 2015, MNRAS, 451, 2390

Hotokezaka K., Nakar E., Gottlieb O., Nissanke S., Masuda K., Hallinan G., Mooley K. P., Deller A. T., 2019, Nature Astronomy, 3, 940

Huang J. S., Cowie L. L., Gardner J. P., Hu E. M., Songaila A., Wainscoat R. J. 1997, ApJ, 476, 12

Hubble E., 1934, ApJ, 79, 8

Huchra J. P., et al., 2012, ApJS, 199, 26

Hudson M. J., Smith R. J., Lucey J. R., Branchini E., 2004, MNRAS, 352, 61

Hummels C. B., et al., 2019, ApJ, 882, 156

Inoue A. K., Hirashita H., Kamaya H., 2000, PASJ, 52, 539

Ivanova N., et al., 2013, A&A Rev., 21, 59

Ivezić Ž., et al., 2019, ApJ, 873, 111

Jackson R. A., et al., 2021, MNRAS, 502, 4262

James P. A., Prescott M., Baldry I. K., 2008, A&A, 484, 703

Jasche J., Lavaux G., 2019, A&A, 625, A64

Jester S., et al., 2005, AJ, 130, 873

Jha S., Riess A. G., Kirshner R. P., 2007, ApJ, 659, 122

Jorgensen I., Franx M., Kjaergaard P., 1996, MNRAS, 280, 167

Jura M., 1977, ApJ, 212, 634

Kaiser N., Peacock J. A., 2016, MNRAS, 455, 4518

Kang X., Macciò A. V., Dutton A. A., 2013, ApJ, 767, 22

Karachentsev I. D., Makarov D. I., Kaisina E. I., 2013, AJ, 145, 101

Karim A., et al., 2011, ApJ, 730, 61

Kauffmann G., et al., 2003, MNRAS, 341, 33

Kaviraj S., 2014a, MNRAS, 437, L41

Kaviraj S., 2014b, MNRAS, 440, 2944

Kaviraj S., et al., 2007, ApJS, 173, 619

Kaviraj S., et al., 2008, MNRAS, 388, 67

Kaviraj S., Peirani S., Khochfar S., Silk J., Kay S., 2009, MNRAS, 394, 1713

Kaviraj S., Tan K.-M., Ellis R. S., Silk J., 2011, MNRAS, 411, 2148

Kaviraj S., et al., 2017, MNRAS, 467, 4739

Keenan R. C., Barger A. J., Cowie L. L., 2013, ApJ, 775, 62

Kelvin L. S., et al., 2014, MNRAS, 444, 1647

Kennicutt Robert C. J., 1998, ARA&A, 36, 189

Kenworthy W. D., Scolnic D., Riess A., 2019, ApJ, 875, 145

Khochfar S., Burkert A., 2003, ApJl, 597, L117

Kim A., Goobar A., Perlmutter S., 1996, PASP, 108, 190

Kim S., et al., 2014, ApJS, 215, 22

Kirby E. N., Cohen J. G., Guhathakurta P., Cheng L., Bullock J. S., Gallazzi A., 2013, ApJ, 779, 102

Klypin A., Yepes G., Gottlöber S., Prada F., Heß S., 2016, MNRAS, 457, 4340

Knebe A., et al., 2018, MNRAS, 474, 5206

Kochanek C. S., et al., 2001, ApJ, 560, 566

Krause O., Tanaka M., Usuda T., Hattori T., Goto M., Birkmann S., Nomoto K., 2008, Nature, 456, 617

Kron R. G., 1980, ApJS, 43, 305

Lahav O., Lilje P. B., Primack J. R., Rees M. J., 1991, MNRAS, 251, 128

Larson R. B., 1974, MNRAS, 166, 585

Lavaux G., Hudson M. J., 2011, MNRAS, 416, 2840

Law N. M., et al., 2009, PASP, 121, 1395

Li C., White S. D. M., 2009, MNRAS, 398, 2177

Li W., Van Dyk S. D., Filippenko A. V., Cuillandre J.-C., Jha S., Bloom J. S., Riess A. G., Livio M., 2006, ApJ, 641, 1060

Li W., Chornock R., Leaman J., Filippenko A. V., Poznanski D., Wang X., Ganeshalingam M., Mannucci F., 2011a, MNRAS, 412, 1473

Li W., Chornock R., Leaman J., Filippenko A. V., Poznanski D., Wang X., Ganeshalingam M., Mannucci F., 2011b, MNRAS, 412, 1473

Licquia T. C., Newman J. A., 2015, ApJ, 806, 96

Lineweaver C. H., Tenorio L., Smoot G. F., Keegstra P., Banday A. J., Lubin P., 1996, ApJ, 470, 38

Lintott C., et al., 2011, MNRAS, 410, 166

Loveday J., Peterson B. A., Efstathiou G., Maddox S. J., 1992, ApJ, 390, 338

Lundgren S. C., Cordes J. M., Ulmer M., Matz S. M., Lomatch S., Foster R. S., Hankins T., 1995, ApJ, 453, 433

Lupton R., Gunn J. E., Ivezić Z., Knapp G. R., Kent S., 2001, , 238, 269

Madau P., Dickinson M., 2014, ARA&A, 52, 415

Maoz D., Mannucci F., Brandt T. D., 2012, MNRAS, 426, 3282

Martin D. C., et al., 2005, ApJl, 619, L1

Martin G., Kaviraj S., Devriendt J. E. G., Dubois Y., Laigle C., Pichon C., 2017, MNRAS, 472, L50

Martin G., Kaviraj S., Devriendt J. E. G., Dubois Y., Pichon C., 2018, MNRAS, 480, 2266

Maund J. R., 2017, MNRAS, 469, 2202

McGaugh S. S., Schombert J. M., Lelli F., 2017, ApJ, 851, 22

McNaught R. H., Beresford A. C., Seargent D. A. J., 1987, IAU Circ., 4421, 2

Merloni A., et al., 2012, arXiv e-prints, p. arXiv:1209.3114

Mihos J. C., Hernquist L., 1994, ApJl, 425, L13

Miluzio M., et al., 2013, A&A, 554, A127

Mo H. J., White S. D. M., 1996, MNRAS, 282, 347

Moore B., Ghigna S., Governato F., Lake G., Quinn T., Stadel J., Tozzi P., 1999, ApJ, 524, L19

Morrissey P., et al., 2007, ApJS, 173, 682

Naab T., Johansson P. H., Ostriker J. P., 2009, ApJl, 699, L178

Neill J. D., Hudson M. J., Conley A., 2007, ApJl, 661, L123

Noeske K. G., et al., 2007a, ApJ, 660, L43

Noeske K. G., et al., 2007b, ApJl, 660, L43

Noll S., Burgarella D., Giovannoli E., Buat V., Marcillac D., Muñoz-Mateos J. C., 2009, A&A, 507, 1793

Nugent P., Kim A., Perlmutter S., 2002, PASP, 114, 803

Nugent P. E., et al., 2011, Nature, 480, 344

Oparin D. V., Moiseev A. V., 2018, Astrophysical Bulletin, 73, 298

Parzen E., 1962, Ann. Math. Statist., 33, 1065

Pasquali A., van den Bosch F. C., Mo H. J., Yang X., Somerville R., 2009, MNRAS, 394, 38

Pearson W. J., et al., 2018, A&A, 615, A146

Peebles P. J. E., 1980, The large-scale structure of the universe

Peebles P. J. E., 1981, ApJl, 243, L119

Peebles P. J. E., 2002, in Metcalfe N., Shanks T., eds, Astronomical Society of the Pacific Conference Series Vol. 283, A New Era in Cosmology. p. 351 (arXiv:astro-ph/0201015)

Peebles P. J. E., Shaviv G., 1982, Space Sci. Rev., 31, 119

Perley D. A., et al., 2016, ApJ, 830, 13

Perlmutter S., Muller R. A., Newberg H. J. M., Pennypacker C. R., Sasseen T. P., Smith C. K., 1992, in Filippenko A. V., ed., Astronomical Society of the Pacific Conference Series Vol. 103, Robotic Telescopes in the 1990s. pp 67–71

Perlmutter S., et al., 1999, ApJ, 517, 565

Pesce D. W., et al., 2020, ApJl, 891, L1

Phillips M. M., 1993, ApJl, 413, L105

Pier J. R., Munn J. A., Hindsley R. B., Hennessy G. S., Kent S. M., Lupton R. H., Ivezić Ž., 2003, AJ, 125, 1559

Piffaretti R., Arnaud M., Pratt G. W., Pointecouteau E., Melin J. B., 2011, A&A, 534, A109

Pillepich A., et al., 2018, MNRAS, 473, 4077

Planck Collaboration et al., 2014, A&A, 571, A1

Planck Collaboration et al., 2018, arXiv e-prints, p. arXiv:1807.06209

Postman M., et al., 2012, ApJS, 199, 25

Preston G. W., Sneden C., Thompson I. B., Shectman S. A., Burley G. S., 2006, AJ, 132, 85

Ratcliffe A., Shanks T., Broadbent A., Parker Q. A., Watson F. G., Oates A. P., Fong R., Collins C. A., 1996, MNRAS, 281, L47

Richardson D., Jenkins Robert L. I., Wright J., Maddox L., 2014, AJ, 147, 118

Riess A. G., et al., 2016, ApJ, 826, 56

Riess A. G., Casertano S., Kenworthy D., Scolnic D., Macri L., 2018a, arXiv e-prints, p. arXiv:1810.03526

Riess A. G., et al., 2018b, ApJ, 861, 126

Riess A. G., et al., 2018c, ApJ, 861, 126

Riess A. G., Casertano S., Yuan W., Macri L. M., Scolnic D., 2019, ApJ, 876, 85

Sabatini S., Davies J., Scaramella R., Smith R., Baes M., Linder S. M., Roberts S., Testa V., 2003, MNRAS, 341, 981

Saglia et al. 1997, in Arnaboldi M., Da Costa G. S., Saha P., eds, Astronomical Society of the Pacific Conference Series Vol. 116, The Nature of Elliptical Galaxies; 2nd Stromlo Symposium. p. 180

Sako M., et al., 2011, ApJ, 738, 162

Sako M., et al., 2018a, PASP, 130, 064002

Sako M., et al., 2018b, PASP, 130, 064002

Salaris M., Cassisi S., 2005, Evolution of Stars and Stellar Populations

Salim S., et al., 2007, ApJS, 173, 267

Salim S., et al., 2016, ApJS, 227, 2

Salim S., Boquien M., Lee J. C., 2018, ApJ, 859, 11

Salpeter E. E., 1955, ApJ, 121, 161

Sandage A., Tammann G. A., Yahil A., 1979, ApJ, 232, 352

Schaye J., et al., 2015, MNRAS, 446, 521

Schechter P., 1976, ApJ, 203, 297

Schlegel D. J., Finkbeiner D. P., Davis M., 1998, ApJ, 500, 525

Schweizer F., Seitzer P., 1992, AJ, 104, 1039

Schweizer F., Seitzer P., Faber S. M., Burstein D., Dalle Ore C. M., Gonzalez J. J., 1990, ApJl, 364, L33

Scolnic D. M., et al., 2018, ApJ, 859, 101

Shanks T., Stevenson P. R. F., Fong R., MacGillivray H. T., 1984, MNRAS, 206, 767

Shanks T., Hogarth L., Metcalfe N., 2018, arXiv e-prints, p. arXiv:1810.07628

Shanks T., Hogarth L. M., Metcalfe N., 2019, MNRAS, 484, L64

Silverman J. M., et al., 2012, MNRAS, 425, 1789

Skillman E. D., 2005, , 49, 453

Skrutskie M. F., et al., 2006, AJ, 131, 1163

Smartt S. J., 2009, ARA&A, 47, 63

Smith N., Tombleson R., 2015, MNRAS, 447, 598

Smith J. A., et al., 2002, AJ, 123, 2121

Smoot G. F., et al., 1992, ApJ, 396, L1

Somerville R. S., Davé R., 2015, ARA&A, 53, 51

Speagle J. S., Steinhardt C. L., Capak P. L., Silverman J. D., 2014, ApJS, 214, 15

Stinson G. S., Dalcanton J. J., Quinn T., Kaufmann T., Wadsley J., 2007, ApJ, 667, 170

Stoll R., Prieto J. L., Stanek K. Z., Pogge R. W., 2013, ApJ, 773, 12

Stoppacher D., et al., 2019, MNRAS, 486, 1316

Stoughton C., et al., 2002, AJ, 123, 485

Strolger L.-G., et al., 2015, ApJ, 813, 93

Sutherland W., Rothnie P., 2015, MNRAS, 446, 3863

Sutherland W., et al., 2015, A&A, 575, A25

Taubenberger S., 2017, The Extremes of Thermonuclear Supernovae. p. 317, doi:10.1007/978-3-319-21846-5_37

Taubenberger S., et al., 2008, MNRAS, 385, 75

Taylor E. N., et al., 2011, MNRAS, 418, 1587

Taylor M., et al., 2014, ApJ, 792, 135

Thom C., et al., 2012, ApJl, 758, L41

Thomas D., Maraston C., Schawinski K., Sarzi M., Silk J., 2010, MNRAS, 404, 1775

Tomczak A. R., et al., 2014, ApJ, 783, 85

Tripp R., 1998, A&A, 331, 815

Tucker D. L., et al., 2006, , 327, 821

Tully R. B., Fisher J. R., 1977, A&A, 54, 661

Tully R. B., et al., 2013, AJ, 146, 86

Tumlinson J., Peeples M. S., Werk J. K., 2017, ARA&A, 55, 389

Turatto M., 2003, Classification of Supernovae. Springer Berlin Heidelberg, Berlin, Heidelberg, pp 21–36, doi:10.1007/3-540-45863-8_3, https://doi.org/10.1007/3-540-45863-8_3

Turner S., et al., 2021, MNRAS, 503, 3010

Umeda H., Nomoto K., 2003, Nature, 422, 871

Utrobin V. P., 1996, A&A, 306, 219

Van Den Bergh S., Tammann G. A., 1991, ARA&A, 29, 363

Van Dyk S. D., Peng C. Y., King J. Y., Filippenko A. V., Treffers R. R., Li W., Richmond M. W., 2000, PASP, 112, 1532

Vattis K., Koushiappas S. M., Loeb A., 2019, Phys. Rev. D, 99, 121302

Veilleux S., Osterbrock D. E., 1987, ApJS, 63, 295

Vulcani B., et al., 2011, MNRAS, 412, 246

Wang J., Deng J. S., Wei J. Y., 2010, MNRAS, 405, 2529

Wheeler J. C., Harkness R. P., 1990, Reports on Progress in Physics, 53, 1467

Whitbourn J. R., Shanks T., 2014, MNRAS, 437, 2146

Whitbourn J. R., Shanks T., 2016, MNRAS, 459, 496

White S. D. M., Rees M. J., 1978, MNRAS, 183, 341

Wong K. C., et al., 2020, MNRAS, 498, 1420

Woosley S. E., Weaver T. A., 1986, ARA&A, 24, 205

Wright A. H., et al., 2017, MNRAS, 470, 283

Wuyts S., et al., 2011, ApJ, 742, 96

Xiao L., Eldridge J. J., 2015, MNRAS, 452, 2597

Yi S. K., 2003, ApJ, 582, 202

York D. G., et al., 2000, AJ, 120, 1579

Zehavi I., Riess A. G., Kirshner R. P., Dekel A., 1998, ApJ, 503, 483

Zhao F.-Y., Strom R. G., Jiang S.-Y., 2006, , 6, 635

Zheng X. Z., Bell E. F., Papovich C., Wolf C., Meisenheimer K., Rix H.-W., Rieke G. H., Somerville R., 2007, ApJ, 661, L41

Zoroddu M. A., Aeseth J., Crisponi G., Medici S., Peana M., Nurchi V. M., 2019, Journal of Inorganic Biochemistry, 195, 120